CHARACTERISATION OF SOLID-LIQUID FLOW IN A CONTINUOUS OSCILLATORY BAFFLED REACTOR USING COMPUTATIONAL FLUID DYNAMICS

Guillermo Jimeno Millor

A thesis submitted for the degree of Doctor of Philosophy

Chemical Engineering

School of Engineering and Physical Sciences

Heriot-Watt University

March 2019

Abstract

Continuous Oscillatory Baffled Reactors (COBRs) have been proven a viable alternative to traditional batch reactors for organic synthesis and crystallization processes. This thesis investigates the behaviour of solids in liquid in a COBR using CFD. Firstly, CFD is used to analyse the validity of two existing models for the estimation of power density in this type of reactors, the "quasi-steady" model (QSM) and the "eddy enhancement" model. By using a revised power law dependency on the number-of-baffles term (n^x) in both models, an appropriate orifice discharge coefficient (C_D) in the QSM and a proposed empirical correlation estimate EEM's "mixing length", both models were successfully validated.

Secondly, energy losses experienced by both liquid and solid phases in COBRs are analysed; for the former, temporal pressure drop profiles and power dissipation rates along the length of a COBR are monitored for a wide range of operating and geometric conditions. The results provide detailed insights into the relationship between power dissipation and pressure drop profiles and reveals that geometries that are perfectly symmetric in the axial direction, i.e. periodically repeatable, do not present signs of energy losses. On the other hand, geometric events such as sections missing one or multiple baffle constrictions led to a decrement in power dissipation rates and velocities, caused by the eddy shedding phenomenon within the missing baffle sections. And sections with a reduced cross-sectional area of the baffle constriction and bend joints do not yield energy losses in the device; instead, they require a higher power density for the flow to overcome these constraints.

A multiphase (S-L) Eulerian- Lagrangian model was employed to simulate the presence of solid particles suspended in a continuous liquid phase in a COBR. The behaviour of these particles was monitored with time as they travelled downstream the device for particles of different sizes; results unveiled that as particles increases in size they experience dampening in oscillatory velocity, translating into smaller axial dispersion, longer residence times and a reduction of particles' suspension. For the determination of axial dispersion, both perfect and imperfect pulse methods were employed, the latter providing more reliable results.

Thirdly, this research introduces an alternative Lagrangian based methodology, i.e. the Smoothed-Particle Hydrodynamics (SPH), for the simulation of fluid flow in an OBR. The results from a bespoke SPH solver are compared with those from Eulerian

modelling, i.e. Finite Volume (FV) method, displaying a high degree of agreement. SPH was able to capture the expected flow characteristics in OBR as clearly and equally as its Eulerian counterpart. Making full use of SPH's capabilities and its Lagrangian feature, two new indexes for the assessment of mixing and plug flow efficiency have also been proposed.

Acknowledgements

Firstly, I would like to thank my supervisors and mentors Professor Xiong-Wei Ni and Doctor Yeaw Chu Lee, whose patience, expertise, understanding and wisdom have enormously helped me throughout the course of my PhD project.

I express my gratitude to the Centre for Innovative Manufacturing in Continuous Manufacturing and Crystallization (CMAC) community for its support and initiative. Furthermore, this research would not be possible without the financial assistance of the UK's Engineering and Physical Sciences Research Council (EPSRC).

Finally, I would like to thank my family and friends for their constant love, support and encouragement; I could have not done it without every single one of you.

ACADEMIC REGISTRY

Research Thesis Submission

Please note this form should be bound into the submitted thesis.

Name:	Guillermo Jimeno Millor		
School:	School of Engineering and Physical Sciences		
Version: *(i.e. First, Resubmission, Final)*	Final	Degree Sought:	Doctor of Philosophy in Chemical Engineering

Declaration

In accordance with the appropriate regulations I hereby submit my thesis and I declare that:

1. The thesis embodies the results of my own work and has been composed by myself
2. Where appropriate, I have made acknowledgement of the work of others
3. Where the thesis contains published outputs under Regulation 6 (9.1.2) these are accompanied by a critical review which accurately describes my contribution to the research and, for multi-author outputs, a signed declaration indicating the contribution of each author (complete Inclusion of Published Works Form – see below)
4. The thesis is the correct version for submission and is the same version as any electronic versions submitted*.
5. My thesis for the award referred to, deposited in the Heriot-Watt University Library, should be made available for loan or photocopying and be available via the Institutional Repository, subject to such conditions as the Librarian may require
6. I understand that as a student of the University I am required to abide by the Regulations of the University and to conform to its discipline.
7. Inclusion of published outputs under Regulation 6 (9.1.2) shall not constitute plagiarism.
8. I confirm that the thesis has been verified against plagiarism via an approved plagiarism detection application e.g. Turnitin.

* *Please note that it is the responsibility of the candidate to ensure that the correct version of the thesis is submitted.*

Signature of Candidate:	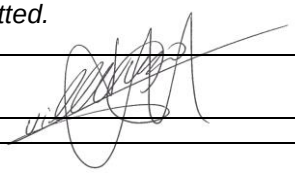	Date:	*21st of July, 2019*

Submission

Submitted By *(name in capitals):*	*GUILLERMO JIMENO MILLOR*
Signature of Individual Submitting:	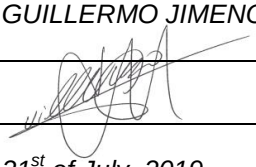
Date Submitted:	*21st of July, 2019*

For Completion in the Student Service Centre (SSC)

Received in the SSC by *(name in capitals):*			
Method of Submission *(Handed in to SSC; posted through internal/external mail):*			
E-thesis Submitted ***(mandatory for final theses)***			
Signature:		Date:	

Table of Contents

List of Tables

List of Figures

Nomenclature

AAE	averaged absolute error (%)
A	reactor's cross-sectional area (m^2)
A_p	cross-sectional area of a particle (m^2)
C	concentration (kg m^{-3})
C_D	orifice discharge coefficient
C_d	drag force coefficient
C_{CFL}	Courant–Friedrichs–Lewy coefficient
c_0	the reference speed of sound (m s^{-1})
D	tube diameter (m)
D_a	axial dispersion coefficient (m^2 s^{-1})
D_b	baffle hole diameter (m)
D_p	diameter of a particle (m)
E	normalised concentration
F	Force (N)
F_D	drag force (N)
F_{PG}	pressure gradient force
F_{VM}	pressure gradient force
f	oscillation frequency (Hz)
g	gravity (m s^{-2})
h	smoothing length of a kernel function (m)
$\underline{\underline{I}}$	identity matrix
K_i	inertial correction factor in the "eddy enhancement" model
κ	smoothing length related constant
k	turbulent kinetic energy (m^2 s^{-2})
κh	the effective area of a kernel function
ℓ	"mixing length" (m)
l_o	turbulent integral length scale (m)
L	reactor's length (m)
L_b	spacing between baffles (m)
L_b^{opt}	optimum spacing between baffles (m)
m	mass (kg)
N	total elements in a summation
n	number of baffles in the system

NM neighbouring mixing index (proposed in this work)

Pe Peclet number

PF plug flow index (proposed in this work)

Q volumetric flow rate (ml min^{-1})

R tube radius (m)

R^2 coefficient of determination

r radial position (m)

$\vec{r}$ position of each infinitesimal particle (m)

Re_o oscillatory Reynolds number

Re_n net flow Reynolds number

Re_o^{NEW} new oscillatory Reynolds number (proposed in this work)

R_V axial to radial velocity ratio

S time-averaged exponential stretch rate (s^{-1})

St Strouhal number

St^* oscillatory Strouhal number proposed by Ni and Gough (1997)

t time (s)

$\bar{t}$ mean residence time (s)

T oscillation period (s)

TR transfer function for "open-open" boundary conditions (s^{-1})

U mean net velocity (m s^{-1})

u velocity (m s^{-1})

u_{inlet} inlet velocity (m s^{-1})

$u_{min\text{-}h}$ minimum velocity required for the suspension of slurry in a horizontal tube

u_{net} net inlet velocity (m s^{-1})

u_t terminal velocity (m s^{-1})

V reactor's volume (m^3)

W kernel function

W_b baffle width (m)

x position in the horizontal axis (m)

x_o oscillatory center-to-peak amplitude (m)

x_p piston's position (m)

y position in the vertical axis (m)

z position in the depth axis (m)

α the ratio of the area of orifice to the area of tube (the restriction ratio)

β optimal to used baffle spacing ratio $\left(L_b{}^{opt}/L_b\right)$

δ phase shift angle (rad)

Δp pressure drop (Pa)

Δp_{net} pressure drop (Pa)

Δp_o maximum center-to-peak pressure drop fluctuation (Pa)

Δt time-step (s)

Δx control volume size (m)

ε turbulent dissipation rate ($m^2\ s^{-3}$)

ε_v power density ($W\ m^{-3}$)

θ normalised time ($t/\bar{t}$)

μ viscosity ($kg\ m^{-1}s^{-1}$)

ρ density ($kg\ m^{-3}$)

σ stress (Pa)

σ^2 variance

$\sigma_\theta{}^2$ dimensionless variance

τ viscus stress (Pa)

υ kinematic viscosity ($m^2\ s^{-1}$)

υ_e eddy kinematic viscosity ($m^2\ s^{-1}$)

ϕ property under evaluation

ψ velocity ratio (Re_o/Re_n)

Ω continuous domain

$\Omega_{\mathbf{r}}$ the $\vec{r}$ point-centred continuous domain

ω oscillation angular frequency ($rad\ s^{-1}$)

List of Publications

Jimeno, G., Y.C. Lee, and X.-W. Ni, *On the evaluation of power density models for oscillatory baffled reactors using CFD*. Chemical Engineering and Processing - Process Intensification, 2018. 134: p. 153-162.

Jimeno, G., Y.C. Lee, and X.-W. Ni, *Smoothed particle hydrodynamics – A new approach for modeling flow in oscillatory baffled reactors*. Computers & Chemical Engineering, 2019. 124: p. 14-27.

Jimeno, G., Y.C. Lee, and X.-W. Ni, *The effect of particle size on flow in a continuous oscillatory baffled reactor using CFD*. Submitted to Computers & Chemical Engineering.

Chapter 1 Introduction

1.1 Motive of the Research

While stirred tank reactors have been the workhorse in chemical industry, tubular plug flow reactors, such as continuous oscillatory baffled reactors (COBR), have emerged as a viable alternative. Significant process and economic benefits were reported in the utilisation of COBR in a broad range of processes, e.g. crystallisation [1-17], reactions [18-20], heterogeneous catalysis [21-23] and fermentation processes [24, 25]. However, research in terms of evaluation and estimation of power dissipation rate for this type of reactors has largely been stagnated for the past 25 years [26]. This gap has been addressed by the content of this PhD work.

How particles behave in COBR? What causes dampening in oscillatory velocity experienced by the liquid phase due to the presence of solid particles in COBR? Being able to understand and avoid this phenomenon is imperative for the optimum design and development of processes in COBRs. The present study has the motivation of targeting and identifying the potential reasons of this phenomenon using CFD.

Extensive literature is available on the characterisation of flows in COBRs by monitoring residence time distribution (RTD) profiles of tracer concentration [27-45], i.e. all these studies were performed for a single liquid phase framework, thus there is a knowledge gap in the design of COBRs for multi-phase flow processes, which was recently pointed out by Ejim et al. [46] and corroborated by Kacker et al. [47]. This work, for the first time, investigates the effects of particle size on axial dispersion, and evaluates residence times and velocities experienced by particles of different sizes, leading to the quantification of the degree of suspension and the oscillation dampening experienced by solid particles in a COBR.

Existing numerical models of mixing processes in oscillatory baffled reactors (OBR) were developed during the 1990s [28, 48-53] in a two-dimensional framework, evolving to 3-D in the following decades [36, 40, 54-64]; however, all these studies were mainly Eulerian-based. While few studies made use of a secondary Lagrangian phase for the modelling of massless tracers [50, 53, 65], its use has rather been limited due to the expensive computational costs of coupling continuous Eulerian-Lagrangian phases. These computational constraints for the coupling of Eulerian-Lagrangian phases become ever more significant when modelling dynamic solid-liquid flows with complex

interactions, e.g. particle agglomeration, breakage, growth, dissolution, etc. The motivation of this work is to introduce an alternative Lagrangian based methodology, namely Smoothed-Particle Hydrodynamics (SPH), for predicting flow patterns and assessing mixing performance in COBR.

1.2 Objectives of the Project

The primary objectives of this PhD research were to:

- Update and validate the two existing models for the estimation of power dissipation rates in OBRs/COBRs;
- Evaluate the effect of different operating conditions and geometric features on pressure drop and power density propagation along the length of a COBR while identifying energy losses in the liquid phase;
- Evaluate the effect of unexpected geometric events, such as un-baffled straight joints, baffle constriction with reduced cross-sectional area and bend joints, on liquid phase energy losses;
- Evaluate the effect of solid particles' sizes on their axial dispersion, residence time distributions, oscillatory velocities and suspension using Eulerian-Lagrangian coupling;
- Develop a Smoothed-Particle Hydrodynamics (SPH) solver for the modelling of fluid flow in a two-dimensional OBR and use its implicit Lagrangian information to find new ways of quantifying mixing efficiency.

1.3 Structure of Thesis

Following this introduction, this thesis commences in Chapter 2 gathering a thorough literature review on oscillatory baffled reactors; this includes: history, mechanics of its flow, different geometric features, power dissipation, methods of evaluating mixing efficiency in OBRs and history of numerical studies that modelled oscillatory baffled flow. Chapter 3 proceeds on describing the geometry of the target device, as well as the numerical setup and grid of the CFD model utilised in this study. The first set of results of this research is presented in Chapter 4, where the "quasi-steady" model and the "eddy enhancement" model for the estimation of power dissipation in oscillatory baffled flow

are updated and validated. Following this, Chapter 5 analyses the evolution of pressure drop and power density along the length of the reactor for a wide range of operating conditions and geometric features. Similarly, Chapter 6 examines the impact of geometric event on pressure drop and power density propagation. Carrying on from this, Chapter 7 presents the results of a two-phase (S-L) flow model, and investigates the effect of particles' size on the behaviour of solids in a COBR. This study focuses on solids' axial dispersion, RTD profiles and the dampening in oscillatory velocity they have experienced, as well as the reduction in their degree of suspension. Furthermore, in Chapter 8, this projects moves away from commercially available CFD packages and goes on to develop a self-written solver using Smoothed-Particle Hydrodynamics methodology for the modelling of fluid flow in an OBR. Finally, the overall conclusions from the research are presented in Chapter 9 together with recommendations for future work.

This thesis interpolates material from three publications by the author. Chapters 4, 7 and 8 are based on References [66], [67] and [68], respectively. Some materials from these publications have also been incorporated into the different sections of Chapters 2 and 3. In doing so, each chapter includes the relevant equations used for the calculation and treatment of results.

Chapter 2 Literature Review

2.1 Introduction

Chemical and process engineering systems often include unit operations with the purpose of separating or mixing difference compounds, this is the case for cyclone separators, fluidised beds and mixing tanks among others. The performance of these processes is greatly linked to flow characteristics in their geometric and operating conditions. While stirred tank reactors have been the workhorse in chemical industry, tubular plug flow reactors, such as continuous oscillatory baffled reactors (COBR), have emerged as a viable alternative for research and industrial applications due to their ability to offer uniform mixing [69] and linear scale up [70].

2.2 History

Oscillatory flow in baffled systems has been an emerging area of research since the mid-1980s. However, precedents date back to 1935 when Van Dijck [71], for the first time, reported the use of a pulsed sieve plate column to enhance liquid-liquid contact, and to 1959 when Karr developed reciprocating-plate extraction columns [72]. A decade and a half later, oscillatory flow through furrowed channels was applied in membrane filtration by Bellhouse et al. in 1973 [73] and the formation of vortexes and mixing patterns in this system was later numerically characterised by Sobey et al. and Stephanoff et al. in 1980 [74, 75]. The outcomes of the last two mentioned publications were in agreement with those by Knott and Mackley [76], also published in 1980, who reported that the interaction of sharp edges with oscillatory flow leads to eddy formation and enhances mixing efficiency.

In 1987, the concept of oscillatory baffle reactor (OBR) was introduced by Mackley [77]. This device simply consisted of a cylindrical tube containing periodically spaced orifice baffles, onto which oscillatory flow was superimposed, generating vortexes during each oscillatory cycle. The formation of eddies and the mixing efficiency of this system was later quantified by Brunold et al. [78] in 1989. That same year, the work published by Dickens et al. showed the efficiency of these types of devices when working in a continuous mode. The work reported near plug flow behaviour under certain operating conditions due to the efficacy of eddy mixing [27]. This represented a benchmark in the field that led to vast research during the 1990s, broadening the

understanding and potential applications of oscillatory baffled reactors. Howes and Mackley (1990) [79] reported similar observations as those found in Dickens et al.'s work and once again proved the capability of OBRs to reduce axial dispersion and mimic plug flow; a detailed study of axial dispersion in OBRs was carried out both experimentally and numerically by Howes (1988) [80].

When compared with traditional stirred tank reactors (STR), OBRs proved to improve efficiency and control over several processes such as mass [81, 82] and heat transfer [83], scale-up correlations [70, 84] and residence time distribution (RTD) [69]. Furthermore, the constant creation and cessation of vortexes in OBRs, caused by the combination of orifice baffles and fluid oscillation, unveiled a more efficient and uniform mixing than that provided by STRs [85]. Such control over different flow characteristics gives COBRs the capability of reproducing near plug flow RTDs even at laminar flow regimes [29, 30, 86], allowing processes to run continuously while providing long residence times.

Conventionally, many processes were run in batch, reporting poor mixing and inconsistent product quality from one batch to another. Therefore, the features presented by OBRs and COBRs revealed great potential for industrial applications of this type of reactors. Numerous studies have been undertaken for processes such as polymerization [18], biodiesel production [19, 20], heterogeneous catalysis [21-23] and fermentation processes [24, 25]. Intensive research on crystallisation in OBRs/COBRs has been performed both in public and confidential domains, e.g. paracetamol [1, 3, 4, 10], L-glutamic acid [2, 5, 8, 14, 15], aspirin [7], a pharmaceutical API [6], sodium chlorate [11, 12, 87], adipic acid [88], urea [89, 90], α-lipoic acid:nicotinamide co-crystal [91], palm oil [92] and cyclopentane hydrate [93]. Seeded cooling crystallisation in NiTech DN15 crystallisers has successfully been running [94] for 10 hours [15] and four weeks in CMAC (Centre for Continuous Manufacturing and Crystallisation). In addition to this, antisolvent crystallisation from both experimental and modelling aspects [16, 17, 95] was also undertaken in a COBR.

2.3 Fluid Mechanics

The flow in oscillatory baffled reactors is dominated by the fluid oscillation that is superimposed onto the net flow, which creates eddies when the flow interacts with the baffles. Mixing is then generated by the formation and cessation of these eddies, leading

to strong radial motions that provide uniform mixing in each inter-baffled section. The oscillatory pulses are periodic and fully reversing, with each cycle of the oscillation consisting of two semi-cycles, each of which contains flow acceleration, a peak velocity and deceleration. This generates a sinusoidal velocity – time function. Vortex rings are formed downstream of the baffles with each acceleration of the flow. Once the peak velocity is reached, the flow decelerates, sweeping the vortices into the bulk [78]; this results in an interaction between vortices generated in each semi-cycle of the oscillation. Hence, the pair of eddies generated during the forward and backward strokes collide and disrupt one another within each baffle-cell, generating highly efficient radial mixing and chaotic fluid patterns within the cell. The mixing efficiency attained within each baffle-cell is similar to that achieved in a perfectly stirred tank. Therefore, an OBR can be compared to a series of multiple perfectly mixed stirred tanks, having the capability of achieving plug flow behaviour along the length of the device. The mixing mechanism in an oscillatory baffled reactor can be understood with the help of Figure 2.1.

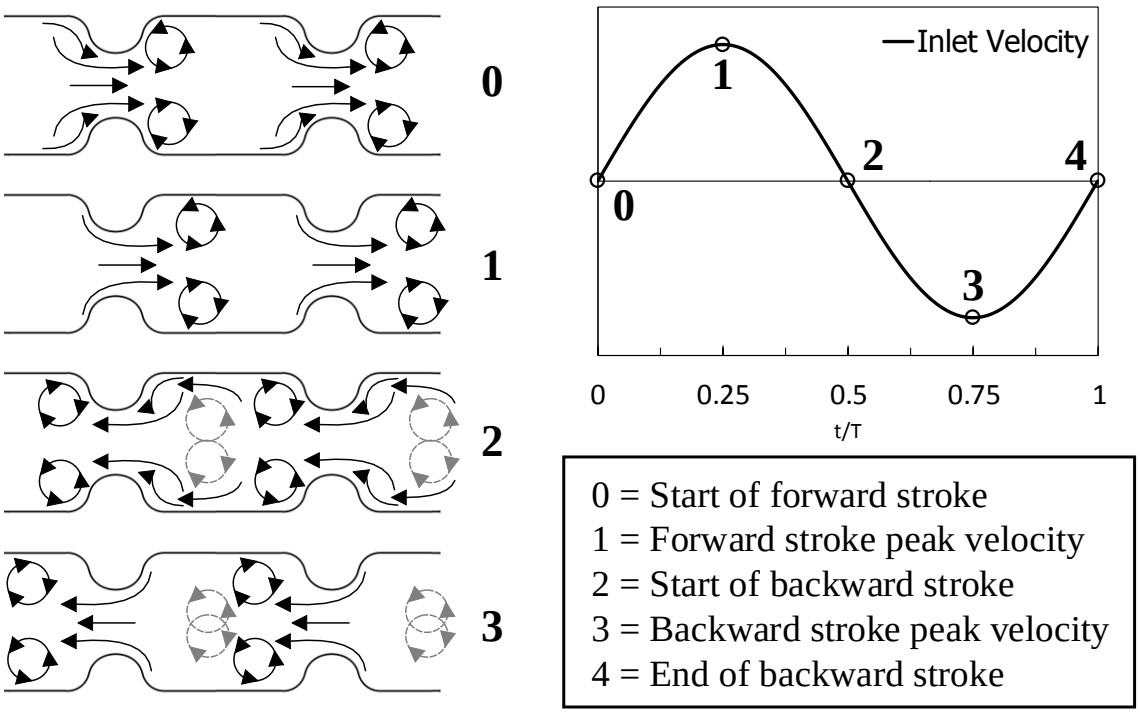

Figure 2.1. *Mixing mechanism in an oscillatory baffled reactor*

The intensity of the mixing in OBRs and COBRs is controlled by two variables: the oscillation amplitude and the oscillation frequency. These are typically modulated by a piston in charge of applying oscillatory motion to the fluid upstream of the system; the

piston is commonly powered by a linear or rotary motor. The temporal displacement of the piston and the oscillatory inlet velocity in an OBR are represented by:

$$x_p(t) = -x_o \cos(\omega t) \tag{2.1}$$

$$u_{inlet}(t) = \omega x_o \sin(\omega t) \tag{2.2}$$

where x_p is the piston's position (m), u_{inlet} the inlet mean velocity (m s^{-1}), $\omega=2\pi f$ the oscillation angular frequency (rad s^{-1}), f the oscillation frequency (Hz), x_o the oscillation centre-to-peak amplitude (m) and t the time (s). For a continuous oscillatory baffled reactor, Equation (2.2) must include the contribution of the net flow of the system, Q (ml min^{-1}), yielding:

$$u_{inlet}(t) = u_{net} + \omega x_o \sin(\omega t) \tag{2.3}$$

where u_{net} is the net inlet velocity (m s^{-1}), which can be calculated as the ratio of the net flow to the cross-sectional area of the tube (A). Figure 2.2 and 2.3 display a generic COBR experimental setup for cooling crystallisation processes and the schematics of continuous oscillatory baffled flow, respectively.

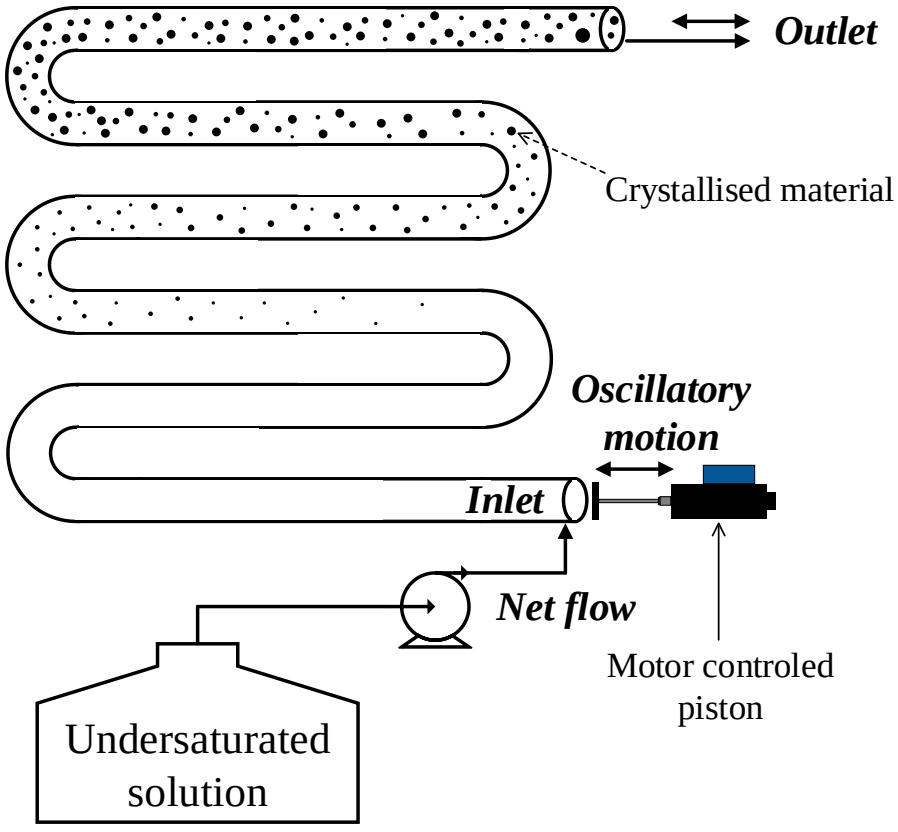

Figure 2.2. *Schematic of a generic COBR setup for cooling crystallisation processes*

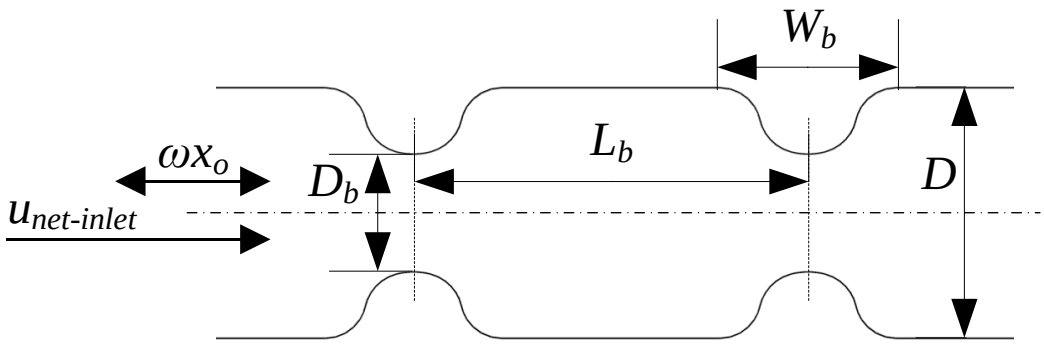

Figure 2.3. *Continuous oscillatory baffled flow*

From a fluid mechanical stand point, flow in a pipe is widely characterised by the Reynolds number (Re), a dimensionless group governed by the ratio of inertial to viscus forces, which helps in understanding and predicting flow behaviours. For flow in a pipe, Reynolds number values < 2000 denote laminar flow, in which viscus forces are dominant and the fluid moving along the pipe presents a streamlined nature. At Re > 4000, the flow is expected to be in the turbulent regime, where the layered structure of the fluid is disrupted, giving rise to tendencies of chaotic eddies as inertial forces take over; at 2000 < Re < 4000 the flow is said to be in the transition regime [96]. However, oscillatory baffled reactors yield complex flow patterns that cannot be characterised by the Reynolds number alone. The dimensionless numbers that govern the conditions of the flow in a COBR are the net flow Reynolds number (Re_n), the oscillatory Reynolds number (Re_o), the Strouhal number (St) and the ratio of the area of the orifice to the area of the tube, known as the restriction ratio (α).

$$\mathrm{Re}_n = \frac{u_{net}\rho D}{\mu} \tag{2.4}$$

$$\mathrm{Re}_o = \frac{\omega x_o \rho D}{\mu} \tag{2.5}$$

$$St = \frac{D}{4\pi x_o} \tag{2.6}$$

$$\alpha = \frac{D_b{}^2}{D^2} \tag{2.7}$$

where ρ is the fluid density (kg m^{-3}) and μ its dynamic viscosity (kg m^{-1} s^{-1}), D is the diameter of the tube (m) and D_b the diameter of the baffle hole (m).

The concept of a pulsating Reynolds number was early introduced in 1945 by Binnie, in order to describe the intensity of the mixing input to the system [97]. The maximum pulsating velocity (m s^{-1}) was then given as the product ωx_o in the work of Sarpkaya [98]; the well accepted derivation of Re_o was defined as per Equation (2.5) by Brunold et al. in 1989 [78]. It has been reported that under low Re_o of 100 – 300, flow patterns are dominated by symmetrical vortexes generated within each baffle cell, leading to potential plug flow behaviour [69, 99]. For high Re_o (>300) this symmetry is broken, leading to intense mixing and chaotic patterns in the flow [28]. The oscillatory Reynolds number is widely used as the dimensionless number for the comparison of results from processes undertaken on COBR geometries or operating conditions. However, while Re_o accounts for the oscillatory variables x_o and f, other operational parameters such as net flow and geometric features like baffle diameter, baffle spacing (L_b) and the restriction ratio remain unaccounted for; further discussion on this is taken up in Section 4.5.

The Strouhal number was initially introduced by Sobey in 1980 [74] to account for the new parameters associated with oscillatory baffled flow, see Figure 2.3. He described its physical meaning as the ratio of scales between channel length and fluid particle displacement [100]. Again, Brunold et al. was responsible for the derivation of St as per Equation (2.6), this dimensionless number was described as the ratio of column diameter to amplitude of oscillation [78]. Further evaluation and analysis on dimensionless groups for oscillatory baffled flow was taken-up by Ni and Gough, who proposed updated derivations for Re_o and St that included relevant geometrical features specific of OBRs [101]. Despite their efforts, subsequent publications in the area continued to use the original forms of these numbers, i.e. Equations (2.5) and (2.6).

An additional dimensionless group regarded as the velocity ratio (ψ) was proposed by Stonestreet and Van Der Veeken (1999), who unveiled residence time distributions in COBRs as a function of Re_n and Re_o. For this reason, the velocity ratio was defined as the ratio of two mentioned Reynolds numbers [102]:

$$\psi = \frac{Re_o}{Re_n} \tag{2.8}$$

Studies in COBRs have reported that plug flow behaviour is more likely to be achieved for velocity ratios of 2 – 10 [102-104]. This brings to light the ability of COBRs to

decouple mixing from the net flow; this feature allows COBRs to achieve plug flow with intense radial mixing under laminar flow regimes.

2.4 Reactor Geometry

Besides operating conditions, the geometric characteristics of OBRs are what determine the intensity and efficiency of the mixing process that takes place in oscillatory baffled flow. The geometric parameters include the type of baffle, its thickness, the dimeter of its orifice and the separation space between baffles. The schematic of a generic moving-baffle OBR is represented in Figure 2.4.

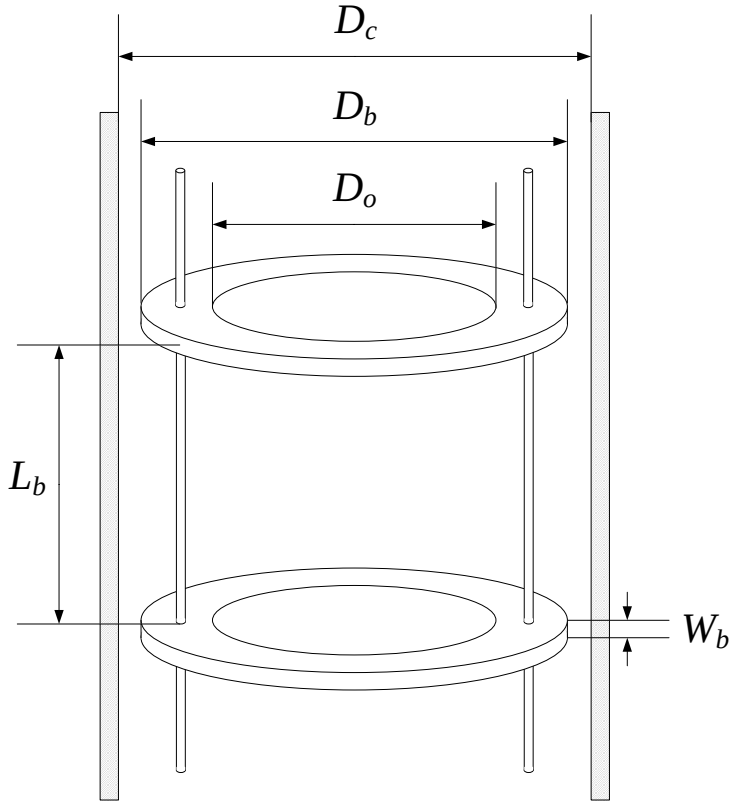

Figure 2.4. *Schematic of a generic moving-baffle OBR*

Where D_c is the column diameter (m), D_b the baffle diameter (m), D_o the orifice dimeter, W_b the baffle width (m) and L_b the baffle spacing (m). Note how in lab COBRs containing smooth-edged baffles, e.g., NiTech DN15, the baffle diameter and baffle orifice become identical ($D_b = D_o$), see Figure 2.3. Besides the geometric difference between reactors with in-wall baffles and reactors with moving-baffles, the oscillatory mechanism of the former is generated by a pulsed flow, i.e. moving fluid, and the latter's is generated by the oscillatory movement of the baffles.

Baffle spacing is a key parameter affecting vortex generation and eddy-eddy interaction. Baffles should be sufficiently spaced from one another in order to leave room for the generation of vortexes, i.e. vortexes will not be created if baffles are too close to each other, resulting in flow channelling through the centre channel of diameter D_o. On the other hand, if the space in between baffle constrictions is too large, vortexes interaction during the change in direction strokes (2 and 4) will diminish. Therefore, the energy carried by eddies will dissipate into the bulk fluid before they collide with one-another, resulting in lower mixing intensity and stagnant regions within the baffle-cell.

The optimal baffle spacing required to provide the highest mixing efficiency in oscillatory baffled flow with smooth-edged baffles has been reported as 1.5 times the tube dimeter (L_b = 1.5D) by Brunold et al. (1989) through visual assessment of flow patterns [78] and by Zhang et al. (1996), who analysed oil – water dispersion efficiency in an OBR [105]. For air – water mass transfer in a similar device, Ni and Gao (1996) reported a value of L_b = 1.8D as the optimum baffle spacing [82]. In a different study, Gough et al. (1997) reported that maximum efficiency of eddy mixing patterns can be achieved with a baffle spacing of up to twice the tube diameter and an oscillation amplitude of a quarter of the baffle spacing; this study was carried out in a moving-baffle reactor [106]. A comparative study on OBRs containing moving-baffles and in-wall baffles was performed by Ni et al. (1998), who reported an optimal value of L_b = 2D for the former and of L_b = 1.8D for the latter [32]. It should be noted that a baffle spacing of 1.5D has been the norm for OBRs and COBRs containing smooth-edged baffles [2, 20, 22, 26, 39, 43, 57, 60, 107-109].

Ni et al. (1998) also reported an optimal baffle thickness of 2 – 3 mm; these findings agreed with those from a study by the same author, where a thickness of 3 mm was identified as optimal for the suspension of methylmethacrylate in OBRs since it gave the best size distribution [110]. Another geometric feature assessed in the comparative study performed by Ni et al. (1998) was the restriction ratio (α), whose optimal value was reported to be in the range of 0.20 – 0.22.

The gap size between baffle disks and the tube diameter ($D_c - D_b$) in moving-baffles OBRs was examined by Ni and Stevenson (1999), who reported its impact on mixing times and concluded that the larger the gap size, the lower is the mixing efficiency in OBRs [33]. Therefore, baffles tightly fitted to the wall are preferred.

In 2000, Ni et al. investigated the effect of baffle geometric design on a larger scale, i.e. D = 0.38 m. Results revealed that the dependency of mixing efficiency on L_b and D_o was of the same magnitude as reported for smaller scales, reinforcing the linear scale-up process of OBRs [111].

The evaluation of flow patterns in OBRs with different baffle types has been a recurrent topic, e.g. disc baffles, annular doughnut baffle, a combination of disc and annular baffles [112], and helical baffles. These types of studies are relevant to this day, the most recent being published in 2016 by Mazubert et al., who compared the mixing performance of single orifice baffles, disc-and-donut baffles and three novel variations of helical blades; their findings suggested that each geometry enhanced different characteristics of the flow, thus *"no firm conclusions can be made at this stage regarding the general performance"* [64, 65].

2.5 Power Dissipation & Energy Losses

During the design and development of any mixing device, its power requirement is a key area that needs understanding [113]. Furthermore, power density is a widely used variable for the comparison of mixing efficiency among different apparatus [3]. Regarding processes undertaken in OBRs, research suggested that this type of reactors is more power efficient than traditional STRs [111, 114], even reporting constant power density values at different scales, thus giving OBRs the upper hand for scaling-up processes.

Essentially two published models have been used in the field of OBRs and COBRs: the "quasi-steady" model (QSM) from the work of Jealous and Johnson [115] and the "eddy enhancement" model (EEM) by Baird and Stonestreet [116, 117]. The latter was developed as an empirical mathematical model to predict dynamic pressure response and power dissipation rates in oscillatory baffled flow; it aimed to overcome the operating limitations of the already existing QSM. However, despite their efforts, QSM has continued to dominate power density calculation in OBRs and COBRs [2, 5, 11, 13, 21, 32, 33, 35, 46, 70, 84, 87, 107, 110, 111, 118, 119]. The origin of both models stemmed from the evaluation of pressure drop over oscillatory devices; and while the equations were empirical, research has neither been carried out on the validation of the above models nor on how these models could be used in continuous operation where there is a net flow.

Further details on the derivation and validity of these two models, along with more information on pressure drop and power dissipations rates in OBRs and COBRs are expanded in Chapter 4.

Hardly any work has been conducted on energy propagation and energy losses in oscillatory baffled flow. A directly proportional dependency between power dissipation rates and the number of baffles present in the system was report in 1989 by Brunold et al. [78]. During the early days of COBR research, 1991, Mackley et al. [120] measured power dissipation values experimentally and computationally, and proved the existence of a phase shift between velocity and pressure oscillation waves; pointing out how this phase shift "*could lead to a significant power reduction of the system*". Not until very recently, academic studies [14, 121] and confidential industrial trials reported a decrease in the oscillatory velocity experienced by liquid tracers and solid particles as they travel downstream a COBR. Further research is yet to be undertaken on this area, in order to understand and avoid the causes of potential energy losses and oscillation dampening experienced in COBRs.

For this reason, a detailed analysis of potential energy losses experienced by a continuous liquid phase in a COBR at different operating conditions and geometric designs is undertaken in Chapter 5. Additionally, an analysis of the impact of unexpected geometric events is laid out in Chapter 6. Lastly, thorough examination of the velocity of solids particles suspended in continuous oscillatory baffled flow is presented in Chapter 7.

2.6 Evaluation of Mixing Efficiency

Numerous studies have been conducted in order to assess the effect of different operational and geometric parameters on mixing efficiency in OBRs and COBRs. The quantification of mixing efficiency is not a trivial matter and the dimensionless numbers aforementioned in Section 2.3 are often insufficient. The two most commonly reported techniques in the assessment of mixing in this type of reactors are:

1. The measurement of residence time distribution (RTD) profiles and

2. The characterisation of the axial dispersion [122].

Residence time distribution (RTD) profiles of tracer concentration have widely been used to characterise flows in OBRs/COBRs, see for example, Dickens et al. (1989) [27]

Mackley and Ni (1991, 93) [29, 69], several publications by Ni where the impact of geometric features was analysed [30-33] and studies where the effect of operational parameters was addressed [37, 123].

Furthermore, RTD data was employed to assess the impact of fluid density in axial dispersion in these types of devices [34, 35] and also to aid the development of a new generation of meso-scale COBRs [38, 39, 41, 42]. The linearity of the scale-up process of OBRs and COBRs was postulated by Ni et al. in 2001 based on the impact of device diameter on axial dispersion [70], this was later corroborated by Smith and Mackley in 2006 [124], who also proposed a multi-orifice baffled design for OBRs/COBRs. Recently, a scaled-down version of the commercially available NiTech DN15 crystalliser was proposed by Olivia et al., also based on the comparison of axial dispersion performance among devices at different operating conditions [125].

Predominantly, RTD studies for axial dispersion assessment in OBRs and COBRs have been performed by injecting homogenous liquid tracers in a continuous liquid phase. RTD profiles are popularly measured using conductivity probes, with the exception of the work by Fitch and Ni, who in 2003 proposed the use of a non-intrusive laser-induced fluorescence (LIF) technique for this purpose [126, 127]. . In 1999, Stonestreet and Van Der Veeken measured tracer RTD profiles in order to obtain optimal operating conditions for plug flow behaviour in a COBR, claiming that the dimensionless velocity ratio (ψ) was sufficient for a priory plug flow efficiency assessment [102]. The ratio ψ is considered an important parameter in COBR operations; minimal dispersion has been reported for ψ values of 2 – 10 [102-104]. However, the majority of the processes performed in COBRs involve interaction between liquid and solid phases, e.g., crystallisation, where solid slurries vary in density throughout the system. Therefore, the analysis of RTD and axial dispersion of liquid phases is not sufficient, for instance, the work of Briggs et at. demonstrated that a ψ of 20 [15] was suitable for a continuous seeded crystallisation of L-glutamic acid, which is a higher value when compared to the range recommended for single liquid phase.

Recent work by Ejim et al. [46] on slurry plug flow behaviour in a continuously operated meso-scale COBR has underlined the lack of information on the behaviour of a secondary solid phase in COBRs. This was further emphasised by Kacker et al. [47] who reported that not only the optimal operating conditions for minimal axial dispersion involving solids were different from that of single phase, but also longer times were

spent by solids in a COBR, highlighting the need to properly address the effect of different solid particles on axial dispersion. Baptista et al. [128] analysed the behaviour of suspended solid particles of different sizes and densities in a baffled reactor; however, their system did not include oscillatory flow and their findings were inconclusive, as the interaction between particles was too substantial for the effects of size and density to be evaluated. To address the knowledge gap in this area of research, the present work provides novel information on RTD performance of secondary solid phase in a COBR for different particles sizes in Chapter 7.

Two other alternative methods and indexes to quantify mixing efficiency in oscillatory flow have been used in a number of computational studies, i.e. the so called axial to radial velocity ratio [43, 57, 58] and stretch rates [50, 53]. Based on the above, a novel mixing assessment coefficient is proposed in this work in Section 8.4.4.

2.6.1 Models for the Quantification of Axial Dispersion

Axial dispersion is a measure of the rate at which a tracer is spread axially into the bulk of a fluid flow in a reactor, which can be used to assess the degree of mixing achieved.

There are two principal models frequently used in literature for the description of axial dispersion in oscillatory baffled flow:

1. The diffusion model and

2. The tank-in-series model.

The diffusion model, firstly applied to OBRs by Mackley and Ni (1991) [69], describes macro-mixing by using an analogy of Levenspiel and Smith's molecular diffusion model [122] and is appropriate in physical processes where a relatively high degree of homogenous mixing is achieved [129]. It has been widely used for the quantification of axial dispersion in COBRs [29, 31-35, 38, 43-47, 65, 69, 104, 123-127]. Further information on the effects of perfect pulse and imperfect pulse methods on dispersion is described in Section 7.4.2.

The tank-in-series model [129] assesses the degree of mixing by calculating the number of well-mixed tanks required to emulate the axial dispersion performance of a given system and it was firstly implemented in OBRs by Dickens et at. (1989) [27]. Dickens et at. discovered that this model produced similar results as the diffusion model

at certain conditions: a minimum value of the inverse Peclet (Pe) number of 0.025 compares closely to the *N* value from the tank-in-series model as Pe ≈ 2*N*.

There are treatments to the tank-in-series models in literature [129] that are able to account for upstream mixing, such as the one utilised by Howes and Mackley (1990) [79], illustrated in Figure 2.5. An imperfect pulse for the injection of the tracer was proposed, which quantifies a single parameter regarded as backmixing coefficient, *F*. This model achieved a reasonable good fit [80] for a modest range of operating conditions. A disadvantage of this treatment is that the backmixing coefficient, *F*, is not a real measure of physical mixing, since a degree of short-recirculating takes place and contributes to its value. Mecklenburg and Hartland (1975) discussed in great detail the relationship of the tank-in-series with backmixing model and the diffusion model, reporting the Peclet number of each baffle-cell as a function of the backmixing coefficient [130].

$$\frac{1}{Pe_{cell}} \approx F + 0.5 \tag{2.9}$$

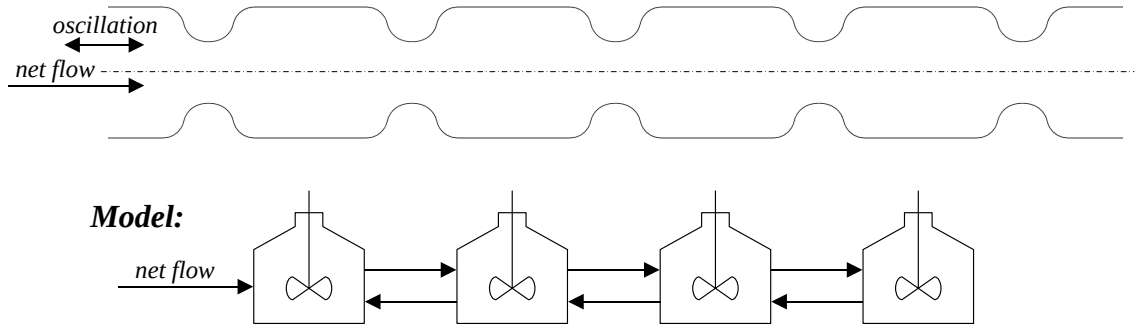

Figure 2.5. *The "tanks-in-series with backmixing" model*

The tank-in-series model has been used in a significant number of studies for axial dispersion assessment in OBRs/COBRs [35, 39, 41, 79, 102, 103, 131].

2.7 Modelling of Oscillatory Flow in Baffled Reactors

The characterisation of oscillatory baffled flow through computational modelling dates back to the early 1980s. The first work was reported by Sobey, who extensively analysed flow through furrowed channels making use of 2D numerical methods in 1980 and 1983 [74, 132]; soon after, in 1986, Ralph performed a 2D numerical study of oscillatory flow in wavy walled tubes [133]. Thereafter, Ghaddar et al. utilised a spectral element method for the assessment of laminar oscillatory flow in periodically-

grooved channel [134] and examined heat transfer enhancement in grooved tubes [135], in 1984 and 1986, respectively. The findings of these studies together with experimental observations pointed the generation of vortexes in oscillatory baffled flow as the cause of highly efficient mixing. In 1988, based on the work by Sobey and Ralph, Howes developed a numerical solver for the assessment of dispersion of unsteady flow in baffled tubes [80]. This work was taken up by Roberts, who expanded it in 1992 with the simulation of 2D oscillatory flows in baffled channels [136]. These studies solved time-dependent Navier-Stokes equations by utilising a vorticity–stream function with finite difference formulation; the fluid considered was incompressible and Newtonian. The flow was assumed to be axi-symmetrical, i.e. flow patterns and eddies are symmetrical to the centre line of the reactor; and periodic in the spatial domain, i.e. identical flow within each baffle-cell. These solvers were able to successfully predict the chaotic nature of the flow in OBRs where asymmetric flow patterns were often observed under certain operating conditions [28, 120]. In 1995, Roberts and Mackley made use of massless Lagrangian particles, whose motion was based on the time-dependent velocity field; the Lagrangian information of these particles was used in the calculation of fluid stretch rates as an alternative method for mixing quantification [50]. This was further explored in 1999 by Mackley and Neves Saraiva, who used this passive Lagrangian tracer for the calculation of stretch rates and concentration fields in oscillatory baffled flow [53]. Although asymmetric flow patterns were successfully reproduced by Roberts and Mackley [51], the two-dimensional nature of these solvers prevented their simulated results to be experimentally validated for chaotic flow in three-dimensional OBRs.

It was not until the beginning of the 21st century that the rapid development of computational fluid dynamics (CFD) software allowed unsteady 3D flow to be modelled, as done by Ni et al. [54], who validated their results with experiments using the digital particle image velocimetry (DPIV) technique. Jian and Ni expanded this work and compared velocity fields obtained from simulations using RANS turbulence models (k-ε) with those obtained from large-eddy simulation (LES) [36]; their study concluded that the time-averaging process in RANS turbulence models prevented them from reproducing asymmetric chaotic patterns in OBRs, thus regarding LES as a more suitable alternative. This led to further work by Ni et al., who investigated the turbulent integral length scale in an oscillatory baffled column using LES and DPIV [55]. Their work also reported the contribution from the sub-grid scale turbulence to be relatively

small for all the conditions considered in their study and the majority of the subsequent modelling studies used a *laminar* solver. The work by Jian and Ni assessed OBR scale-up behaviour through the analysis of simulated OBR velocity fields [58]; and the work by Fitch et al. investigated the effects of fluid viscosity on flow patterns in OBRs using DPIV and CFD codes [57].

Since the mid-2000s until now, numerous studies have utilised CFD codes for the assessment and characterisation of flow in OBRs and COBRs. Chew et al. and Chew and Ristic used simulated shear rate distribution to compare flow patterns between an OBR and an impeller-driven stirred vessel (IDSV) [3, 56]. CFD codes and the use of particle image velocimetry (PIV) measurements played a major role in the development of so-called meso-scale OBRs by Reis et al. in 2005 [59], which presented different, albeit similar flow features, suitable for chemicals' manufacturing and catalysis screening. Their simulated flow patterns also aid in the understanding of RTD performance in meso-scale COBRs [40]. The effects of different operating conditions on the generation of asymmetric oscillatory flow in a tube containing sharp-edged periodic baffles was studied by Zheng et al. in 2007 using PIV measurements and CFD codes [60]. PIV measurements were also utilised by Nogueira et al., in 2012, for the validation of numerical models to simulate oscillatory flow in an OBR containing periodic-tri-orifice baffle geometries [63]. Most recently, commercial CFD packages were used in the work of Mazubert et al., who analysed mixing efficiency for different geometric designs of COBRs [64]; and also in the examination of heat transfer and power dissipation in COBRs at different operating conditions performed by González-Juárez et al. [109].

All of the aforementioned studies were performed exclusively for single liquid phase with Eulerian based numerical simulations. Modelling of multiphase flow in COBRs has been limited to the simulation of a homogenous tracer by the addition of a transport of species model. Examples of this are the work of Manninen et al., who examined the impact of fluid viscosity on mixing efficiency [43]; the work of González-Juárez et al., who analysed RTD and axial dispersion performance in different geometric designs of COBRs [44]; and the work of Kimuli et al. who investigated axial dispersion in a meso-scale COBR at different operating conditions [45]. The simulation of discrete Lagrangian phases in oscillatory baffled flow was performed with the sole purpose of modelling passive tracers, consisting of massless particles whose movement is driven by the velocity field of an Eulerian phase, e.g. the abovementioned studies of Roberts

and Mackley [50], Mackley and Neves Saraiva [53] and a recent investigation on mixing performance in COBRs for five different baffle designs [65]. The limited work reported in this area can easily be attributed to the expensive computational costs of coupling continuous Eulerian-Lagrangian phases for dynamic fluid-solids modelling including their complex interactions. Coupling CFD with the Population Balance Equation (PBE) to model crystallisation processes in stirred tank crystallisers is a well-documented example [137]. The question remains if the complexity of these coupled methodologies can be avoided and if all phases can be modelled using a Lagrangian scheme.

As a result, this work presents a novel approach to modelling oscillatory baffled flow using a mesh-free Lagrangian method, i.e. Smoothed-Particle Hydrodynamics (SPH); this is presented in Chapter 8.

Chapter 3 Problem Definition & Simulation Method

3.1 Geometry

The target device of this study is the commercially available NiTech DN15 COBR reactor (http://www.nitechsolutions.co.uk/products/dn15-range/), as shown in Figure 3.1. The geometric dimensions of the DN15 and all design details were provided by the manufacturer, Alconbury Weston Ltd (http://www.a-w-l.co.uk/); Figure 3.2 presents the two CAD detailed geometries supplied by the manufacturer. The total length of the reactor is 752 mm, containing 32 baffle-cells; Figure 3.3 shows a detailed schematic with the geometric dimensions of the DN15 straight section.

Figure 3.1. *Commercially available NiTech DN15 COBR reactor (http://www.nitechsolutions.co.uk/products/dn15-range/)*

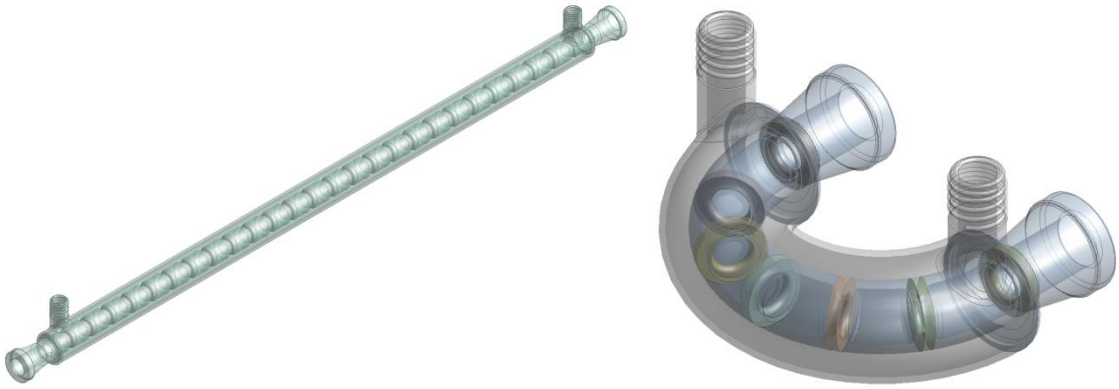

Figure 3.2. *Detailed CAD geometry of a straight section (left) and a bend joint (right) of the NiTech DN15*

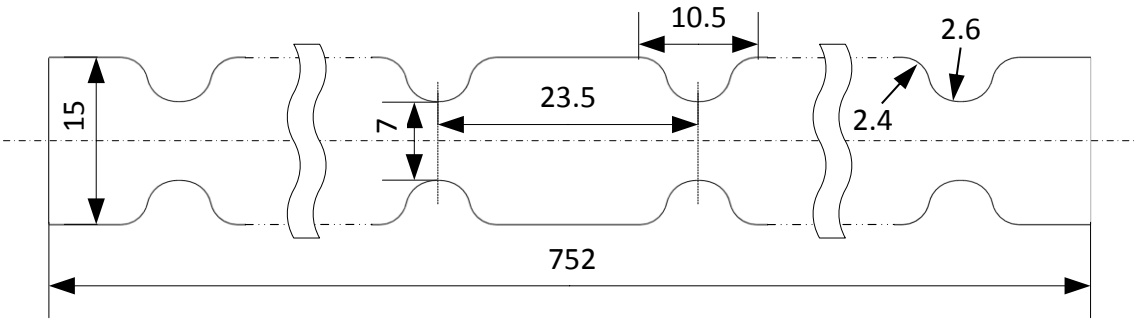

Figure 3.3. *Dimensions of the NiTech DN15 straight section used in CFD simulations; all dimensions are in mm* [66]

The vast majority of CFD simulations performed during the present work were undertaken for the geometry shown in Figure 3.3, however, for the effect of different geometric parameters on energy dissipation, pressure drop and flow patterns in COBRs, certain geometric features of the device were modified for specific runs; any geometry that differs from Figure 3.3 is described in the corresponding chapter where its results are presented.

3.2 Numerical Simulations Setup

There are two main branches that compose the study of fluid mechanics: kinematics, which describes the motion of a fluid based on the structure of its velocity field; and dynamics, which analyses the forces that develop within the fluid as a result of its motion. The fundamentals of both kinematics and dynamics are combined with Newton's second law and the mass conservation principal in order to derive a system of

differential equations describing the structure of a steady flow and the evolution of an unsteady flow [138].

Let's consider the flow of a homogenous fluid consisting of a single phase, and a particular fluid parcel with centre at point $\vec{x}$. Taking the limit when the size of the parcel tends to zero, at time *t*, this fluid parcel experiences a velocity $\vec{u}(\vec{x},t)$; therefore, $\vec{u}(\vec{x},t)$ is an infinitely differentiable function of position and time. This is the foundation of the *continuum approximation*, which is valid as long as a continuous fluid is discretised above the molecular scale where random molecular motions manifest [138]. Similarly, the density (ρ) of a fluid parcel can be computed as the ratio of fluid mass to fluid volume contained in the parcel; in doing so and taking the limit when the size of the parcel becomes infinitesimal, density becomes a function of position and time, $\rho(\vec{x},t)$.

This very process can be applied to any kinematic or thermodynamic property, *f*, such as a temporal or spatial derivative of the velocity, the kinetic or thermal energy, the entropy or the enthalpy per unit mass of the fluid. Hence, this variable can also be regarded as a function of position and time, $f(\vec{x},t)$. This method of describing the kinematic structure of the flow, as well as the thermodynamic and physical properties of the fluid, is regarded as *Eulerian framework*. This methodology focuses on spatially fixed spaces, whose properties are given by the fluid that flows through them at a specific moment in time [138].

On the other hand, sometimes, it can be mathematically convenient to describe a fluid domain as a continuous set of point particles, whose state and motion define the state of the fluid and the properties of the flow. Each point particle is then assigned an identification vector, $\vec{P}_P$, containing three dimensionless scalar variables, i.e. $\vec{P}_P\left(P_{Px},P_{Py},P_{Pz}\right)$. In doing so, any physical, thermodynamic or kinematic property at a specific location, $\vec{x}$, and time, *t*, can be regarded as the property of the fluid point particle that happens to be at that particular location at that precise instant: $f(\vec{x},t)=f\left(\vec{X}\left(\vec{P}_P,t\right),t\right)$; where $\vec{X}$ is the position of the particle point $\vec{P}_P$ at the exact instant *t*. This methodology is regarded as *Lagrangian framework*, which focuses on tracking individual fluid particles that move through space and time.

Eulerian and Lagrangian formulations are related by the material derivative (D/Dt); this mathematical relationship is further explained in Appendix 1. Figure 3.4 displays an explanatory scheme of the differences between these two methodologies.

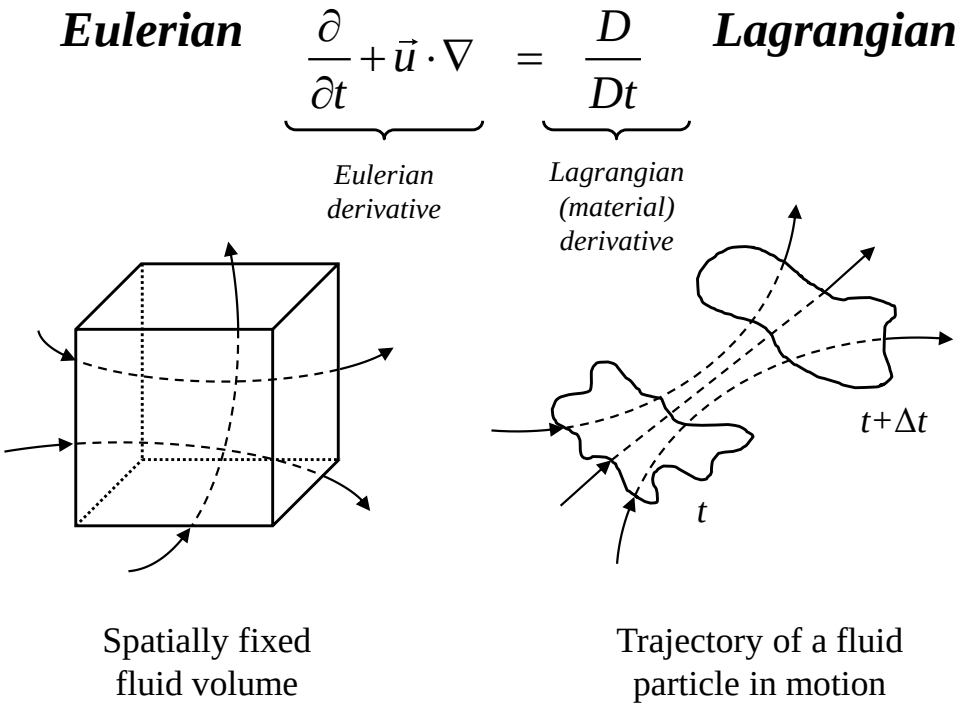

Figure 3.4. *Explanatory scheme of Eulerian and Lagrangian frameworks*

All the numerical modelling of this study is performed under a *Eulerian framework* using the commercially available ANSYS® Fluent 15.0 CFD package; with the exception of the secondary discrete phase modelled in Chapter 7 and the novel approach to model oscillatory baffled flow presented in Chapter 8, which are solved under a *Lagrangian framework*. The relevant theory describing these Lagrangian methods is explained in the corresponding chapters.

3.2.1 Model Equations

The equations that describe fluid flow consist of the continuity equation, or mass continuity equation, and the Navier–Stokes equations, or equations of motion (momentum). The equations of mass and momentum conservation are described by Equations (3.1) and (3.2), respectively:

$$\frac{D\rho}{Dt} + \rho \nabla \cdot \vec{u} = 0 \tag{3.1}$$

$$\frac{D(\rho\vec{u})}{Dt} = \nabla \cdot \underline{\underline{\sigma}} + \rho\vec{g} + \sum \vec{F} \tag{3.2}$$

where $\frac{D}{Dt}$ is the material derivative, ∇ the gradient vector operator, ρ the density, $\vec{u}$ the velocity vector, $\underline{\underline{\sigma}}$ the total stress tensor defined as $\underline{\underline{\sigma}} = -p\underline{\underline{I}} + \underline{\underline{\tau}}$ and $\sum \vec{F}$ the summation of any external forces. Within the total stress tensor, $\underline{\underline{I}}$ is the identity matrix, p the pressure, $\underline{\underline{\tau}} = \left(-\frac{2}{3}\mu\nabla\cdot\vec{u}\right)\underline{\underline{I}} + 2\mu\underline{\underline{E}}$ is the viscus stress tensor with $\underline{\underline{E}}$, the rate of strain tensor, given by $\underline{\underline{E}} = \frac{1}{2}\left[(\nabla\vec{u}) + (\nabla\vec{u})^T\right]$. Additional information on the derivation of the mass continuity and Navier-Stokes equations is included in Appendix 3.

Equations (3.1) and (3.2) can be expanded by partial derivatives for Cartesian coordinates (x, y, z) into Equations (3.3) and (3.4), respectively:

$$\frac{\partial\rho}{\partial t} + \frac{\partial(\rho u_x)}{\partial x} + \frac{\partial(\rho u_y)}{\partial y} + \frac{\partial(\rho u_z)}{\partial z} = 0 \tag{3.3}$$

$$\frac{\partial(\rho u_x)}{\partial t} + u_x\frac{\partial(\rho u_x)}{\partial x} + u_y\frac{\partial(\rho u_x)}{\partial y} + u_z\frac{\partial(\rho u_x)}{\partial z} = \rho g_x - \frac{\partial p}{\partial x} + \left(\frac{\partial\tau_{xx}}{\partial x} + \frac{\partial\tau_{yx}}{\partial y} + \frac{\partial\tau_{zx}}{\partial z}\right) \tag{3.4a}$$

$$\frac{\partial(\rho u_y)}{\partial t} + u_x\frac{\partial(\rho u_y)}{\partial x} + u_y\frac{\partial(\rho u_y)}{\partial y} + u_z\frac{\partial(\rho u_y)}{\partial z} = \rho g_y - \frac{\partial p}{\partial y} + \left(\frac{\partial\tau_{xy}}{\partial x} + \frac{\partial\tau_{yy}}{\partial y} + \frac{\partial\tau_{zy}}{\partial z}\right) \tag{3.4b}$$

$$\frac{\partial(\rho u_z)}{\partial t} + u_x\frac{\partial(\rho u_z)}{\partial x} + u_y\frac{\partial(\rho u_z)}{\partial y} + u_z\frac{\partial(\rho u_z)}{\partial z} = \rho g_z - \frac{\partial p}{\partial z} + \left(\frac{\partial\tau_{xz}}{\partial x} + \frac{\partial\tau_{yz}}{\partial y} + \frac{\partial\tau_{zz}}{\partial z}\right) \tag{3.4c}$$

where the components of the stress tensor can be expressed in terms of velocity gradients as:

$$\tau_{xx} = -2\mu\frac{\partial u_x}{\partial x} - \frac{2}{3}\mu\nabla\cdot\vec{u} \tag{3.5a}$$

$$\tau_{yy} = 2\mu\frac{\partial u_y}{\partial y} - \frac{2}{3}\mu\nabla\cdot\vec{u} \tag{3.5b}$$

$$\tau_{zz} = 2\mu \frac{\partial u_z}{\partial z} - \frac{2}{3}\mu \nabla \cdot \vec{u} \tag{3.5c}$$

$$\tau_{xy} = \tau_{yx} = \mu \left(\frac{\partial u_x}{\partial y} + \frac{\partial u_y}{\partial x} \right) \tag{3.5d}$$

$$\tau_{zx} = \tau_{xz} = \mu \left(\frac{\partial u_x}{\partial z} + \frac{\partial u_z}{\partial x} \right) \tag{3.5e}$$

$$\tau_{yz} = \tau_{zy} = \mu \left(\frac{\partial u_y}{\partial z} + \frac{\partial u_z}{\partial y} \right) \tag{3.5f}$$

The equations of mass and momentum conservation for an incompressible flow with constant viscosity can substantially be simplified and are given by Equations (3.6) and (3.7), respectively; assuming that the system is fully flooded with a single-phase fluid:

$$\nabla \cdot \vec{u} = 0 \tag{3.6}$$

$$\rho \left(\frac{\partial \vec{u}}{\partial t} + \vec{u} \cdot \nabla \vec{u} \right) = -\nabla p + \mu \nabla^2 \vec{u} \tag{3.7}$$

Equations (3.6) and (3.7) can be decomposed using partial derivatives for Cartesian coordinates into Equations (3.8) and (3.9):

$$\frac{\partial u_x}{\partial x} + \frac{\partial u_y}{\partial y} + \frac{\partial u_z}{\partial z} = 0 \tag{3.8}$$

$$\rho \left(\frac{\partial u_x}{\partial t} + u_x \frac{\partial u_x}{\partial x} + u_y \frac{\partial u_x}{\partial y} + u_z \frac{\partial u_x}{\partial z} \right) = -\frac{\partial p}{\partial x} + \mu \left(\frac{\partial^2 u_x}{\partial x^2} + \frac{\partial^2 u_x}{\partial y^2} + \frac{\partial^2 u_x}{\partial z^2} \right) \tag{3.9a}$$

$$\rho \left(\frac{\partial u_y}{\partial t} + u_x \frac{\partial u_y}{\partial x} + u_y \frac{\partial u_y}{\partial y} + u_z \frac{\partial u_y}{\partial z} \right) = -\frac{\partial p}{\partial y} + \mu \left(\frac{\partial^2 u_y}{\partial x^2} + \frac{\partial^2 u_y}{\partial y^2} + \frac{\partial^2 u_y}{\partial z^2} \right) \tag{3.9b}$$

$$\rho \left(\frac{\partial u_z}{\partial t} + u_x \frac{\partial u_z}{\partial x} + u_y \frac{\partial u_z}{\partial y} + u_z \frac{\partial u_z}{\partial z} \right) = -\frac{\partial p}{\partial z} + \mu \left(\frac{\partial^2 u_z}{\partial x^2} + \frac{\partial^2 u_z}{\partial y^2} + \frac{\partial^2 u_z}{\partial z^2} \right) \tag{3.9c}$$

All the numerical simulations performed in this study, using the commercially available ANSYS® Fluent 15.0 CFD package, solve for the three-dimensional time-dependent mass conservation and momentum conversation equations described as per Equations

(3.8) and (3.9), respectively. These equations solve for the velocity field, $\vec{u} = \left(u_x, u_y, u_z\right)$, and pressure field, *p*, given that sufficient initial and boundary conditions are provided. In order to do so, these partial differential equations are integrated and discretised, $\iiint dx\,dy\,dz = \Delta x \Delta y \Delta z$, resulting in a system of algebraic equations. Consequently, the domain upon which these equations are applied and solved must be discretised [138]. The three most popular methods for the discretisation of these equations are *finite difference*, *finite element* and *finite volume*. This study makes use of the *finite volume method*, which is the norm for the most well-established commercially available CFD codes, such as PHOENICS, STAR-CD, ANSYS® CFX and ANSYS® Fluent. The *finite volume method* is implemented as per the following summarised steps [139]:

- Division of the domain into a set of discrete control volumes using a computational grid/mesh.
- Integration of governing equation of fluid flow over each individual control volume, generating algebraic equations for the discrete variables, i.e. pressure, velocities, temperature and any other conserved scalars.
- Solutions of the resultant equation system by an iterative method.

3.2.2 Solver

All simulations were performed using a *laminar solver*; which is consistent with literature. This solver has extensively been used during the past [54, 57, 59] and present decade [44, 45, 64, 65, 109] when modelling fluid flow through oscillatory baffled reactors using CFD, including flows at relatively high Re_o (up to 8043) [43, 58].

The solver is defined in ANSYS® Fluent as pressure-based segregated, in which the mass conservation constraint of the velocity field is achieved by solving a pressure correction equation. The pressure correction equation is derived from the continuity equation and the conservation of momentum equations, in such a way that the velocity field, corrected by the pressure, satisfies the continuity [139]. This algorithm belongs to the class of methods known as the projection methods [140]. The pressure field is therefore obtained from the pressure correction equation; for additional information on the derivation and form of this equation, refer to ANSYS® Fluent Theory Guide [139].

In the pressure-based segregated solver, the governing equations are solved sequentially, i.e. segregated from one another. Due to the non-linear and coupled nature of the equations, this process requires an iterative solution process until convergence is achieved; each iterative step is illustrated in Figure 3.5.

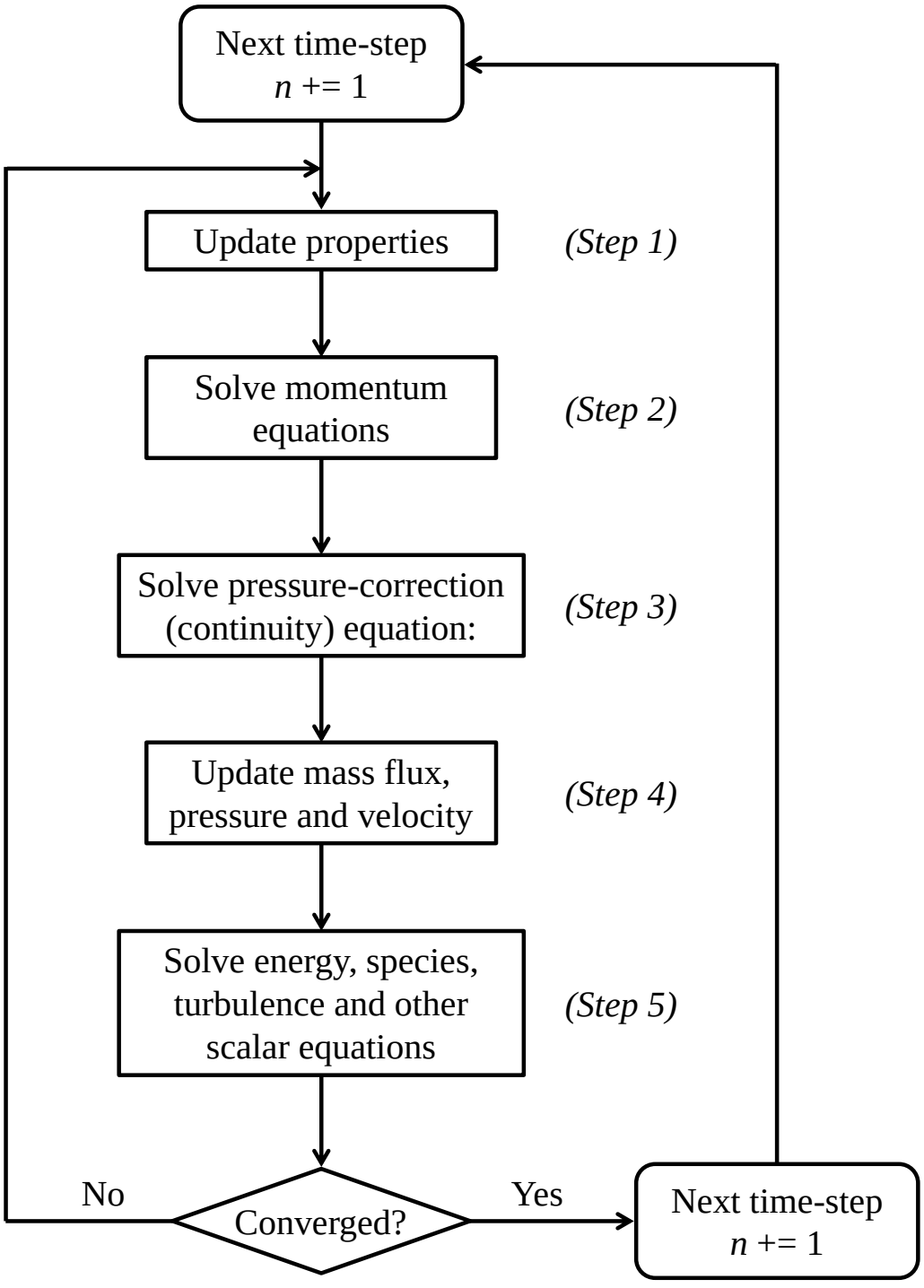

Figure 3.5. *Pressure-based segregated solver solution method*

In addition, because of the coupled nature of the governing equations, this segregated method requires a pressure-velocity coupling algorithm that is implemented into the

pressure correction equation, in order to satisfy the continuity equation. ANSYS® Fluent's SIMPLE pressure-velocity coupling algorithm was used for all the simulations of this study. For additional information on this algorithm refer to ANSYS® Fluent Theory Guide [139].

3.2.3 Discretisation Schemes

By default, ANSYS® Fluent stores values of variables at the centre of the control volume cells (ϕ_c) and the values at the centre of every face of each control volume cell (ϕ_f) are calculated according to the spatial discretisation scheme selected. The difference between cell-centred and face-centred values is illustrated in Figure 3.6.

A *second order upwind* scheme was utilised for the spatial discretisation of the momentum equation [139]:

$$\phi_f = \phi_{c_i} + \nabla\phi_{c_i} \cdot \vec{d}_{f_i} \tag{3.10}$$

where ϕ_{c_i} and $\nabla\phi_{c_i}$ are the cell-centred value and its gradient in the upstream control volume cell, *i*. $\vec{d}_{f_i}$ is the displacement vector from the centroid of the upstream control volume cell, *i*, to the centre of the face, *f*. The gradient $\nabla\phi_{c_i}$ is computed following the *least squares cell-based* method. This method assumes variables to change linearly from the centre of a control volume cell, *i*, to the centre of a contiguous cell, *j* [139]:

$$\nabla\phi_{c_i} \cdot \vec{d}_{ij} = \left(\phi_{c_i} - \phi_{c_j}\right) \tag{3.11}$$

where $\vec{d}_{ij}$ is the displacement vector from the centroid of the control volume cell, *i*, to the centroid of a contiguous cell, j. Equation 3.11 is written for every cell contiguous to cell *i*, resulting in a system of linear equations, which is solved in a least-squares sense [139].

A *second order* scheme was utilised for the interpolation of pressure at the faces of the grid [139]:

$$p_{f_{ij}} = \frac{1}{2}\left(p_{c_i} + p_{c_j}\right) + \frac{1}{2}\left(\nabla p_{c_i} \cdot \vec{d}_{f_i} + \nabla p_{c_j} \cdot \vec{d}_{f_j}\right) \tag{3.12}$$

where $p_{f_{ij}}$ is the pressure at the centre of face common to two contiguous control volumes cell, f_{ij}; $\vec{d}_{f_i}$ and $\vec{d}_{f_j}$ are the displacement vectors to the centre of the face f from the centroid of control volume cell i and j, respectively.

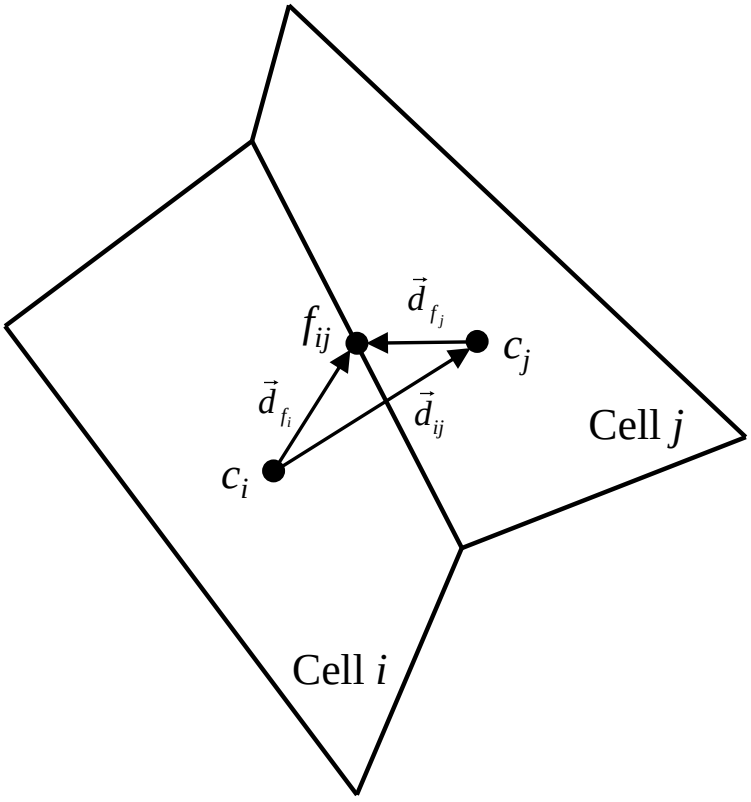

Figure 3.6. *Illustration of spatial discretisation of two-dimensional control volume cells*

As aforementioned, all simulations were performed under a *transient* framework; therefore the governing equations must also be discretised in time. This requires the integration of every term in the partial differential equations over a time-step, Δt, as illustrated in Figure 3.5. The change of a given variable, ϕ, with time is defined as $\frac{\partial \phi}{\partial t} = F(\phi)$, where $F(\phi)$ includes any spatial discretisation. A *first order implicit* scheme was utilised for the temporal discretisation in this study [139]:

$$\phi^{n+1} = \phi^n + \Delta t F\left(\phi^{n+1}\right) \tag{3.13}$$

The time-step was set to 2 ms throughout all simulations, except for run #5 (f = 8 Hz) – refer to table 4.1 – where a time-step of 0.5 ms was selected. This ensured that the convergence criteria (residuals of 10^{-3} and 10^{-4} for continuity and momentum equations respectively) were met and the number of time-steps per oscillation cycle was above 125, which is higher than others reported in recent literature for these types of

oscillatory baffled devices [44, 65]. The average value of the Courant–Friedrichs–Lewy coefficient (C_{CFL}) [141] was consistently maintained below 6 and the maximum C_{CFL} value below 50.

$$C_{CFL} = u\frac{\Delta t}{\Delta x} \tag{3.13}$$

where Δx is the size of a control volume cell and u the velocity at that control volume cell.

3.2.4 Boundary Conditions

Incompressible water (ρ = 998.2 kg m^{-3}, $\mu = 1.003 \cdot 10^{-3}$ kg m^{-1} s^{-1}) was the selected fluid for this study. The inlet and outlet of the device were modelled as open boundaries. Time-dependent inlet velocity profile was imposed with a User Defined Function (UDF) as per Equation (2.3). In order to minimize the impact of inlet boundary conditions on the main flow, the inlet oscillatory velocity was imposed with a fully developed parabolic profile as:

$$u_{inlet}(r,t) = 2 \cdot \left[u_{net} + \omega x_o \sin(\omega t) \right] \cdot \left(1 - \frac{r^2}{R^2} \right) \tag{3.14}$$

where R is the COBR outer radius and r is calculated as: $r = \sqrt{y^2 + z^2}$.

The outlet boundary conditions were set at constant gauge pressure of 0 Pa, and operating temperature and pressure conditions were set at 300 K and 101325 Pa, respectively. Walls in the system were modelled as *no-slip* boundaries.

For consistency with the vast majority of literature on OBRs and COBRs, the net flow velocity at the inlet is named in this work as u_{net}. This should not be confused with the *mean* net velocity of the system, termed as U in this work. The net volumetric flow rate, Q, is constant and u_{net} is calculated from Q/A. However, while both Q and u_{net} are constant, the net flow velocity does change along the length of the reactor due to the presence of smooth-edged orifice baffles, as shown in Figure 3.3. It should be noted that sharp-edged baffles were used in previous studies, smooth-edged baffles are fabricated in all DN15 series and used in this work, where $V \neq L \cdot A$. Subsequently, the velocity through orifices ($u_{net\text{-}baffle}$) is defined as Q/A_b and the *mean* net velocity (U) of the system is within the range of $Q/A \leq U \leq Q/A_b$, where A_b is the cross-sectional area of the

baffle orifice $\left(\frac{\pi D_b^{\,2}}{4}\right)$. When the volume of the DN15 reactor is known, U is calculated as QL/V.

3.3 Mesh Generation

The computational domain illustrated in Figure 3.3, thirty-two DN15 baffle-cells, is discretised into a large number of small volume control cells through the generation of a computational grid. The density of the selected mesh is of ~117 k nodes per baffle-cell.

The number of computational nodes per baffle was selected through a mesh sensitivity analysis undertaken on a 5-baffle-cell tube geometry, illustrated in Figure 3.7, considering global mesh refinement. This analysis was performed at the most adverse conditions considered in this study, proving the highest axial velocities (Re_o = 10505) and the most rapid changes of flow direction (f = 8 Hz), hence requiring a finer mesh. Simulations were run for 24 oscillatory cycles. Pressure drop vs time profiles, $\Delta p(t) = p_1(t) - p_2(t)$, and velocity magnitude vs time profiles extracted at lines 1 & 2 and planes 1 & 2 (as shown in Figure 3.7) were cycle-averaged. The resulting pressure drop and velocity profiles (duration of an oscillatory cycle) were compared for meshes of five different resolutions, using the coefficient of determination (R^2):

$$R^2 = 1 - \frac{SS_{res}}{SS_{tot}} = 1 - \frac{\sum_{i=1}^{n}\left(\phi_{j,i} - \phi_{1,i}\right)^2}{\sum_{i=1}^{n}\left(\phi_{1,i} - \overline{\phi_{1,i}}\right)^2} \tag{3.15}$$

where SS_{tot} is the total sum of squares of the target profile (that from mesh #1) and SS_{res} is the sum of squares of residuals between the profile under evaluation (from mesh #j) and the target profile. The subscripts i and n represent, respectively, a single data point and the total number of data points of a certain profile, while j is the index of a certain mesh and ϕ the variable under evaluation.

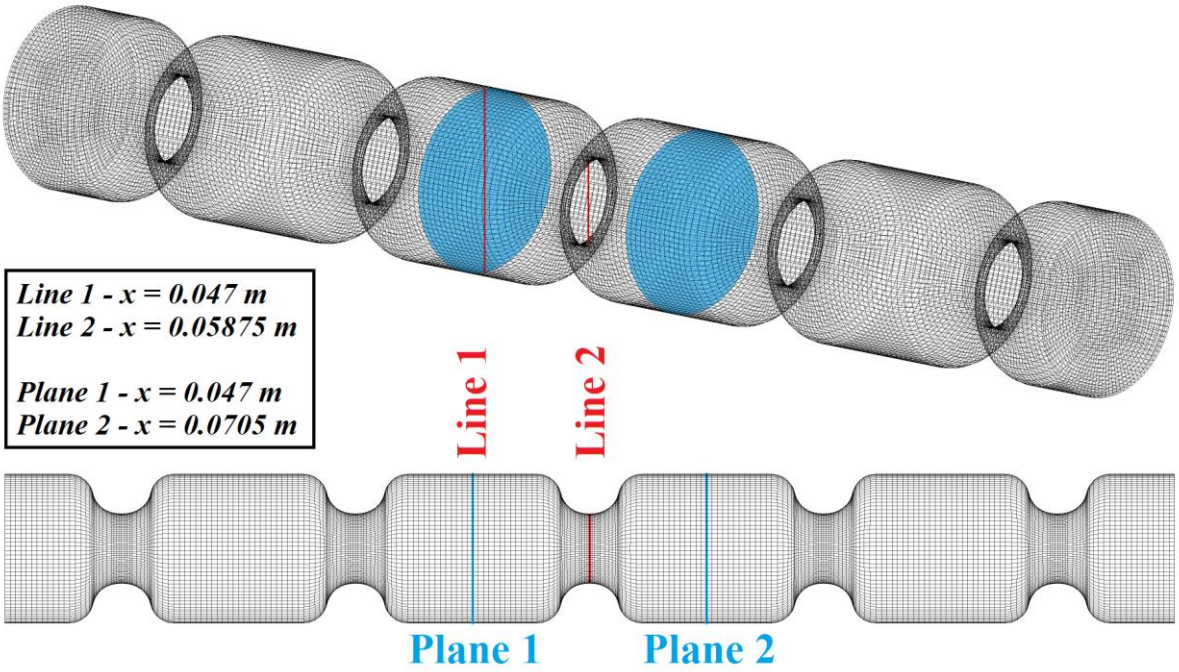

Figure 3.7. *Five-baffle-cells geometry, lines and planes where variables were monitored during mesh independency test* [66]

The results from each subsequent mesh were compared to those from mesh #1. Table 3.1 summarizes the results of the mesh independency analysis; mesh #2 was chosen for this study on the balance of accuracy and efficiency, and its density is above the norm reported in literature [43, 45, 54, 58, 59, 62, 142]. All meshes were O-grid structured containing only hexahedral elements and were created on ANSYS® ICEM.

Table 3.1. *Mesh sensitivity analysis results, reporting R^2 for each variable tested (Q = 50 ml min^{-1}, f = 8 Hz, x_o = 14 mm)*

			Velocity Magnitude at			
Mesh	# Nodes*	Δp**	Line 1	Line 2	Plane 1	Plane 2
1	236 k	–	–	–	–	–
2	**117 k**	**0.978**	**0.990**	**0.997**	**0.995**	**1.000**
3	64 k	0.940	0.984	0.996	0.984	0.999
4	31 k	0.922	0.984	0.996	0.980	0.999
5	7 k	0.670	0.911	0.989	0.825	0.997

* *Number of nodes per baffle cell.*
** *Pressure drop profile between planes 1 and 2:* $\Delta p(t) = p_1(t) - p_2(t)$.

Indexes such as absolute error (%), as given by Equation (3.16), were considered for the evaluation of this mesh independency analysis, in order to quantify errors between profiles of different meshes.

$$error(\%) = \frac{\sum_{i=1}^{n}\left(\frac{\left|\phi_{j,i} - \phi_{1,i}\right|}{\phi_{1,i}} \times 100\right)}{n} \tag{3.16}$$

However, the nature of the profiles compared is oscillatory, meaning that values oscillate from positive to negative, in the case of pressure drop profiles, and values drastically decrease in magnitude (close to zero) at certain times, in the case of velocity profiles. When pressure drop and/or velocity values approximate to zero, small differences between two profiles are greatly magnified, due to the small magnitude of the denominator in $\left|\phi_{j,i} - \phi_{1,i}\right| / \phi_{1,i}$. This results in low percentage errors at the peaks of these profiles (large values) and high percentage error at times when the profile crosses or gets close to a small value (zero). Due to this difference of scales within the same profile, absolute error was discarded as a valid index to quantify resemblance among profiles. The root-mean-square coefficient (RMSE) was also considered for the quantification of the mesh sensitivity analysis. However, RMSE is not a normalised coefficient, i.e. it is sensitive to the magnitude of the profiles; hence it is not suitable for comparison between profiles of different variables and results.

$$RMSE = \sqrt{\frac{\sum_{i=1}^{n}\left(\phi_{j,i} - \phi_{1,i}\right)^2}{n}} \tag{3.17}$$

Therefore, the coefficient of determination was selected for the quantification of resemblance between profiles of different meshes.

3.4 Model Assumptions

The selection and implementation of the utilised time discretisation scheme and residual criteria was made taking computational resources and time constraints into consideration. An assessment was carried out to quantify the impact of this decision on the accuracy of results nonetheless. Following the same methodology used for the mesh sensitivity study, and making use of the same 5-baffle-cell geometry and the selected mesh (#2), the results obtained using a *first order implicit* time discretisation scheme were compared to those from a *second order implicit* scheme. The results of this comparison between schemes was also reported for the highest Re_o simulated (Re_o = 10505), see Table 3.2. It is worth noting that although a *second order implicit* scheme

may presumably give more accurate results, it also presents difficulties in achieving high convergence rates, requiring smaller C_{CFL}; hence a smaller time-step, i.e. 1/16th of the time-step used for a *first order implicit* scheme was required to achieve convergence. Such a small time-step increased the computational time up to 750%, i.e. this simulation was run for 231 hours as opposed to the 27 hours required by the *first order implicit* time discretisation scheme, both running in parallel on 48 processors cores. This is not feasible within the time constraint of the project, taking into account the already computationally expensive nature of these simulations. Hence, on the balance of accuracy and computing time a *second order implicit* scheme was discarded.

Similarly, the effect of the selected convergence residual criteria on the accuracy of results was also quantified. The results obtained utilising a residual criterion of 10^{-3} (ANSYS® Fluent's default) and 10^{-4} for continuity and momentum equations, respectively, were compared to those using an overall 10^{-5} residual criterion. The difference between the results is reported in Table 3.2.

While a higher grid resolution was implemented near the wall, a fine-resolution wall inflation layer was not utilised in the simulations performed in this study. This decision was again made to balance the competing needs for accuracy and computation time, and the effects of the presence vs absence of such inflation layer were quantified by comparing the results obtained with the selected discretisation schemes, and mesh (#2), and those using a 12-layer inflation layer. This comparison was also performed at the operating conditions providing the highest mixing intensity (Re_o = 10505). During this assessment, the maximum wall shear stressed, τ_w, was monitored with time, and its time-averaged value was used for the calculation of y^+, defined as:

$$y^+ = \frac{u_f y}{\upsilon} \tag{3.18}$$

where υ is the kinematic viscosity (m^2 s^{-1}), u_f the frictional velocity defined as $u_f = \sqrt{\tau_w / \rho}$ and y the distance from the wall to the nearest computational node. It was found that the maximum wall shear rate was consistently experienced on the wall around the centre of the baffle orifice, reporting an average value of τ_w = 125.0 Pa. In this region (Line 2 in Figure 3.7), the nearest to the wall computational node was located at $y = 6.24\times10^{-6}$ m. Hence, a y^+ value of 2.2 was reported for the simulated operating conditions (run #5 in Table 3.2); the inflation layer had a growth of 1.3. The performance of the simulation including this inflation layer, on a 5 baffled-cells domain,

for 24 oscillatory cycles (3 real seconds at f = 8 Hz) lasted 269 hours running on 48 processors cores. Hence, the use of an even finer and denser inflation layer was not contemplated. It should be noted that due to the unsteady and non-uniform nature of the flow in oscillatory baffled reactors, the actual thickness of the viscus layer is unknown. Therefore an estimate value based on a worst-case-scenario-basis was performed as described above. Bearing all this information in mind, the difference among results with and without the aforementioned inflation layer is reported in Table 3.2. It must be mentioned that while this analysis was done on a 5-baffle-cell geometry, all the simulations performed in this work were done for a 0.752 m long COBR. This translated into 3.7M nodes for the selected mesh #2; the presence of the tested inflation layer would increase the number of computational nodes up to 5.7M. Therefore, the absence of such inflation layer allowed for the simulations times of this study to be significantly reduced.

Table 3.2. *Accuracy analysis between results obtained with different model features, reporting R^2 for each variable tested (Q = 50ml min^{-1}, f = 8Hz, xo = 14mm)*

	Velocity Magnitude				
Comparing	Line 1	Line 2	Plane 1	Plane 2	$\Delta p(t)^{**}$
Time discretisation scheme: 1st vs. 2nd order	0.986	0.995	0.950	0.997	0.942
Residual criteria (10^{-3} & 10^{-4} vs. 10^{-5})	0.990	0.997	0.995	1.000	0.976
Inflation layer: without vs. with	0.968	0.975	0.988	0.998	0.930

***Pressure drop profile between planes 1 and 2:* $\Delta p(t) = p_1(t) - p_2(t)$.

The geometry modelled in this study, described in Section 3.1, required a large number of computing resources. Additionally, the same geometry/mesh used for a single phase study that analysed pressure drop propagation and energy losses on a COBR, Chapters 4 – 6, was utilised for a multi-phase (S-L) study that examined axial dispersion, residence time, velocity and suspension experienced by solid particles in a COBR. In the latter, a discrete phase model (DPM) is coupled to the continuous Eulerian phase, solid particles are then injected and flow through the device is simulated until these particles completely leave the domain. This resulted in simulation runs taking up to 60 days to complete, running on 48 processors, for a single scenario. The chosen time discretisation scheme, residual criteria and the absence of a denser boundary layer helped the optimization of computing resources, allowing this research to perform the required number of simulations for the aforementioned studies.

Chapter 4 Validation of Power Dissipation Models in OBRs

4.1 Introduction

While continuous oscillatory baffled reactors (COBR) have been proven a viable alternative to traditional batch reactors for organic synthesis and crystallisation, research into the estimation of power density for this type of device has largely been stagnated for the past 25 years. Essentially two published models have been used in the field of COBR and OBR (oscillatory baffled reactors): the "quasi-steady" model (QSM) from the work of Jealous and Johnson [115] and the "eddy enhancement" model (EEM) by Baird and Stonestreet [116, 117] The origin of both models was stemmed from the evaluation of pressure drop over oscillatory devices; while the equations were empirical, research has neither been carried out on the validation of the above models nor on how these models could be used in continuous operation where there is a net flow. In this chapter, a detailed analysis and examination of the applicability, the capability and the deficiencies of the two models are, for the first time, reported using a CFD methodology. This chapter has been published in the Journal of Chemical Engineering and Processing: Process Intensification, Vol. 134, 2018, pages 153-162 [66].

4.2 Background on Power Dissipation Models for OBRs

It should be noted that power density (ε_v) is often regarded as power dissipation rate. These two nomenclatures have been used interchangeably in literature and both refer to the same variable: ε_v (W m^{-3}). The nomenclature *power dissipation rate* is not to be confused with the change in power with time (W s^{-1}); instead, it only refers to the change in energy with time per unit volume of fluid (J s^{-1} m^{-3}). Hence, it should be more accurately named as *energy dissipation rate*. However, for the purpose of consistency with previous literature, ε_v is referred to in this work as both *power dissipation rate* and *power density*; this is the power experienced by liquid.

In order to predict power density due to pulse generation in pulsed columns, Jealous and Johnson in 1955 developed the QSM from pressure drop, which accounted for inertial and frictional effects of the flow, as well as pressure drop due to a static head that was present on their experimental setup [115]. QSM power density equation for oscillatory baffled reactors was then derived from the work of Jealous and Johnson as [116, 117]:

$$\varepsilon_v = \frac{2n\rho\left(\omega x_o\right)^3\left(1/\alpha^2 - 1\right)}{3\pi {C_D}^2 L} \tag{4.1}$$

Due to the constriction of an orifice baffle, it is the frictional losses, instead of inertia, that resulted in the overall gain in kinetic energy. The geometric parameters taking part in Equation (4.1) include the orifice discharge coefficient (C_D), usually taken as 0.6 – 0.7 [32, 84, 107, 115-118], the reactor's length (L) in meters, the number of baffles (n) and the ratio of the area of the orifice over the area of the tube, known as the restriction ratio ($\alpha = D_b^2 / D^2$), D is the diameter of the tube (m) and D_b is the diameter of the baffle hole (m); operational parameters involve $\omega=2\pi f$ as the oscillation angular frequency (rad s^{-1}), x_o the oscillation centre-to-peak amplitude (m) and f the oscillation frequency (Hz); physical parameter is the fluid density (ρ) (kg m^{-3}). Note that a term counting for the net flow velocity was not included in Equation (4.1), as pulse columns have been operated batch-wise.

It is generally thought that QSM works well for low frequencies (below 5 Hz) and high amplitudes (above 5 mm) [70, 115, 116]. However, this is not in full agreement with the work of Panton and Goldman, who, after investigating the derivations of QSM, reported that QSM was not strictly valid when $\left(3 < \left(\omega x_o\right)/\left(\upsilon\omega\right)^{1/2} < 100\right)$ where υ is the kinematic viscosity (m^2 s^{-1}) [143]; note that all the conditions presented in this study are within the aforementioned range. In addition, selection of the C_D value in the QSM also affects the accuracy of the model. Furthermore, the assumption made by Jealous and Johnson that there is a linear relationship between the number of baffles in the device and the frictional pressure losses due to their orifice constriction is yet to be proven for OBRs/COBRs. This argument is further examined, developed and addressed in Section 4.5.2.

Braid and Stonestreet developed an empirical EEM model to predict overall power dissipation rates, coupling acoustic behaviour with local eddy turbulence [116], based on the prediction of frictional pressure drop as the acoustic resistance of a single orifice plate:

$$\varepsilon_v = \frac{1.5n\rho\omega^3 {x_o}^2 \ell}{\alpha L} \tag{4.2}$$

While similar geometric, physical and operational parameters are involved in this model, "mixing length" ℓ (m) is an additional parameter and has a value similar to a characteristic length scale of the reactor, e.g. a value of 7 mm was selected in previous research with a tube diameter of 12 mm [116]. This model was proposed for higher frequencies (above 5 Hz) and lower amplitudes (below 5 mm), hence filling the gap left by the QSM. However, the dependence of power dissipation rate on mixing length casts doubts, as mixing length is often unknown and has not accurately been predicted in OBR. Furthermore, it was unclear whether this model is suitable for continuous operation. The EEM, similarly to the QSM, also assumes a linear relationship between the number of baffles and frictional pressure losses.

Accompanying the EEM, the phase shift between velocity and pressure waves was given as [116]:

$$\delta = \tan^{-1}\left(\frac{LK_i}{3n\ell}\right) \tag{4.3}$$

where K_i is a geometry-dependent inertial corrector factor (a value of 0.9 was selected by Braid and Stonestreet in their work). Although the two empirical models mentioned above, QSM in particular, have commonly been used by researchers in order to compare performances of oscillatory baffled reactors with other types of devices, no validation has yet been conducted.

4.3 Power Dissipation & Pressure Drop in OBRs

In oscillatory flow devices, both inlet velocity and pressure drop follow sinusoidal wave forms, separated by a phase shift (δ), as represented in Figure 4.1. The time-averaged power density, referred to as power density (ε_v) from this point onwards, in a COBR can be calculated by solving:

$$\varepsilon_v = \frac{1}{VT}\int_0^T Q(t)\Delta p(t)\,dt \tag{4.4}$$

where V is the volume of the system (m^3), T the oscillation period (s), $Q(t)$ the volumetric flow rate (m^3 min^{-1}) defined as $Q(t) = A \cdot u(t)$, A being the cross-sectional area (m^2), the velocity profile $u(t) = u_{net} + \omega x_o \sin(\omega t)$ and u_{net} is the inlet net velocity (m s^{-1}). The temporal pressure drop profile across the device $\Delta p(t)$ (Pa) has often been

assumed to have a sinusoidal wave form similar to that of the flow motion, defined as $\Delta p(t) = \Delta p_{net} + \Delta p_o \sin(\omega t + \delta)$ [116, 117, 120], where Δp_o is the maximum centre-to-peak pressure drop fluctuation, Δp_{net} the net pressure drop and δ the phase shift. Making use of this hypothesis, the integration of Equation (4.4) over an oscillatory cycle results in:

$$\varepsilon_v = \frac{\omega x_o \Delta p_o \cos(\delta) + 2u_{net}\Delta p_{net}}{2(V/A)} \approx \frac{\omega x_o \Delta p_o \cos(\delta)}{2(V/A)} \tag{4.5}$$

The volume to cross-sectional area ratio in Equation (4.5) is often substituted by the reactor's length (L); however, while this is true for sharp-edged disk-like baffles, it is far from reality for smooth-edged baffles as observed in Figure 4.1, e.g. the percentage difference between V/A and L is 25% for all runs, except for runs #8 – 11 where this difference ranges from 5 to 30%. For this reason, V/A was used in Equations (4.1), (4.2) and (4.5) as opposed to L throughout this study.

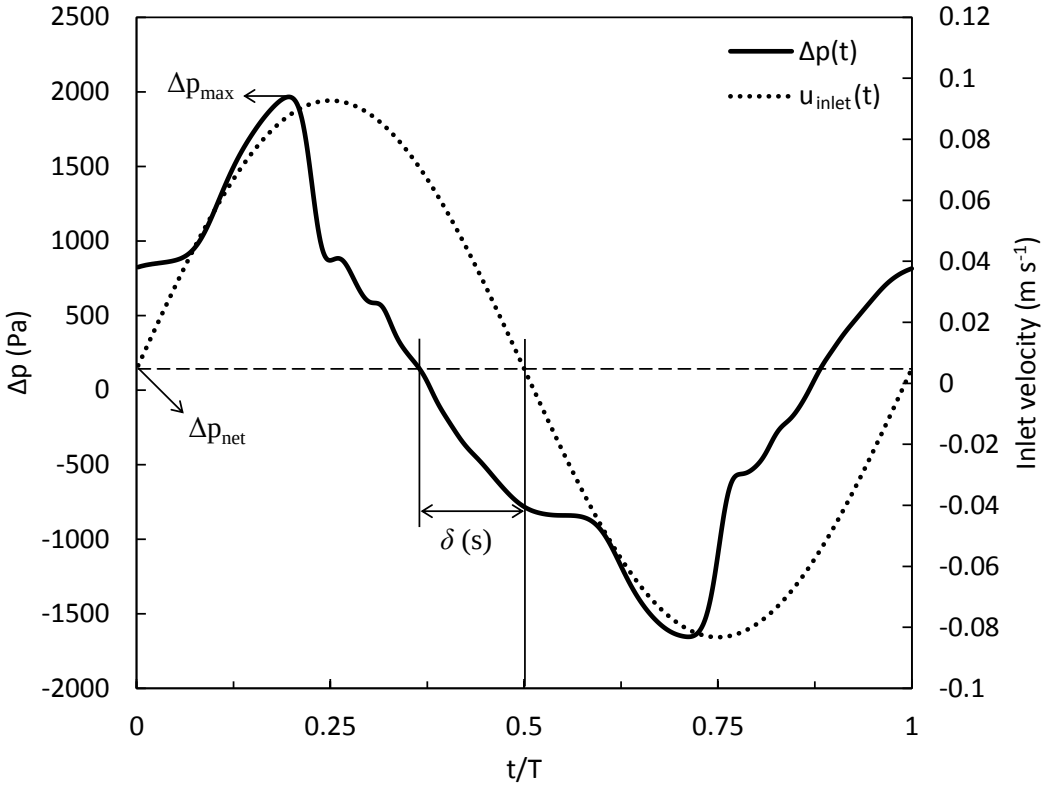

Figure 4.1. *Inlet velocity and pressure drop wave forms illustrating phase shift; cycle-averaged simulated data from run #2* [66]

4.4 Methodology – Parametric Study

This study was undertaken for a standard NiTech DN15 COBR reactor, whose geometric details and characteristics are earlier described under Section 3.1.

However, the present work follows the research path suggested by Braid and Stonestreet [116] to study the effect of a wide range of geometric and operating parameters on the pressure drop and power dissipation experienced in COBRs; the parameters include baffle hole diameter (D_b), baffle spacing (L_b), volumetric flow rate (Q), oscillation frequency (f) and centre-to-peak amplitude (x_o). All the conditions modelled in this study are listed in Table 4.1, along with their respective net flow Reynolds numbers ($Re_n = u_{net}\rho D/\mu$) and oscillatory Reynolds numbers ($Re_o = \omega x_o \rho D/\mu$) which are included in the last two columns of the table. Additionally, Figure 4.2 displays the geometric dimensions and design details of baffle constrictions with 5 mm and 9 mm baffle diameter; Figure 4.3 shows all the different geometries modelled during this parametric study.

Table 4.1. *Parametric study list of conditions simulated*

Run #	Q (ml min^{-1})	f (Hz)	x_o (mm)	D_b (mm)	L_b (mm)	Re_n	Re_o	St
1	50	0.5	14	7	23.5	70.5	657	0.0853
2	50	1	14	7	23.5	70.5	1313	0.0853
3	50	2	14	7	23.5	70.5	2626	0.0853
4	50	4	14	7	23.5	70.5	5253	0.0853
5	50	8	14	7	23.5	70.5	10505	0.0853
6	50	1	5	7	23.5	70.5	469	0.239
7	50	1	23	7	23.5	70.5	2157	0.0519
8	50	1	14	5	23.5	70.5	1313	0.0853
9	50	1	14	9	23.5	70.5	1313	0.0853
10	50	1	14	7	47	70.5	1313	0.0853
11	50	1	14	7	94	70.5	1313	0.0853
12	100	2	5	7	23.5	141	938	0.239
13	100	2	7	7	23.5	141	1313	0.171
14	100	2	10	7	23.5	141	1876	0.119
15	100	2	14	7	23.5	141	2626	0.0853

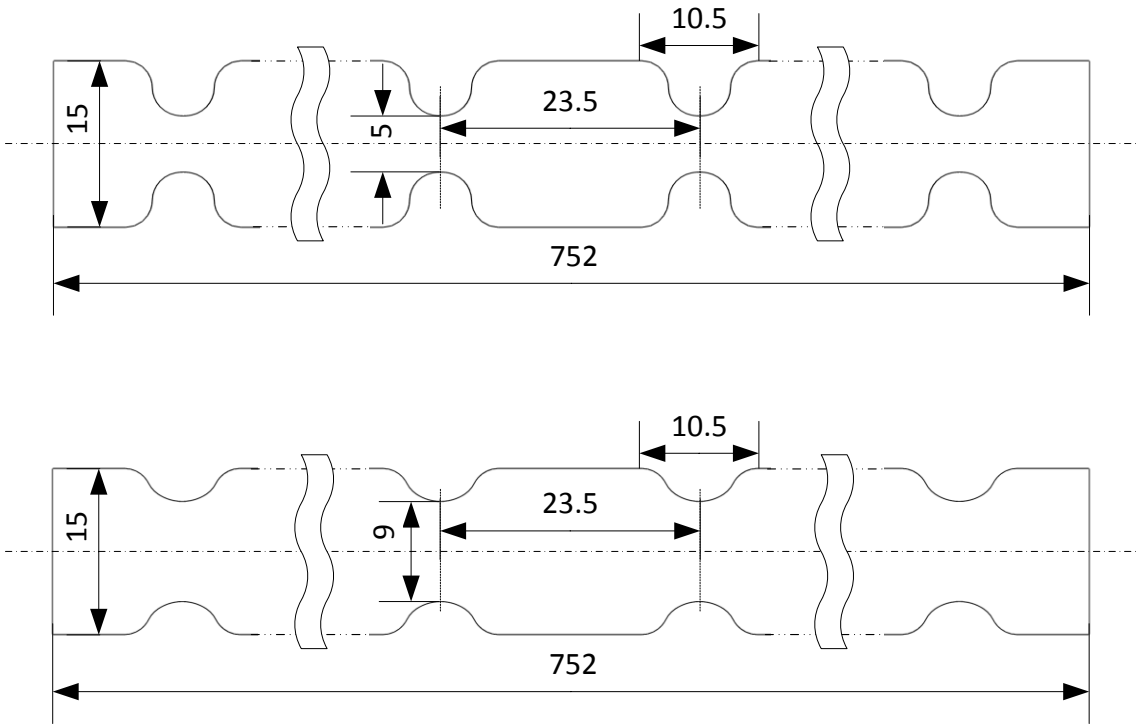

Figure 4.2. *Dimensions of the NiTech DN15 straight section with D_b = 5 mm (top) and D_b = 9 mm (bottom) used in CFD simulations; all dimensions are in mm*

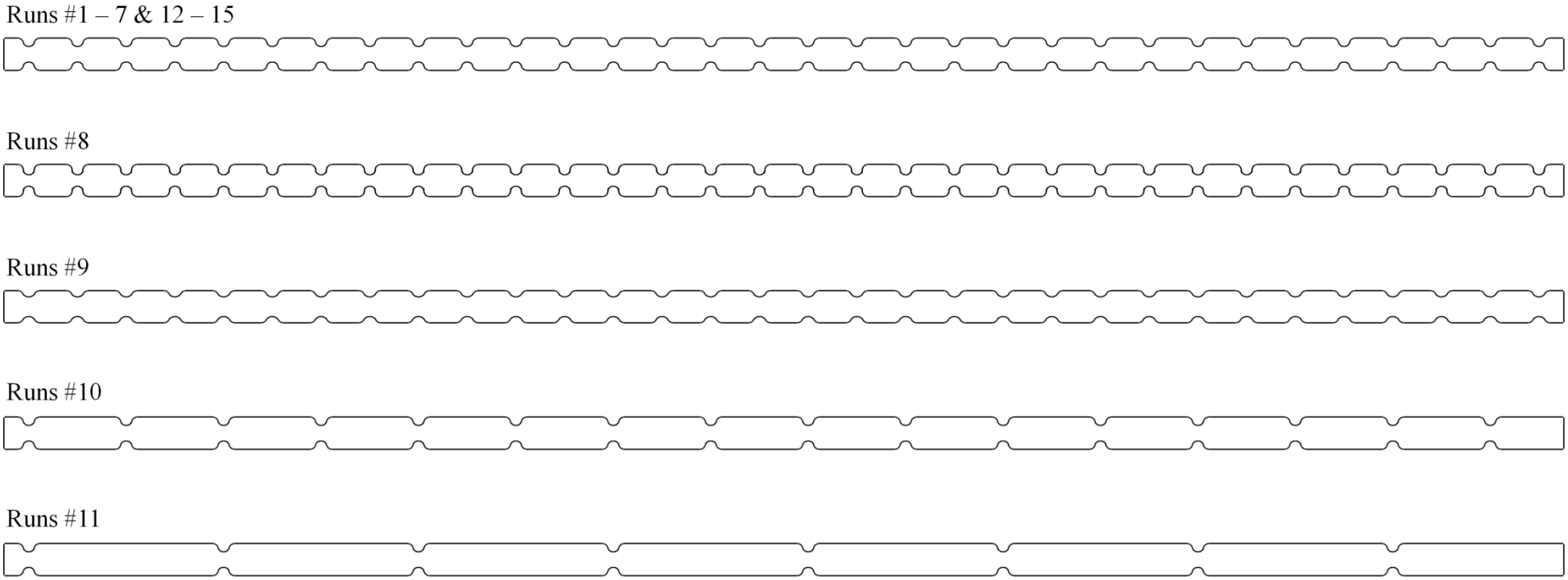

Figure 4.3. *Geometries employed on the parametric study*

The validation of the "quasi-steady" model (QSM) and the "eddy enhancement" model (EEM) starts by generating temporal pressure drop profiles over a reactor's fixed length. Each simulation consisted of a 0.752 m long straight section and was run for 10 oscillatory cycles. In order to minimize the effect of the open boundary conditions at the inlet and outlet, the equivalent of the first two and last two baffle constrictions, when L_B = 23.5 mm, were discarded. In order to assess temporal pressure drop across the device, the area-weighted averaged static pressure was monitored at two cross-sectional planes: Plane 1 (p_1), placed 47 mm from the inlet and Plane 2 (p_2), placed 47 mm from the outlet. The pressure drop profile was obtained over the remaining 0.658 m, equivalent to 28 baffle-cells if L_B = 23.5 mm, as $\Delta p(t) = p_2(t) - p_1(t)$.

For each run, the simulated time-dependent pressure drop profile, $\Delta p(t)$, was extracted and utilised in the numerical integration of Equation (4.4) for the calculation of power density. The simulated power density of a particular run is then compared with the power density estimated by the QSM and EEM, which are directly calculated with Equations (4.1) and (4.222); a mixing length of 7 mm was used for the EEM calculations as previously proposed by Braid and Stonestreet [116]. The comparison between simulated and model estimated power density values enabled a detailed examination and comparison of the QSM and EEM for a wide range of operational and geometric conditions.

The averaged absolute error (AAE) (%) between the simulated and model predicted power densities was quantified as:

$$AAE(\%) = \frac{\sum_{i=1}^{n}\left(\frac{\left|\phi_i^{predicted} - \phi_i^{simulated}\right|}{\phi_i^{simulated}} \times 100\right)}{n} \tag{4.6}$$

where i is a single case/run, n the total number of cases in this study and ϕ the property under evaluation (ε_v).

4.5 Results & Discussion

In previous CFD simulations of OBR and COBR [144], a quasi-steady state, indicating the flow was fully developed and cycle-repeatable, was achieved in 5-7 cycles of

oscillation. Flow patterns in oscillatory baffled reactors tend to be chaotic in nature, due to the constant formation and disruption of eddies. For this reason, monitoring variables at specific points of the domain to assess an overall quasi-steady-state is not feasible for these types of devices. Hence, the procedure presented by Jian's work [144] is followed in this study, i.e. the volume-weighted average strain rate is monitored with time, which serves the purpose of visually assessing when a quasi-steady-state is achieved. Figure 4.4 (left) shows the change of the volume-weighted averaged strain rate with time; a quasi-steady state is seen after cycle 5. Being conservative, all the data presented on this study were taken from the cycle 7 (included) onwards. Furthermore, Figure 4.4 (right) plots $\Delta p(t)$ at different oscillatory cycles, visually confirming the repeatability of the results after cycle 7. The monitored strain rate shows larger amplitude peaks at the forward strokes, followed by smaller values at the backward stroke of the oscillation. This is due to the net flow effect, i.e. the forward oscillation is in favour of the flow, while the reversal stroke is against flow.

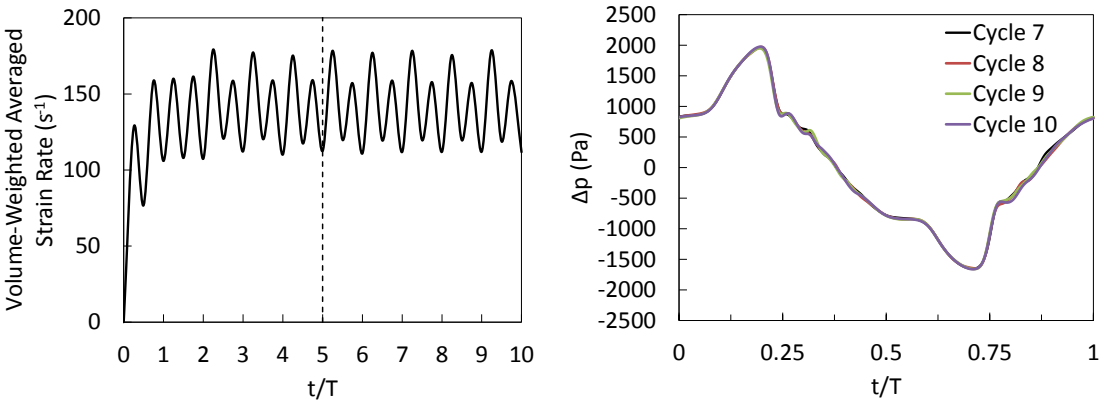

Figure 4.4. *Convergence of strain rate with time (left) and pressure drop wave forms for cycles 7 to 10 (right) (Q = 50ml min^{-1}, f = 1Hz, x_o = 14mm)* [66]

Mazubert et al. predicted Δp_o and ε_v for different types of baffle configurations using CFD simulations [64], their results were the basis for comparison with ours. For a single orifice plate, D = 15 mm, D_b = 8 mm, L_b = 26 mm, f = 1.05 Hz, x_o = 16.5 mm, u_{net} = 14.05 mm s^{-1}, they reported a maximum centre-to-peak pressure drop fluctuation per length and a power density of 0.73 kPa m^{-1} and 23.8 W m^{-3} respectively. The baffles utilised by Mazubert et al. were sharp-edged with a width (W_b) of 2 mm, in the axial direction, as opposed to the 10.5 mm of the smooth-edged baffles used in the present work (Figure 4.1). While a direct comparison is not possible due to different geometric and operational parameters, since Δp_o and ε_v are proportional to θ, where θ =

$(x_o W_b)/(\alpha L_b)$, the maximum centre-to-peak pressure drop fluctuation per length and the power density reported by Mazubert et al. can be compared with those obtained in #2 of our work (2.3 kPa m^{-1} and 88.1 W m^{-3}) by multiplying Mazubert's data by a ratio of $\theta^{Ours}/\theta^{Mazubert}$. In doing so, the data of Mazubert et al. become 2.5 kPa m^{-1} and 81.8 W m^{-3} respectively, which are very similar to our results obtained from run #2. Note that to compensate for the shape difference in baffles, i.e. smooth vs sharp edges, W_b = 5.6 mm was used in the calculation of θ^{Ours}; this is the baffle width a sharp-edged baffle of D_b = 7 mm should have in order for the area under its curve (*AC*) to be equal to that of the smooth-edged baffle of the DN15 used in this investigation, as displayed in Figure 4.5.

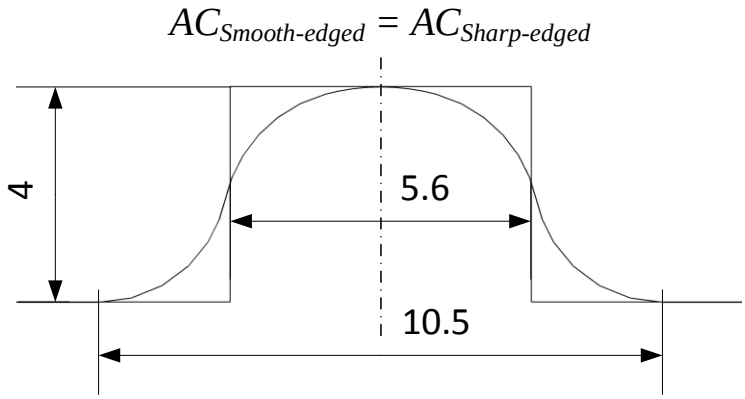

Figure 4.5. *Dimensions of DN15's smooth-edged baffle and a sharp-edged baffle with equal area under their curvature; all dimensions are in mm*

Mackley et al. plotted power density over a section of OBR against $\omega x_o D$ (m^2 s^{-1}), showing a third order power law dependency [120]. For the sake of comparison, the same plot was displayed using our simulated data (Figure 4.6 left) and a similar third order power law trend was observed here. However, $\omega x_o D$ is not a dimensionless group; it has neither physical meaning nor importance, as it does not include all design and operational parameters. When plotting power density against $\omega x_o D$ or the widely used oscillatory Reynolds number, see Figure 4.6 (right), multiple power density values (provided at different operation conditions) are obtained at the same $\omega x_o D$ and Re_o. There is generally a knowledge gap in the governing dimensionless groups in this area, because none of the existing dimensionless groups capture *all* key design and operational parameters, e.g., the oscillatory Reynolds number was directly derived by replacing the net flow velocity with the oscillatory velocity; the Strouhal number only describes a ratio of tube diameter to oscillation amplitude. A revised oscillatory Reynolds number was proposed by Ni and Gough [101] as $Re_o^* = Re_o/\sqrt{\alpha}$, accounting

for the effect of the baffle diameter, since the smaller the D_b, the higher the inertia forces of the fluid. This was a step forward, it however did not include the effects of baffle spacing and the net flow of the system; baffle spacing controls the connectivity of eddies and net flow is an essential part of plug flow. In order to capture the effects of *all* key design and operational parameters, a new dimensionless number is proposed in this study as:

$$Re_o^{NEW} = \frac{u_T \rho D}{\mu}\sqrt{\frac{\beta}{\alpha}} \tag{4.7}$$

where u_T is the total inlet maximum velocity of the system covering both the net and oscillatory flows $\left(u_T = \omega x_o + u_{net}\right)$ (m s^{-1}) and β is defined as the ratio of the optimal to user's baffle spacing as $\beta = L_b^{opt} / L_b$, and L_b^{opt} = *1.5D*. The optimal L_b/D ratio was identified as 1.5 by visually analysing flow patterns [78], and as 1.8 by quantitatively assessing the gas-liquid mass transfer coefficient in an OBR [84]. Since 1.5 has most commonly been reported in literature [2, 20, 22, 26, 39, 43, 57, 60, 107-109]; it was selected as reference in Re_o^{NEW}. When β is greater than one, more baffles than the optimal would be present, increasing the inertia forces of the fluid and vice versa. In this work β = 0.96 for all cases, except for runs #12 and 13 where β = 0.48 and 0.24, respectively. This new index (4.10) is used throughout the validation work.

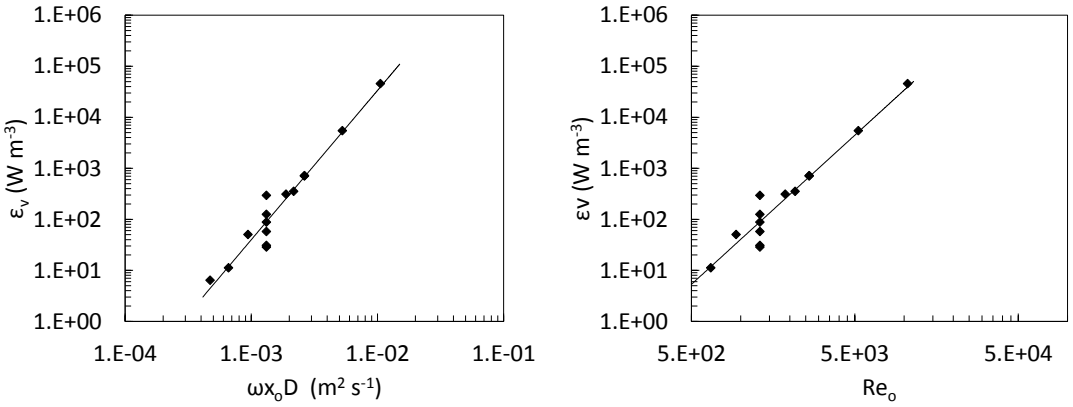

Figure 4.6. *Power density plotted as a function of $\omega x_o D$ (left) and Re_o (right) for runs #1 to 15* [66]

4.5.1 Power Dissipation Rates (ε_v)

In order to assess the validity of Equation (4.5), where $\Delta p(t)$ is assumed sinusoidal, values of Δp_{net}, Δp_o and δ were obtained from the simulated $\Delta p(t)$ as:

- Δp_{net} is calculated as the time-averaged value of the simulated pressure drop $\Delta p_{net} = \overline{\Delta p(t)}$.

- Phase shift is calculated by monitoring the times at which $\Delta p(t)$ crosses its Δp_{net} value, e.g. every $T/2$ seconds, where T is the period of the oscillation. These times are then subtracted from the times at which velocity's sinusoidal wave crosses its u_{net} value. The resultant values are averaged among cycles 7 to 10 and converted from seconds into radians: $\delta(\text{rad}) = (2\pi/T)\,\delta(\text{s}) = \omega\delta(\text{s})$.

- The maximum centre-to-peak pressure drop fluctuation, Δp_o, can be obtained by equating the first part of Equation (4.5), which includes the contributions from the net flow (Δp_{net} and u_{net}), to the power density obtained from the numerical integration of Equation (4.4) and by solving it for Δp_o, let's call this value $\Delta p_o'$. However, it can also be calculated by obtaining the maximum value of the cycle-averaged $\Delta p(t)$ profile and then computing $\Delta p_o = \Delta p_{max} - \Delta p_{net}$, let's call this value $\Delta p_o''$.

Table 4.2 gathers all the information extracted from the simulated data for all the runs performed in this study. Although both the overall pressure drop and overall velocity in the DN15 contain a term counting for net flow, simulated results showed that the contributions of the net flow (Δp_{net} and u_{net}) to power density were negligible in all conditions tested. This was assessed by calculating power density using Equation (4.4) and the simplified version of Equation (4.5) (right-hand side) for each simulated condition listed in Table 4.1, making use of the known variables u_{net}, ω and x_o, as well as Δp_{net}, $\Delta p_o'$ and δ extracted from the simulated $\Delta p(t)$ profile. The relative percentage differences between the results provided by both equations were then computed, all of which were below 3.6%. However, it should be noted that the accuracy of Equation (4.5) is heavily dependent on the appropriate estimation of Δp_o. Table 4.2 shows how different $\Delta p_o'$ and $\Delta p_o''$ could be, reporting relative percentage differences as big as 37%. Figure 4.7 plots the cycle-averaged pressure drop profile for run #2, along with the hypothetical sinusoidal profile that $\Delta p(t)$ would display if $\Delta p_o = \Delta p_o'$ and if $\Delta p_o =$

$\Delta p_o''$. The latter presents a much larger area under its curve; it in turn reports a larger power density than the actual non-perfectly-sinusoidal profile. Note that it is advisable to act with caution when making use of Equation (4.5), as the estimation of Δp_o could lead to erroneous results if the temporal evolution of $\Delta p(t)$ is unknown. Cycle-averaged pressure drop profiles for all simulated conditions are presented in Appendix 6.

Pressure drop and power dissipation results are presented in its dimensionless form, p^* and $\varepsilon_v{}^*$ respectively, in Table 4.3, where $p = p^* A$, $\varepsilon_v = \varepsilon_v{}^* B$. The scaling factors A and B are defined as: $A = \rho\left(u_{net} + \omega x_o\right)^2 \sqrt{\beta/\alpha}$ and $B = \rho f \left(u_{net} + \omega x_o\right)^2 \sqrt{\beta/\alpha}$.

Table 4.2. *Summary of results extracted from CFD simulations*

Run #	Δp_{net} (Pa)	$\Delta p_o'$ (Pa)	$\Delta p_o''$ (Pa)	δ (rad)	ε_v Eq. (4.4) (W m^{-3})	$^{\dagger}\varepsilon_v$ Eq. (4.5) (W m^{-3})	Re_o	St	Re_o NEW
1	35.3	395.4	502.6	0.853	11.2	10.9	657	0.0853	1525
2	58.6	1490.1	1907.7	0.791	88.1	87.6	1313	0.0853	2901
3	120.0	5997.1	7409.0	0.786	709.0	708.0	2626	0.0853	5655
4	215.9	22632.8	28169.3	0.769	5439.5	5437.5	5253	0.0853	11161
5	458.0	83695.5	99453.0	0.621	45503.7	45499.6	10505	0.0853	22175
6	15.1	352.7	356.6	0.936	6.4	6.2	469	0.239	1131
7	111.6	3189.0	4071.8	0.636	353.1	352.1	2157	0.0519	4671
8	232.5	3923.9	5365.2	0.540	293.8	291.6	1313	0.0853	4062
9	28.3	710.2	642.1	1.002	30.9	30.6	1313	0.0853	2257
10	54.8	1021.5	1020.4	0.716	57.7	57.2	1313	0.0853	2051
11	27.9	638.2	600.2	0.886	28.6	28.4	1313	0.0853	1451
12	100.0	1329.5	1328.1	0.911	50.4	48.6	938	0.239	2262
13	171.1	2100.8	2292.0	0.803	125.0	121.9	1313	0.171	3049
14	245.4	4415.3	4185.6	0.953	309.9	305.5	1876	0.119	4229
15	248.2	5907.2	7578.9	0.768	714.9	710.4	2626	0.0853	5803

† *Calculated with the simplified version of Equation (4.5) (right-hand side) and* $\Delta p_o = \Delta p_o'$

Table 4.3. *Summary of results extracted from CFD simulations in dimensionless form*

Run #	$\Delta p_{net}{}^*$	$\Delta p_o'^*$	$\varepsilon_v{}^*$	A	B
1	7.10	79.63	4.51	5.0	2.5
2	3.26	82.87	4.90	18.0	18.0
3	1.76	87.80	5.19	68.3	136.6
4	0.81	85.05	5.11	266.1	1064.5
5	0.44	79.68	5.41	1050.5	8403.6
6	5.51	129.03	2.33	2.7	2.7
7	2.39	68.41	7.58	46.6	46.6
8	9.24	155.87	11.67	25.2	25.2
9	2.02	50.78	2.21	14.0	14.0

10	4.31	80.34	4.54	12.7	12.7
11	3.10	70.98	3.18	9.0	9.0
12	9.14	121.59	2.31	10.9	21.9
13	8.61	105.77	3.15	19.9	39.7
14	6.42	115.56	4.06	38.2	76.4
15	3.45	82.13	4.97	71.9	143.9

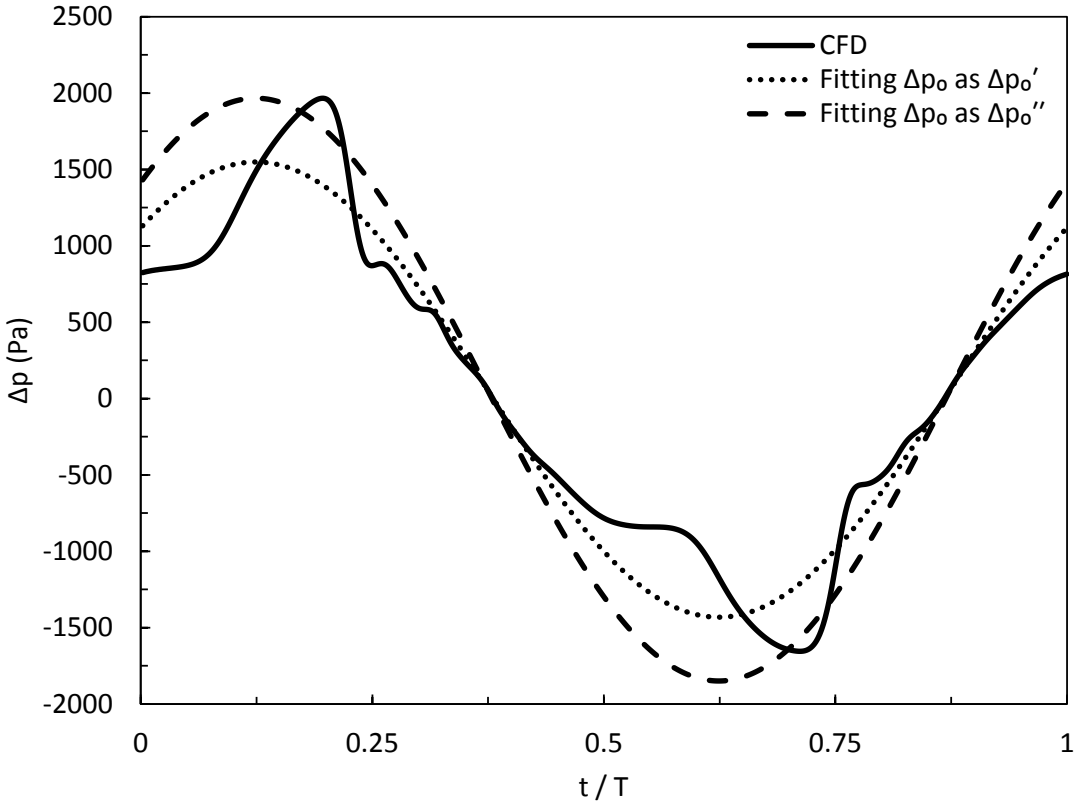

Figure 4.7. *Cycle-averaged Δp(t) and its hypothetical sinusoidal form, estimating Δp_o as $\Delta p_o'$ and $\Delta p_o''$, for run #2* [66]

4.5.2 Validation of Quasi-Steady Flow Model (QSM)

Following the described procedures, power density was calculated using the QSM for all conditions listed in Table 4.1 and compared with those predicted by CFD simulation as shown in Figure 4.8, where the power density is plotted against Re_o^{NEW}. It is clearly observed that power density values predicted by the QSM for every condition were consistently higher than the simulated data; reporting an averaged absolute error (AAE) of 333% and 218% for C_D = 0.6 and C_D = 0.7, respectively. This over-estimation is coming from two sources:

- The orifice discharge coefficient (C_D). A value of $0.6 \leq C_D \leq 0.7$ has commonly been used for the QSM in previous work [32, 84, 107, 115-118]; this is typically true for a standard orifice made of a sharp-edged thin plate. However, DN15 have wall baffles of smoother curvature as shown in Figure 4.1; hence C_D should have a higher value [145].

- Jealous and Johnson [115] modelled frictional losses as the total gain in kinetic energy due to baffle's constriction. While this is true for a single orifice, consecutive resistances (baffles) will not necessarily increment kinetic energy linearly. Jealous and Johnson made the assumption that the effect of consecutive orifice resistances on pressure drop was linear; there was no pressure recovery because orifices were so close to one another that no calming section was available. COBRs contain orifices of smooth curvature and optimized baffle spacing, some degree of recovery would then be expected; the effect of consecutive baffles on pressure drop should thus be of a power law relationship.

This study found that by re-adjusting the value of C_D better agreement could be obtained between the power dissipation rates predicted by the QSM and that obtained from CFD simulations. However, the best fit arrives when C_D = 1.3, this is neither physically or practically feasible as C_D must have a value within a 0 – 1 range. As a result, an exponent is added to the number-of-baffles term in the QSM, and the best fits are obtained (as shown in Figure 4.9) when C_D = 0.8 and n is replaced by $n^{0.7}$, proving an AAE of 12%, as:

$$\varepsilon_v = \frac{2n^{0.7}\rho\left(\omega x_o\right)^3\left(1/\alpha^2 - 1\right)}{3\pi C_D{}^2\left(V/A\right)} \tag{4.8}$$

In summary, the existing QSM returned higher power dissipation rates due to some of the geometric parameters of its formulation not being applicable to modern oscillatory baffled devices; this can be corrected by applying a power law dependency with n and an appropriate C_D value to account for smooth-edged baffles, as show in Figure 4.8. In doing so, not only have the QSM been validated, but also done for a much wider application range than previously outlined. Furthermore, it can also be stated that this newly revised QSM is valid for both batch and continuous operations, as the contribution of net flow to power dissipation rates is negligible (see Table 4.2).

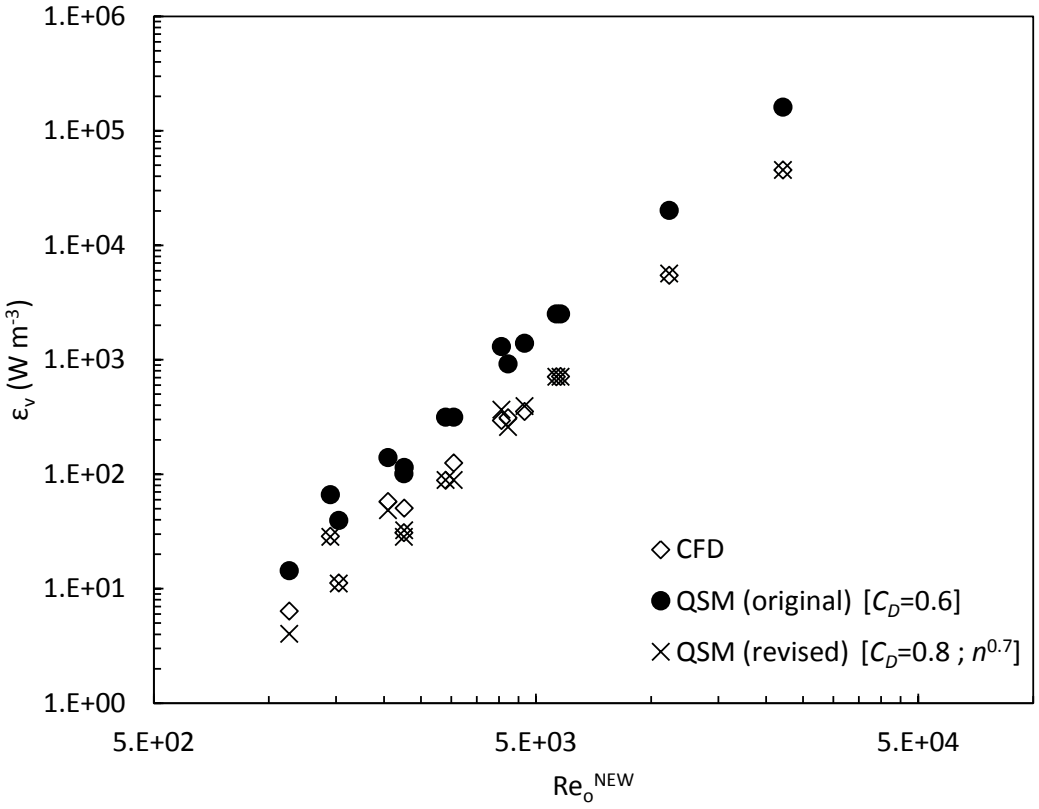

Figure 4.8. *Simulated and QSM predicted power density as a function of* Re_o^{NEW} *for runs #1 to #15* [66]

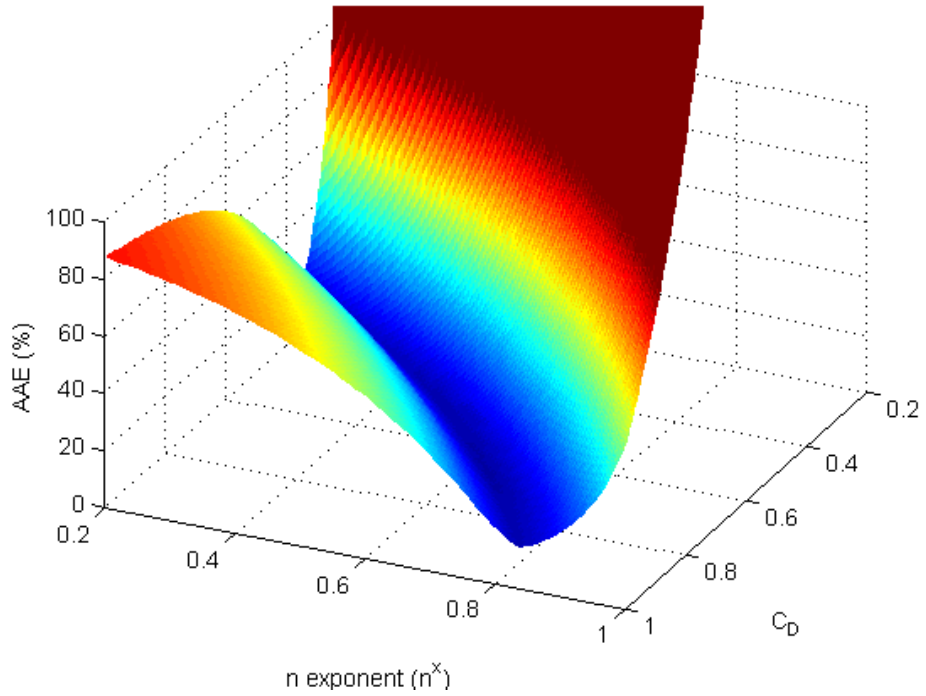

Figure 4.9. *AAE (%) as a function of* C_D *and n power law exponent; minimum reached at* $C_D = 0.8$ *and* $x = 0.7$ [66]

4.5.3 Validation of Eddy Enhancement Model (EEM)

Power density from the EEM is calculated using Equation (4.2) taking a mixing length of 7 mm, as suggested in previous work [116], and then compared in Figure 4.10 with the power density directly obtained from CFD simulations. The estimations of power density using the EEM show a better overall fit with the simulated data (AAE = 58%). However, the accuracy of EEM can further be improved by implementing the same power law dependency proposed earlier ($n^{0.7}$) to the number of baffles in the system:

$$\varepsilon_v = \frac{1.5 n^{0.7} \rho \omega^3 x_o{}^2 \ell}{\alpha (V/A)} \tag{4.9}$$

reducing the averaged absolute error to 42%. Additionally, the accuracy of the model can significantly be improved by properly estimating the "mixing length", which is dependent on operational and geometric characteristics. Further discussion on this very "mixing length" is taken-up in the next sub-section. Along with ε_v values obtained from Equation (4.2) and those obtained from CFD simulations, Figure 4.10 displays power dissipation rates obtained from Equation (4.9), inputting estimated "mixing length" values as proposed in Section 4.5.3.1. In summary, not only has the EEM been validated, but also done so for a much wider application range than previously outlined. Again, due to the minimal effects of net flow on power density, our validation of the EEM is applicable for both batch and continuous operations.

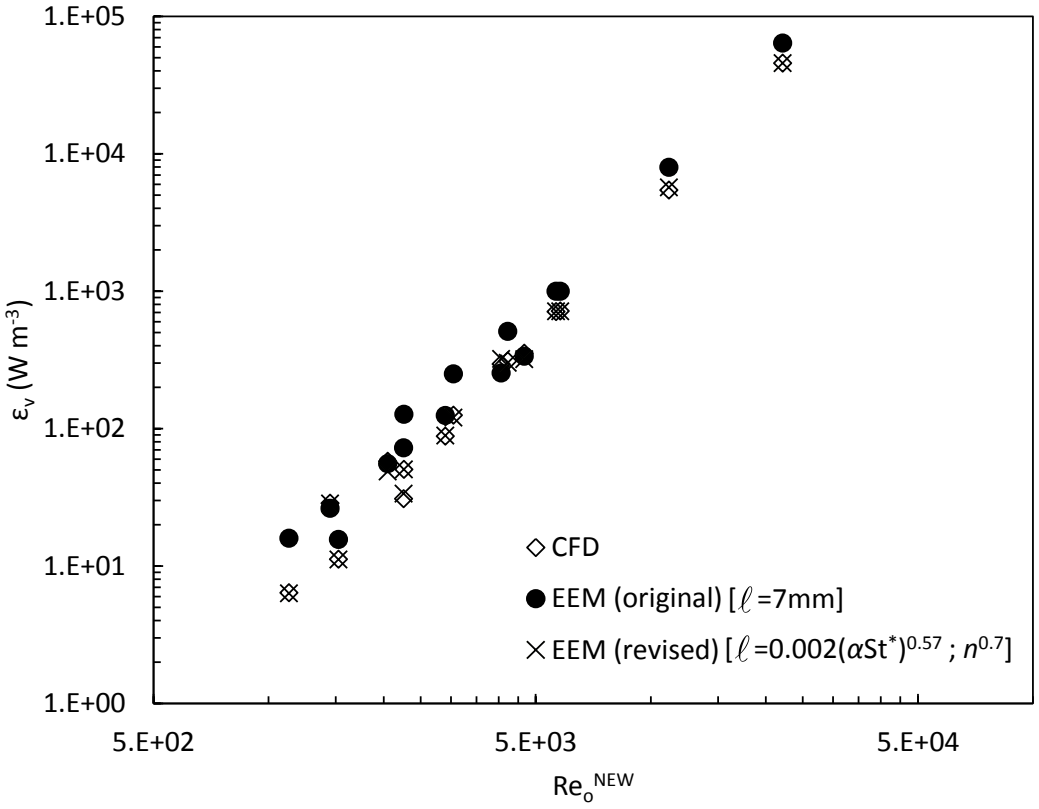

Figure 4.10. *Simulated and EEM predicted power density as a function of Re_o^{NEW} for runs #1 to #15* [66]

4.5.3.1 Discussion on Mixing Length

As aforementioned, the EEM bases the prediction of frictional pressure drop on the acoustic resistance of a single orifice plate [116] as $\Delta p_o^{friction} = 3u\rho(\upsilon\omega)^{0.5}$, arguing that kinematic viscosity (υ) can be substituted by an eddy kinematic viscosity, $\upsilon_e = \ell^2\omega$, at high velocities. In this way, the "mixing length" (ℓ) variable was introduced in EEM; ℓ is however a rather loose term, as the former viscosity often refers to macro scales, while mixing length is associated with micro scale. In turbulent flows, large eddies are generated and dissipated into small ones, those further dissipate into smaller eddies and so on, i.e. energy cascading. There are generally three turbulent length scales: Kolmogorov scale, Taylor scale and integral length scale. The latter is comparable to the characteristic length scale of any given system, and sometimes referred to as the turbulent integral length scale $\left(l_o \propto k^{3/2}/\varepsilon\right)$ where k is turbulent kinetic energy and ε the turbulent dissipation rate of this kinetic energy. Turbulent integral length scale denotes the distance over which fluid elements are moved due to turbulent eddies; the

determination of such a length scale for any reactor system is not a trivial matter, a good example of this is the work by Ni et al. where a sub-grid turbulent model was employed [55]. It is unknown whether the "mixing length" in Equation (4.2) refers to the turbulent integral length scale; however, Baird and Stonestreet [116] referred to it as "the average distance of travel of turbulent eddies" and gave it a value of 7 mm, which is within the same scale as the characteristic length of the system. Hence, thinking of it as the turbulent integral length scale seems appropriate.

By equating Equation (4.9) to the power density obtained from simulated results using Equation (4.4), the "mixing length" can directly be calculated for all the simulated conditions; by doing so, the dependency of the "mixing length" on both geometric and operational parameters can be examined as shown in Figure 4.11. Clearly, baffle diameter and oscillation amplitude are the key parameters affecting "mixing length", while the rest have little impact. The influence of amplitude on "mixing length" discovered in our work agrees with the findings reported by Reis et al. [37], in which an increment in amplitude (at constant frequency) resulted essentially in an increment in mixing length, thus increasing mixing in the axial direction and reducing it radially. Similarly, when D_b is small, formed eddies occupy more radial space enhancing radial mixing and suspension of solids (if present), while a bigger D_b leads eddies to occupy more axial space. The values of "mixing length" found in our work range from 7.6 to 22.1 mm, agreeing with the concept of "mixing length", which cannot be greater than L_b (L_b = 23.5 mm for all runs except for #10 and 11). Baffle spacing set the maximum value mixing length could achieve for a given system, however L_b alone does not have an impact on mixing length if the rest of operating and geometric parameters are kept constant. It is the combination of the oscillatory amplitude and the baffle orifice diameter that determines the scale of the mixing length.

A good rough estimation for "mixing length" is $\ell = x_o$, which reduced the AAE reported down to 18%. This study concludes that the "mixing length" is not a constant for a given device and should appropriately be estimated for each individual run. Figure 4.12 plots the "mixing length" as a function of the dimensionless group αSt^*, which captures the direct and inverse relationship of "mixing length" with x_o and D_b respectively, where $St^* = \frac{D_b}{\pi x_o}$ is the revised Strouhal number proposed by Ni and Gough [101]. Hence, an empirical correlation for the estimation of "mixing length" is

proposed: $\ell = 0.002\left(\alpha St^{*}\right)^{-0.57}$. This correlation for the estimation of ℓ, as opposed to a borrowed value of 7 mm, significantly improves the accuracy of EEM, reducing the averaged absolute error from 42% to 4%.

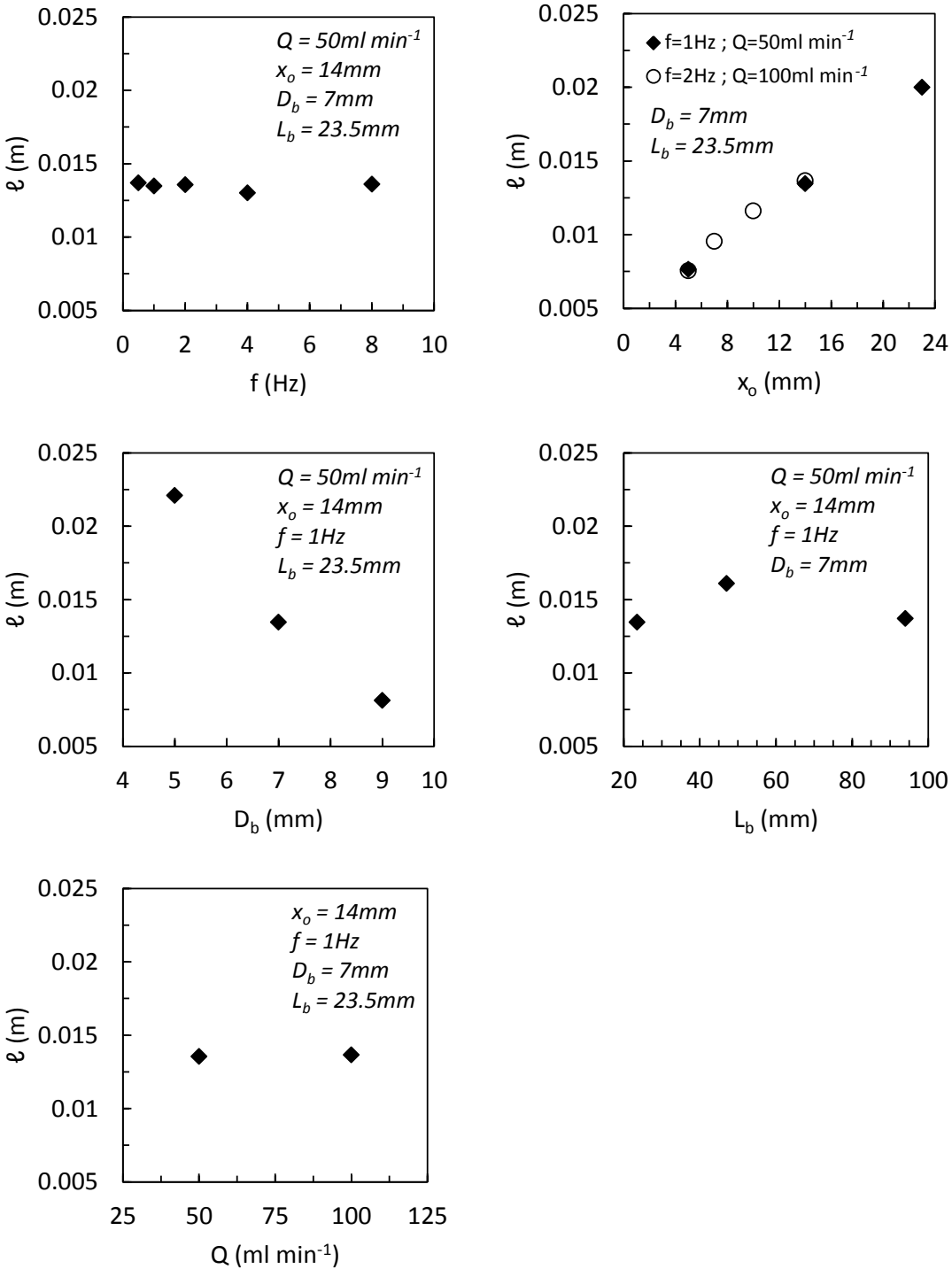

Figure 4.11. *Mixing length change with f, x_o, D_b, L_b and Q* [66]

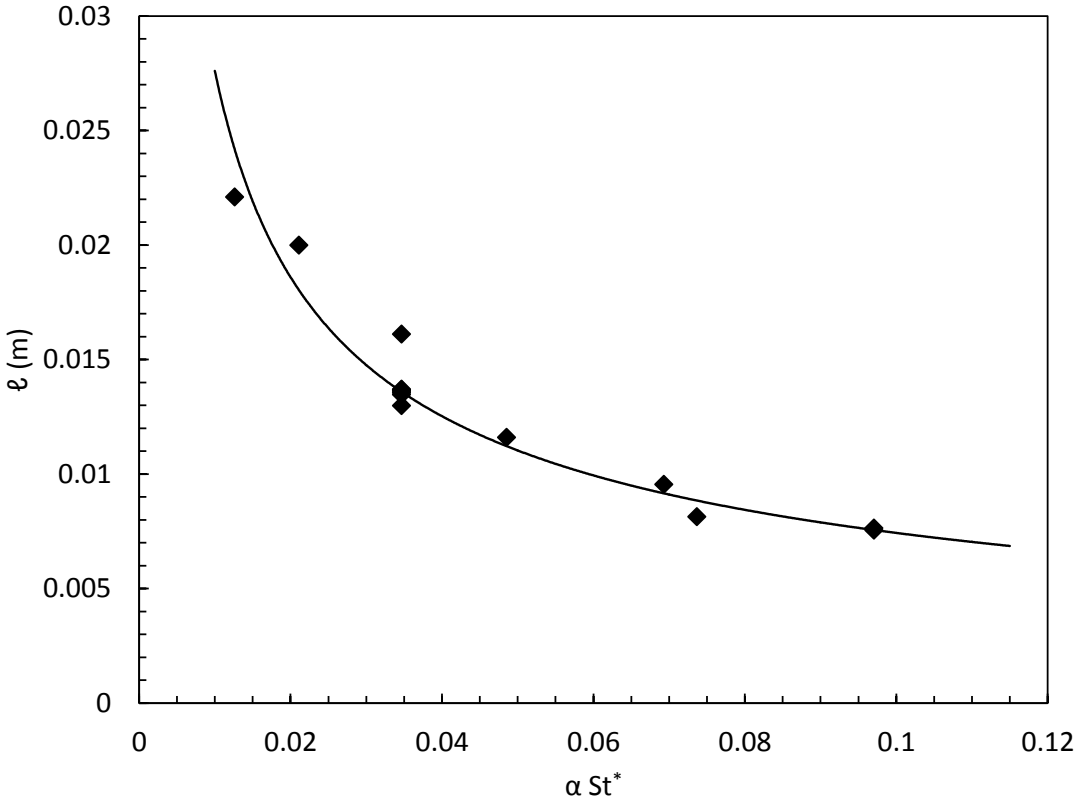

Figure 4.12. *Mixing length as a function of αSt^* for runs #1 to 15* [66]

4.5.3.2 Discussion on K_i

K_i is a geometric factor in Equation (4.3) that corrects the assumption that the flow behaves as a central plug of baffle diameter [116], approaching one as baffle spacing decreases. In order to understand the physics behind this factor, K_i was directly be calculated from Equation (4.3) by equating it to the simulated phase shift values and utilising the calculated mixing length values reported in the previous sub-section. The calculated K_i values ranged from 0 to 2, when K_i should never be greater than one. This was solved by implementing a power law dependency with n as $\delta = \tan^{-1}\left(LK_i / 3n^{0.7}\ell\right)$ and solving for K_i. Figure 4.13 shows the dependency of K_i on all parameters listed in Table 4.1, displaying a non-existing dependency on flow rate and baffle diameter. However, not only its expected inversely proportional relationship with baffle spacing is not strictly linear, but it also shows a rather complex dependency with amplitude, especially at a 100 ml min^{-1} flow rate, and an inversely proportional with oscillatory frequency. Additionally, a K_i value of 0.9 as suggested by Braid and Stonestreet [116] was not obtained for any of the simulated conditions. These findings suggest that this geometric factor is merely a fitting coefficient, thus questioning the validity of Equation (4.3).

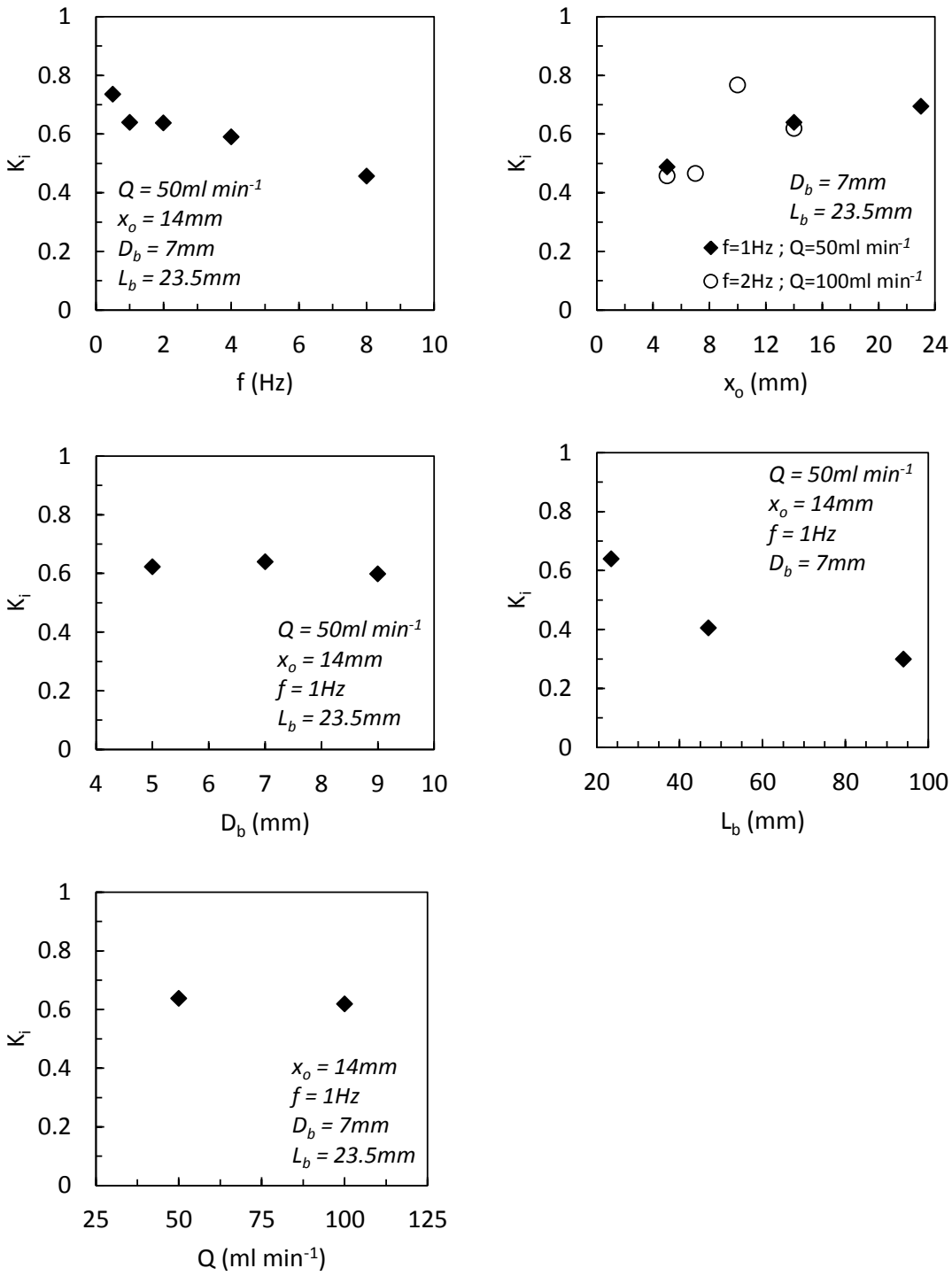

Figure 4.13. *K_i change with f, x_o, D_b, L_b and Q*

4.6 Conclusion

This work, for the first time, provides CFD validations to the two existing models for the estimation of power density in oscillatory baffled devices. The existing QSM over-estimates power dissipation rates due to the inappropriate formulation of two of its geometric parameters for modern OBRs/COBRs. By using a revised power law

dependency on the number-of-baffles term (n^x) and an appropriate C_D, the QSM was subsequently validated for a much wider application range than previously outlined. The EEM generally provides better predictions of power density for the conditions tested; however, its accuracy can substantially be improved by making use of the same power law dependency on n and an empirical correlation of estimating EEM's "mixing length" that is proposed in this work; the EEM has hence been validated for a much wider application range than originally stated. This work has also demonstrated that both the QSM and EEM are applicable for continuous operations, as net flow contribution to power dissipation rates is negligible in oscillatory baffled reactors. In addition, both revised models consistently predict similar power densities for every case, both presenting a high degree of agreement with our CFD simulations and reporting small AAE values for the wide range of geometric and operating conditions tested. This suggests that these two models can be used interchangeably with high confidence.

Chapter 5 Characterisation of Pressure Drop & Power Dissipation in Continuous OBRs (COBRs)

5.1 Introduction

As aforementioned in Section 2.5, previous studies [14, 121] and confidential industrial trials revealed dampening in the oscillatory velocity experienced by the liquid phase, observed with the use of tracers, and by solid particles as they travel downstream in oscillatory baffled devices. Occasionally, this phenomenon resulted in sudden settling of solids, having a tremendous impact on the control of processes such as crystallisation of pharmaceuticals because of its effect on solids' suspension, mixing efficiency and the quality of the product, i.e. crystals. Hence, understanding the potential causes of oscillation dampening and energy losses in these types of reactors is essential so strategies can be proposed to avoid such events. Little or no research has been undertaken in this area; the only exception was the early work of Brunold et al. [78] who reported an increment in overall energy dissipation with an increase in the number of baffles in the systems, and the work of Mackley et al. [120] who for the first time claimed that the phase shift between the velocity and pressure drop wave forms could lead to significant reduction of the system's power. However, a detailed analysis of the evolution of energy dissipation across the lengths of the device has never been reported. The purpose of the research presented hereunder is to tackle this knowledge gap.

5.2 Methodology

This study was also undertaken in the standard NiTech DN15 COBR reactor, utilising the data obtained during the simulation of all the cases presented in Chapter 4, see Table 4.1. The effects of different operational and geometric parameters on the power dissipation rates and phase shift in COBR are studied by analysing the results reported in Table 4.2. Additionally, temporal pressure drop profiles across multiple longitudinal sections of the devices are extracted and the evolution of power density, ε_v, the maximum centre-to-peak pressure drop fluctuation, Δp_o, and phase shift, δ, along the length of the device are examined for a wide range of operational and geometric conditions. For this purpose, the area-weighted averaged static pressure was monitored at cross-sectional planes spaced 23.5 mm from each other, as shown in Figure 5.1. This allowed for the analysis of 32 temporal pressure drop profiles, one per baffle constriction when L_B = 23.5 mm, along the modelled 0.752 m long straight section; each

profile was computed as $\Delta p_i(t) = p_{i-1}(t) - p_i(t)$, where i is the index of the section under evaluation ranging from 1 to 32, see Figure 5.1. As mentioned earlier in Section 4.4, the equivalent of the first two and last two baffle constrictions, when L_B = 23.5 mm, were discarded in order to minimize the effect of the open boundary conditions at the inlet and outlet. Hence, the results obtained for $\Delta p_1(t)$, $\Delta p_2(t)$, $\Delta p_{31}(t)$ and $\Delta p_{32}(t)$ are not presented. Each simulated $\Delta p(t)$ profile was utilised to calculate power density by numerically integrating Equation (4.4), and for the calculation of Δp_{net}, Δp_o and δ as previously described in Section 4.5.1 ($\Delta p_o = \Delta p_o'$).

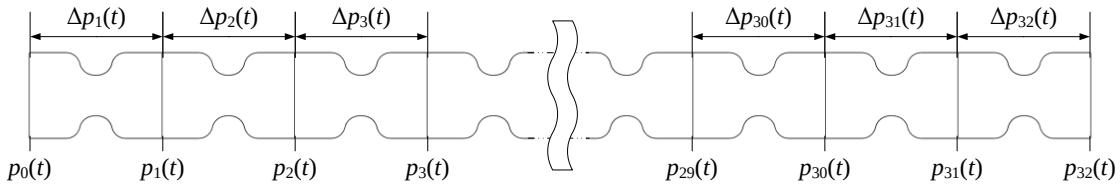

Figure 5.1. *Scheme for the extraction of temporal pressure drop profiles*

The contribution of net flow, i.e. net inlet velocity and net pressure drop, to power density was computed by comparing the results from Equation (4.4) and the simplified version of Equation (4.5); the relative percentage differences between both results were consistently below 3.6%. Similarly, by comparing the results of Δp_{net} and $\Delta p_o'$ presented in Table 4.2, it is seen that the former is consistently less than 8.9% of the latter, $\Delta p_{net} < 0.089\Delta p_o'$, representing a rather negligible contribution to the pressure drop across any section. Hence, only the evolution of ε_v, Δp_o and δ along the length of the device are analysed in this study.

An additional simulation was run in order to analyse the change of these variables with length in compressible flow in a COBR. This simulation was performed under the same operating conditions used for run #5. Air ($\mu = 1.7894 \cdot 10^{-5}$ kg m^{-1} s^{-1}) was selected as the working fluid and its density in Equations (3.1) and (3.2) is solved as per the ideal gas law:

$$\rho = \frac{pM}{RT} \tag{5.1}$$

where R is the ideal gas constant (8.3144598 kg m^2 s^{-2} K^{-1} mol^{-1}), M the molar mass (kg mol^{-1}) and T temperature (K). This simulation was performed as per the same

framework earlier described in Sections 3.2 – 3.4 with the addition of a *second order upwind* scheme, utilised for the spatial discretisation of density.

5.3 Results & Discussion

5.3.1 The Effect of Operational and Geometric parameters on Power Density and Phase Shift

The power dissipation rates reported in Table 4.2 are hereby presented as a function of the different operational and geometrical parameters analysed in this study, see Table 4.1. Figure 5.2 unveils a power law dependency on all these parameters, with the exception of flow rate. Both oscillatory amplitude and frequency show a directly proportional power law relationship, as an increase in either of these parameters results in higher power density required by the system; oscillatory frequency plays the most dominant role, with a third order power law. These are expected.

Both baffle diameter and baffle spacing exhibit an inversely proportional relationship with power density, i.e. an increase in the number of baffle constrictions in the system and a reduction in the diameter of baffle constrictions translate into a higher power density requirement, however, the change experienced in ε_v with L_b is substantially minor.

While flow rate had a directly proportional impact on ε_v, its effect seems minimal and practically negligible for the conditions tested in comparison with the rest of the parameters under evaluation. Based on the above discussion, the following function can be deduced: $\varepsilon_v = f\left(f, x_o, D_b^{-1}\right)$.

While power density indicates the amount of energy required by the system to overcome all the geometric and operational constraints of the flow, it also denotes the rate at which the energy applied to the system is being dissipated into the fluid, thereby translating into fluid movement. This implies that the higher the power density, the higher is the energy gained and experienced by the fluid.

In a similar manner, the dependency of phase shift on different operational and geometrical parameters was also analysed, as presented in Figure 5.3. Baffle diameter was revealed as the parameter with the largest influence on δ, displaying a positive proportional linear relationship. Oscillatory frequency and amplitude display an inverse

linear relationship with phase shift, the former showing a slightly larger impact on δ than the latter. The dependency on baffle spacing is not strictly linear and its impact seems to be rather negligible. For the conditions tested, flow rate also displayed a minimal impact on phase shift, much like the case of power density. Hence, the largest influence of operational and geometric parameters in phase shift can be summarised as $\delta = f\left(D_b, f^{-1}, x_o^{-1}\right)$.

It should be noted how all the parameters under this study have the inverse effect on power density and phase shift. For example, an increase in oscillatory frequency will result in a smaller phase shift and a larger power dissipation rate. On the contrary, baffle constrictions of smaller diameter will lead to a smaller phase shift value and a higher power density. Therefore, it can be concluded that power dissipation rates and phase shift values have an inverse relationship, i.e. $\varepsilon_v = f\left(\delta^{-1}\right)$. These findings significantly help in understanding the physical implications of δ, its relationship with ε_v and its overall impact on the flow in COBRs.

Phase shift accounts for the temporal separation between the inlet velocity and pressure drop sinusoidal wave forms. This implies that if at *time* = *t* s, pressure drop reaches a value of $\Delta p(t) = \Delta p_o$, then at *time* = $(t + \delta)$ s the inlet velocity will be $u_{inlet}(t) = \omega x_o$. Therefore, δ is the time taken for the energy generated due to pressure drop to be converted into fluid's kinetic energy. If δ decreases, the rate at which energy generated by pressure drop dissipates into the fluid as kinetic energy increases, resulting in higher power density. On the contrary, larger phase shift values imply lower power dissipation rates. Decrements and increments in phase shift are qualitatively represented in Figure 5.4, where the inlet velocity sinusoidal wave form is also displayed and a random value of $\delta = (\pi/2)$ rad is taken as reference.

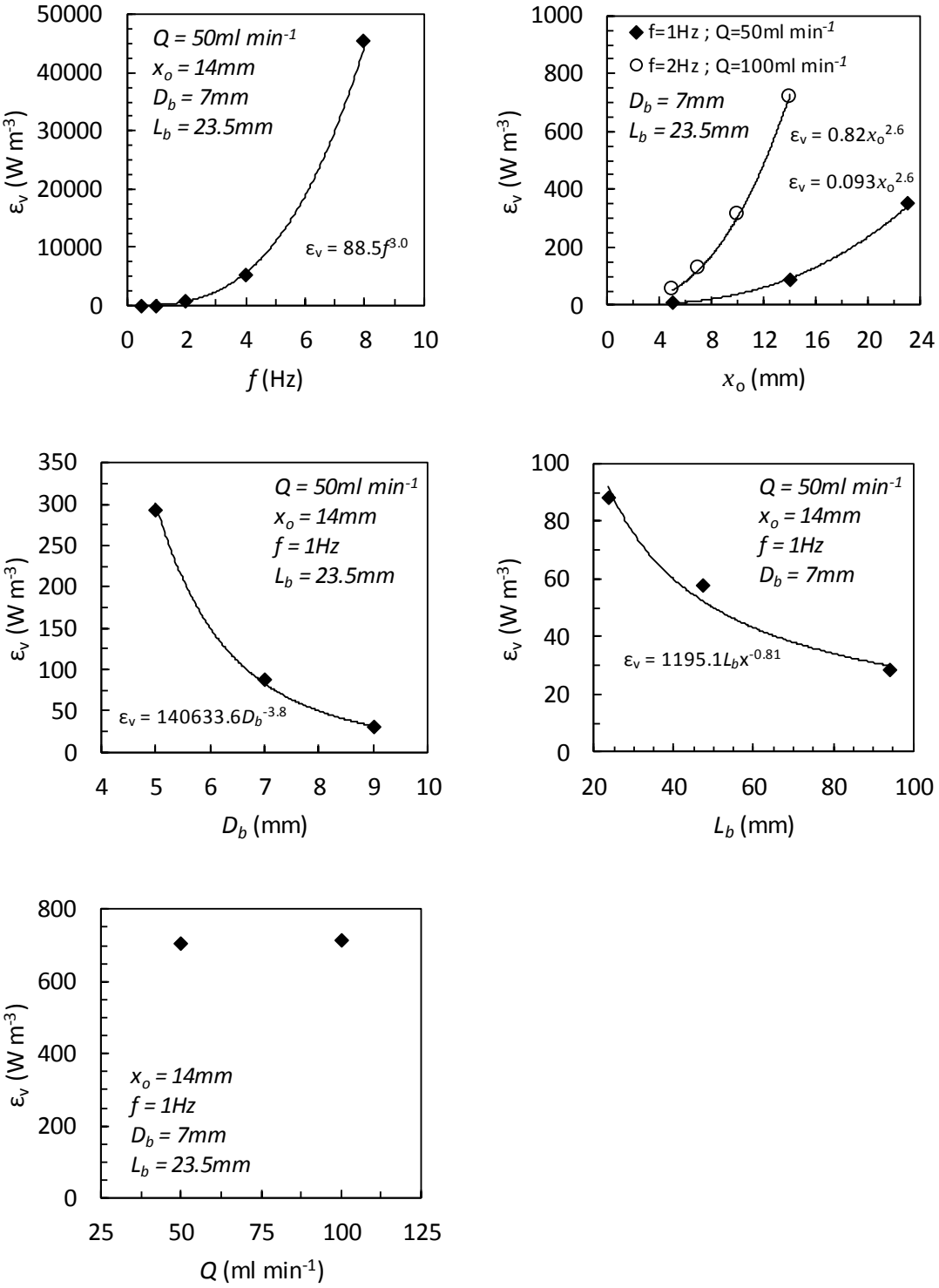

Figure 5.2. *Power density change with f, x_o, D_b, L_b and Q*

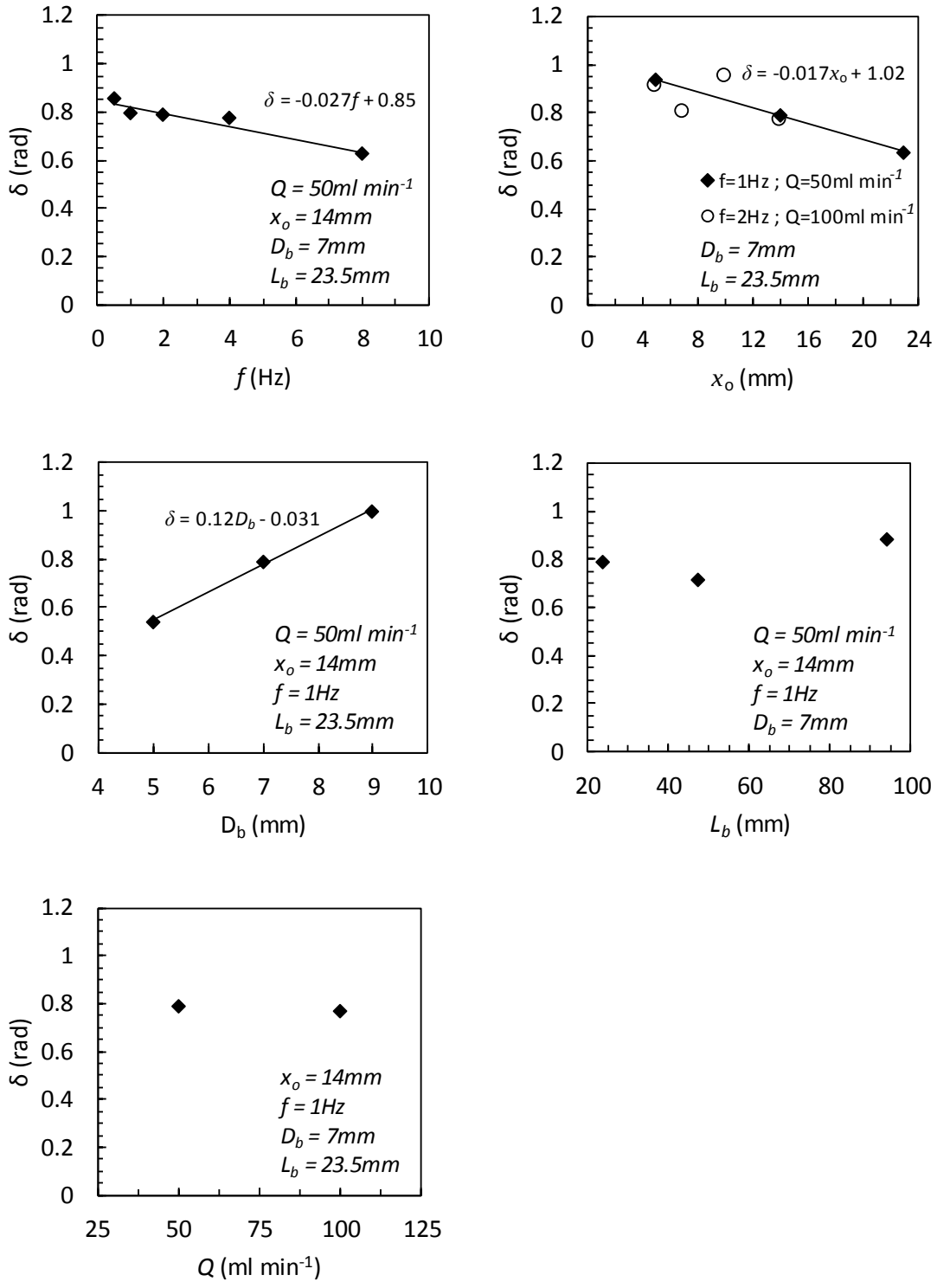

Figure 5.3. *Phase shift change with f, x_o, D_b, L_b and Q*

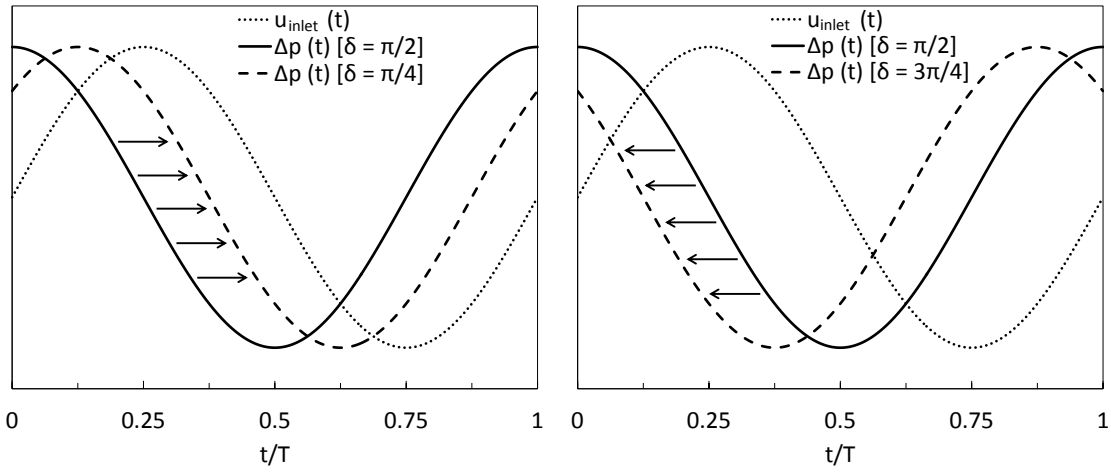

Figure 5.4. *Scheme of pressure drop wave forms illustrating a decrement (left) and an increment (right) in phase shift*

5.3.2 Evolution of Power Density, Pressure Drop and Phase Shift with Length

Values of power dissipation rate, maximum centre-to-peak pressure drop fluctuation and phase shift obtained for consecutive sections (23.5 mm long each) of the reactor are plotted in Figure 5.5, displaying the evolution of these variables with length for all the conditions listed in Table 4.1.

It is observed that the three analysed variables (ε_v, Δp_o and δ) remain practically constant along the length of the reactor for all the conditions under evaluation, see runs #1 – 9 and #12 – 15, with the exception of runs #10 and 11. Figure 5.6 shows the power density calculated from pressure drop profiles over a total length of 0.658 m and the section-averaged ε_v are plotted against Re_o^{NEW}.

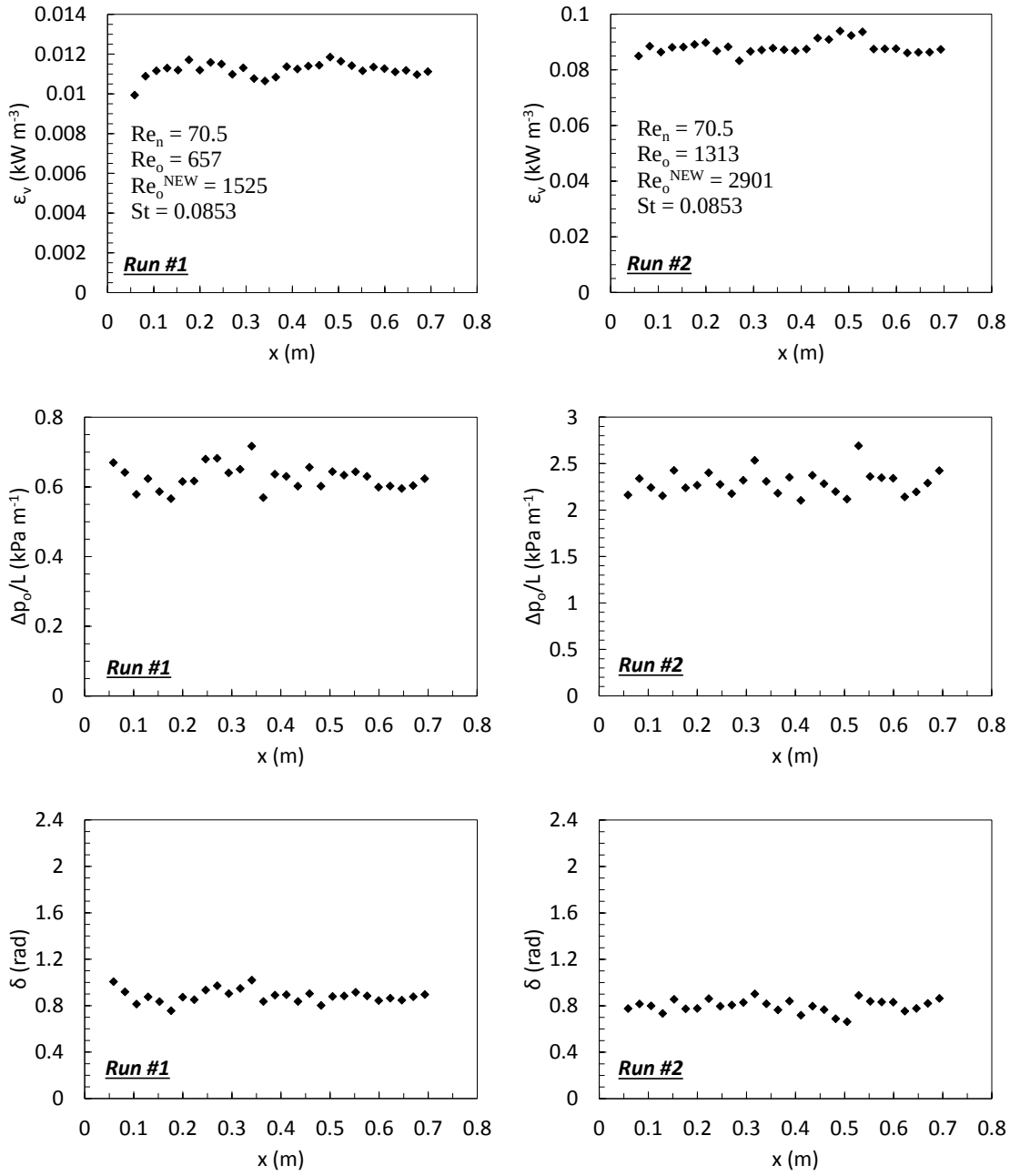

Figure 5.5. *Power density, maximum centre-to-peak pressure drop fluctuation and phase shift as a function of reactor's length*

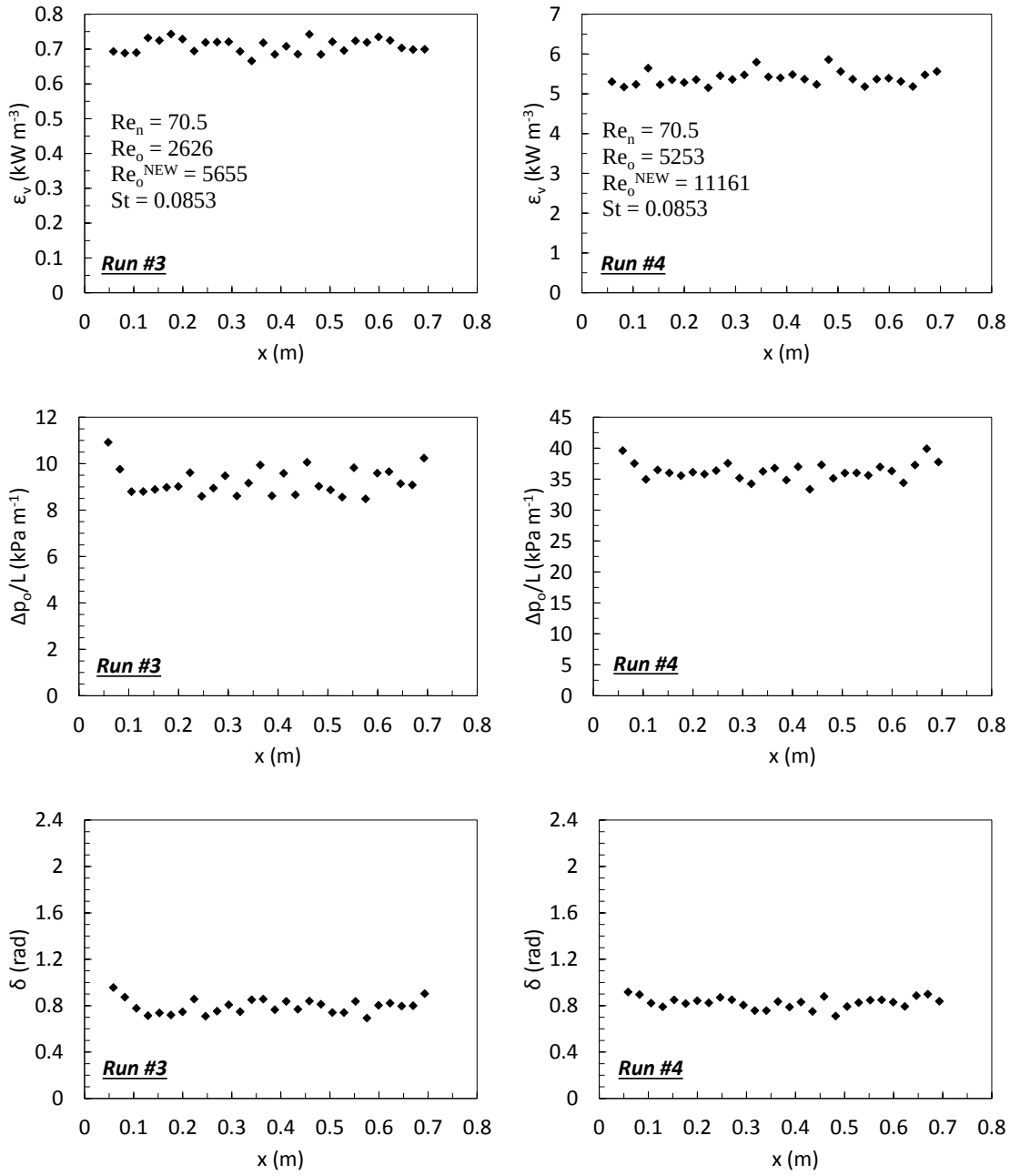

Figure 5.5. (continuation) *Power density, maximum centre-to-peak pressure drop fluctuation and phase shift as a function of reactor's length*

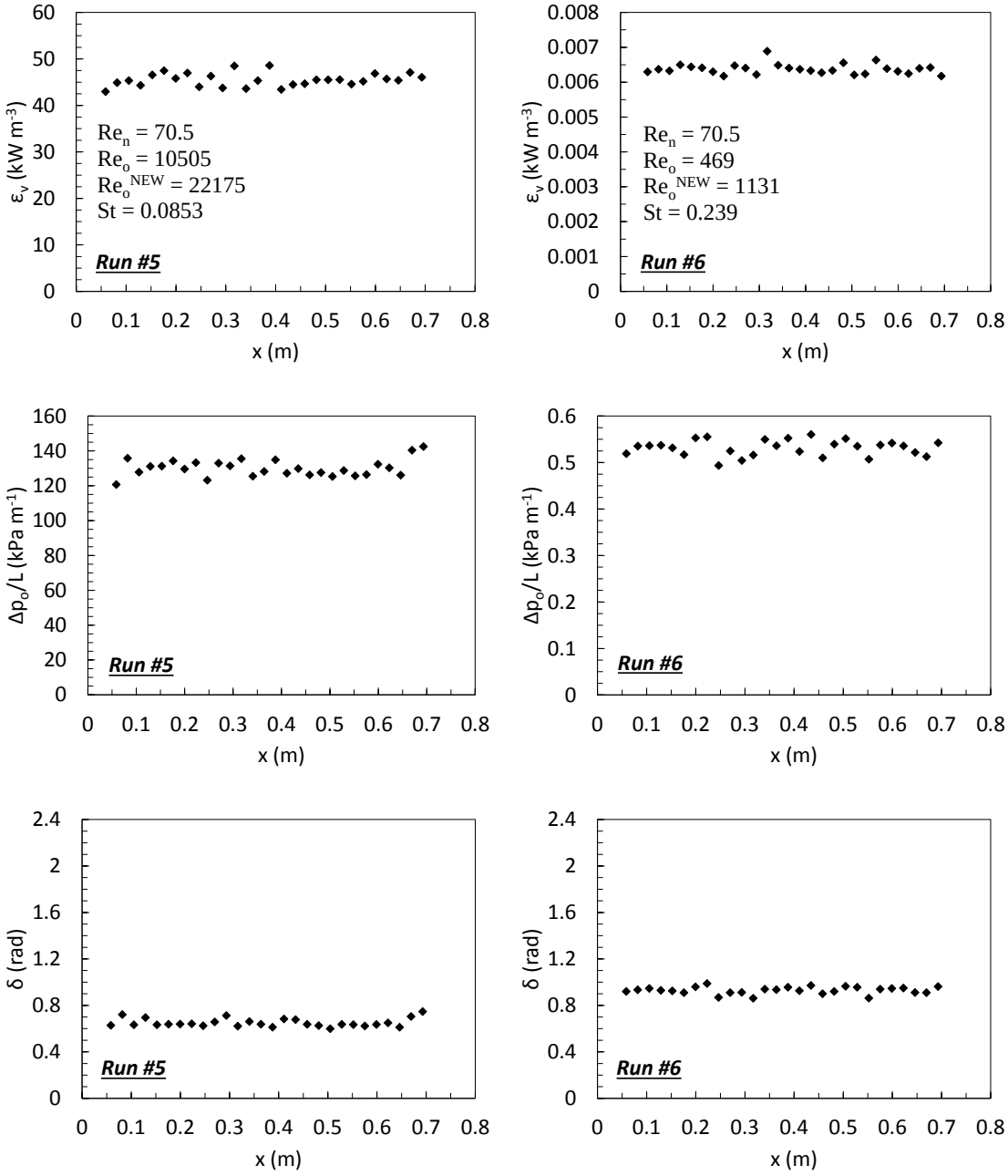

Figure 5.5. (continuation) *Power density, maximum centre-to-peak pressure drop fluctuation and phase shift as a function of reactor's length*

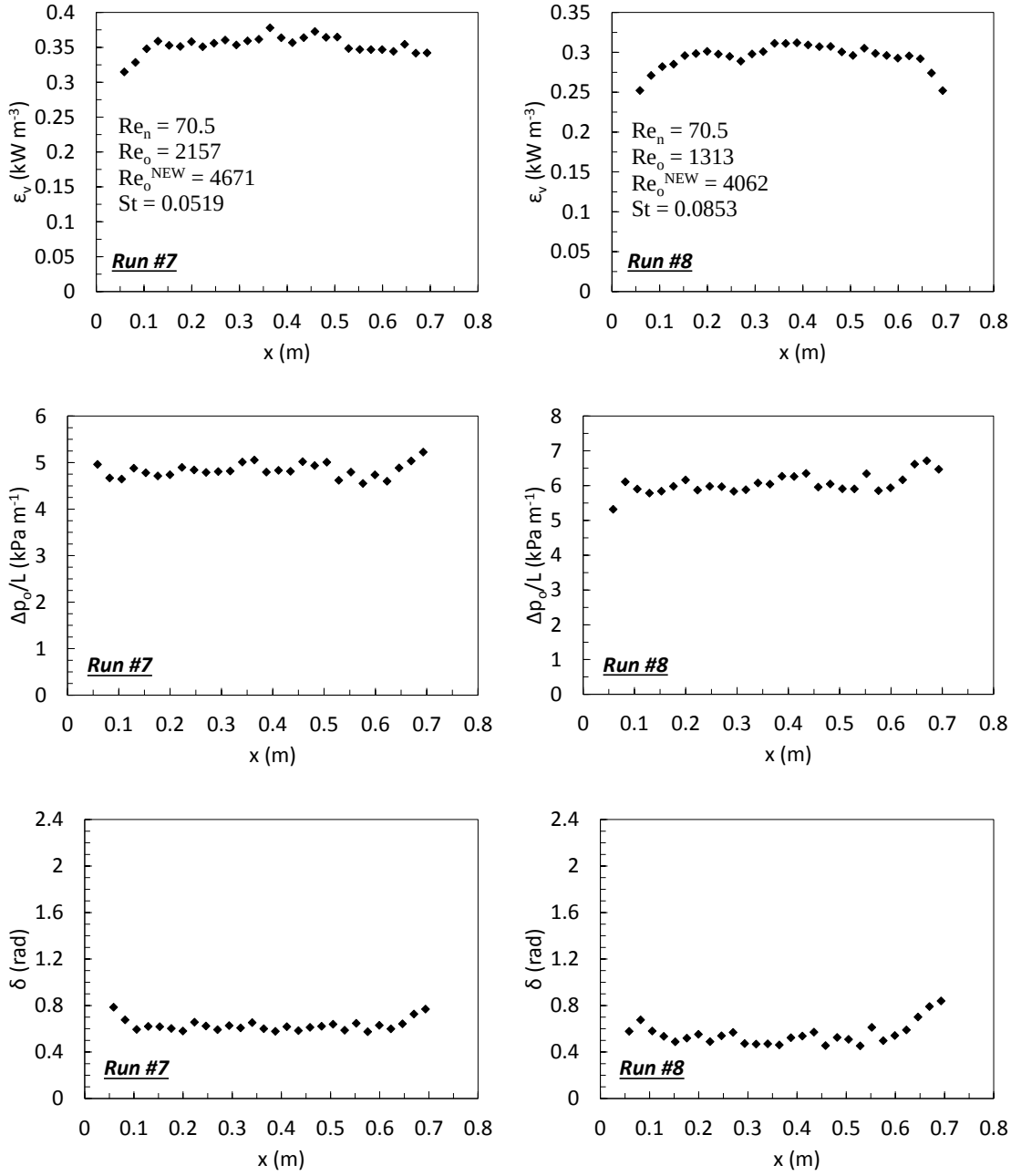

Figure 5.5. (continuation) *Power density, maximum centre-to-peak pressure drop fluctuation and phase shift as a function of reactor's length*

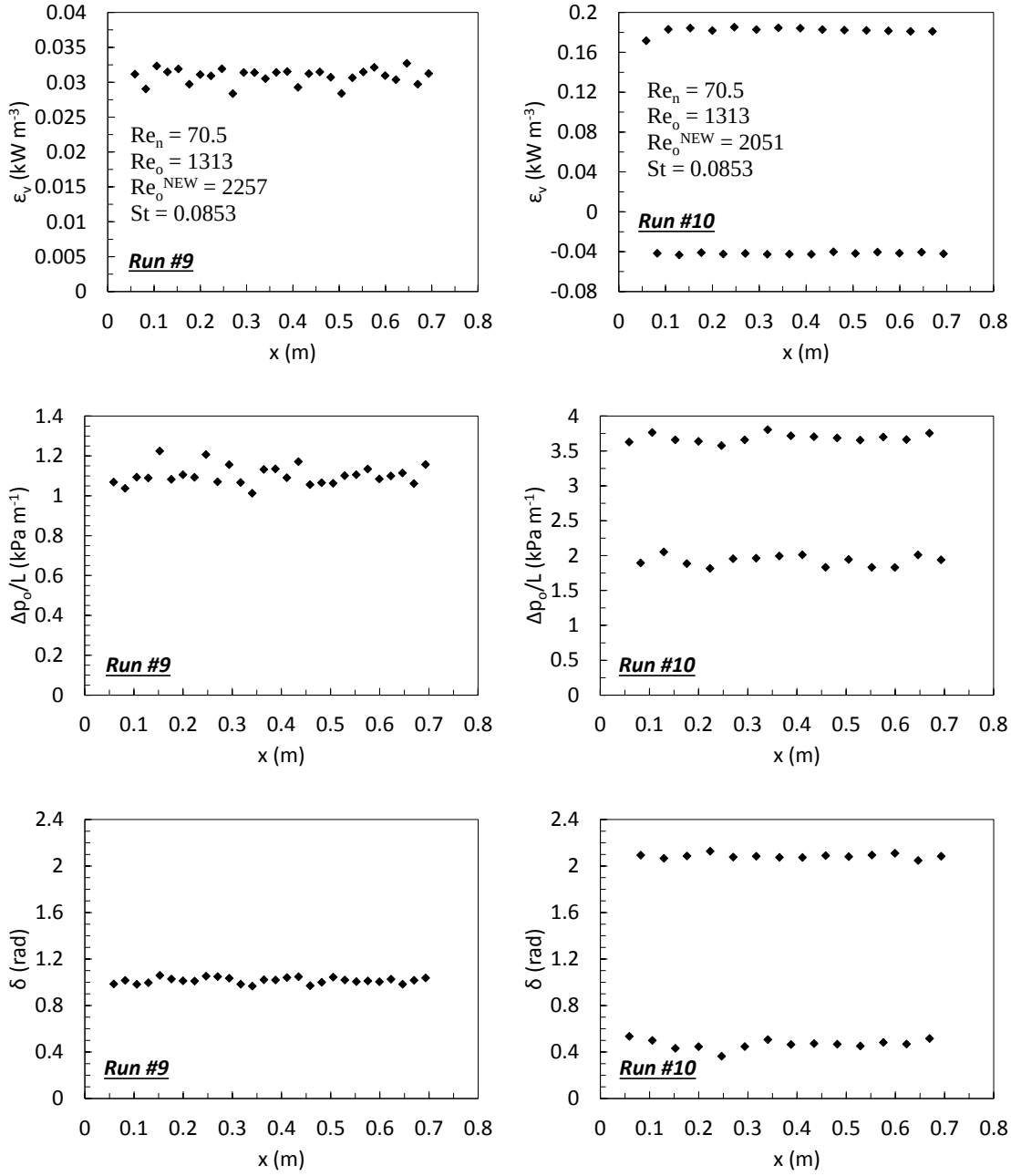

Figure 5.5. (continuation) *Power density, maximum centre-to-peak pressure drop fluctuation and phase shift as a function of reactor's length*

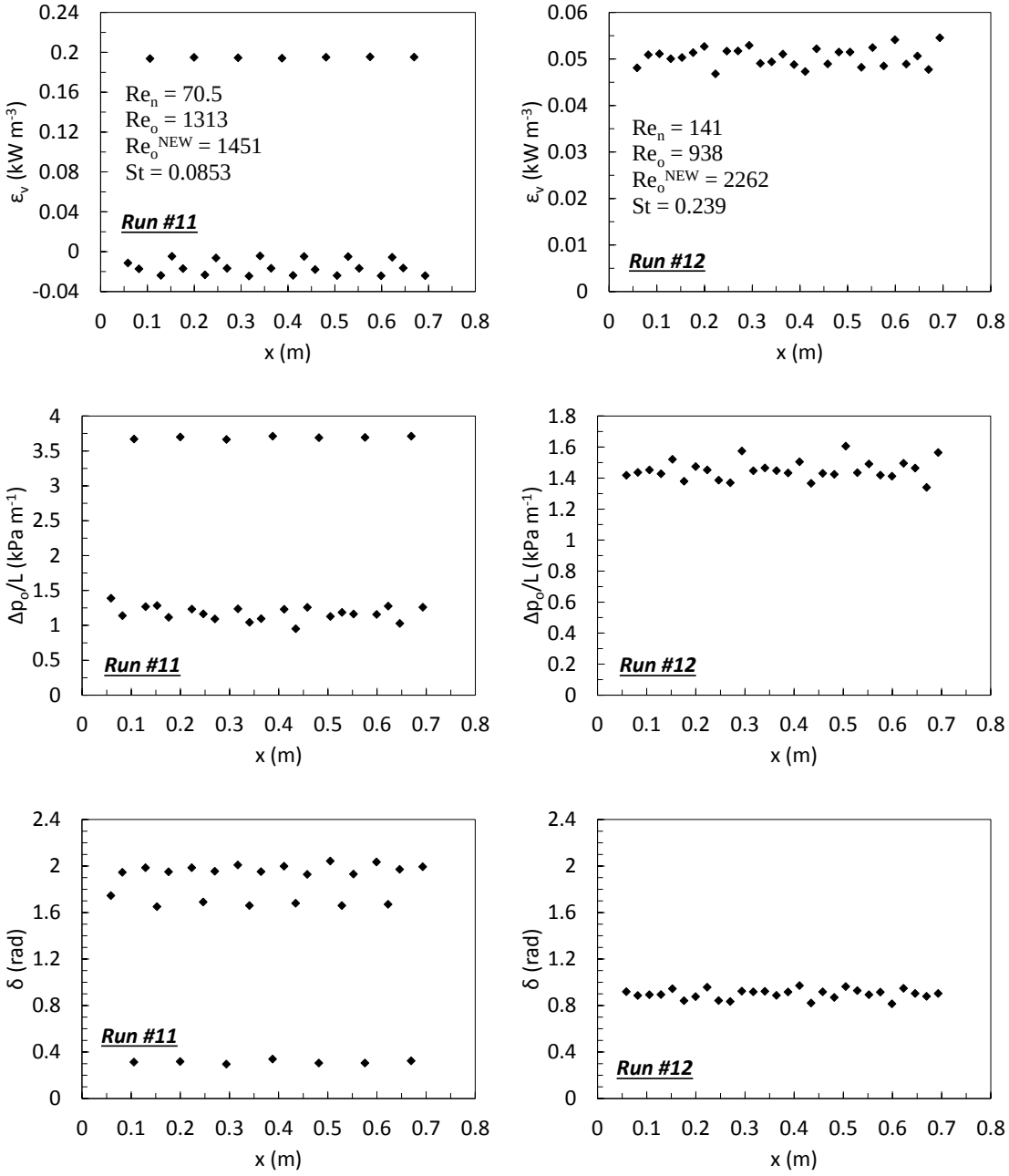

Figure 5.5. (continuation) *Power density, maximum centre-to-peak pressure drop fluctuation and phase shift as a function of reactor's length*

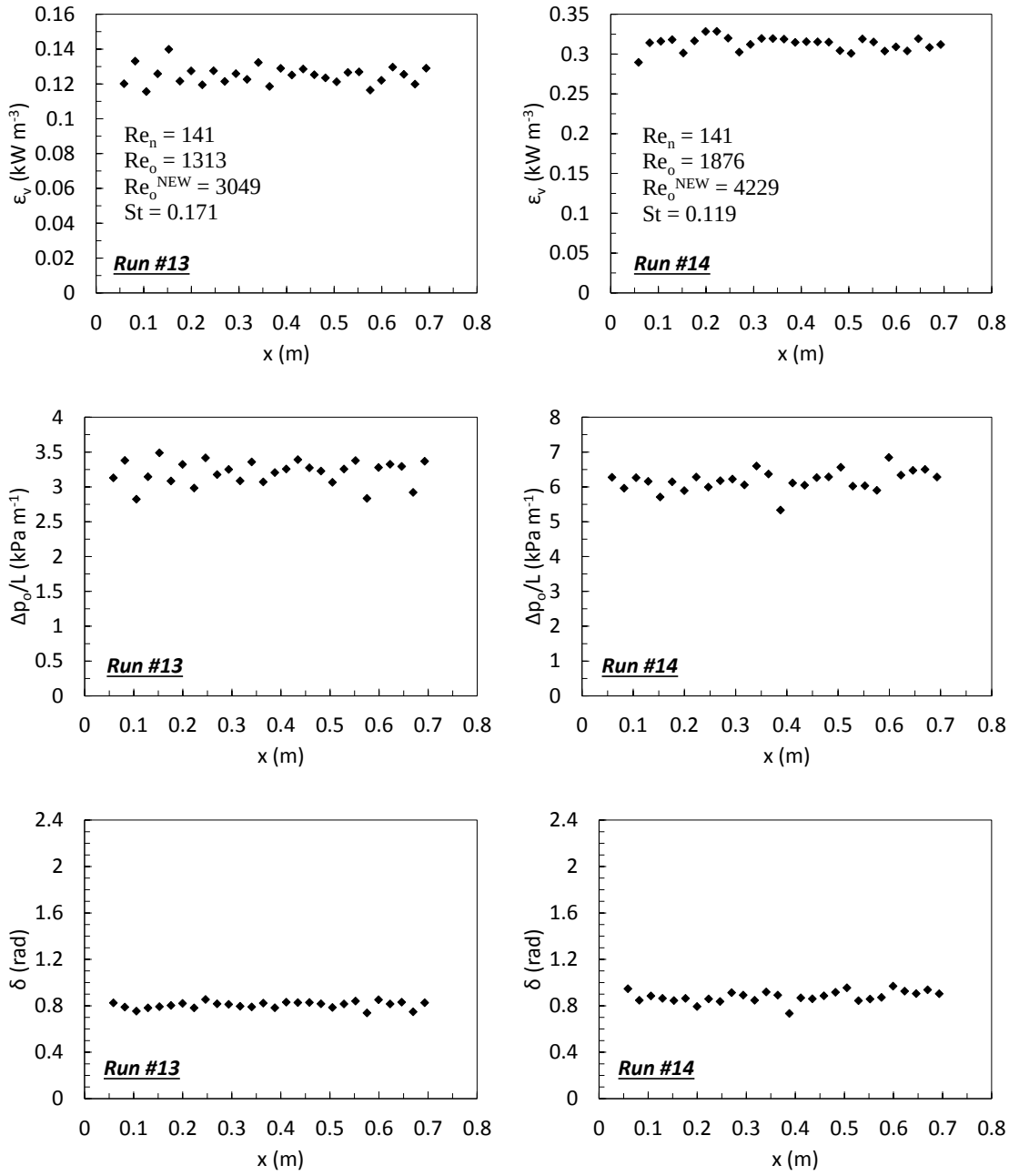

Figure 5.5. (continuation) *Power density, maximum centre-to-peak pressure drop fluctuation and phase shift as a function of reactor's length*

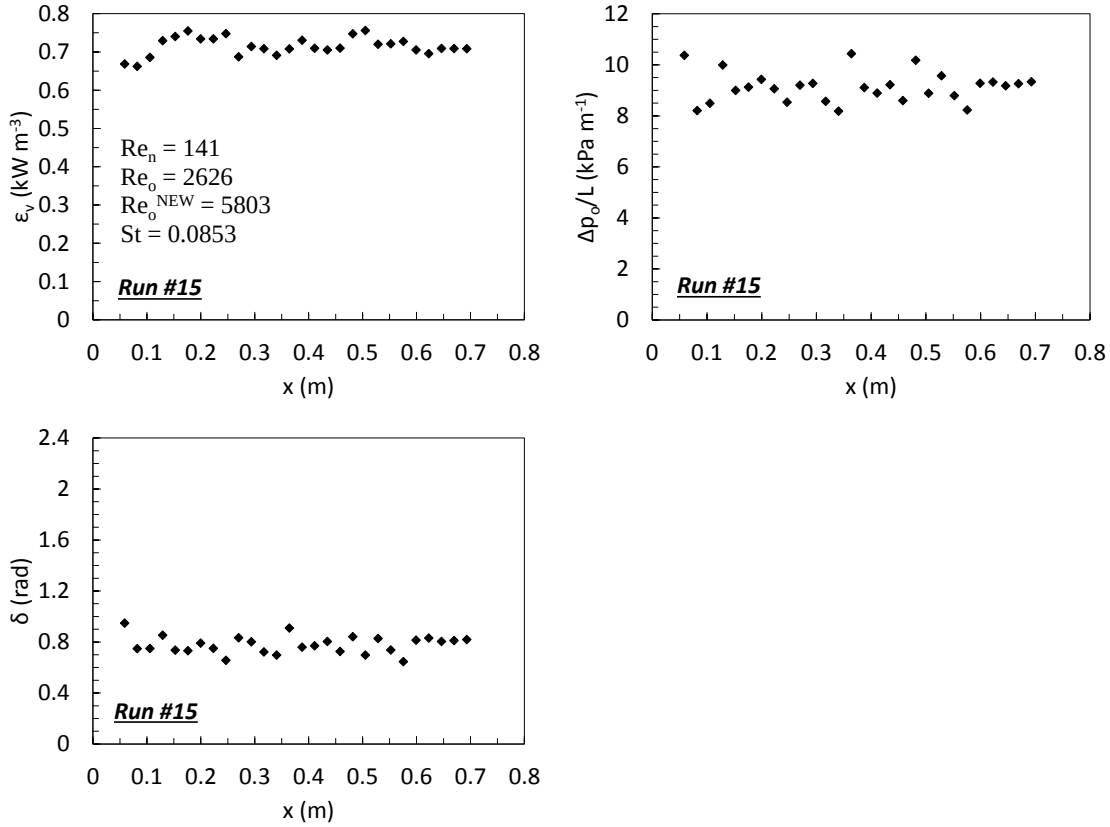

Figure 5.5. (continuation) *Power density, maximum centre-to-peak pressure drop fluctuation and phase shift as a function of reactor's length*

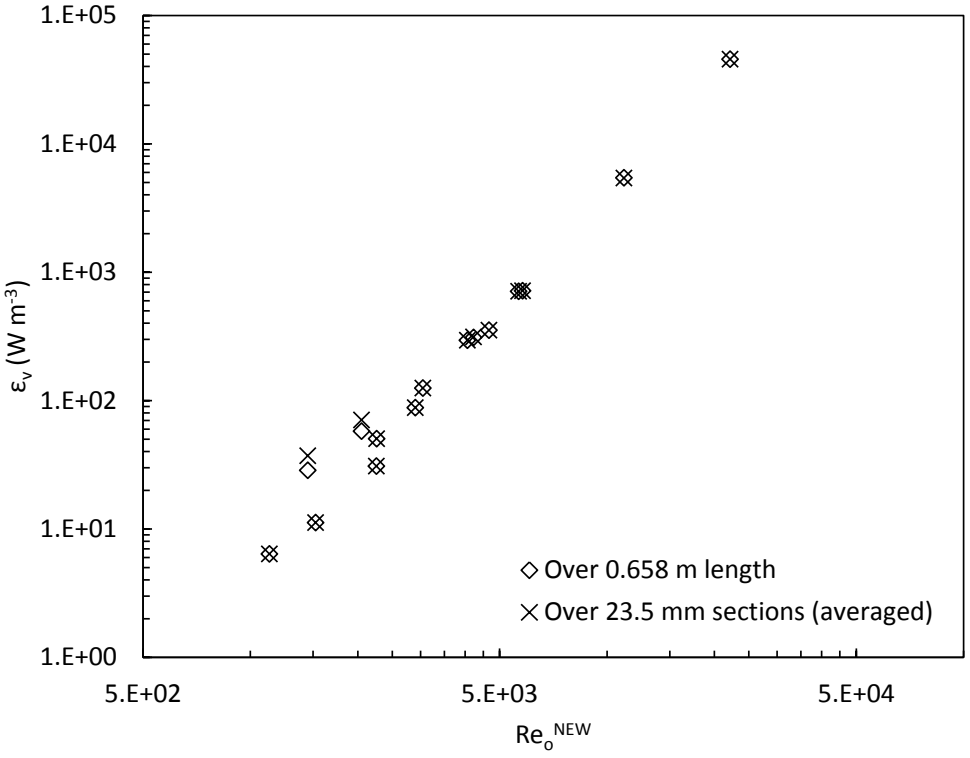

Figure 5.6. *Overall and section-averaged power density as a function of Re_o^{NEW} for runs #1 to #15*

When looking closely at the geometric domain simulated in run #10, Figure 4.3, it is observed that the domain can be divided into thirty-two 23.5 mm long sections, sixteen of which contain a baffle constriction while the rest do not; sections with baffle constrictions are alternated with no baffles. This geometric feature results in two distinguishable sets of values for each of the three variables under evaluation. As expected, the power dissipation rates reported at the sections containing a baffle constriction were of higher magnitude, while power density values for the non-baffled sections were reported as negative. Non-baffled sections have also displayed four times higher values in δ and approximately a half in Δp_o. Figure 5.7 is the velocity vector map during the backward pulse and the stroke of change of direction of oscillation. It is observed how eddies formed during the backward stroke are visibly detached from the edge of the baffle constriction and then dissipate into the bulk fluid, at least to a certain degree, before colliding with eddies formed during the forward-stroke. Therefore, at the time of interaction between eddies formed at opposite strokes, part of their energy has already been dissipated into the bulk fluid. This behaviour results in lower mixing intensity with the region between two baffle constrictions.

This very phenomenon is further accentuated with an increase in distance between constrictions, as simulated in run #11. This geometry comprises three 23.5 mm long sections between every two baffle constrictions, containing a total of only eight constrictions (instead of thirty-two) over the total length of the reactor, see Figure 4.3. Eddies generated during the forward or backward strokes are detached from the edge of the baffle walls and ejected into the bulk fluid, where they fully dissipate during the change of direction strokes without interacting with each other, i.e. the eddies are not connected or there is no eddy current. This leads to non-mixing within the region between two baffle constrictions, generating regions of local stalling; this phenomenon is noticeably observed in Figure 5.8. The cycle-averaged pressure drop profiles obtained over baffle constrictions and non-baffled sections for runs #10 and 11 are presented in Figure 5.9. It should be noted how the sudden increase in phase shift within the sections containing no baffle constriction leads to almost reversed pressure drop profiles in comparison to those extracted across baffle constrictions.

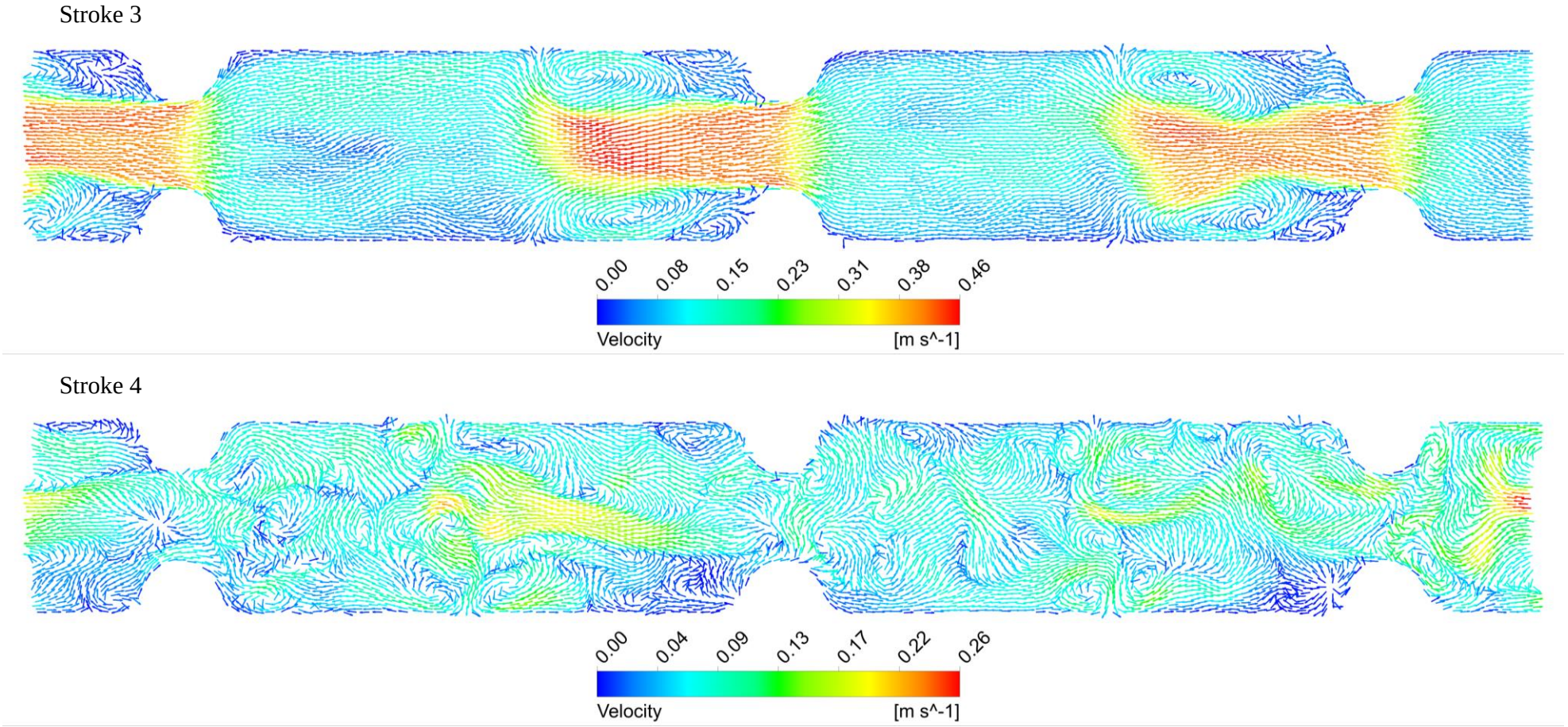

Figure 5.7. *Velocity vector map of sections 15 – 19 at strokes 3 and 4 of simulated cycle 10 for run #10 (Q = 50ml min^{-1}, f = 1Hz, x_o = 14mm)*

Stroke 3

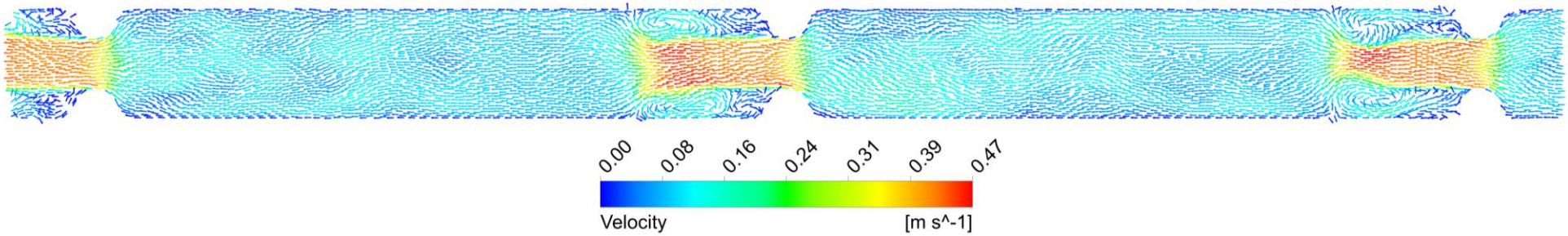

Stroke 4

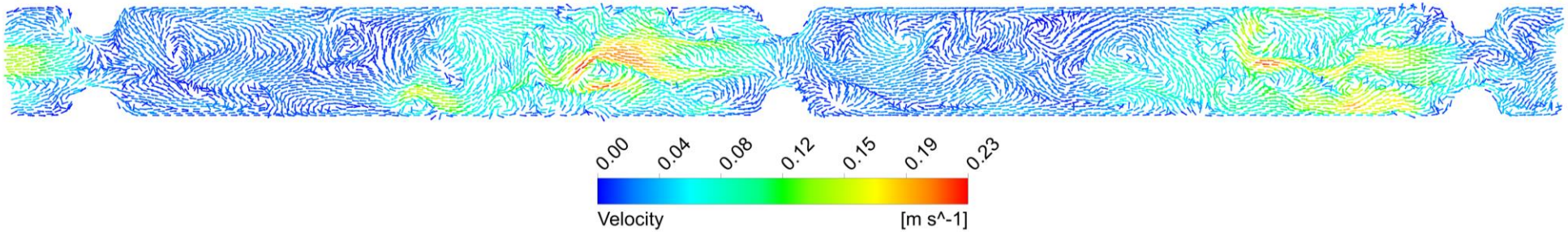

Figure 5.8. *Velocity vector map of sections 13 – 21 at strokes 3 and 4 of simulated cycle 10 for run #11 (Q = 50ml min^{-1}, f = 1Hz, x_o = 14mm)*

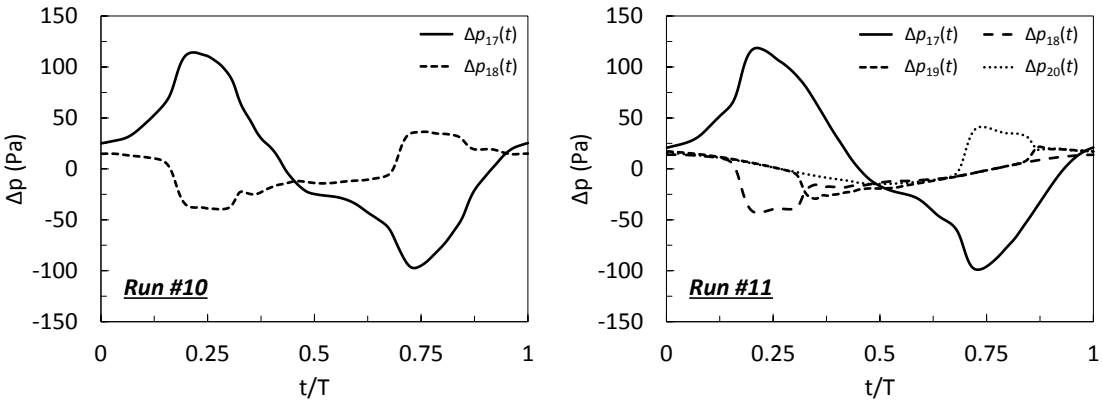

Figure 5.9. *Cycle-averaged pressure drop profiles measured at different sections for runs #10 and 11 (Q = 50ml min^{-1}, f = 1Hz, x_o = 14mm)*

While decrement in power density denotes less amount of energy being gained by the fluid, negative ε_v implies that the fluid is undergoing energy loss. The findings obtained in this study indicate that eddy shedding during the change of directions of the flow in geometries with larger baffle spacing leads the fluid to experience local energy losses which translates into regions of lower energy due to pressure drop, ultimately resulting in fluid zones with lower kinetic energy.

However, it is worth noting that while the three variables under study present different sets of values for run #10 and 11, the values within each set remain constant with length or revolve around a nearly constant value. Therefore, there are no signs of potential energy losses undergone by the fluid as it moves downstream for these runs. Velocity vector maps at strokes 1 – 4 of oscillatory cycle 10 for all simulated conditions are presented in Appendix 7.

5.3.3 Evolution of Power Density, Pressure Drop and Phase Shift with Length in Compressible Flow in a COBR

In order to fully verify that no energy losses can be experienced in a COBR as the fluid moves downstream, an additional case with compressible air flow in a COBR was simulated. Tables 5.1 and 5.2 list the simulation conditions for this case and the obtained ε_v, Δp_{net}, Δp_o and δ values extracted from the $\Delta p(t)$ profile measure over a total length of 0.658 m, respectively. Analogous to the study presented in the previous

section, the evolution of ε_v, Δp_o and δ with length along the device is shown in Figure 5.10.

Table 5.1. *Conditions under which compressible flow was simulated*

Q (ml min^{-1})	f (Hz)	x_o (mm)	D_b (mm)	L_b (mm)	Re_n	Re_o	St
50	8	14	7	23.5	4.6	685	0.0853

Table 5.2. *Summary of results extracted from CFD simulated compressible flow*

Δp_{net} (Pa)	Δp_o (Pa)	δ (rad)	ε_v (W m^{-3})
1.5	150.2	1.09	46.8

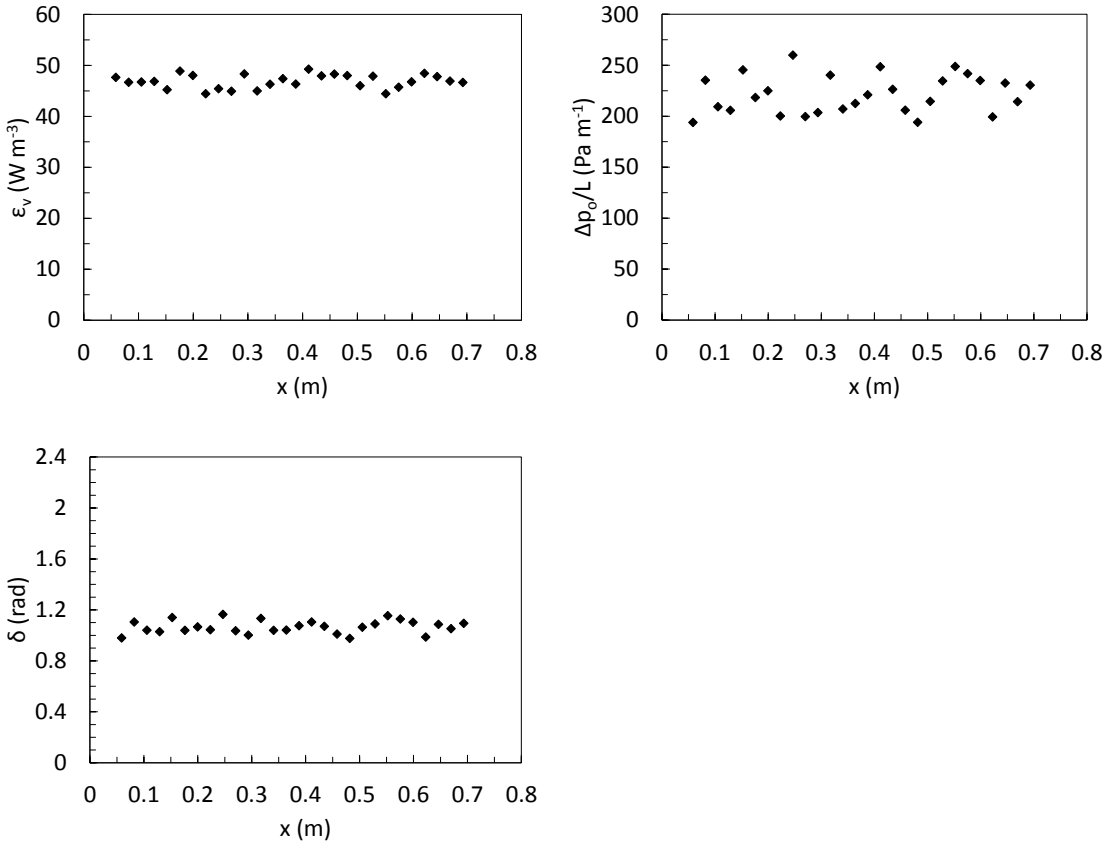

Figure 5.10. *Power density, maximum centre-to-peak pressure drop fluctuation and phase shift as a function of reactor's length for compressible flow*

As anticipated, the obtained ε_v and Δp_o values are significantly lower than those reported for run #5, due to the much lower density of air in comparison with water. The lower power dissipation rate also translated into a larger phase shift value. Again, there

are no signs of potential energy losses as the fluid moves downstream the reactor, reporting nearly constant power density and phase shift values with length. While the maximum centre-to-peak pressure drop fluctuation seemed to vary slightly, it visually revolved around a rather constant value; it should be noted that even very small variations in δ result in larger changes of Δp_o, as the latter is calculated from Equation (4.5).

Additionally, the maximum and volume-weighted averaged Mach numbers were monitored with time. The cycle-averaged Mach number and $\Delta p(t)$ profile measure over a total length of 0.658 m are shown in Figure 5.11, the former was consistently reported below 0.016. These findings confirm that even for a fully compressible fluid, the flow always remains within the subsonic range (Mach < 0.8) for all the conditions tested in this study. Hence, the possibility of energy losses due to local compression of the fluid in compressible flow in a COBR is discarded; this includes the potential compressibility of liquid flow due to the presence of air bubbles.

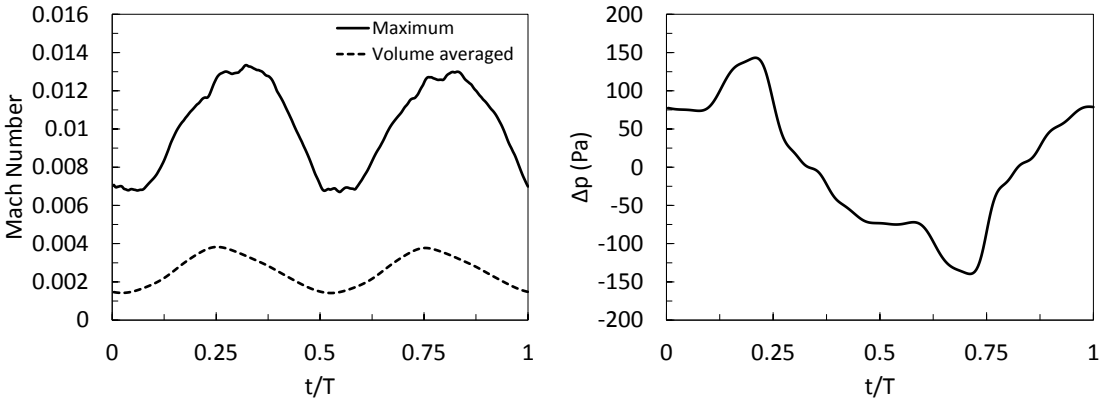

Figure 5.11. *Cycle-averaged Mach number (left) and pressure drop profiles (right) measured over a total length of 0.658 m for compressible flow*

5.4 Conclusions

The current work presented a detailed analysis on the effect of a wide range of operational and geometrical conditions on power dissipation rates in COBRs. This analysis also revealed an inversely proportional relationship between power density and phase shift, providing a physical explanation for this dependency. Further examination of the evolution of power density, pressure drop and phase shift along the length of the device reported virtually no change in these variables. These findings suggest that perfectly symmetric geometries, in the axial direction, do not present signs of energy

losses. This conclusion was further reinforced by evaluating compressible flow under the most adverse conditions simulated in this study; this evaluation also displayed no signs of energy losses across the length of the device and reporting Mach numbers within the subsonic range. These findings discredit the possibility of energy losses due to the presence of air bubbles which could add a certain degree of compressibility to a liquid phase.

Additionally, geometries with larger baffle spacing proved to promote eddy shedding, preventing any connectivity or interaction of vortexes formed during the forward and backward strokes. This results in local negative power density values, i.e. local energy losses experienced by the fluid, a sudden decrease in pressure drop and an increase in phase shift.

Chapter 6 The Effect of Geometric Events on Pressure Drop & Power Dissipation in COBRs

6.1 Introduction

All the geometrical conditions described in Section 3.1 are symmetrical along the axial direction, i.e. periodically repeatable, this chapter deals with cases where non-symmetrical geometry is involved. Examples of such geometric events include small joints without baffle constriction that connect two straight sections; a reduction in the baffle constriction cross-sectional area which may be experienced due to fouling around a baffle's wall; and bend joints commonly used to connect straight tubes.

This work uses some imaginary geometries with irregularities and geometric events that break the symmetry of the system to assess their impact on power dissipation rates and pressure drop profiles in COBRs.

6.2 Methodology

The standard NiTech DN15 COBR reactor was used again as the target device of this study. However, geometric modifications were made in order to implement the following geometric events: sections with a missing baffle constriction, baffle constrictions with a reduced cross-sectional area and bend joints. Table 6.1 lists all the geometries modelled and the operating conditions under which simulations were run. Figure 6.1 shows the geometric dimensions of the DN15 bend joint used for the connection of two straight sections. In the same manner as described in Section 5.2, temporal pressure drop profiles were monitored across multiple longitudinal sections of the devices, each of them 23.5 mm long, refer to Figure 5.1. In order to minimize the effect of the open boundary conditions, the first two and last two 23.5 mm long sections were discarded. This allowed for the extraction of a pressure drop profile over the remaining 0.658m of the device as $\Delta p(t) = p_2(t) - p_{30}(t)$, as well as the individual pressure drop profile of each longitudinal section as $\Delta p_i(t) = p_{i-1}(t) - p_i(t)$. The procedure for the calculation of ε_v, Δp_{net}, Δp_o and δ from each pressure drop profile was as earlier described in Sections 4.4 and 4.5.

Table 6.1. *List of conditions simulated containing a geometric event*

Run #	Event	Event section	Q (ml min^{-1})	f (Hz)	x_o (mm)	Re_n	Re_o	St
16	1B (baffle) miss	16	50	1	14	70.5	1313	0.0853
17	2B miss: consecutive	16 – 17	50	1	14	70.5	1313	0.0853
18	3B miss: consecutive	16 – 18	50	1	14	70.5	1313	0.0853
19	2B miss: separate	7, 16	50	1	14	70.5	1313	0.0853
20	3B miss: separate	7, 16, 25	50	1	14	70.5	1313	0.0853
21	1B D_b = 5	16	50	1	14	70.5	1313	0.0853
22	2B D_b = 5: consecutive	16 – 17	50	1	14	70.5	1313	0.0853
23	3B D_b = 5: consecutive	16 – 18	50	1	14	70.5	1313	0.0853
24	2B D_b = 5: separate	7, 16	50	1	14	70.5	1313	0.0853
25	3B D_b = 5: separate	7, 16, 25	50	1	14	70.5	1313	0.0853
26	Bend joint	17 – 23	50	1	14	70.5	1313	0.0853
27	Bend joint	17 – 23	100	2	7	141	1313	0.171

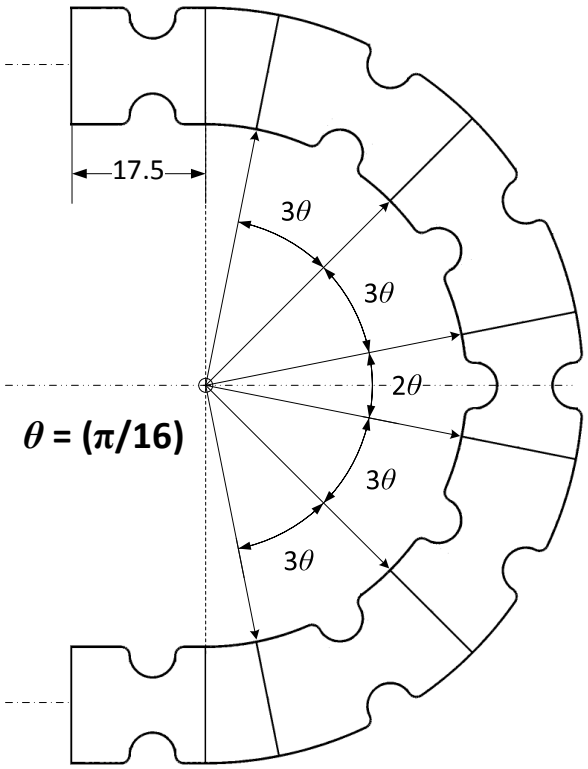

Figure 6.1. *Dimensions of the bend joint connecting two NiTech DN15 straight sections used in CFD simulations; all dimensions are in mm*

Figure 6.2 shows all the different geometries modelled during this study. Sections containing either missing baffles or baffle constrictions with a reduced cross-sectional area are distributed in such a way that the effect of multiple events is analysed when these are set in consecutive and in alterative manner. For better visualisation, baffle

constrictions with a reduced cross-sectional (D_b = 5 mm) were framed with a dotted square.

Runs #26 and 27 comprise two straight DN15 sections containing sixteen baffle constrictions each, both connected with a bend joint as displayed in Figure 6.3, adding up to a total of thirty-nine baffle constrictions. A scheme for the extraction of temporal pressure drop profiles for these runs is also presented in Figure 6.3. Results from individual $\Delta p(t)$ profiles for each of the thirty-nine baffle constrictions are extracted and presented in Section 6.3.3, with the first two and last two baffle constrictions being discarded. The overall temporal pressure drop profile extracted over a total of twenty-eight baffle constrictions was calculated as $\Delta p(t) = p_5(t) - p_{33}(t)$; this comprises eleven baffle constrictions from the first straight section, i.e. 0.2585 m, seven from the bend joint, i.e. 0.1662 m , and ten from the second straight section, i.e. 0.235 m, adding up a total of 0.6597 m.

Due to the geometric complexity of runs #26 and 27, the mesh was automatically generated using the commercial application ANSYS® Meshing. The grid contained only tetrahedral elements and had a resolution of 120 k nodes per baffle constriction, which is even higher than the 117 k nodes from the structured hexahedral mesh used for runs #1 – 25; this was reflected by the number of tetrahedral elements that had to be generated: 418 k elements per baffle constriction as opposed to the 113 k hexahedral elements from the mesh used for runs #1 – 25.

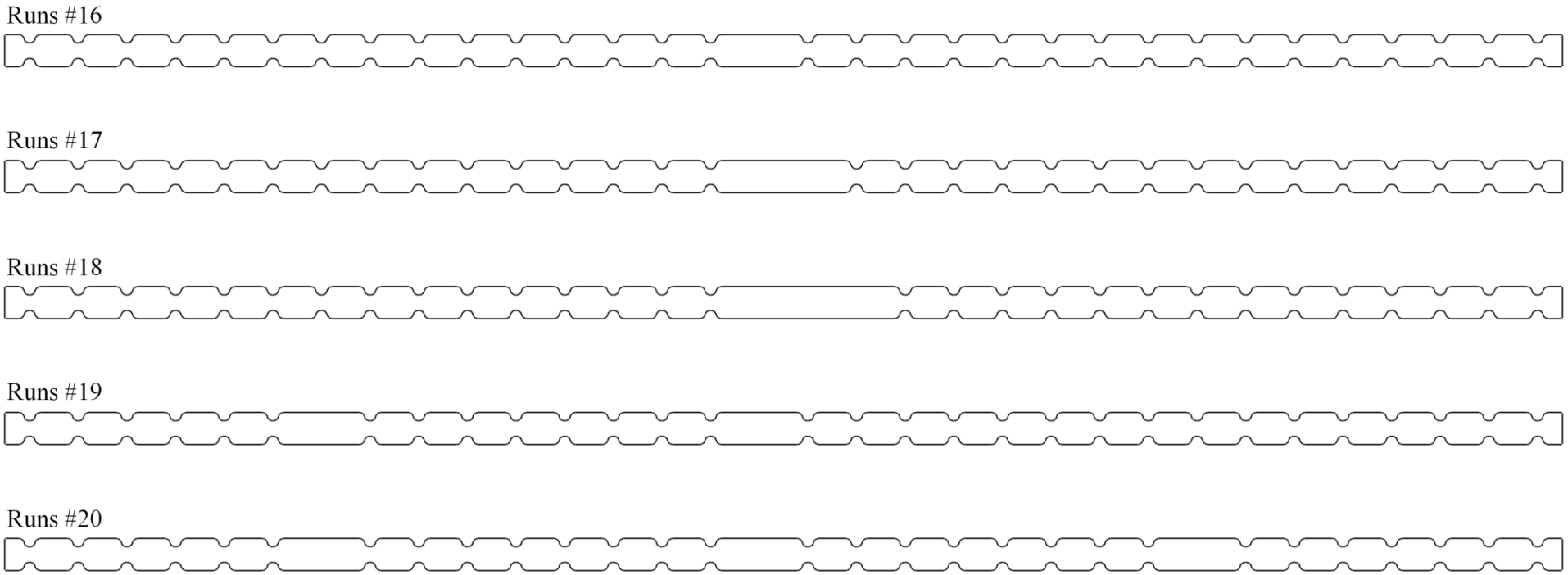

Figure 6.2. *Geometries employed for runs #16 – 27*

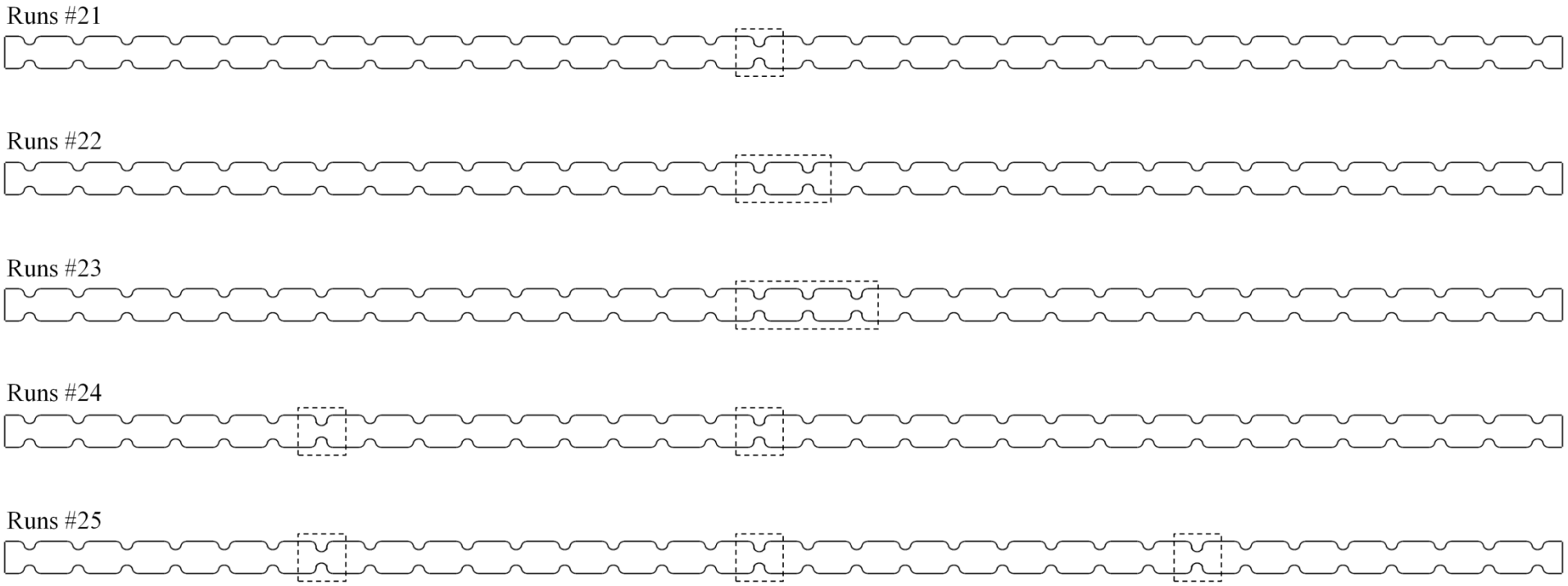

Figure 6.2. (continuation) *Geometries employed for runs #16 – 27; the highlighting cells are related to reduced baffle restrictions*

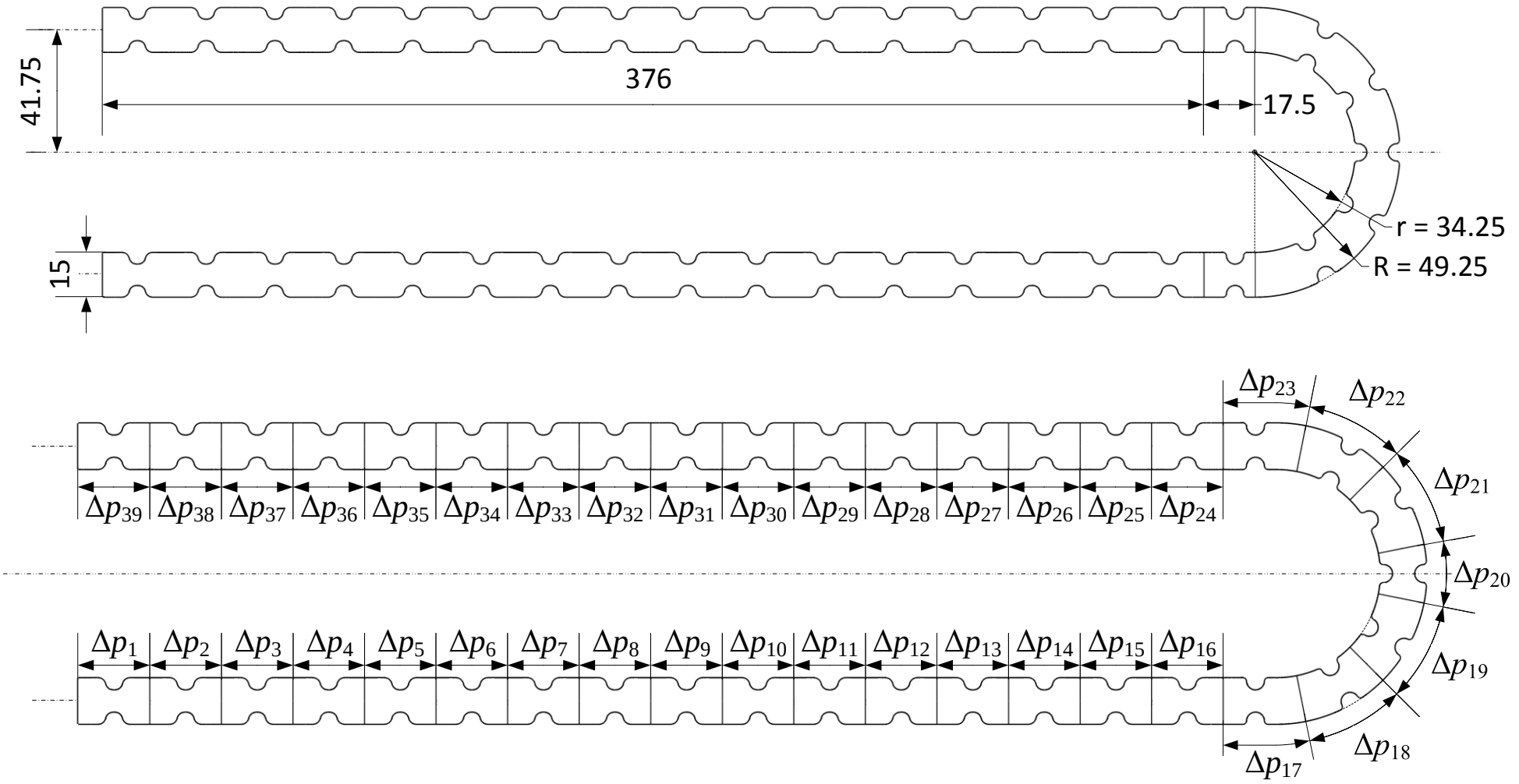

Figure 6.3. *Geometry containing a bend joint used for runs #26 & 27 (top) and scheme for the extraction of temporal pressure drop profiles (bottom)*

6.3 Results & Discussion

6.3.1 The Effect of Missing Baffles

Missing baffles result in lower power dissipation rates and pressure drop fluctuations together with larger phase shift values, as anticipated from the findings extracted from run#10 and 11. Table 6.2 displays the information extracted from the simulated $\Delta p(t)$ profiles over a total length of 0.658m for runs #16 – 20; cycle-averaged pressure drop profiles for all simulated conditions are presented in Appendix 6. Results from run #2 are also displayed for comparison, in order to quantify the percentage difference in ε_v, Δp_o and δ caused by different arrangements of the missing baffle sections. The impact of missing baffles on these variables is accumulative, as it increases with the number of missing baffles; however, it should be noted that consecutive sections with missing baffles have a larger impact as opposed to when they are distributed along the entire length of the device. Thus, both the number and length of sections with missing baffles contribute to potential energy losses in COBR.

Table 6.2. *Summary of results extracted from CFD simulations for runs #16 – 20*

Run #	Δp_{net} (Pa)	$\Delta p_o/L$ (Pa m^{-1})	$\Delta p_o/L$ diff. (%)	δ (rad)	δ diff. (%)	ε_v (W m^{-3})	ε_v diff. (%)	Re_o	St
2	58.6	2264.6	–	0.791	–	88.1	–	1313	0.0853
16	44.1	2262.0	-0.1	0.798	0.9	86.5	-1.9	1313	0.0853
17	39.9	2212.0	-2.3	0.814	2.9	82.4	-6.5	1313	0.0853
18	36.9	2154.4	-4.9	0.824	4.2	78.7	-10.6	1313	0.0853
19	42.5	2241.6	-1.0	0.819	3.6	83.0	-5.8	1313	0.0853
20	41.3	2226.7	-1.7	0.823	4.0	81.5	-7.5	1313	0.0853

The evolution of power dissipation rate, the maximum centre-to-peak pressure drop fluctuation and phase shift with length for runs #16 – 20 is presented in Figure 6.4, which displays results obtained for consecutive 23.5 mm long sections of the reactor. These variables undergo minimal changes with length; the only exception being the results obtained within the missing baffle sections and their neighbouring sections in both directions. Run #16 clearly shows a drastic decrease in ε_v within the missing baffle section, reporting a negative power dissipation rate; this is also reflected by a decrease in Δp_o and a large increase in δ within this section.

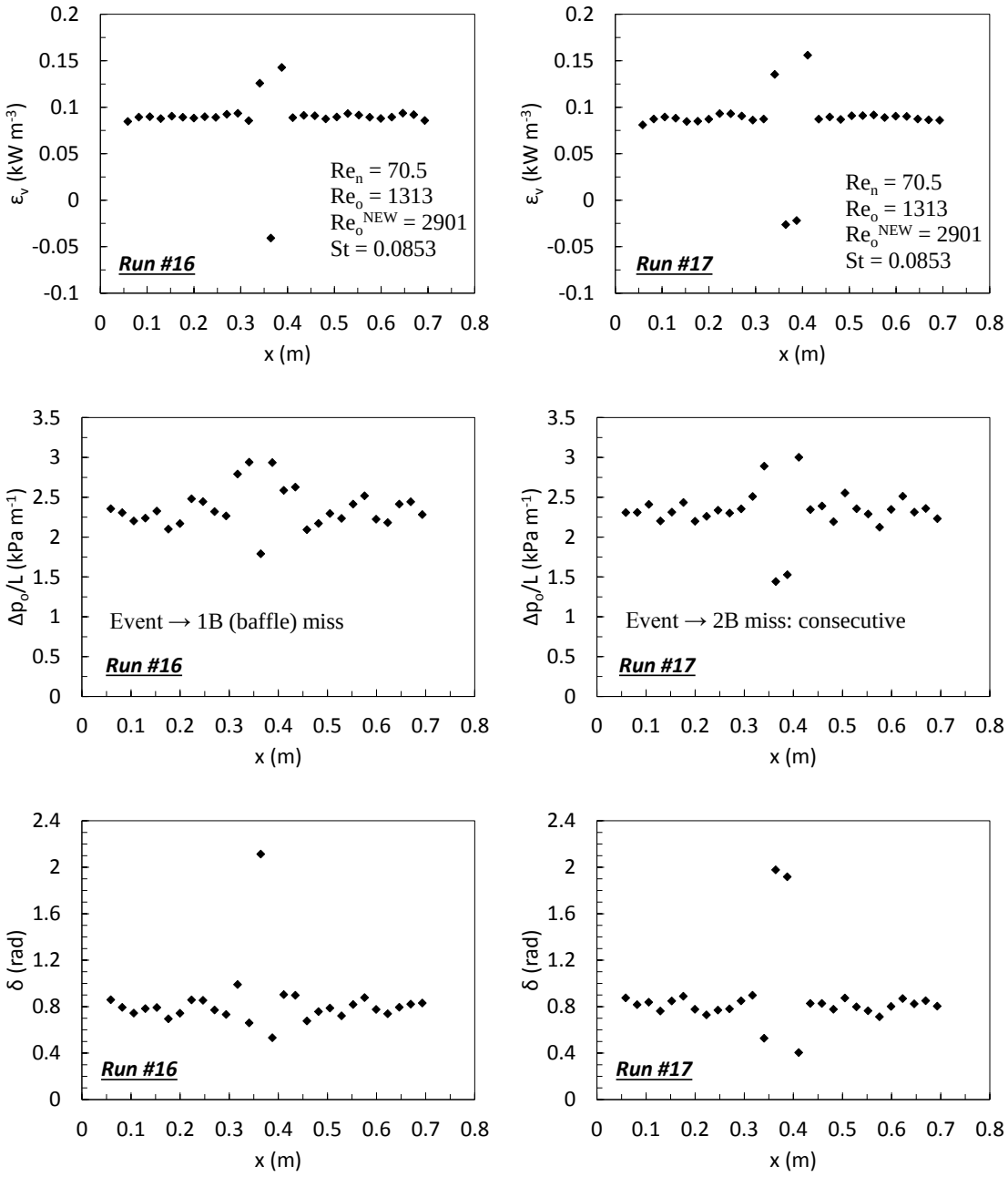

Figure 6.4. *Power density, maximum centre-to-peak pressure drop fluctuation and phase shift as a function of reactor's length for runs #16 – 20*

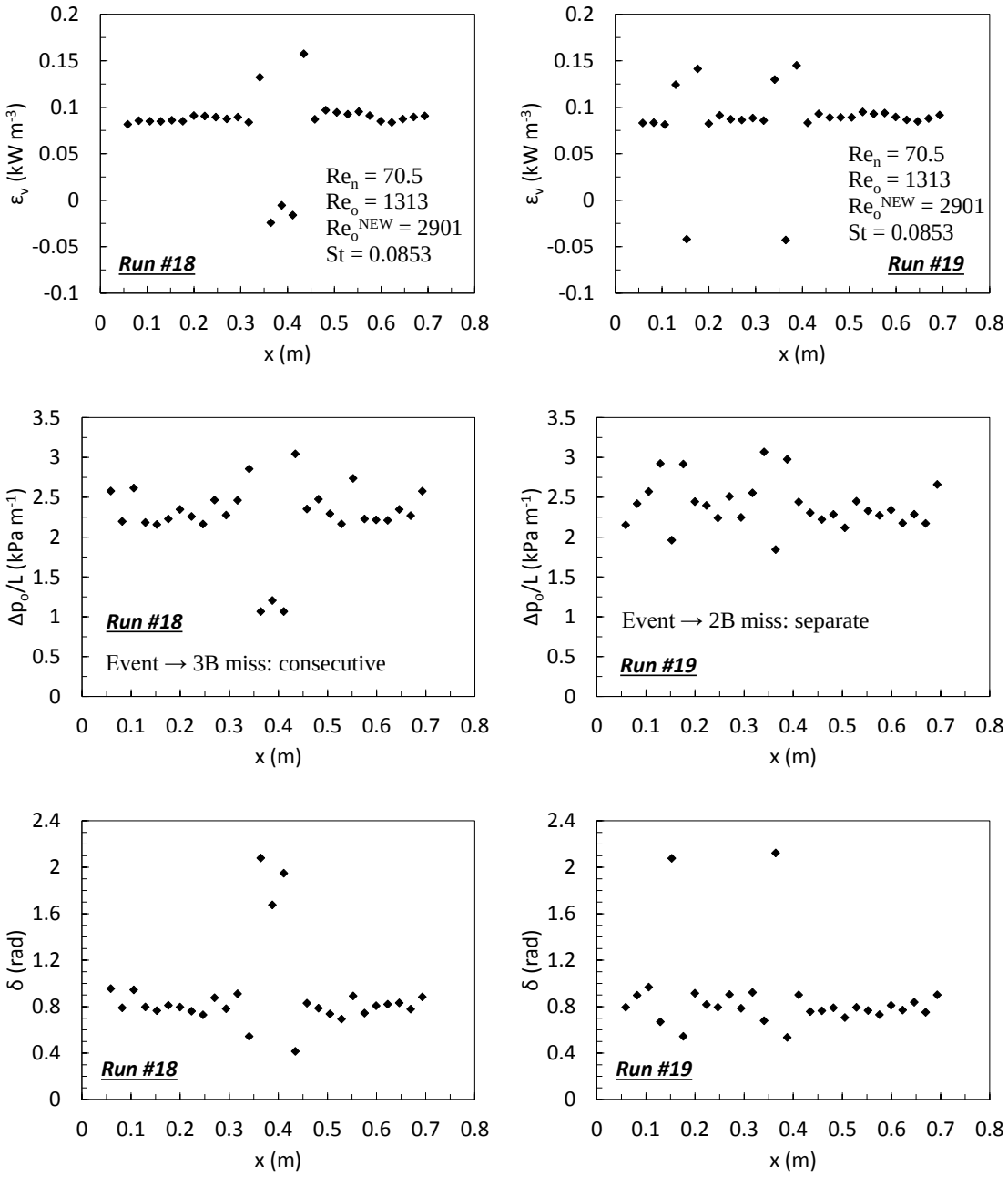

Figure 6.4. (continuation) *Power density, maximum centre-to-peak pressure drop fluctuation and phase shift as a function of reactor's length for runs #16 – 20*

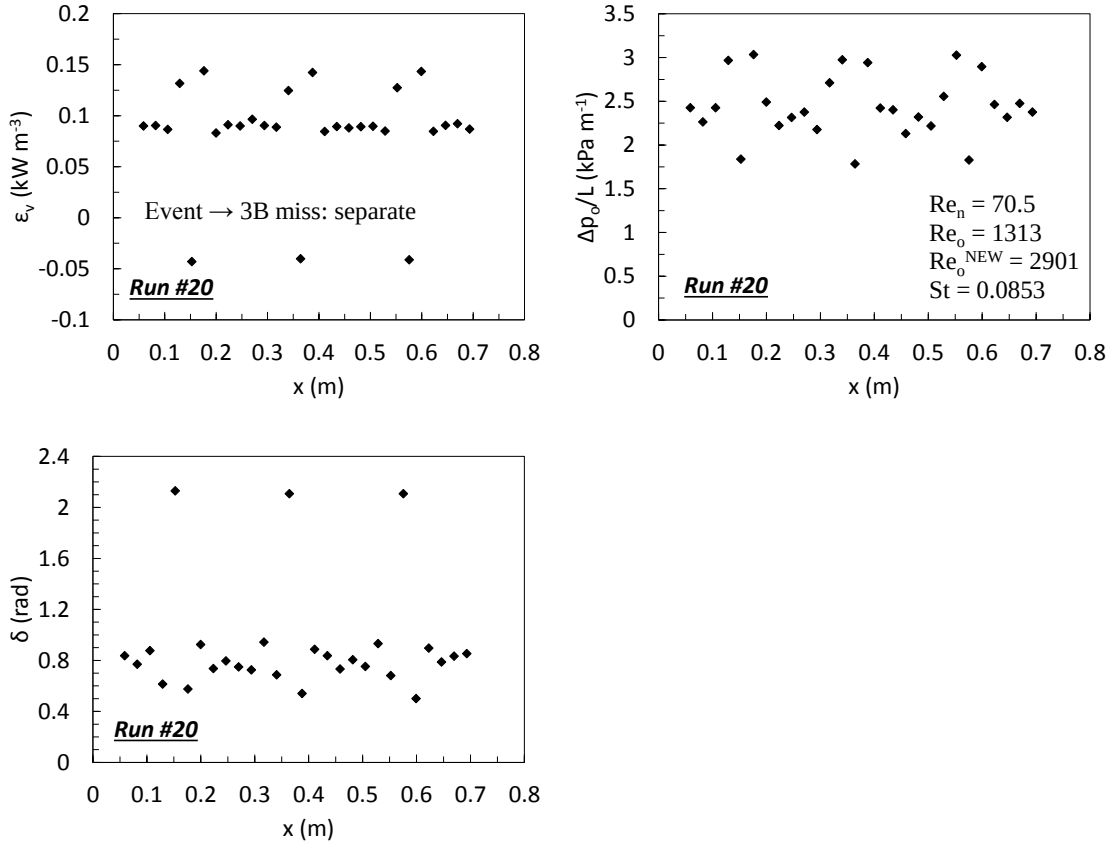

Figure 6.4. (continuation) *Power density, maximum centre-to-peak pressure drop fluctuation and phase shift as a function of reactor's length for runs #16 – 20*

While eddies formed during the forward and backward strokes within every baffle-cell are detached from the edge of the baffle constriction, eddy shedding leading to further dissipation into the bulk fluid only takes place within the missing baffle section; this is visually observed in Figure 6.5. Hence, the energy carried by eddies decreases before they interact and collide with those formed in the previous oscillatory stroke. This translates into local energy losses experienced by the fluid within these sections. Figure 6.7 demonstrates how the increment in phase shift results in an almost reversed pressure drop profiles in comparison with those extracted across sections with baffle constrictions. Furthermore, it is observed that the maximum centre-to-peak pressure drop fluctuation undergoes an increase during the forward stroke of the oscillation at the following section (17) contiguous to the missing baffle section (16). Similarly, an increment in Δp_o during the backward stroke at the preceding section is also observed. This happens as a result of local fluid stalling within the missing baffle section; thus, a higher pressure drop is required to move this fluid element through the next baffle constriction during the forward stroke and through the previous baffle constriction

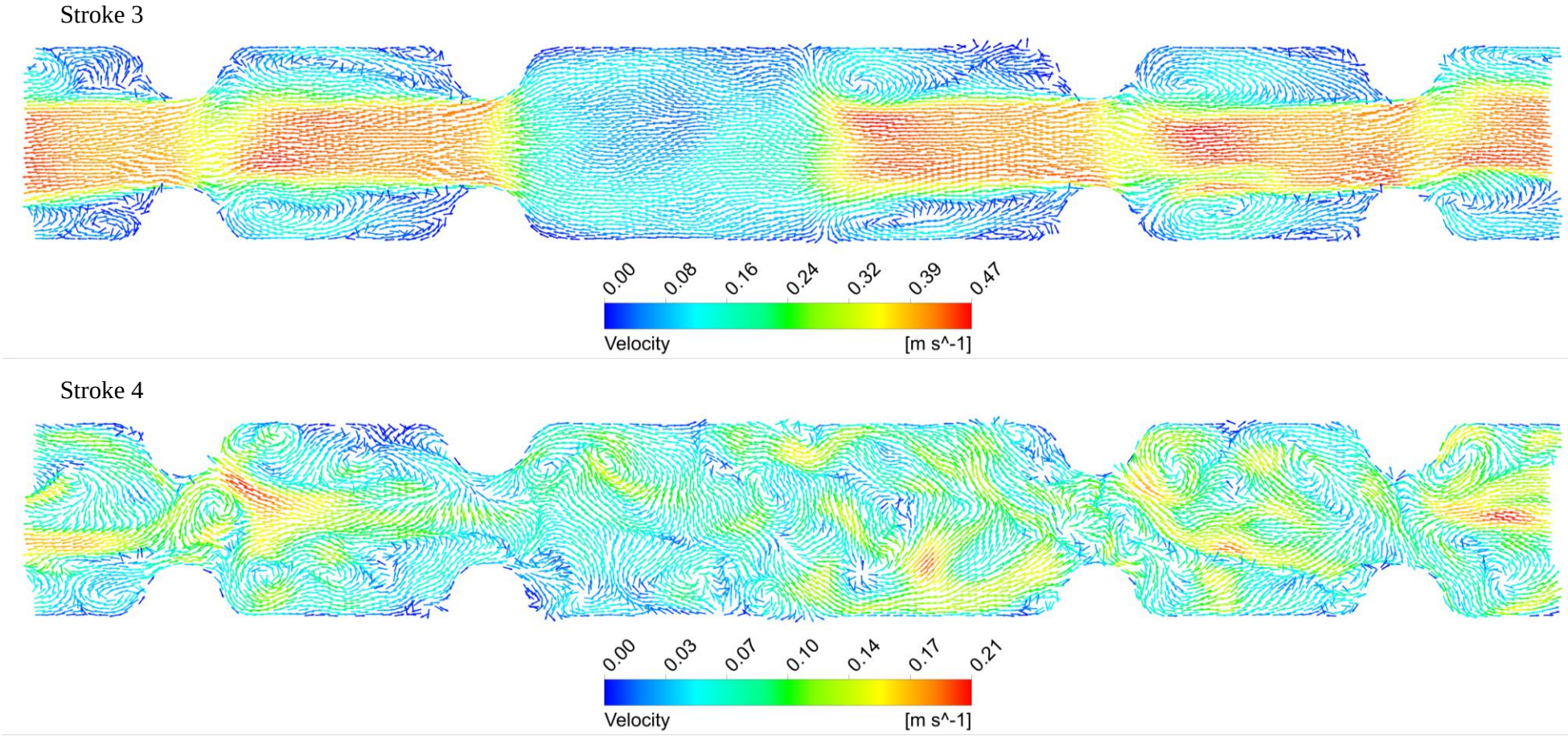

Figure 6.5. *Velocity vector map of sections 14 – 18 at strokes 3 and 4 of simulated cycle 10 for run #16 (Q = 50ml min^{-1}, f = 1Hz, x_o = 14mm)*

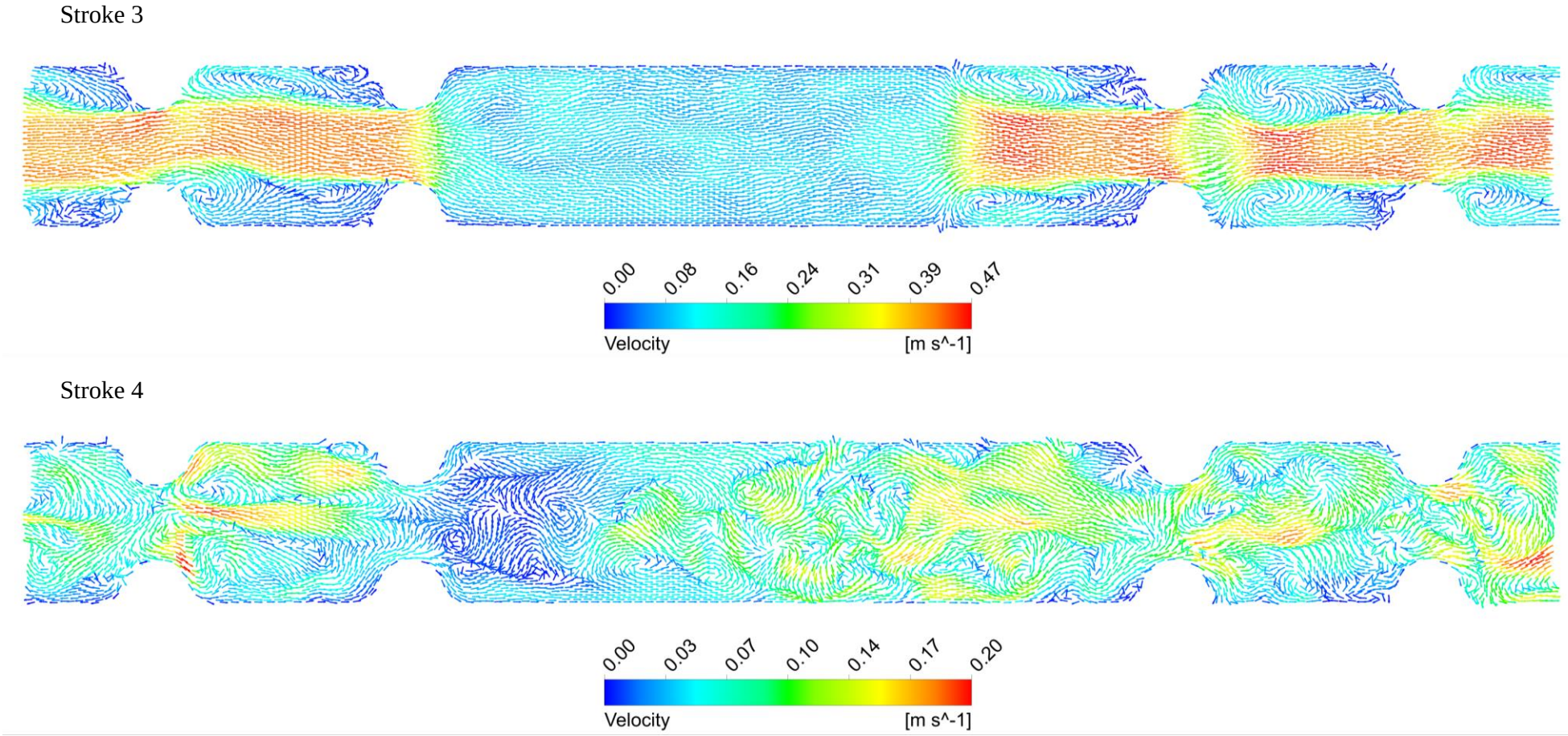

Figure 6.6. *Velocity vector map of sections 14 – 19 at strokes 3 and 4 of simulated cycle 10 for run #17 (Q = 50ml min^{-1}, f = 1Hz, x_o = 14mm)*

during the backward stroke backward stroke. This phenomenon is reflected by the higher power dissipation rates reported within the adjacent sections (15 and 17), thus showing slightly lower phase shift values.

Results obtained for missing baffle sections distributed along the entire length of the device are very similar to those from run #16; every missing baffle section reports very similar ε_v, Δp_o and δ values. On the other hand, as the number of consecutive missing baffles increases, i.e. increase in the length of the missing baffle section, the region where local energy losses occur also increases. This is shown in Figure 6.6. Power dissipation rates and phase shift values obtained within longer missing baffle sections remain relatively constant; however, small changes in these variables led to a slightly more accentuated variation in Δp_o values. Additionally, in runs #17 and 18, regions experiencing a local increase in power density only occur at the single section preceding and following the set of consecutive missing baffles.

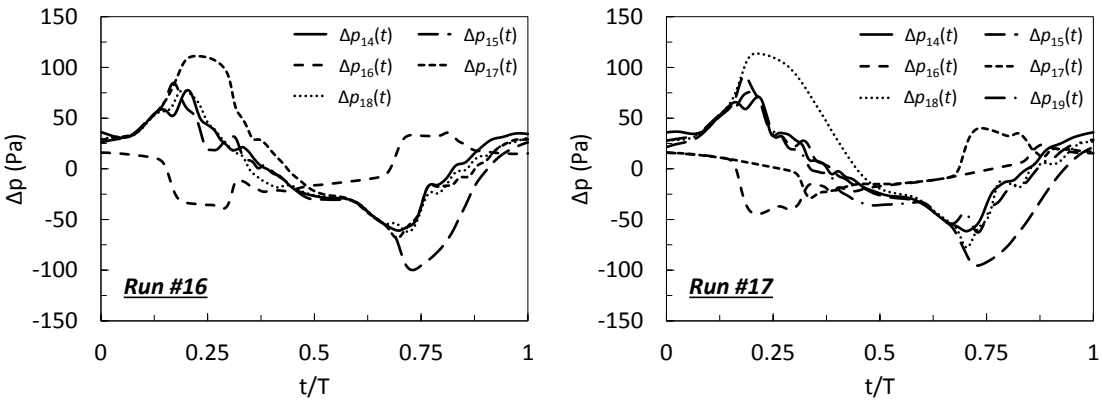

Figure 6.7. *Cycle-averaged pressure drop profiles measured at different sections for runs #16 and 17 (Q = 50ml min^{-1}, f = 1Hz, x_o = 14mm)*

It should be noted that the local decrement in power dissipation rates reported for sections missing a baffle constriction are much higher than the increment observed in the adjacent sections. Hence, the overall effect of these geometric events in COBRs is a reduction in power density. As the region experiencing local fluid energy losses increases, the overall impact on power density in a COBR also increases as reported earlier in Table 6.2. Results show that consecutive missing baffles present a larger impact on the overall ε_v of the system, leading to greater energy losses. Therefore, it is preferable to have multiple shorter sections missing baffle constrictions along the entire length of the reactor than having a long single section without the presence of baffles.

6.3.2 The Effect of Baffle Constrictions with Reduced Cross-sectional Area

As aforementioned in Section 5.3.1, power density in COBRs proved to be inversely proportional to baffle diameter. Therefore, increases in power dissipation rates are expected with the presence of baffle constrictions with smaller cross-sectional area. This is reinforced by the results laid out in Table 6.3, which presents the information extracted from the simulated $\Delta p(t)$ profiles over a total length of 0.658 m for runs #21 – 25. Again, for the sake of comparison, results for from run #2 are included and used for the calculation of the percentage difference in ε_v, Δp_o and δ caused by narrower baffle constrictions. These results undeniably show an increment in ε_v and Δp_o, and a decrement in δ with the presence of narrower baffle constrictions. However, it is also observed that this phenomenon becomes more accentuated when narrower baffle constrictions are distributed along the reactor's entire length as opposed to when they are placed consecutively.

Table 6.3. *Summary of results extracted from CFD simulations for runs #21 – 25*

Run #	Δp_{net} (Pa)	$\Delta p_o/L$ (Pa m^{-1})	$\Delta p_o/L$ diff. (%)	δ (rad)	δ diff. (%)	ε_v (W m^{-3})	ε_v diff. (%)	Re_o	St
2	58.6	2264.6	–	0.791	–	88.1	–	1313	0.0853
21	71.8	2463.0	8.8	0.757	-4.2	99.2	12.6	1313	0.0853
22	77.7	2572.0	13.6	0.723	-8.6	107.1	21.5	1313	0.0853
23	88.6	2666.1	17.7	0.689	-12.9	114.4	29.8	1313	0.0853
24	81.6	2590.9	14.4	0.704	-10.9	109.6	24.4	1313	0.0853
25	99.0	2727.1	20.4	0.677	-14.4	118.2	34.2	1313	0.0853

Figure 6.8 displays the results obtained for consecutive 23.5 mm long sections of the reactor for runs #21 – 25, illustrating the evolution of power dissipation rate, the maximum centre-to-peak pressure drop fluctuation and phase shift with length. These variables experience very minimal change until a geometric event is encountered. Results from run #21 report a large increment in ε_v and Δp_o, and a decrement in δ within the narrower baffle constriction because higher energy is required to move the fluid through a reduced cross-sectional area, i.e. section (16). This translates into larger velocities as the fluids passes through this constriction, which is visually observed in Figure 6.9. The fluid leaves the narrower baffle constriction with high kinetic energy and then enters a contiguous normal baffle constriction (D_b = 7 mm). This causes a decrease in power density, since less energy is required to move a volume of fluid that

is flowing at high velocity into these neighbouring sections with a standard cross-sectional area.

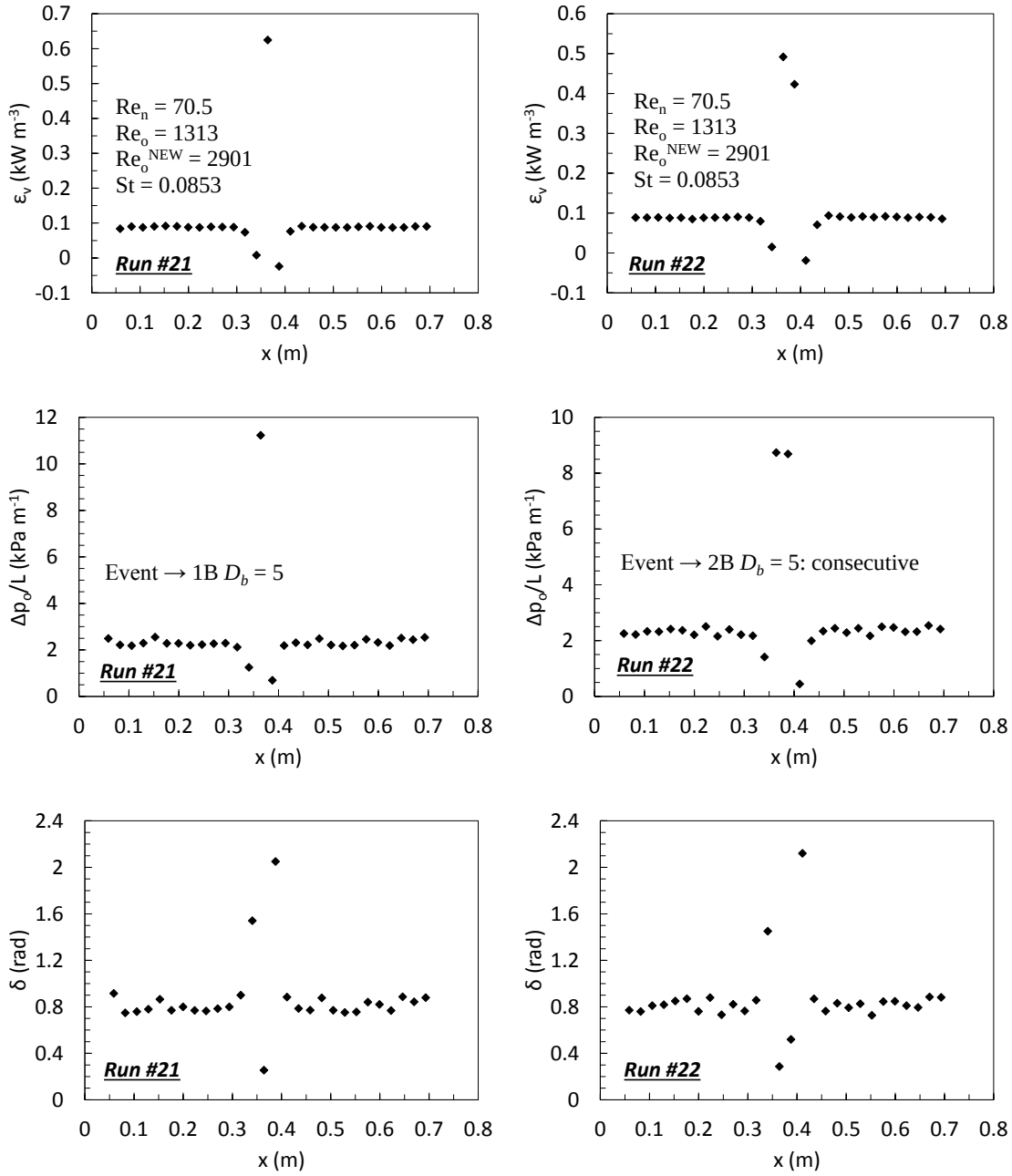

Figure 6.8. *Power density, maximum centre-to-peak pressure drop fluctuation and phase shift as a function of reactor's length for runs #21 – 25*

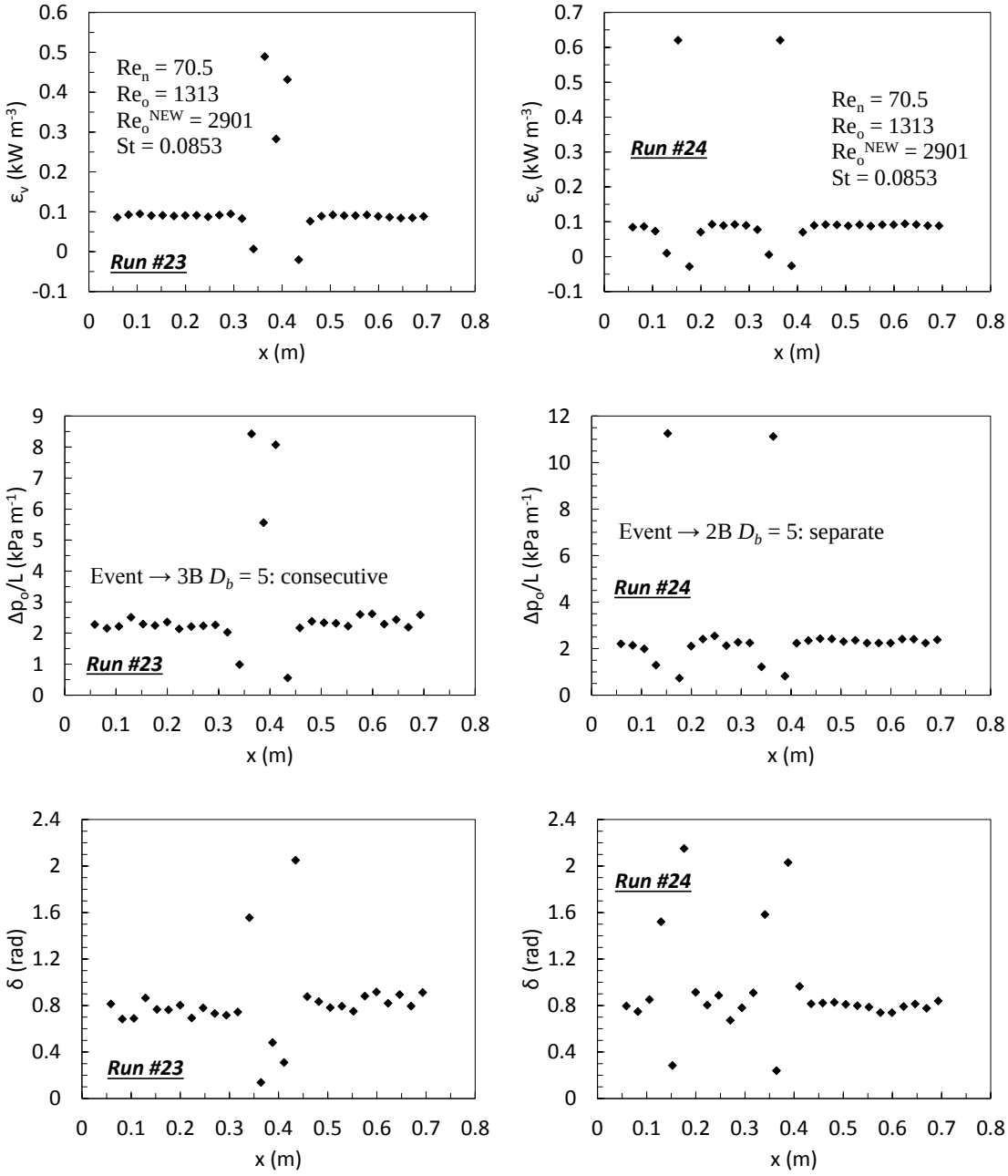

Figure 6.8. (continuation) *Power density, maximum centre-to-peak pressure drop fluctuation and phase shift as a function of reactor's length for runs #21 – 25*

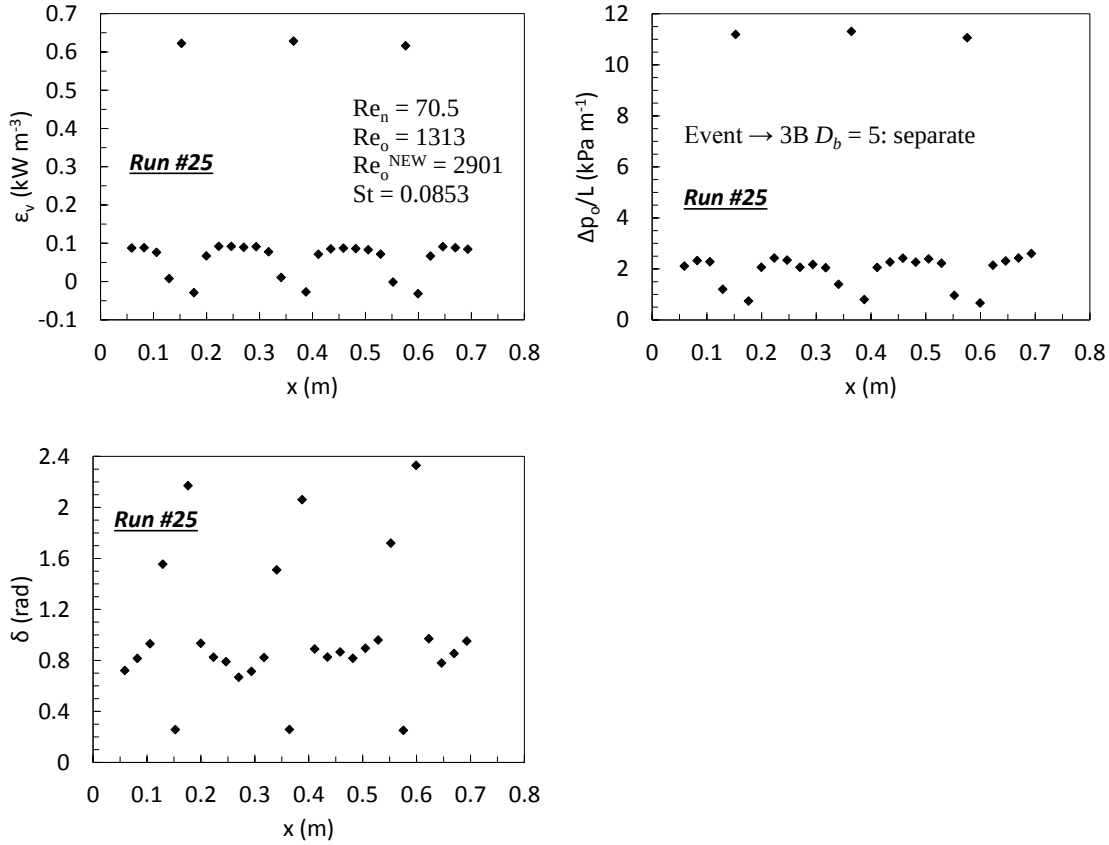

Figure 6.8. (continuation) *Power density, maximum centre-to-peak pressure drop fluctuation and phase shift as a function of reactor's length for runs #21 – 25*

This very phenomenon is observed at every narrower baffle constriction when they are distributed along the reactor's entire length (runs #24 and 25), and their impact on the overall flow adds up as shown from the results in Table 6.3. On the other hand, if these geometric events occur consecutively, e.g. run #23, the power density required to move the fluid through the second or third narrower constriction, i.e. sections (17) and (18) is smaller than that required for section (16). This is because the fluid leaving the first baffle constriction with reduced cross-sectional area already possesses high kinetic energy, thus not requiring an increment in energy to flow through any of the consecutive narrower baffle constrictions. As a consequence, regions showing local energy losses experienced by the fluid, i.e. negative ε_v, only occur at the single section preceding and following the set of consecutive narrower baffle constrictions.

The larger power dissipation rates reported for the sections containing a narrower baffle are also reflected by very small phase shifts. On the contrary, those sections reporting a decrease in ε_v also present an increase in δ. The effect of different δ values and large power densities on pressure profiles is observed in Figure 6.11.

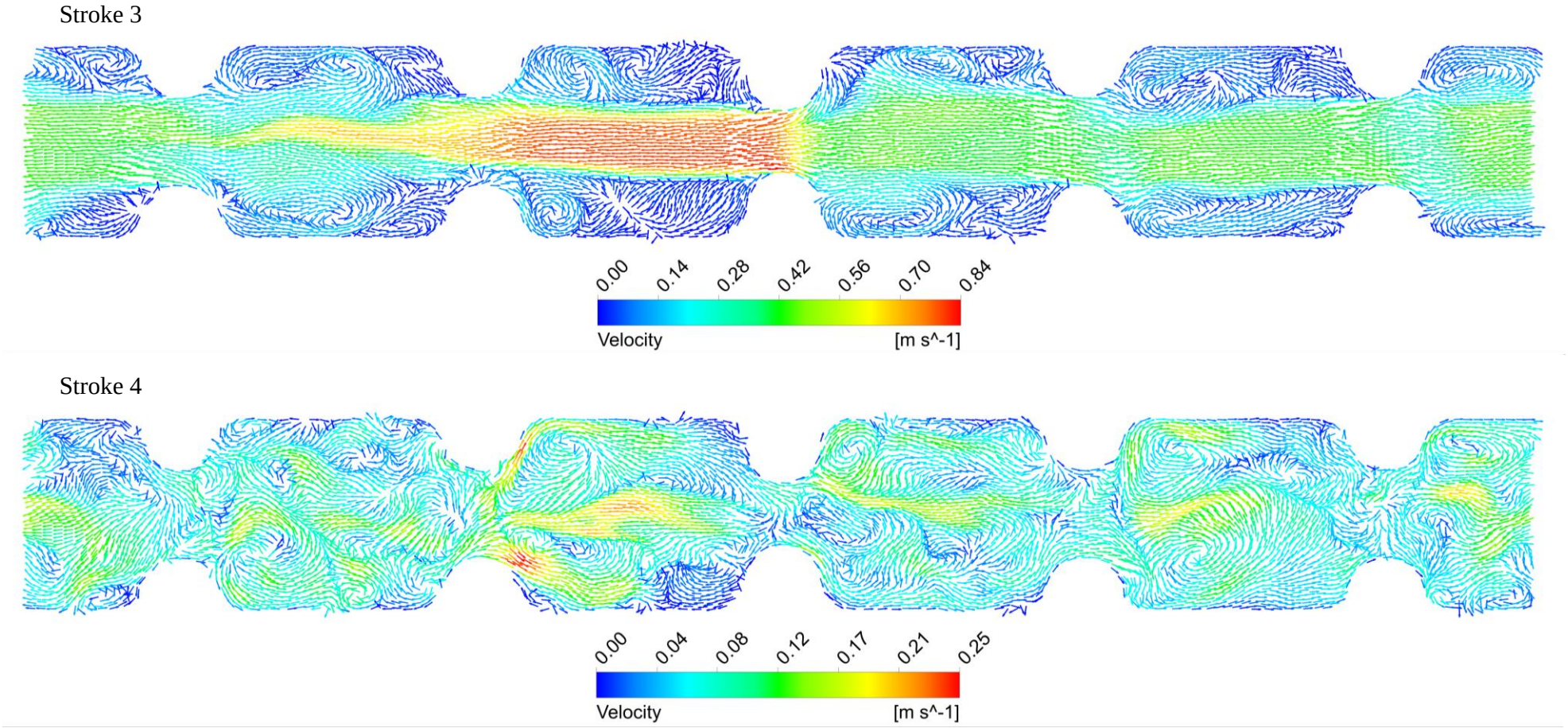

Figure 6.9. *Velocity vector map of sections 14 – 18 at strokes 3 and 4 of simulated cycle 10 for run #21 (Q = 50ml min^{-1}, f = 1Hz, x_o = 14mm)*

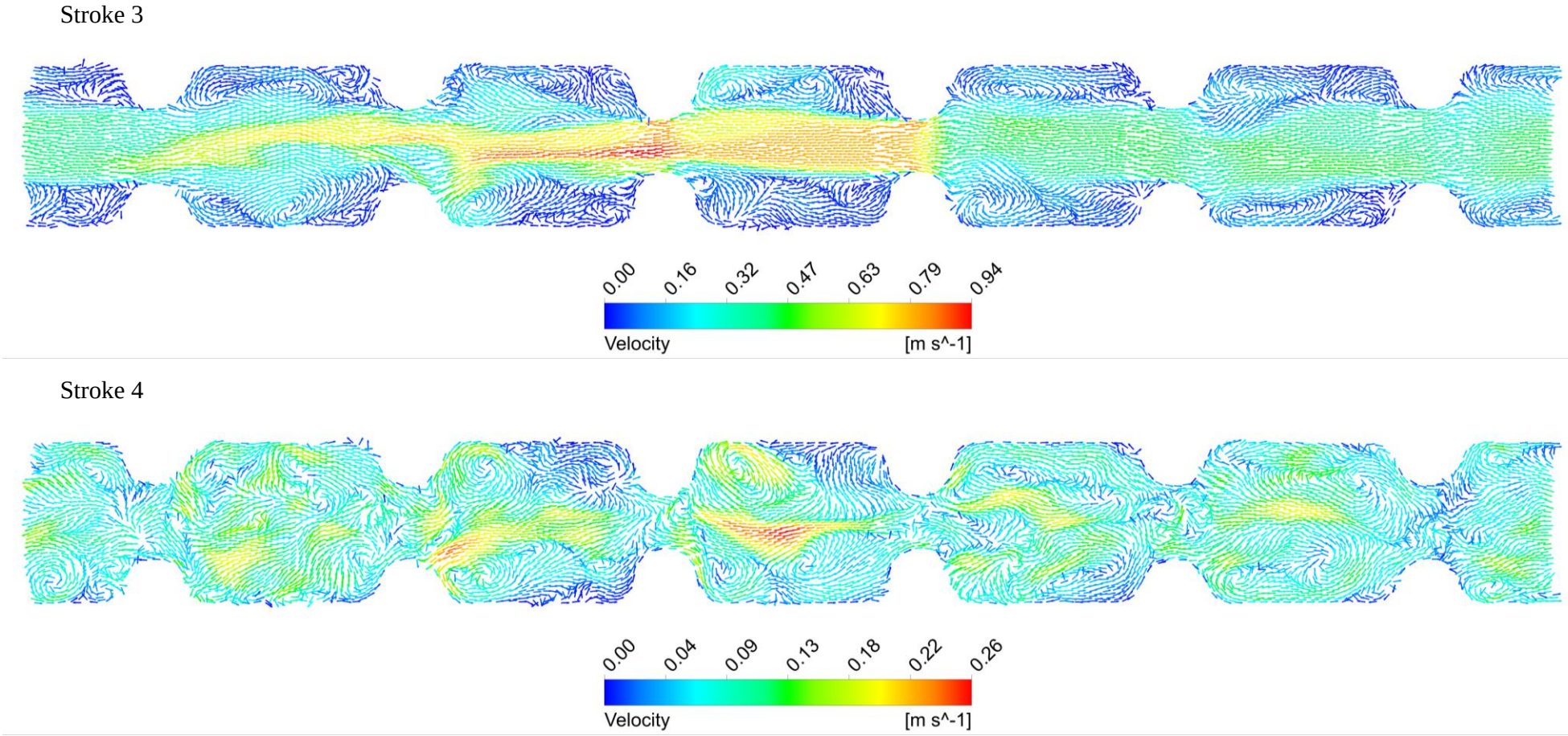

Figure 6.10. *Velocity vector map of sections 14 – 19 at strokes 3 and 4 of simulated cycle 10 for run #22 (Q = 50ml min^{-1}, f = 1Hz, x_o = 14mm)*

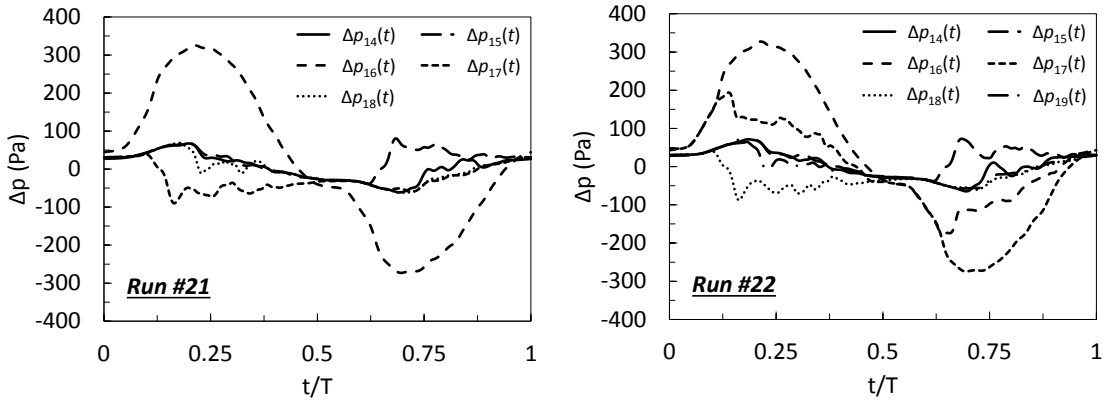

Figure 6.11. *Cycle-averaged pressure drop profiles measured at different sections for runs #21 and 22 (Q = 50ml min^{-1}, f = 1Hz, x_o = 14mm)*

It is preferable to have consecutive narrower constrictions in one region of the device than having multiple baffle constrictions with reduced cross-sectional area distributed along the entire length of the device. This is because each time the fluid has to overcome a narrower baffle constriction, it requires a higher amount of energy (ε_v). On the other hand, when narrower baffle constrictions are distributed consecutively, higher ε_v is only required in the first section.

It should be noted that although local negative dissipation rates are reported, these decrements in ε_v are largely surpassed by the increment in power density reported at the baffle constrictions with reduced cross-sectional area. Therefore, the overall contribution to the flow of these geometric events leads to an increase in power density for COBRs.

6.3.3 The Effect of Bend Joints

Straight horizontal DN15 sections are commonly connected with bend joints in order to form a flow path. The effect of these bend joints on ε_v, Δp_o and δ was assessed under two operating conditions, refer to Table 6.1 by calculating the percentage difference in the variables reported. Information extracted from the simulated $\Delta p(t)$ profiles over a total length of 0.6597 m for runs #26 and 27 is presented in Table 6.4 and compared with those from run #2 and #13, respectively. Note that for runs #2 and 13, $\Delta p(t)$ profiles were obtained over a length of 0.658 m, as opposed to the 0.6597 m length of runs #26 and 27. This small difference, however, does not affect the comparison of results, since power density has units of watts per meter cube and the maximum centre-to-peak pressure drop fluctuation is reported in Pascals per meter.

Table 6.4. *Summary of results extracted from CFD simulations for runs #26 and 27*

Run #	Δp_{net} (Pa)	$\Delta p_o/L$ (Pa m^{-1})	$\Delta p_o/L$ diff. (%)	δ (rad)	δ diff. (%)	ε_v (W m^{-3})	ε_v diff. (%)	Re_o	St
2	58.6	2264.6	–	0.791	–	88.1	–	1313	0.0853
13	171.1	3192.6	–	0.803	–	125.0	–	1313	0.171
26	78.3	2330.2	2.9	0.735	-7.1	95.2	8.0	1313	0.0853
27	171.0	3193.4	0.023	0.804	0.1	124.1	-0.7	1313	0. 171

Results clearly indicate an increase in the power density of the system for run #26. On the other hand, run #27 shows completely negligible changes in ε_v, Δp_o or δ in comparison with the results from run #13. Comparing the operating conditions between runs #26 and 27, the amplitude and frequency of the former are set, respectively, as double and half of the latter. From the results earlier reported in Section 5.3.1, it is known that an increment in oscillatory frequency causes a larger increase in ε_v than an increase in oscillatory amplitude does. However, this seems not applicable in the presence of bend joints, where a noticeable increase in power dissipation rates was attained by doubling the amplitude and halving the frequency.

In order to further analyse this behaviour, the evolution of ε_v, Δp_o and δ along the length of the reactor for runs #26 and 27 is assessed and presented in Figure 6.12; results were obtained for each individual baffle constriction contained in the device. Results from run #26 show a minimal change in any of the three variables along the two straight horizontal sections modelled. However, values obtained for the baffle constrictions contained within the bend joint show a clear increment in power dissipation rates, which reaches its maximum value at section (20), i.e. perpendicular to the horizontal plane, and then decreases as it gets closer to the beginning of the second horizontal section. This increment in ε_v is simultaneous with a decrement in δ. Higher fluid velocities are thus reported within the bend joint, suggesting mixing enhancement; similar conclusions have been drawn from the work carried out by Taylor (1954) [146] and Brunold et al. (1989) [78] in curved pipes and 90 bends, respectively.. This is visually observed in the velocity vector map displayed in Figure 6.13.

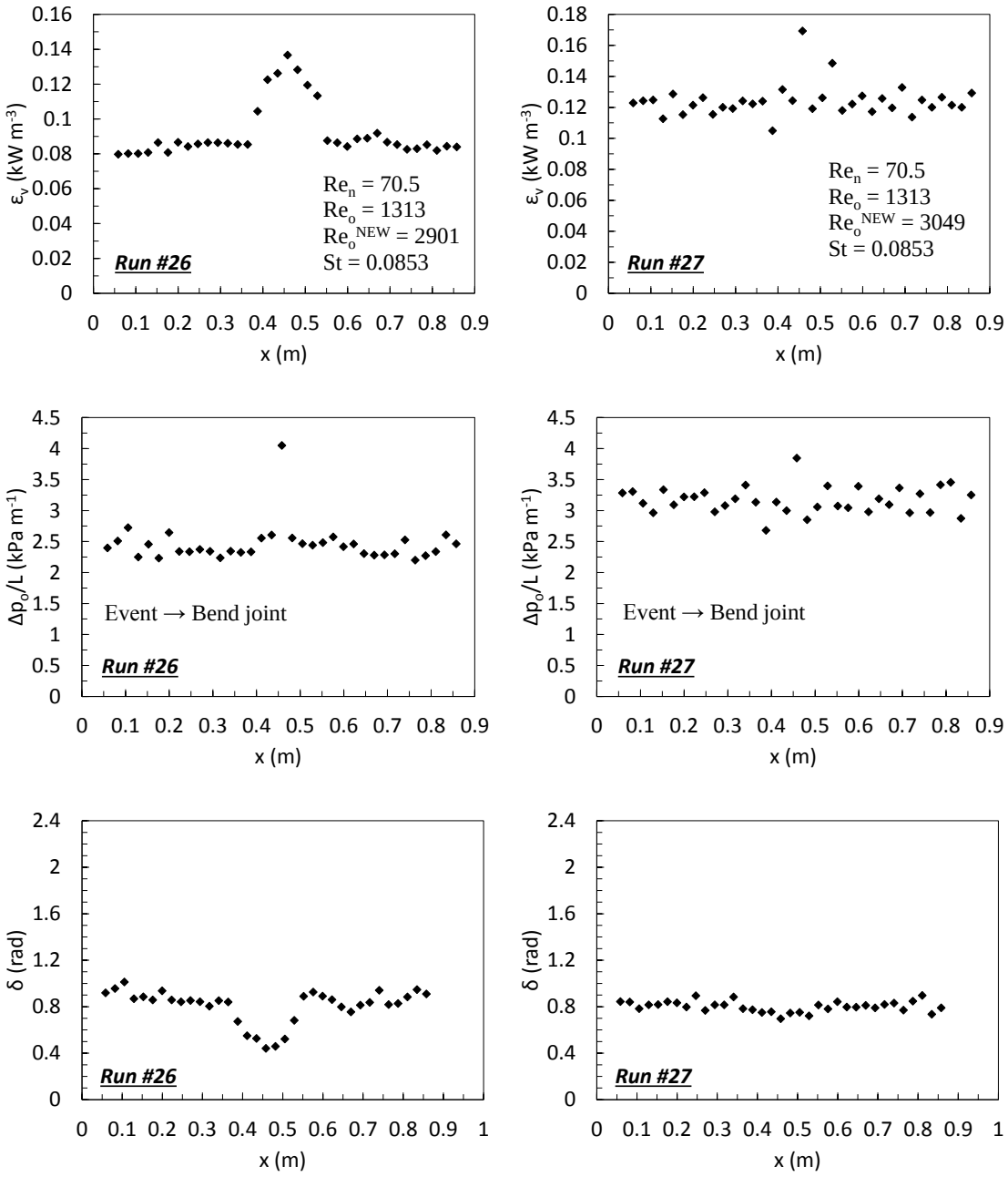

Figure 6.12. *Power density, maximum centre-to-peak pressure drop fluctuation and phase shift as a function of reactor's length for runs #26 and 27*

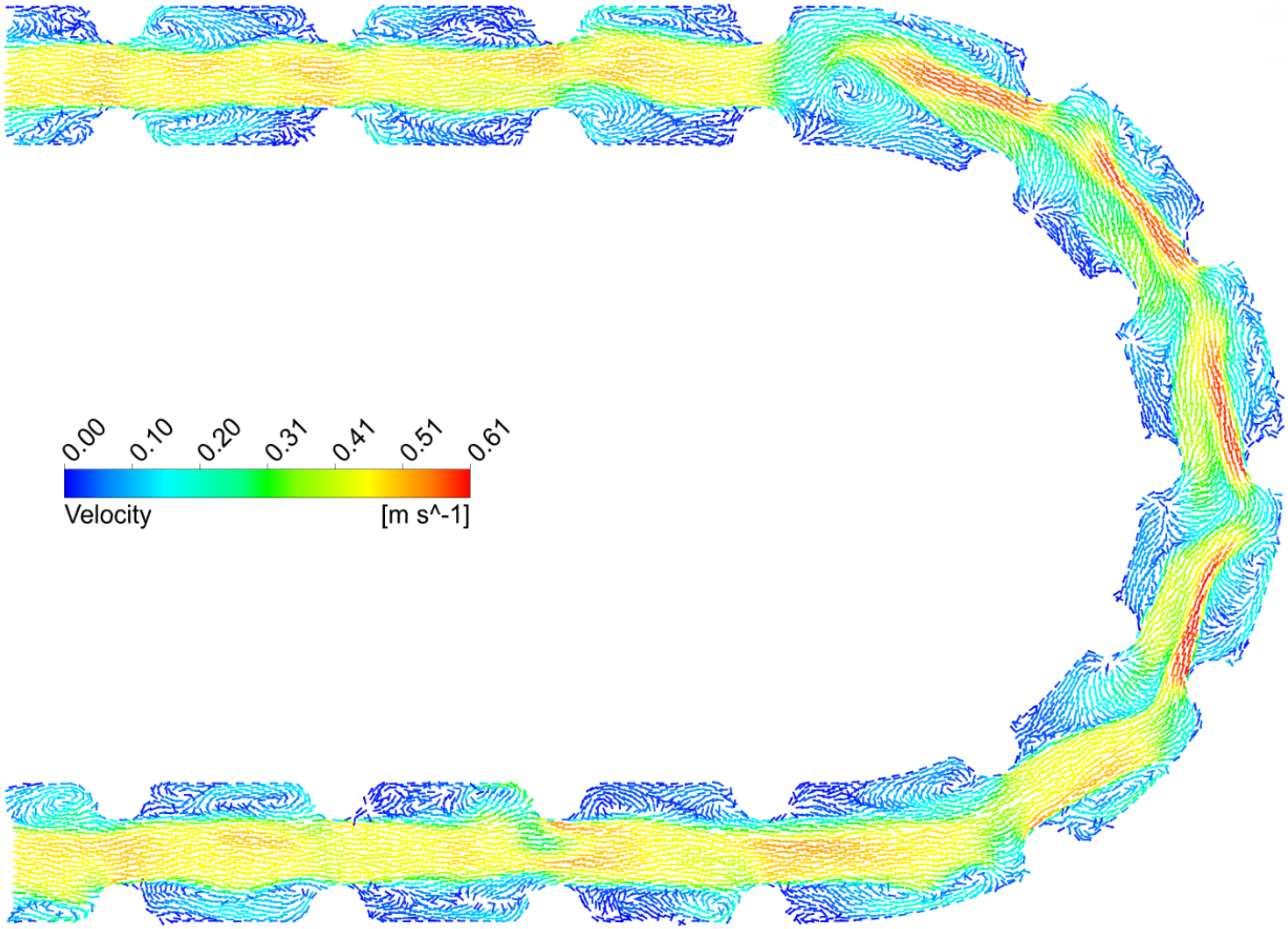

Figure 6.13. *Velocity vector map of sections 14 – 26 at strokes 1 and 2 of simulated cycle 10 for run #26 (Q = 50ml min^{-1}, f = 1Hz, x_o = 14mm)*

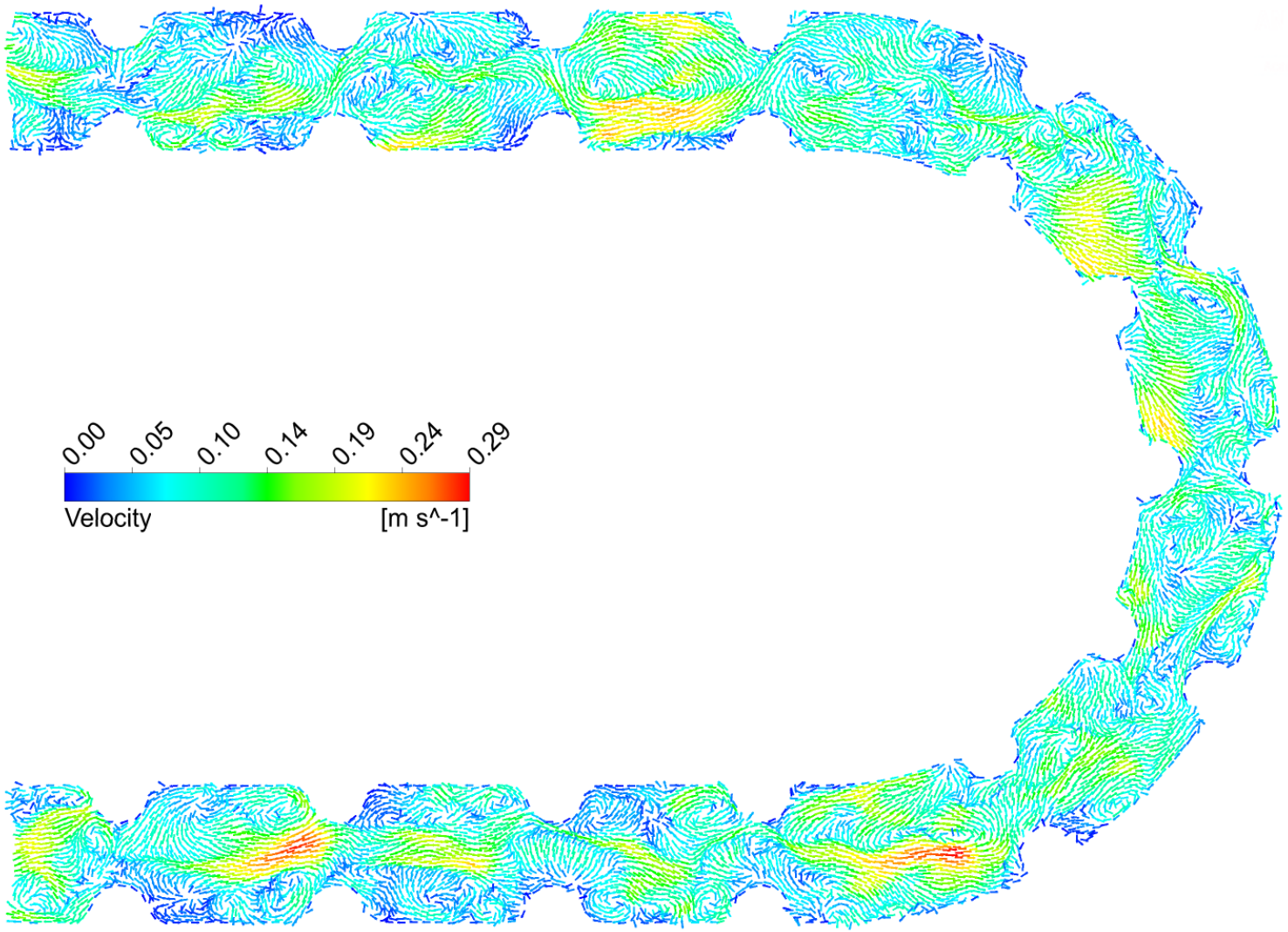

Figure 6.13. (continuation) *Velocity vector map of sections 14 – 26 at strokes 1 and 2 of simulated cycle 10 for run #26*

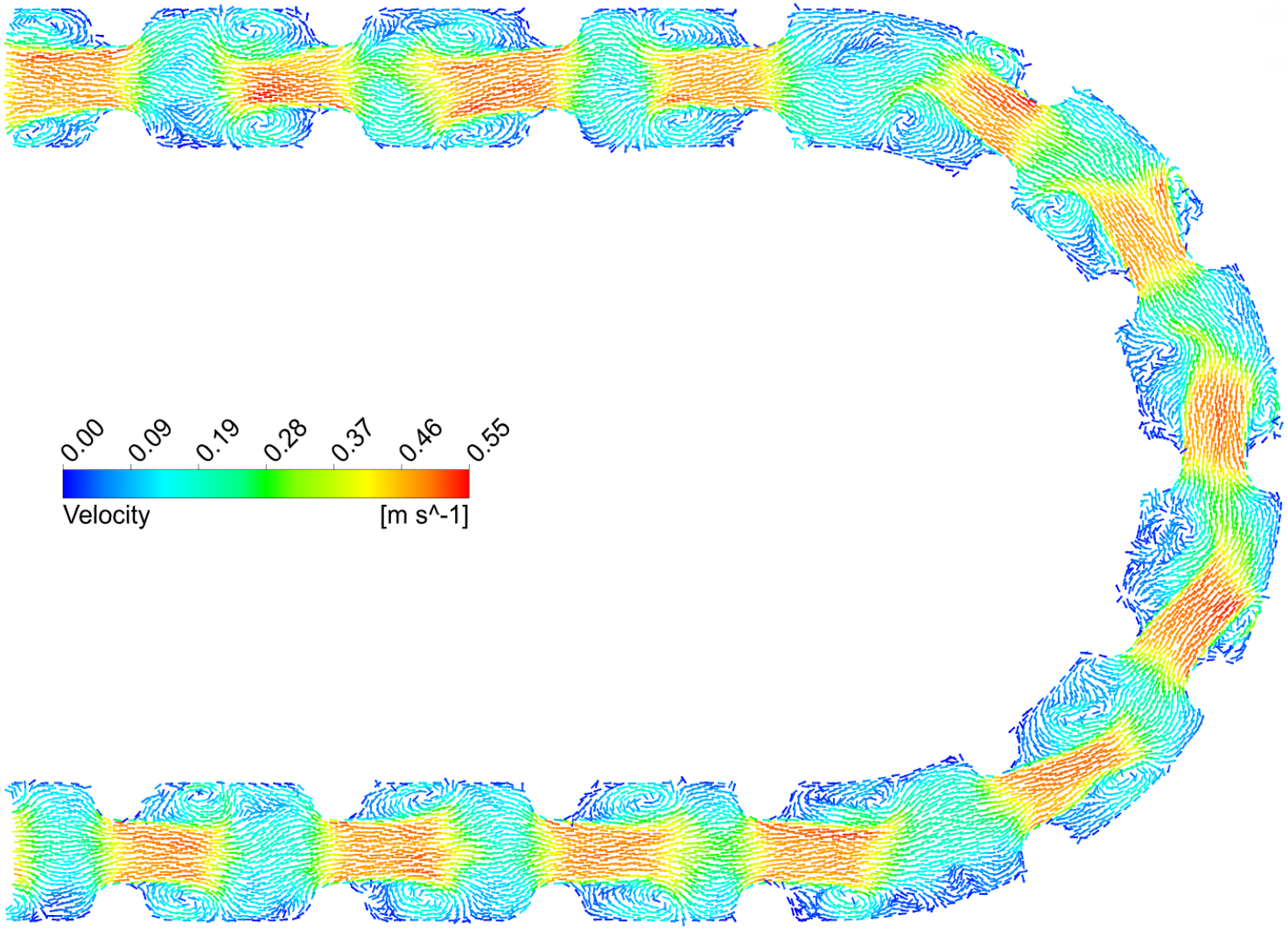

Figure 6.14. *Velocity vector map of sections 14 – 26 at strokes 1 and 2 of simulated cycle 10 for run #27 (Q = 100ml min^{-1}, f = 2Hz, x_o = 7mm)*

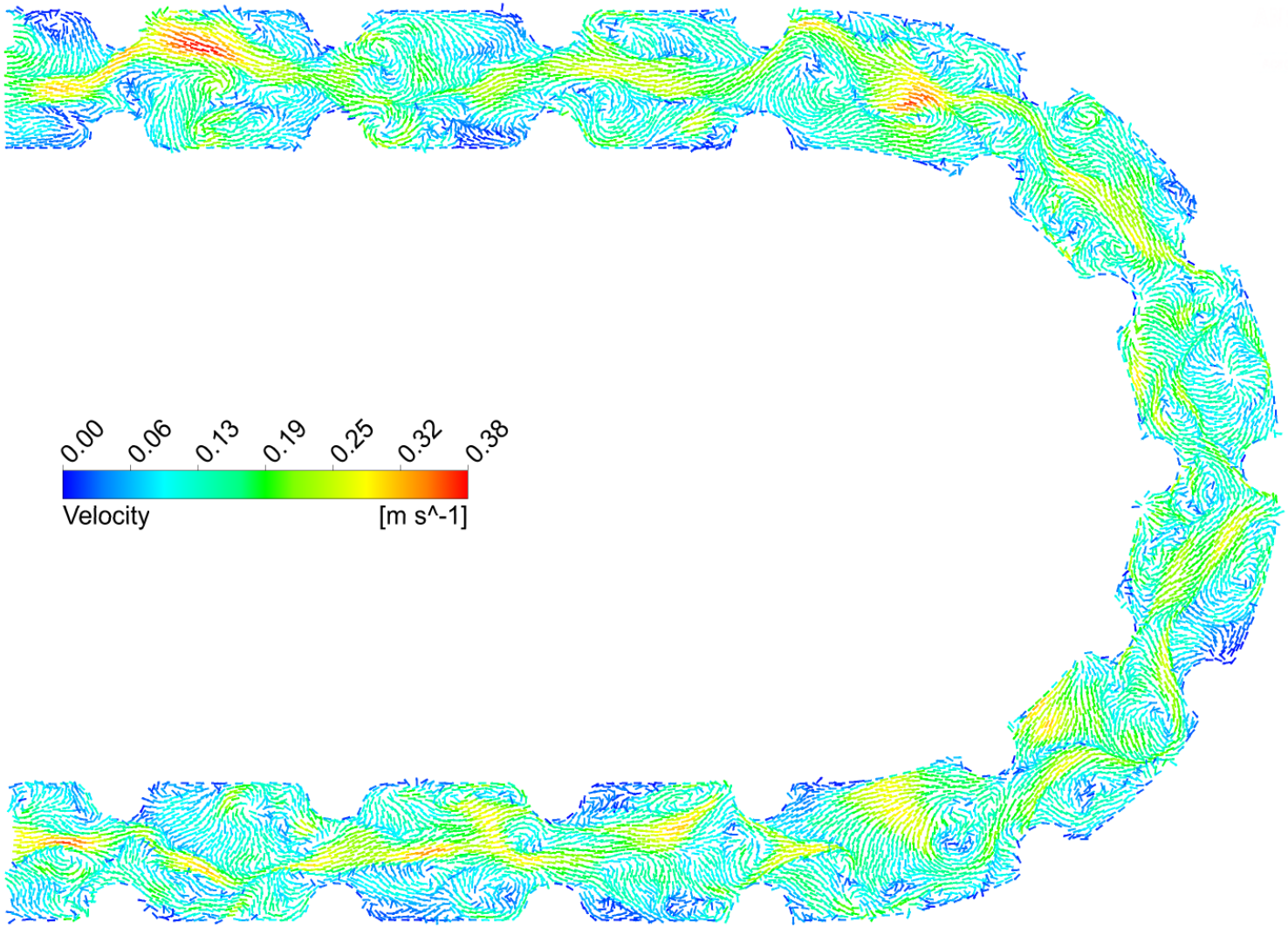

Figure 6.14. (continuation) *Velocity vector map of sections 14 – 26 at strokes 1 and 2 of simulated cycle 10 for run #27*

On the other hand, results from run #27 denote a more stable behaviour of the fluid as it passes through the bend joint. While values of ε_v, Δp_o and δ show fluctuations with length to a certain degree, they seem to revolve around a rather constant value. Only the results obtained for section (20) show a moderate increment in power dissipation rate and a slight decrement in phase shift, both values being the maximum and minimum reported for ε_v and δ respectively.

The velocity vector map for the forward stroke of run #26 can be compared with that of run #27; refer to Figure 6.14. It is interesting to see how fluid velocities throughout the bend joint are higher than those experienced in the straight horizontal sections for run #26. However, this is not the case for run #27, where velocities of very similar magnitude are reported throughout all the baffle constrictions of the domain, including those in the bend joint. In order to further evaluate this behaviour, temporal pressure drop profiles were extracted over the length of the seven baffle constrictions preceding the bend joint, the seven baffles contained in the bend joint and the seven baffles following the bend joint, i.e. $\Delta p_{9\text{-}16}(t)$, $\Delta p_{16\text{-}23}(t)$ and $\Delta p_{23\text{-}30}(t)$. The results extracted from these pressure drop profiles for both runs are presented in Table 6.5. Results obtained for the bend joint and the following seven baffle constrictions, i.e. second straight section, are compared with those obtained for the seven baffles preceding the bend joint. This is done by calculating the percentage difference of the reported variables.

Table 6.5. *Summary of results extracted from three sections of seven baffle constrictions for runs #26 and 27*

Run #	Δp_{net} (Pa)	$\Delta p_o/L$ (Pa m^{-1})	$\Delta p_o/L$ diff. (%)	δ (rad)	δ diff. (%)	ε_v (W m^{-3})	ε_v diff. (%)
26: 9-16	7.3	2256.8	–	0.812	–	85.6	–
26: 16-23	28.8	2616.9	16.0	0.521	-35.9	122.7	43.2
26: 23-30	15.4	2312.3	2.5	0.815	0.4	87.7	2.4
27: 9-16	36.6	3123.4	–	0.806	–	121.5	–
27: 16-23	62.1	3348.4	7.2	0.780	-3.3	131.9	8.6
27: 23-30	38.0	3144.9	0.7	0.800	-0.8	123.2	1.4

Undoubtedly, the flow through the bend joint undergoes an increase in power dissipation rate and the maximum centre-to-peak pressure drop fluctuation, and a decrement in phase shift. These findings are in agreement with the work of Brunold et

al. (1989) [78], where angled bends proved to enhance mixing in oscillatory flow reactors, thus increasing the kinetic energy of the fluid as it passes through them. Furthermore, similar results were reported by Taylor (1954), who demonstrated an increase in diffusion as a fluid flows through a curved pipe, enhancing mixing [146]. However, these changes are of a much larger magnitude for run #26 than #27, the former requiring five times higher increment in ε_v and experiencing ten times greater decrement in δ than the latter. This is visually appreciated in the cycle-averaged $\Delta p(t)$ profiles shown in Figure 6.15.

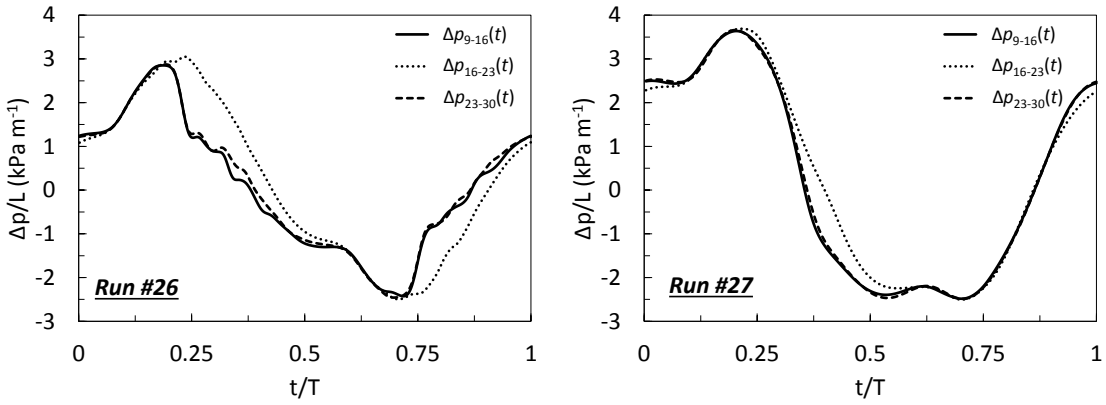

Figure 6.15. *Cycle-averaged pressure drop profiles measured at three sections of seven baffle constrictions for runs #26 (Q = 50ml min^{-1}, f = 1Hz, x_o = 14mm) and 27 (Q = 100ml min^{-1}, f = 2Hz, x_o = 7mm)*

These findings suggest that while increases in oscillatory frequency are the primary reason for the overall COBR power density to increase, oscillatory amplitude is the parameter with the biggest impact on the magnitude of local power dissipation rates in bend joints. The reason behind this phenomenon is the change in direction of the flow and the amount of fluid moved during each forward and backward stroke of the oscillation, the latter being dependent on the oscillatory amplitude and not on frequency. Figure 6.13 shows that as amplitude decreases, so does the effect of bend joints on power dissipation rates and pressure drop profiles in COBRs.

Both simulated conditions did show a maximum and minimum value in ε_v and δ, respectively, for section (20) as reflected by the cycle-averaged $\Delta p(t)$ profiles shown in Figure 6.16. This does not come as a surprise, since section (20) is perpendicular to the horizontal plane and is precisely where the fluid experiences a complete change in direction, i.e. from moving positively in the axial axis due to the net flow, to moving

forward in the opposite direction. As a result, a local increment in power density is experienced in this section.

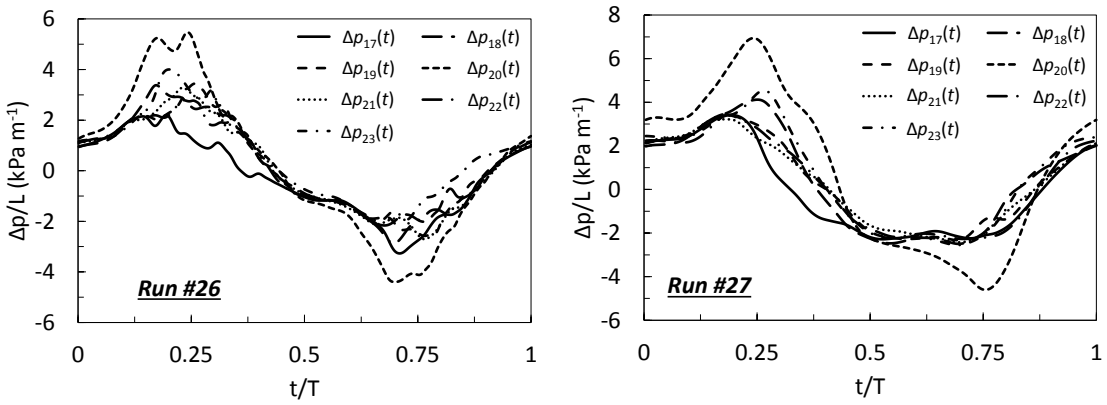

Figure 6.16. *Cycle-averaged pressure drop profiles measured at different sections for runs #26 (Q = 50ml min^{-1}, f = 1Hz, x_o = 14mm) and 27 (Q = 100ml min^{-1}, f = 2Hz, x_o = 7mm)*

While local increments in ε_v were observed as a consequence of the presence of bend joints, these geometric events did not report any sign of energy losses for the conditions studied.

6.4 Conclusions

This chapter studied the impact of three different types of geometric events, which disrupt the axial symmetry of the device, on power density and pressure drop in COBRs. Furthermore, their effect on the flow throughout the length of the reactor was evaluated by analysing local flow patterns and monitoring power dissipation rates, the maximum centre-to-peak pressure drop fluctuation and phase shift along consecutive sections. Velocity vector maps at strokes 1 – 4 of oscillatory cycle 10 for all simulated conditions are presented in Appendix 7.

Results show an increment in power dissipation rates caused by the presence of bend joints, agreeing with the early work in bends carried out by Brunold et al. (1989) [78]. Higher power dissipations rates are reported with the presence of baffle constrictions with reduced cross-sectional area, leading to an increment in the velocity experienced by the fluid while passing through these geometric events. This, however, also increases the power density of the system. Hence, one should be mindful of the number of bend joints comprised in the configuration of a COBR and the number of potential sections

with narrower baffle constrictions, and ensure the motor of the piston is able to provide the energy demanded by the system.

Additionally, findings suggest that sections of the device missing one or multiple baffle constrictions lead to a decrement in power dissipation rates, causing a reduction in the kinetic energy experienced by the fluid due to eddy shedding and dissipating within the missing baffle sections. While these phenomena yield local energy losses, the effects add up to an overall decrement in power density when multiple baffle constrictions are missing, thus increasing the risk of potential particle settling in the presence of solids. Hence, in order to ensure good mixing and suspension throughout the whole length of the reactor, this type of geometric event must be avoided.

Chapter 7 The Effect of Particle Size on Flow in a COBR

7.1 Introduction

Oscillatory Baffled Reactors (OBRs) offer uniform mixing [69] and linear scale up [70], making them an attractive alternative to stirred tank reactors for research and industrial applications in reaction [18, 20, 21, 23, 147] and crystallisation processes [2, 6, 9-11, 16, 17, 94, 148]. Residence time distribution (RTD) profiles of tracer concentration have widely been used to characterise flows in COBR in both experimental and numerical studies, see for examples in the quantification of plug flow efficiency [30, 31], the analysis of flow patterns [28, 36], the optimization of operating oscillatory conditions [27, 29, 37, 43] and geometric design features [32, 33, 44], in the assessment of fluid density impact on axial dispersion [34, 35] and in the development of meso-scale COBRs [38-42, 45]. All these studies were performed in single phase using trackable liquid tracers. An early study involving a secondary solid phase was conducted by Baptista et al. (1996) [128] to analyse the behaviour of suspended solid particles of different sizes and densities in a baffled reactor; however, their system did not have oscillatory flow and their findings were inconclusive, as the interactions among particles were too significant for the effects of sizes and densities to be evaluated. Mazubert et al. [65] employed numerical discrete particle tracking of a secondary phase to measure concentration profiles and analyse the performance of different geometric designs; however, their secondary phase consisted of massless particles that essentially followed the velocity field of the continuous Eulerian phase. Recent work by Ejim et al. [46] highlighted the differences and the knowledge gap in the design of COBRs for multi-phase flow processes using correlations obtained from single phase studies; this was further emphasized by Kacker et al. [47] who reported that not only the optimal operating conditions for minimal axial dispersion involving solids were different from that of single phase, but also longer times were spent by solids in a COBR, underlining the need to properly address the effect of different solid particles on axial dispersion and mean residence times.

The present CFD work solves two phases concurrently, investigates the effect of particle size on axial dispersion and evaluates the residence times and velocities experienced by solid particles and their impact on solids suspension in a COBR. To authors' best knowledge, this is the first study of its kind in the area of COBR research and development where a continuous Eulerian phase is coupled with a discrete

Lagrangian (solid) phase. This chapter is submitted to the Computers & Chemical Engineering in April 2019.

7.2 Geometry & Operating Conditions

The target device of this study is the NiTech DN15 COBR reactor, as earlier described in Section 3.1. The operating oscillatory conditions were chosen partially based on the characteristics of the simulated particles, the simulated domain and literature, in particular, the work of Kacker et al. [47] who used a net flow rate of 100 ml min^{-1} and identified an oscillatory amplitude of 2 mm and frequency of 2 Hz as optimal conditions for solid suspension and near plug flow behaviour of melamine crystals (mean particle size = 100 μm). Hence, Q = 100 ml min^{-1} and f = 2 Hz were selected for this study.

Extensive literature has reported a proportional relationship between oscillatory amplitude and axial dispersion [27, 29, 37, 39, 47, 123]. However, while minimal dispersion and near plug flow behaviour are desirable, Oliva et al. [125] stated that the minimal energy required to ensure solid suspension should be considered. For this reason and considering paracetamol particles of up to 150 μm in diameter were simulated in this work, a moderate oscillatory amplitude of $x_o = D_b$ (7 mm) was selected based on the work by González-Juárez et al. [44]. This is within the ranges suggested in literature for optimal plug flow behaviour, e.g. Gough et al. (1997) advised the utilisation of a centre-to-peak amplitude as one-quarter of the baffle spacing [106]. It should be noted that while the chosen 7 mm amplitude is within the reported range for RTD studies in DN15 [47, 125], it is lower than that used in crystallisation processes where it commonly ranged between 12 and 30 mm [15, 91, 94, 148, 149].

7.3 Computational Simulation Setup

All numerical simulations were performed using ANSYS® Fluent 15.0 CFD package, which discretises the computational domain using finite volume to solve the flow field of a continuous phase. Additionally, Fluent allows for Lagrangian particle tracking by implementing a so-called Discrete Phase Model (DPM) as an add-on to an existing Eulerian phase, this capability was utilised to model tracer and solid particles.

7.3.1 Numerical Model for Eulerian Phase

The fluid selected for this study was water (ρ = 998.2 kg m^{-3}, μ = 1.003·10^{-3} kg m^{-1} s^{-1}). The equations of the model, the solver, the discretisation schemes, the boundary conditions and the mesh used in this study are as earlier described in Chapter 3.

7.3.2 Numerical Model for Lagrangian Phase

In order for this numerical study to closely link with research work in crystallisation from the Centre for Continuous Manufacturing and Crystallisation (CMAC) as well as other parts of the world [1, 3, 4, 94, 95, 150-153], paracetamol (ρ = 1263 kg m^{-3}) was selected as the discrete solid phase. While the shape of paracetamol crystals ranges from needle-like to plate-like to octahedral blocks [94, 150, 154], the discrete solid phase was modelled as mono-sized spherical particles of diameters, D_p = 50, 100 and 150 μm for the purpose of simplicity. Liquid phase information was obtained from discrete *massless* particles that act as a perfect tracer as they move according to the flow field of the continuous liquid phase. The trajectory of each discrete particle is predicted by integrating the force balance on the particle as [139]:

$$m_p \frac{d\vec{u}_p}{dt} = \vec{F}_D + m_p \vec{g}\left(\frac{\rho_p - \rho}{\rho_p}\right) + \vec{F} \tag{7.1}$$

where m_p, $\vec{u}_p$ and ρ_p are, respectively, the mass, velocity and density of the particle. The second term in the right-hand side of Equation (7.1) accounts for the force due to the weight of the particle and the buoyancy effect, the first term $\vec{F}_D$ is the drag force defined as [139]:

$$\vec{F}_D = \frac{1}{2}\rho C_d A_p \left|\vec{u}_p - \vec{u}\right|\left(\vec{u} - \vec{u}_p\right) \tag{7.2}$$

where A_p is the cross-sectional area of the particle and C_d is the drag force coefficient, calculated as the spherical drag law proposed by Morsi and Alexander [155]. The third term, $\vec{F}$, includes the so-called "virtual mass", $\vec{F}_{VM}$, and the pressure gradient force, $\vec{F}_{PG}$, the former accounts for the force required to accelerate the fluid surrounding the particle and the latter is the resultant force from the pressure gradient along the fluid flow around the particle [139]:

$$\vec{F}_{VM} = \frac{1}{2} m_p \frac{\rho}{\rho_p} \left(\frac{D\vec{u}}{Dt} - \frac{d\vec{u}_p}{dt} \right) \tag{7.3}$$

$$\vec{F}_{PG} = m_p \frac{\rho}{\rho_p} \frac{D\vec{u}}{Dt} \tag{7.4}$$

where $\frac{D}{Dt}$ is the material derivative. The position of each particle, $\vec{x}_p$, is governed by:

$$\frac{d\vec{x}_p}{dt} = \vec{u}_p \tag{7.5}$$

Equations (7.1) and (7.5) are integrated using a trapezoidal discretisation scheme with the same time-step as the Eulerian phase (2 ms). When particles are defined as *massless*, the particle velocity equals to the velocity of the continuous phase, $\vec{u}_p = \vec{u}$, hence only Equation (7.5) is required to predict their trajectories [139]. Note that the implementation of ANSYS® Fluent Discrete Phase Model for the modelling of solid particles does not alter or influence the velocity field of the Eulerian phase. This model is appropriate for concentrations of a secondary phase below 10% in volume fraction, according to ANSYS® Fluent User's Guide [156]; the highest volume fraction of solids injected in this work is 0.007% (paracetamol particles of D_p = 150 μm). All particles were modelled as perfect spheres and were released along a cross-sectional plane at the middle of a pre-defined baffle-cell; this is known as "surface injection". In order to cope with the potential computational limitation of modelling too many particles, ANSYS® Fluent tracks so-called "parcels". A parcel may contain multiple particles; its position is defined by a tracked representative particle and its diameter is that of a sphere whose volume is the ratio of the total parcel mass to particle density. However, in this work, in order to model and predict the behaviour of individual particles, the mass of each parcel was set as that of a single particle, i.e. each parcel contained one particle and thus the concept of parcel and particle are interchangeable in this study. The number of particles released in the system was set to 4050; further analysis on the sensitivity of the number of tracked particles on results will be discussed on Section 7.5.1. No particle – particle interaction or particle diffusion in the liquid phase were included in the model.

The terminal (or settling) velocity, u_t, of a particle is achieved when drag forces balance the weight of the particle and the buoyancy force [138]; solving for velocity in spherical particles u_t is determined as:

$$u_t = \sqrt{\frac{4gD_p}{3C_d}\left(\frac{\rho_s - \rho}{\rho}\right)} \tag{7.6}$$

The drag force coefficient of spherical particles at Re = 1000, i.e. C_d = 0.46 [155], was used in this work for the estimation of the terminal velocities reported in Table 7.1.

7.4 Analysis Method

7.4.1 Injection of Discrete Particles

Due to the nature of oscillatory flow in COBRs, forward and backward mixing are generated during oscillations, resulting in particles flowing in and out of a control domain. It is thus crucial to select the injection point for the solid phase particles as well as subsequent location of measuring points to ensure that open boundary effects on particles, due to the inlet and outlet, are minimized. In terms of the particles injection point, it was set at baffle-cell number 15, i.e. 352.5 mm from the inlet, to ensured that less than 0.1% of the injected particles leave the system through the inlet for all the simulated conditions, see Table 7.1. Figure 7.1 displays a sketch of the injection point and measuring cells in the control zone of this work. The position and velocity of every injected particle are extracted and stored at every simulated time-step; this information is post-processed to calculate concentration profiles at any given measuring point. Effectively, measuring cells act as laboratory concentration probes, monitoring the number of particles present within their baffle-cells. For example, a measuring point (M) accounts for the particles contained within a distance of $L_b M \pm (L_b/2)$, where M ranges from 0 to 32. Collectively, concentration of particles (#particles m^{-3}) is monitored over the whole domain, i.e. the total number of monitored particles coincides with the total number of particles present in the system at all times. The optimal measuring points for the conditions tested in this study were identified baffle-cell numbers between 17 and 27 (Figure 7.1), ensuring that over 99.9% of the injected particles pass through these points as they propagate downstream; further discussion on the selection of measuring points is available in Section 7.5.2.

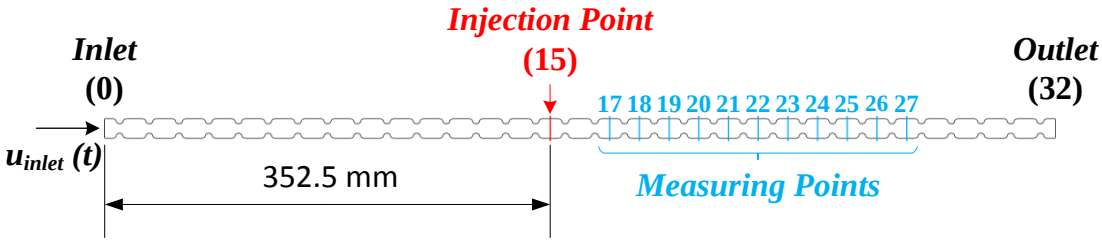

Figure 7.1. *Definition of the injection and measuring points across the NiTech DN15*

Table 7.1. *List of all simulated conditions*

Run #	Q (ml min^{-1})	f (Hz)	x_o (mm)	Re_n	Re_o	St	Material injected	D_p (μm)	u_t (m s^{-1})
1	100	2	5	141	938	0.239	Tracer (massless)	–	–
2	100	2	7	141	1313	0.171	Tracer (massless)	–	–
3	100	2	7	141	1313	0.171	Paracetamol	50	0.019
4	100	2	7	141	1313	0.171	Paracetamol	100	0.027
5	100	2	7	141	1313	0.171	Paracetamol	150	0.034

7.4.2 Determination of Axial Dispersion

In a tubular reactor, mixing is commonly quantified by the axial dispersion coefficient (D_a), which describes the degree of spreading (in the axial direction) of a tracer injected upstream as a pulse (ideally). Analogous to the molecular diffusion model given by Fick's law, Levenspiel and Smith [122] proposed the following equation to evaluate the axial dispersion coefficient:

$$\frac{\partial C}{\partial t} = D_a \frac{\partial^2 C}{\partial x^2} - U \frac{\partial C}{\partial x} \tag{7.7}$$

where C is the tracer concentration as a function of time, t, and position, x, and U is the mean net flow velocity of the system ($U = QL/V$). Although equation (7.7) was originally derived for a single phase flow, it can also be used for two phase (solid-liquid) cases. When the concentration of a liquid tracer is defined as $C_L = m_L/V_L$ and the concentration of solids as $C_S = m_S/(V_L + V_S)$, Equation (7.7) becomes independent of the volume of the secondary solid phase ($V_L + V_S \approx V_L$) when $V_S << V_L$, which is the case in the present study. This is also consistent with literature, e.g. the work of Ejim et al. [46] and Kacker et al. [47], who applied this model to measured concentrations of PVC and solid melamine particles, respectively, in order to assess their axial dispersion

coefficients in water. If a perfect input pulse injection is assumed, typical boundary conditions for Equation (7.7) are:

$$C(x,0) = \frac{n}{A}\delta(x) \tag{7.8}$$

$$\lim_{x\to\pm\infty} C(x,\mathrm{t}) = 0 \tag{7.9}$$

where n is the volume of tracer/secondary phase injected, A the cross-sectional area of the device and $\delta(x)$ a Dirac delta function. Thus, the analytical solution to Equation (7.7) at fixed values of D_a and U is given by:

$$C(x,t) = \frac{1}{\sqrt{4\pi D_a t}} \exp\left(-\frac{(x-Ut)^2}{4D_a t}\right) \tag{7.10}$$

Under the assumption of a perfect pulse injection, the plug flow with axial dispersion model can be re-derived and solved based on an inverse Peclet number ($Pe = UL/D_a$) as [122]:

$$\sigma_\theta{}^2 = \frac{\sigma^2}{\bar{t}^{\,2}} = 2\frac{1}{Pe} + 8\left(\frac{1}{Pe}\right)^2 \tag{7.11}$$

where $\sigma_\theta{}^2$ is the dimensionless variance, σ^2 the variance and $\bar{t}$ the mean residence time of the tracer concentration defined as:

$$\sigma^2 = \frac{\int_0^\infty (t-\bar{t})^2 C_w(t)\,dt}{\int_0^\infty C_w(t)\,dt} = \frac{\sum_{i=1}^{N} (t_i-\bar{t})^2 C_w(t_i)\Delta t_i}{\sum_{i=1}^{N} C_w(t_i)\Delta t_i} \tag{7.12}$$

$$\bar{t} = \frac{\int_0^\infty t C_w(t)\,dt}{\int_0^\infty C_w(t)\,dt} = \frac{\sum_{i=1}^{N} t C_w(t_i)\Delta t_i}{\sum_{i=1}^{N} C_w(t_i)\Delta t_i} \tag{7.13}$$

where N is the total number of measured concentration data and C_w is the concentration of particles (#particles m^{-3}) at time t, weighted by particles' initial velocity (u_{net}) and normalised by the maximum velocity in the device (ωx_o); this approach has successfully been implemented for the analysis of RTD profiles in micro-channels by Aubin et al.

[157] and in COBRs by Mazubert et al. [65]. Equation (7.11) is used to evaluate the axial dispersion coefficient under the perfect pulse method (PPM).

A perfect input pulse is unachievable in practice and unmeasurable experimentally. Hence, Aris (1959) proposed an imperfect pulse method (IPM) [158] where the concentration profile of the tracer/secondary phase is measured at two points downstream of the tracer injection, i.e. $C_1(t)$ and $C_2(t)$; thus the form of the impulse becomes irrelevant. This method is implicitly more accurate, since no assumption is made regarding the nature of the tracer/secondary phase injection and upstream RTD data are used to predict the downstream response. This method was firstly implemented in OBRs by Mackley and Ni [69], who adopted the solution of Göeble et al. [159] and used a normalised concentration $E(t)$ [160] for better comparison among results:

$$E(t) = \frac{C_w(t)}{\int_0^\infty C_w(t)\,dt} = \frac{C_w(t_i)}{\sum_{i=1}^{N} C_w(t_i)\,\Delta t_i} \tag{7.14}$$

Mackley and Ni [69] suggested that the normalised concentration measured at an upstream point (1) during a short time interval, Δt, can be regarded as a perfect pulse injection with an injected volume $E(t_1)\Delta t$ at time $t = t_1$. Taking the limit $\Delta t \rightarrow 0$ and integrating over all possible injection times, t_1, the normalised concentration at point (2) can be estimated by the convolution integral equation below:

$$E_2'(t) = \int_0^t E_1(t_1)\,TR(t-t_1)\,dt_1 = \sum_{i=1}^{N} E_1(t_{1,i})\,TR(t-t_{1,i})\,\Delta t_{1,i} \tag{7.15}$$

where $TR(t)$ is the transfer function for "open-open" boundary conditions. The formulation of the transfer function reported by Mackley and Ni was in disagreement with the one proposed by Westerterp et al. [161]. However, later work by Smith [162] proved that the formulation of Westerterp et al. was the most accurate, hence it is used in the current work as:

$$TR(t) = \frac{1}{\sqrt{4\pi D_a \frac{t^3}{L^2}}} \exp\left(-\frac{(L-Ut)^2}{4D_a t}\right) \tag{7.16}$$

where the distance from the injection point, L, is essentially the distance between measuring points (1) and (2). The normalised concentration predicted at point (2), $E_2'(t)$,

is compared with the measured normalised concentration at such point, $E_2(t)$, and the axial dispersion coefficient is fitted in order to satisfy the target function:

$$\Delta E = \sum_{i=1}^{N} \left\{ E_2(t_i) - E_2'(t_i) \right\}^2 \tag{7.17}$$

where N is the total number of normalised concentration data. The optimal axial dispersion coefficient is obtained when the target function (10) is minimized. While the value of the mean net flow velocity, U, as aforementioned, can be assumed as $U = QL/V$, a more accurate method, making use of the available upstream and downstream RTD profiles, is to calculate the time it takes for the tracer/secondary phase to travel from measuring points (1) to (2) as [162]:

$$U = \frac{L}{\int_0^\infty tE_2(t)\,dt - \int_0^\infty tE_1(t)\,dt} = \frac{L}{\sum_{i=1}^{N} tE_2(t)\Delta t - \sum_{i=1}^{N} tE_1(t)\Delta t} \tag{7.18}$$

Equation (7.18) significantly increases the accuracy of results, especially for RTD analysis of tracer and solids whose velocity may differ from that of the primary liquid phase (QL/V); this is clearly evident in Sections 7.5.3 and 7.6.2, and in Figures 7.5 and 7.12 respectively, where a decrease in net velocity is observed as particle size increases. The imperfect pulse method [29, 34, 38, 45, 123, 124] as well as the perfect pulse method [44, 47, 65, 125] have been used to quantify axial dispersion in COBRs. Consequently, both methods (PPM and IPM) are used in this work, enabling comparison and assessment of the impact of length (from injection to measuring point) on their accuracy. For better comparison, most of the RTD curves reported in this work are presented in their normalised form as $E(\theta)$ vs θ, where $E(\theta) = \bar{t}\,E(t)$ and $\theta = t/\bar{t}$.

7.5 Method Validation

7.5.1 Effect on Number of Simulated Particles

Discrete particles were injected into a cross-sectional plane in the middle of a baffle-cell containing 4050 computational cells; the "surface" injection type releases one particle per computational cell, thus 4050 particles were injected. This number is significantly larger than what is reported in literature, e.g. Mazubert et al. [65] used 2484 massless particles to characterise axial dispersion, mean residence times and fluid stretch rates of

a single liquid phase in a COBR. In the present study, the sensitivity of results on the number of particles injected was tested by examining and comparing two injections of 4050 and 8100 particles, respectively. The injection releasing 8100 particles was implemented by performing a "surface" injection simultaneously at two cross-sectional planes (4050 computational cells each) placed in the middle of the 15th baffle-cell; these two planes were 0.75 mm apart from one another. This analysis was performed for massless particles under the operating conditions of run #2 (see Table 7.1). Figure 7.2 (left) displays the profiles of $E(\theta)$ vs θ measured at the baffle-cell (27) for both numbers of particles injected; the degree of agreement between profiles is very good as both profiles overlap one another. Additionally, the axial dispersion coefficients calculated using the PPM, Equation (7.11), and the IPM, Equations (7.15) – (7.18), at different lengths of the reactor for both numbers of injected particles are presented in Figure 7.2 (right). Again, the agreement between results is remarkable, reporting an average percentage error of 2.8%. Results obtained with the IPM were calculated using baffle-cell (17) for C_1 and baffle-cells (19) – (27) for C_2. On the balance of accuracy and computing time, it was determined that a "surface" injection of 4050 particles is sufficient for reproducing the flow patterns in the COBR.

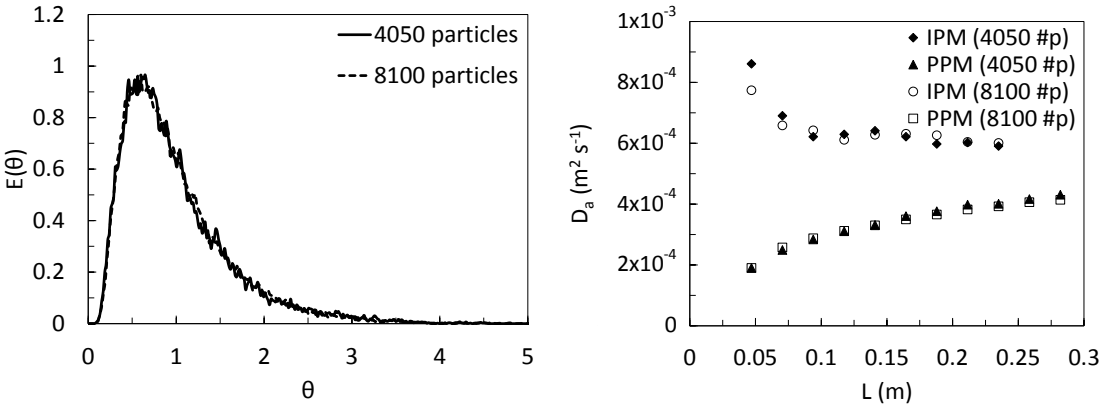

Figure 7.2. *E(θ) vs θ profiles (left) and Da vs L (right) for two numbers of injected discrete phase particles at operating conditions of run #2 (Q = 100ml min^{-1}, f = 2Hz, x_o = 7mm)*

7.5.2 Measuring Points

While CFD simulated RTD curves can be monitored at any length of the reactor, the effect of "open-open" boundary conditions at the inlet and outlet of the baffled reactor must be taken into account. Due to the oscillatory nature of the flow, particles would pass through a certain section of the domain multiple times, since the oscillatory

velocities are considerably higher than the net flow velocity; for this reason, measuring points must cautiously be selected. If a measuring point is too close to an open boundary, particles would escape the system prematurely. In order to select appropriate measuring points, RTD curves were monitored for all baffle-cells of the modelled device. The area under the curves of these RTD profiles is then calculated as $C_o = \int_0^\infty C(t)\,dt = \sum_{i=1}^{N} C(t_i)\,\Delta t_i$, and plotted as a function of length (from the injection point) in Figure 7.3 (right); RTD curves measured at three different baffle-cells during run #2 are presented in Figure 7.3 (left).

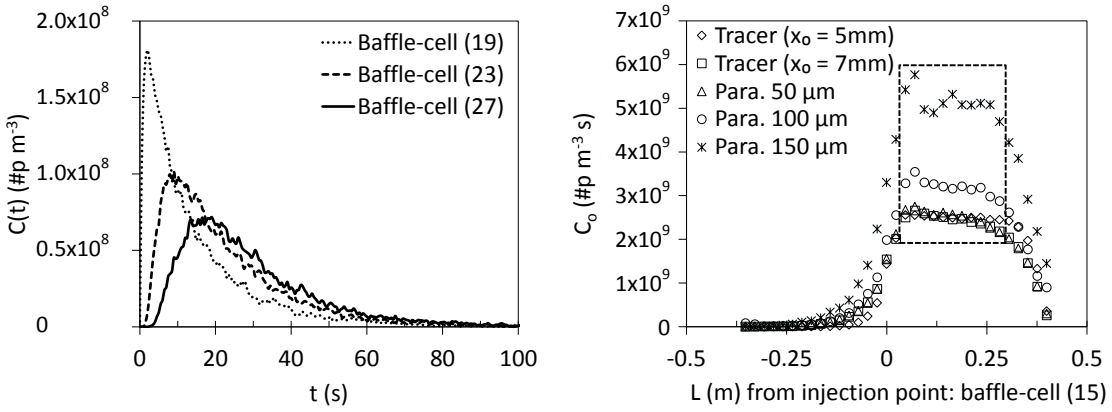

Figure 7.3. *RTD curves measured at different baffle-cells at operating conditions of run #2 (left) (Q = 100ml min^{-1}, f = 2Hz, x_o = 7mm) and RTD area under the curve (C_o) with length for all simulated conditions (right)*

When particles leave the system and disappear pre-maturely, via an opening boundary, it results in a lower value of the area under the RTD curve measured at a certain baffle-cell, C_o. A constant C_o value along the reactor's length for each simulated run is hence a good guide for selecting measuring points, as indicated by the squared region in Figure 7.3 (right). Consequently, RTD data obtained from baffle-cells (17) to (27) (0.047 – 0.282 m from the injection point) was selected for analysis, while the remaining concentration profiles measured at baffle-cells (28) to (32) were discarded as the effect of open boundaries on the number of particles escaping the system pre-maturely was too large for reliable $C(t)$ curves to be measured.

Note that C_o values reported for particles of 100 and 150 µm diameter are approximately 30% and 110% higher than those of the tracer (x_o = 7 mm), respectively. This is due to the fact that C_o has units of (#particles m^{-3} s) and particles of larger size

spend more time in the reactor, resulting in wider RTD profiles, i.e. larger area under the profiles' curve; this is further explored and commented in Section 7.6.1.

7.5.3 Perfect & Imperfect Pulse Method

Figure 7.4 shows the axial dispersion coefficients obtained from both the PPM and IPM methods as a function of length for all runs (refer to Table 7.1). Results provided by IPM were calculated with baffle-cell (17) as C_1 and baffle-cells (19) – (27) as C_2.

The axial dispersion coefficient (D_a) of a fluid material or a secondary phase, at given operating conditions, is expected to be constant from the governing equation (7.7), but in reality changes slightly with time as the trace/secondary phase travels downstream the device [29, 69]. The results obtained by PPM are undoubtedly dependent on the length at which RTD curves were measured; as a matter of fact, the length of the device over which this analysis has been performed is not sufficient for PPM to reach a completely asymptotic D_a value. On the other hand, IPM reaches an asymptotic D_a value at a very early stage for all simulated runs, reporting nearly constant values around this asymptotic D_a with length. Figure 7.4 shows the results obtained with the IPM by assuming $U = QL/V$ and by calculating U as per Equation (7.18); both provided very similar results and trends of D_a vs L. However, the residual errors from IPM's target function, Equation (7.17), were consistently higher when U was assumed to be equal to QL/V; the average residual error reported for each simulated run are presented in Table 7.2. Hence, the IPM's asymptotic values of D_a were calculated by averaging the coefficients (D_a) obtained when baffle-cells (20) to (27) were set as C_2 and when U was estimated with Equation (7.18). A straight horizontal line is used to represent the asymptotic D_a values in Figure 7.4. Although D_a values computed via IPM fluctuate around the asymptotic value, they are much more stable than those obtained with PPM and are thus chosen as the final results in this study.

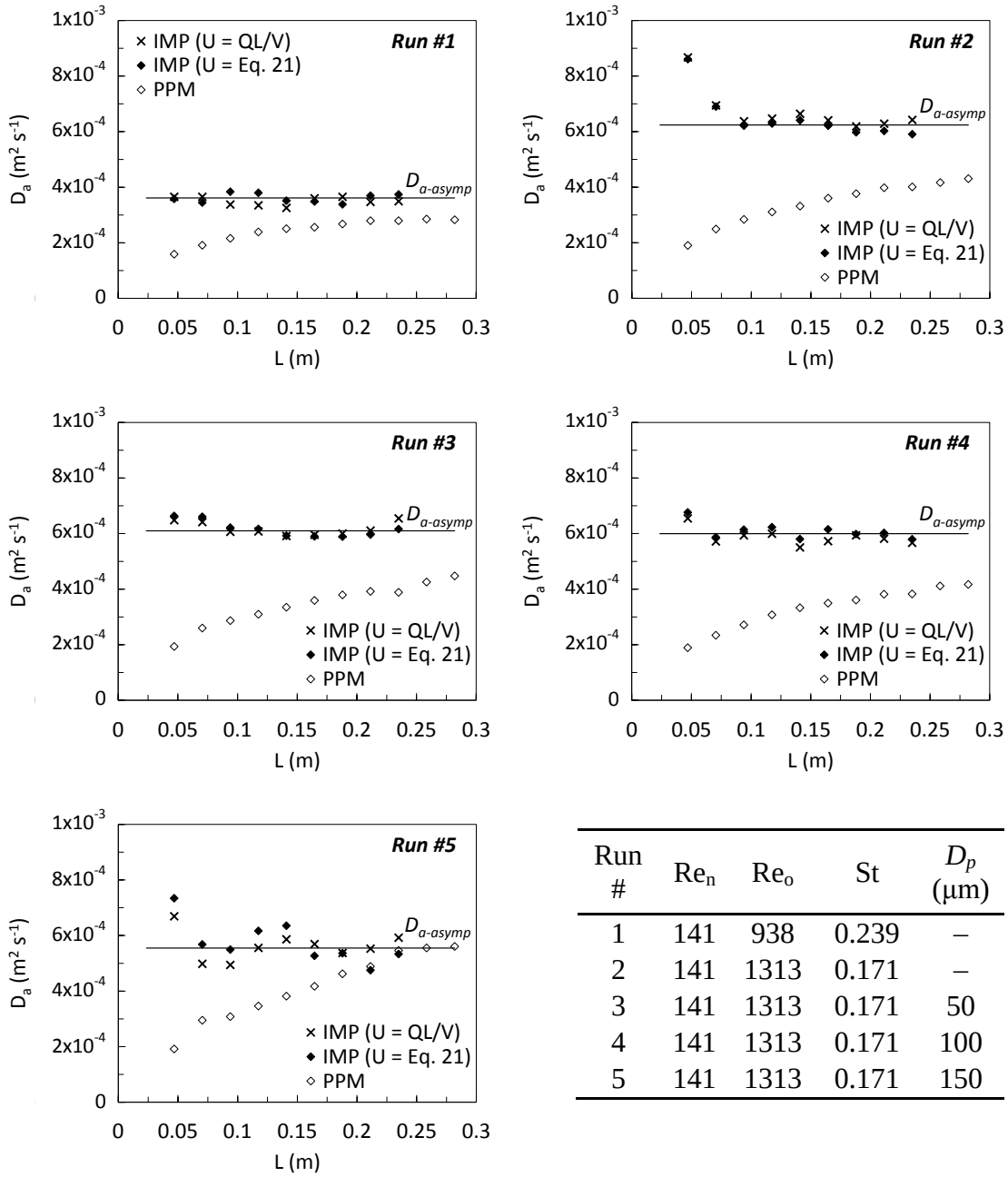

Run #	Re_n	Re_o	St	D_p (μm)
1	141	938	0.239	–
2	141	1313	0.171	–
3	141	1313	0.171	50
4	141	1313	0.171	100
5	141	1313	0.171	150

Figure 7.4. *D_a calculated from RTD curves measured at different lengths (from the injection point) using the imperfect (IPM) and the perfect pulse (PPM) methods for all runs simulated*

Table 7.2. *Average residual errors from IPM's target function, Equation (7.17)*

Run #	$\overline{\Delta E}^{\text{Eq.(7.17)}}$ (U = QL/V)	$\overline{\Delta E}^{\text{Eq.(7.17)}}$ (U = Eq. 7.18)
1	3.5 x10^3	3.2 x10^3
2	3.9 x10^3	3.6 x10^3
3	4.4 x10^3	4.1 x10^3
4	1.1 x10^2	5.2 x10^3
5	2.1 x10^2	5.4 x10^3

As aforementioned, Equation (7.18) provides a more accurate estimation of the mean net velocity of particles that travel from point (1) to point (2), since it uses RTD profiles measured at both points. Figure 7.5 supports this argument by showing the velocity values obtained during the fitting process of IPM, calculated via Equation (7.18) at different lengths of the reactor, and comparing it to $U = QL/V$. In reality, U from Equation (7.18) represents the mean net velocity of particles experienced while travelling from the measuring point (1) to point (2). As one could have anticipated, the results clearly indicate that while $U = QL/V$ is a fair estimation of liquid phase velocity, the velocity of a secondary solid phase is dependent on particle size, with velocity of small particles (50 μm diameter) close to that of the liquid phase and that of larger particles being significantly smaller. These trends are in agreement with results presented later in Section 7.6.2, see Figure 7.12 (left). Based on the current findings, Equation (7.18) was employed for the calculation of U in the IPM for all results presented on this study.

It should be noted that the PPM does not allow for the implementation of Equation (7.18), since it only uses information of one RTD profile measured at the reactor length under investigation. Hence, $U = QL/V$ is assumed when calculating axial dispersion coefficients via PPM, which evidently leads to less accurate results. It is worth pointing out that the accuracy of Equation (7.18) may vary depending on the distance between point (1) and point (2). This velocity is smoothed out further as the measuring point (2) is moved along the length of the device while keeping the measuring point (1) fixed, thereby increasing the length over which RTD curves are examined.

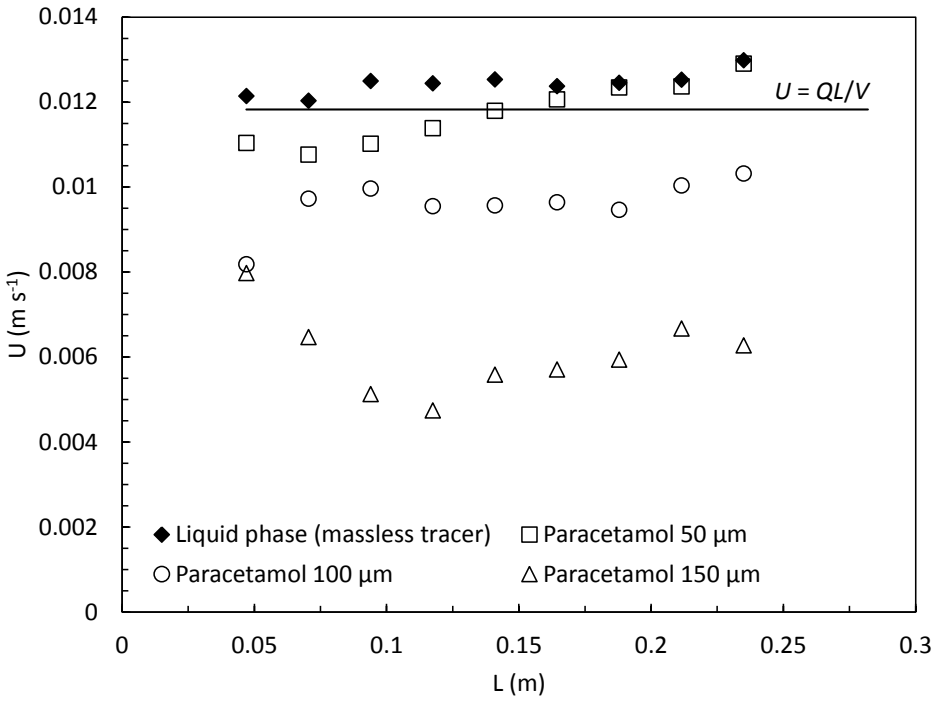

Figure 7.5. *Velocity calculated with Equation (*7.18*) with measuring point (1) fix at baffle-cell (17) and measuring point ranging from baffle-cell (19) to (27) (Q = 100ml* min^{-1}*, f = 2Hz,* x_o *= 7mm)*

7.5.4 Validation of Simulated Results

For the validation of the CFD methodology and the estimation of axial dispersion coefficients, results of Kacker et al.'s work [47] are compared with those obtained in this study. Kacker et al. undertook their experimental investigation in a DN15 and analysed axial dispersion for a wide range of operating conditions using a homogenous tracer (methylene blue) and a heterogeneous phase (melamine). The results of their homogenous tracer are compared with that of the present massless particles analysis (asymptotic values from Figure 7.4) and are plotted in Figure 7.6 (left). It shows that the order of magnitude and the trend of D_a vs x_o bear great similarity to those of Kacker et al., thus validating the proposed model developed here.

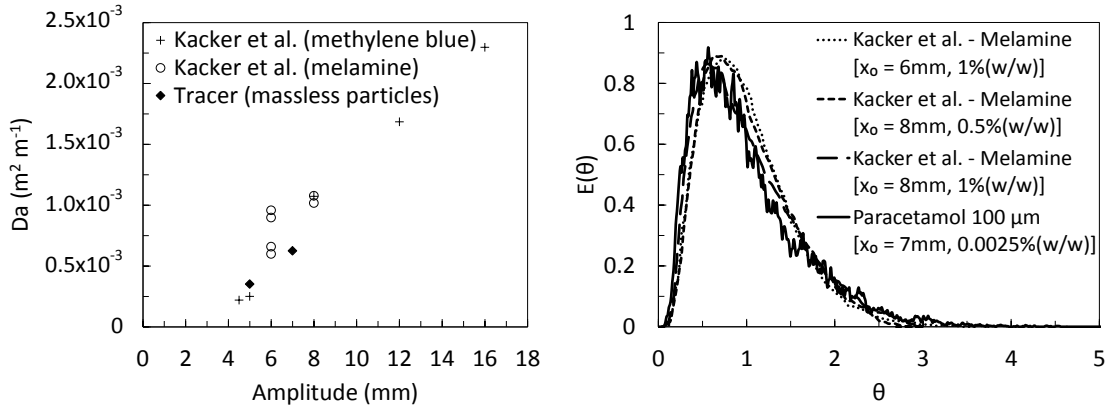

Figure 7.6. *Comparison of axial dispersion coefficients and RTD profiles with those reported by Kacker et al. [47]*

Figure 7.6 (left) also shows the axial dispersion coefficient obtained by Kacker et al. using melamine (ρ = 1575 kg m^{-3}) particles of 100 µm mean particle size at different solid concentrations. While the effect of concentration on axial dispersion was not clear from the work of Kacker et al., their results pointed to an axial dispersion coefficient of around 0.0006 – 0.001 m^2 s^{-1} at oscillatory amplitude of 7mm. In the current study, a D_a of 0.0006 m^2 s^{-1} (asymptotic value from Figure 7.4) was obtained from run #4. By taking the density difference between the two studies into consideration and using the correlation from Ni et al. [35], D_a is multiplied by a density ratio ($\rho_{melamine}$ / $\rho_{paracetamol}$), giving a value of D_a = 0.000748 m^2 s^{-1}, which is within the range suggested by Kacker et al.

Additionally, comparison with the RTD curves reported by Kacker et at. was performed by plotting $E(\theta)$ vs θ profiles of their heterogeneous tracer along with that from run #4 of this work in Figure 7.6 (right). The results they obtained from injection port 1 and measuring port 1 ($L \approx 0.72$ m) were chosen as the basis for comparison; the profile measured at baffle-cell (27) of our device (L = 0.282 m) shown in Figure 7.6 (right) exhibits a remarkable similarity both in magnitude and shape, which further verified the appropriateness of the proposed model.

The validity of ANSYS® Fluent's DPM model was also tested by comparing axial velocity of the continuous liquid phase with that of the tracer (massless particles). The velocity of the Eulerian liquid phase (ELP) was calculated as the volume-weighted average, $\overline{u}_{x-ELP}$, of the whole simulated domain, and the average velocity in the axial

direction, $\bar{u}_x$, experienced by particles (tracer and/or solid) at any given time, *t*, was calculated as:

$$\bar{u}_x(t) = \frac{\sum_{i=1}^{N(t)} u_{x,i}(t)}{N(t)} \tag{7.19}$$

where the index *i* represents a specific particle and *N*(*t*) the total number of particles present in the system at time *t*. Figure 7.7 plots the velocity profiles of the Eulerian and Lagrangian phases side by side at a given time range. The degree of agreement between profiles is exceptional, overlapping one another to the point that distinguishing them is nearly impossible.

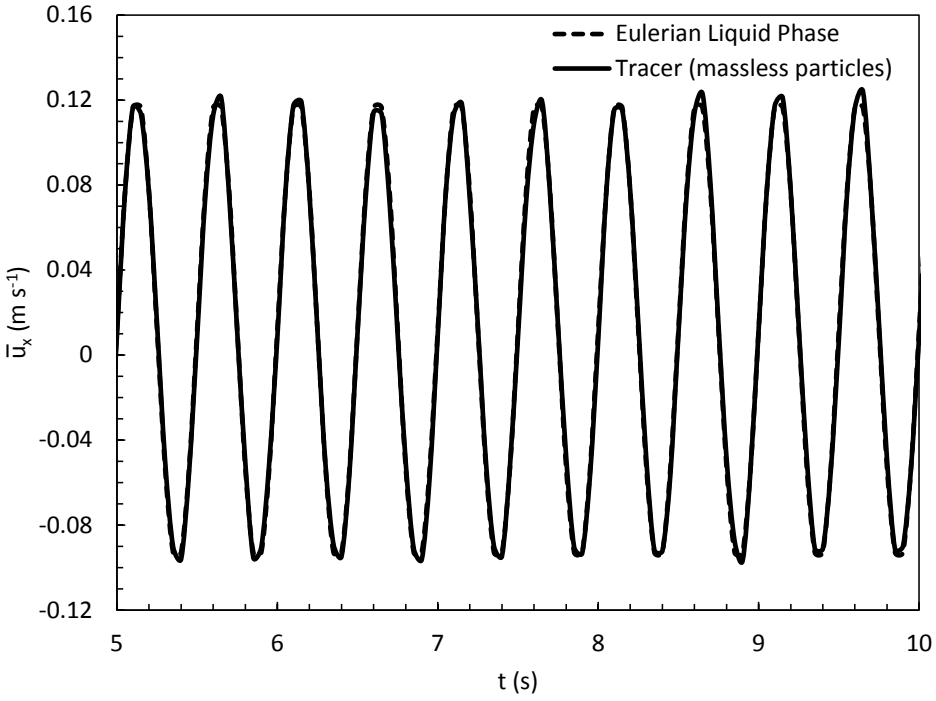

Figure 7.7. *Axial velocity of the liquid Eulerian phase and the Lagrangian tracer for a certain time range (Q = 100ml min^{-1}, f = 2Hz, x_o = 7mm)*

7.6 Results & Discussion

7.6.1 Effect of Size of Particle on Axial Dispersion and Residence Time

The effect of particle size on axial dispersion is graphically presented in Figure 7.8 (left), displaying profiles of $E(\theta)$ vs θ of the baffle-cell (27) for all runs performed (see

Table 7.1). While the impact of particle size on axial dispersion of the secondary phase is qualitatively minimal (Figure 7.8 left), the asymptotic D_a values from Figure (7.4) decrease with the increase of particle size (Table 7.3). Additionally, Table 7.3 presents the percentage difference of D_a and $\bar{t}$ in comparison with the liquid phase, labelled as ΔD_a and $\Delta\bar{t}$ respectively. The mean residence time required for particles to reach baffle-cell (27) from the injection cell (15) becomes longer as particle size increases, displaying a noticeable shift in the profiles of $E(\theta)$ vs t (Figure 7.8 right). It is observed that the residence time for particles of 50 μm diameter barely changes in comparison to that of the liquid phase (represented by massless particles), the degree of agreement between both $E(\theta)$ vs t profiles is very good as they overlap one another, suggesting that small solid particles (50 μm) follow the liquid phase flow. On the contrary, particles of 100 or 150 μm diameters undergo an increase in residence time of up to 139% (Table 7.3), thus displaying a noticeable shift in time in their $E(\theta)$ vs t profiles.

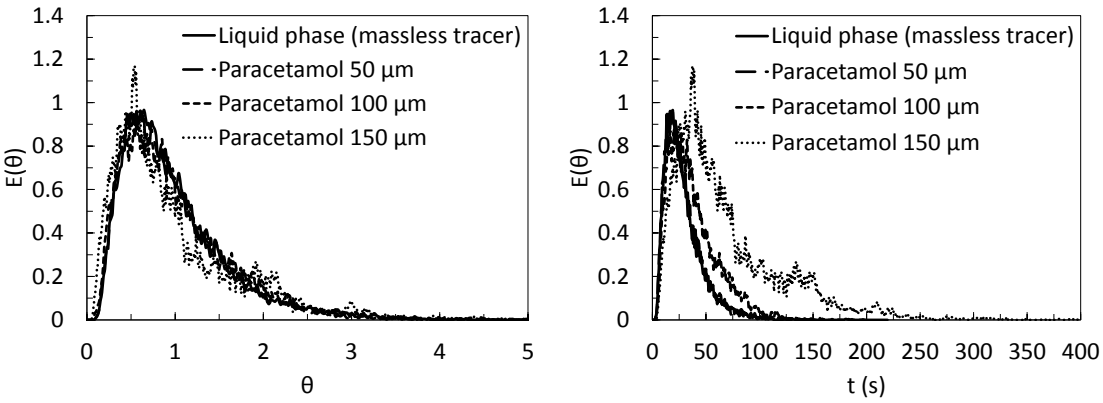

Figure 7.8. *E(θ) vs θ (left) and E(θ) vs t (right) profiles for different particle sizes (Q = 100 ml min^{-1}, f = 2Hz, x_o = 7mm)*

Table 7.3. *D_a and $\bar{t}$ values for different particle sizes (Q = 100ml min^{-1}, f = 2Hz, x_o = 7mm)*

	D_a (m^2 s^{-1})	ΔD_a [††] (%)	$\bar{t}$ [**] (s)	$\Delta\bar{t}$ [††] (%)
Tracer (massless)	6.24 x10^4	–	29.3	–
Paracetamol 50 μm	6.10 x10^4	-2.2	29.6	0.9
Paracetamol 100 μm	6.00 x10^4	-3.9	38.1	29.9
Paracetamol 150 μm	5.55 x10^4	-11.1	70.1	138.9

[**] *Mean residence time at baffle-cell (27), where L (from injection point) = 0.282 m*
[††] *With respect to the values provided by the liquid phase (massless tracer)*

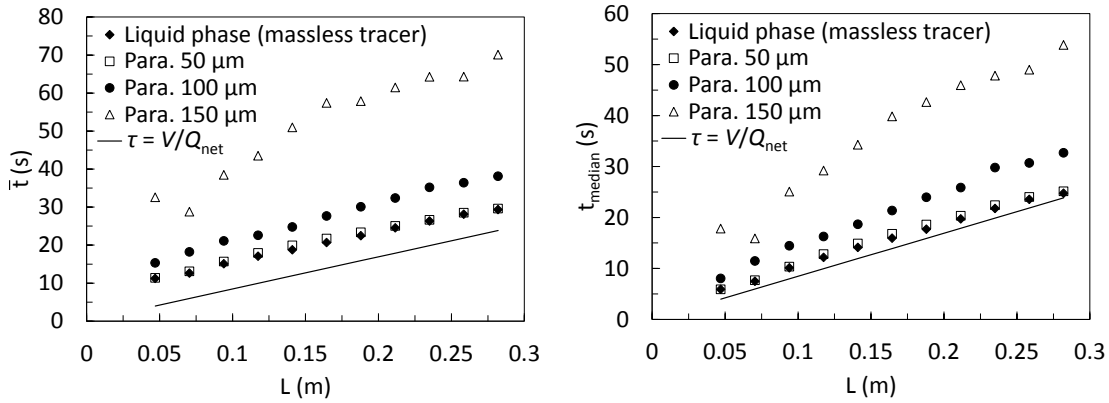

Figure 7.9. *Mean residence time as a function of length (from the injection point) for different particle sizes (Q = 100 ml min^{-1}, f = 2Hz, x_o = 7mm)*

Figure 7.9 (left) shows the mean residence time, $\bar{t}$, spent by particles from baffle-cell (15) to (27) calculated via Equation (7.13), with $\tau = V/Q_{net}$ as the basis for comparison. A significant increase in mean residence times is observed as particles grow in size. This is due to decay in oscillatory axial velocity with the presence of particles, leading to smaller axial dispersion and longer residence times. These findings are consistent with the work of Ejim et al. and Kacker et al. [46, 47] and should be considered when designing COBRs for crystallisation processes where particles' residence time is a key factor affecting crystal growth.

It is also seen from Figure 7.9 that the slopes of increasing residence times for liquid phase and for solid phase (paracetamol of 50 µm diameter) are the same, indicating that both move axially at a constant mean net velocity. The slopes for particles of 100 and 150 µm diameter are moderately higher, denoting an increasing decay in their mean net velocities with length. At constant solid particles' density, an increase in particle size translates into bigger volume of each particle, thus larger a cross-sectional area, A_p. This has a direct impact on the drag force experienced by each particle; larger drag forces result in more stressed particle deceleration, i.e. negative $\frac{d\bar{u}_p}{dt}$, leading to a decay in the net velocity of the particle. This reduction in velocity experienced by particles of bigger size is further analysed and discussed in the next subsection.

It is also observed that the overall mean residence times experienced by massless particles are higher than $\tau = V/Q_{net}$, which is interesting. These results could be deceiving, as one may infer that particles' mean net velocity is lower than QL/V, however this is only true for solid particles, not for the single phase, as revealed in the

next subsection. The reason for the overall high values of mean residence time is a small degree of skewness displayed by the RTD profiles for the oscillatory conditions simulated, thus deviating slightly from a Gaussian function (Figure 7.3 left). This translates into a shifted mean value, as opposed to the 50^{th} percentile, i.e. statistical median. For the sake of comparison and in order to support this argument, Figure 7.9 (right) shows the median residence times, t_{median}, as the function of length. Note that both mean and median residence times display identical trends.

7.6.2 Effect of Particle Size on their Velocity – the Dampening Phenomenon

The average velocity magnitude, $\overline{u}_m$,and the average velocity in the axial direction, $\overline{u}_x$, experienced by tracer and/or solid particles at any given time, *t*, were calculated as per Equation (7.19). Because the total number of particles is a function of time, results for each simulated run are only reported until the mean residence time measured at baffle-cell (27) is reached, i.e. $t = \overline{t}_{baffle-cell-27}$ (see Table 7.3), ensuring that no effects from the open boundary outlet are present. Figure 7.10 displays the mean axial velocity profiles experienced by particles of different sizes over a certain time frame, along with the inlet velocity profile as a basis of reference. A dampening on the oscillation amplitude experienced by particles as they increase in size is clearly observed; the percentage of oscillatory velocity lost by solid particles at the peaks of the oscillation in comparison to the velocity of the liquid phase is reported in Table 7.4 as $\Delta\overline{u}_{x-peaks}$. As aforementioned, this reduction in velocity experienced by solid particles is due to an increase of the drag force they undergo as their sizes increase.

Figure 7.11 plots $\overline{u}_x$ with time for particles of different sizes. The liquid phase and small particles (50 μm) show a nearly constant trend of their oscillatory axial velocity peaks with time, while a decreasing trend in the magnitudes of oscillatory axial peaks is evident for paracetamol solids of 100 μm (left) and 150 μm (right) diameter.

Note that the velocity profiles presented in Figures 7.10 and 7.11 are the mean axial velocity averaged over all particles present in the entirety of the system at any time.

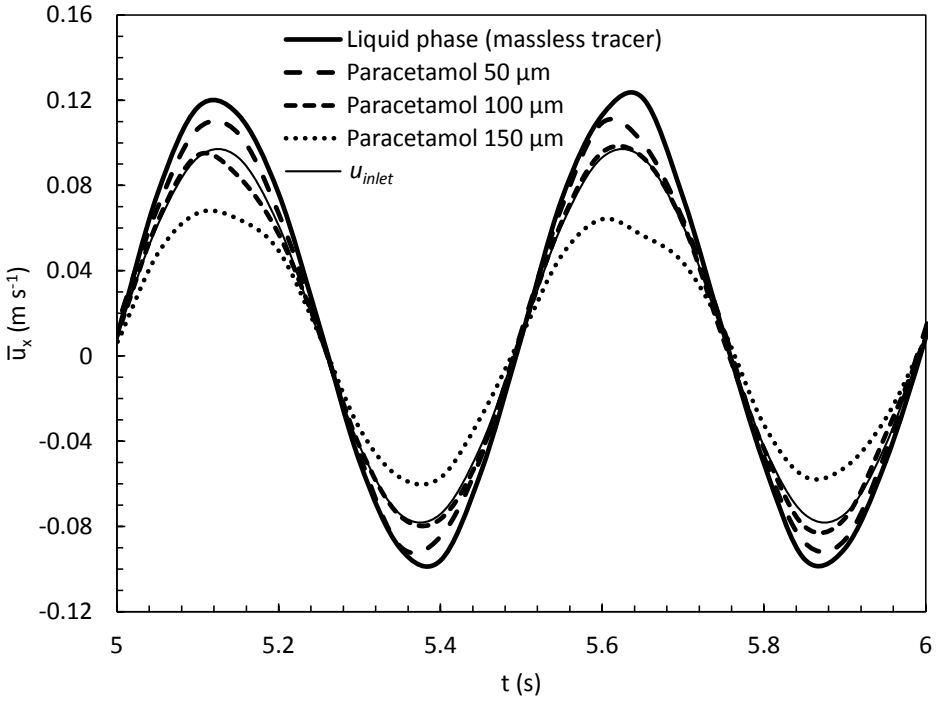

Figure 7.10. *Axial velocity of particles of different sizes for a certain time range (Q = 100 ml min^{-1}, f = 2Hz, x_o = 7mm)*

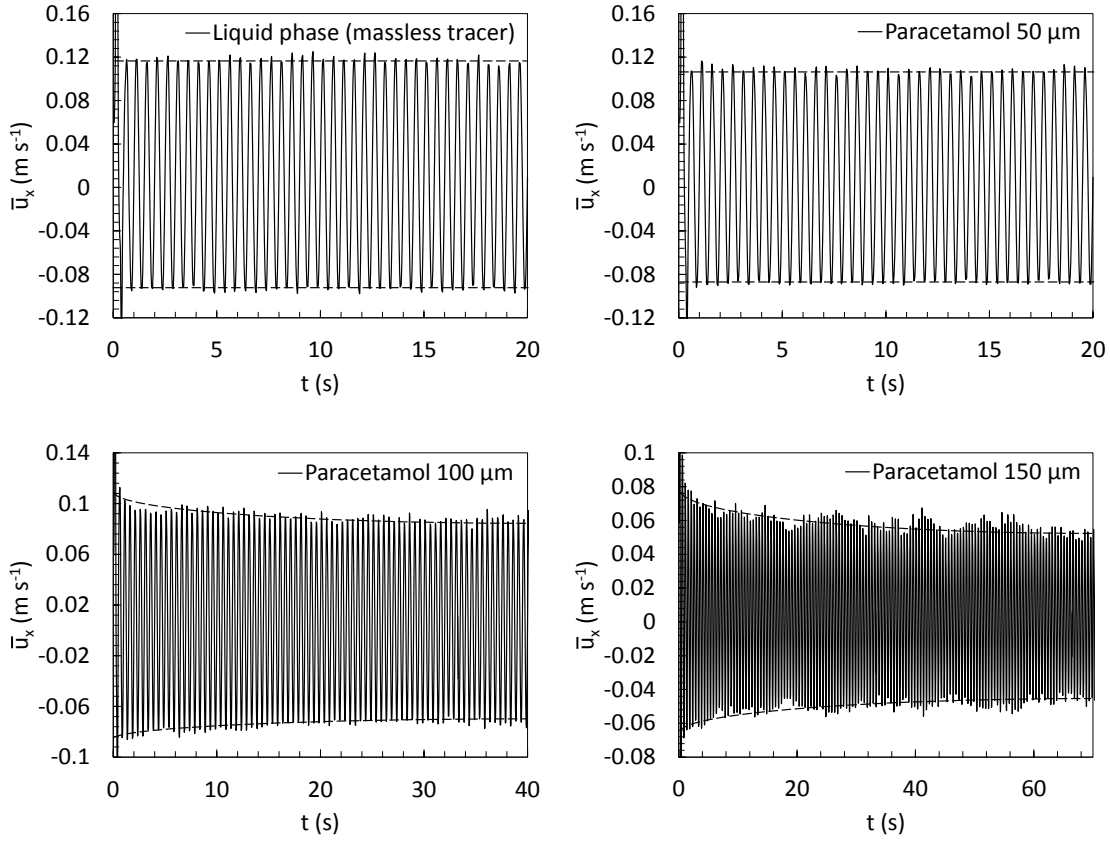

Figure 7.11. *Axial velocity evolution with time for particles of different sizes (Q = 100 ml min^{-1}, f = 2Hz, x_o = 7mm)*

The dampening effect of oscillatory velocity, occurring as either particles grow in size or particles of a certain size (100 and 150) move along the reactor, should not be confused with an overall decay in the net axial velocity. While particles of different sizes may experience different oscillatory velocity peaks, their net axial velocities can be identical. Similarly, particles may experience a decrease in oscillatory axial velocity with time, yet maintain a net axial velocity. For this reason, the evolution of the net axial velocity with time is also analysed, but displaying the evolution of $\bar{u}_x$ with time for different particle sizes in the same figure is too complex, as the oscillatory velocity peaks from different profiles overlap, preventing the ability to distinguish one from another. To avoid this, the axial velocities and velocity magnitudes obtained from Equation (7.19) – and its analogous for velocity magnitude – were averaged for each oscillatory cycle and plotted with time in Figure 7.12. It shows that the liquid phase and small solid particles (50 μm) experience a rather constant trend of net velocity in the axial direction with time, the former fluctuating at around the expected *QL/V* value. On the contrary, paracetamol solids of 100 and 150 μm diameter have an overall lower net axial velocity, which moderately decays with time. The kinetic energy losses experienced by particles of 100 and 150 μm as they move downstream, whether it is by the dampening of oscillatory velocity or by the reduction of net axial velocity, have a visible impact on the overall velocity magnitude that particles are subjected to, see Figure 7.12 (right). These findings highlight a potential need of adjusting oscillation conditions, e.g. increasing oscillation amplitude in order to prevent solids settling, depending on the size and terminal velocities of the solids involved. The percentages of the reduction in the net axial velocity, $\Delta\bar{u}_x$, undergone by solid particles of difference size are gathered in Table 7.4, along with the percentage reduction in the mean velocity magnitude, $\Delta\bar{u}_m$; all of which in comparison to the velocity of the liquid phase.

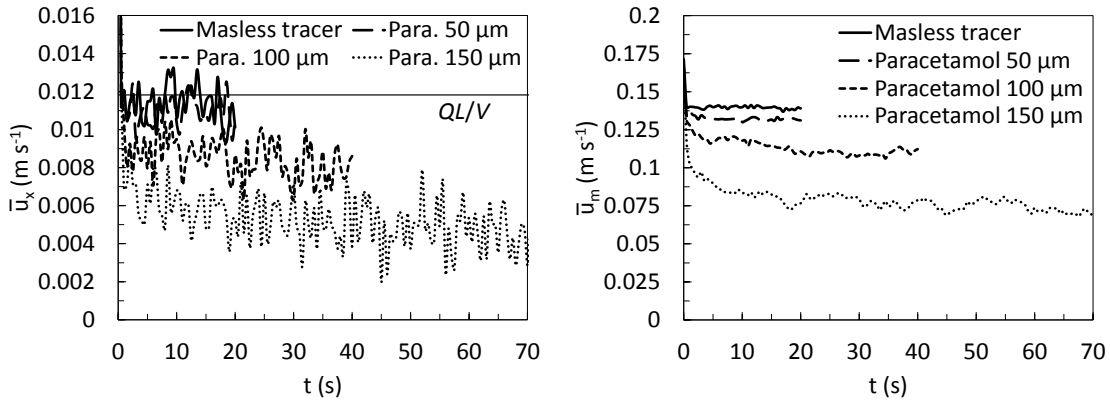

Figure 7.12. *Average (per cycle) axial velocity (left) and velocity magnitude (right) evolution with time for particles of different sizes (Q = 100 ml min^{-1}, f = 2Hz, x_o = 7mm)*

The minimum transport velocity required for the suspension of slurry in a horizontal tube (u_{min-h}) is given by the modified Durand equation [163, 164]:

$$u_{min-h} = C_{mh}\left[2g\left(\frac{\rho_p}{\rho}-1\right)D\right]\left(\frac{d_p}{D}\right)^{1/6} \tag{7.20}$$

where D is the diameter of the tube, d_p the diameter of the particle and C_{mh} an empirical constant that ranges from 0.4 to 1.5 [163]. A C_{mh} of 1.5 utilised in recent literature [164] was used in the present study. Table 7.4 shows the u_{min-h} required by each set of simulated solid particles, along with the percentage of the time that the oscillatory axial velocity at the inlet and in the tube are higher than the minimum transport velocity, i.e. $\left|\bar{u}_{x-inlet}(t)\right| > u_{min-h}$ and $\left|\bar{u}_{x-ELP}(t)\right| > u_{min-h}$.

Table 7.4. *Percentage of oscillatory dampening and minimum transport velocity for paracetamol solids of different sizes (Q = 100ml min^{-1}, f = 2Hz, x_o = 7mm)*

	$\Delta\bar{u}_{x-peaks}$ † (%)	$\Delta\bar{u}_x$ † (%)	$\Delta\bar{u}_m$ † (%)	u_{min-h} (m s^{-1})	$\left\|\bar{u}_{x-inlet}(t)\right\| > u_{min-h}$ (%)	$\left\|\bar{u}_{x-ELP}(t)\right\| > u_{min-h}$ (%)
Paracetamol 50 µm	-10	-4	-5	0.045	65.3	72.8
Paracetamol 100 µm	-21	-26	-21	0.051	60.4	68.8
Paracetamol 150 µm	-45	-54	-46	0.054	57.1	67.2

† *With respect to the values provided by the liquid phase (massless tracer)*

The minimum transport velocity required for slurry suspension in a horizontal tube increases by 20% as particles grow from 50 μm to 150 μm of diameter. The inlet oscillatory velocity is greater in magnitude than $u_{min\text{-}h}$ more than 50% of time for all simulated particles; hence, it is expected for all particles to stay suspended throughout their journey downstream the reactor. However, the results also point to a reduction in the degree of suspension as particles grow in size.

7.6.3 Effect of Particle Size on their Suspension

Suspension of particles was qualitative assessed by visually observing their position as they travel downstream the reactor; this is displayed in Figures 7.13 to 7.16. The first sign of a reduction in the degree of suspension is given by the distribution of particles displayed after the first oscillatory cycle, t = 0.5 s. At this time, massless particles display a perfectly symmetrical distribution; this symmetry gets however disrupted as particles increase in size, with subtle changes observed in particles of 50 μm diameter to very noticeable and drastic changes in particles of 100 and 150 μm diameter, respectively. As time passes, the effect of the axial dispersion becomes evident for all simulated runs and particles are spread throughout the length of the device. It is however detected how solid particles of larger size (100 and 150 μm diameter) present a higher concentration of particles towards the bottom wall of the reactor, i.e. particles seem to gather around the bottom area, this becomes especially acute for particles of 150 μm diameter.

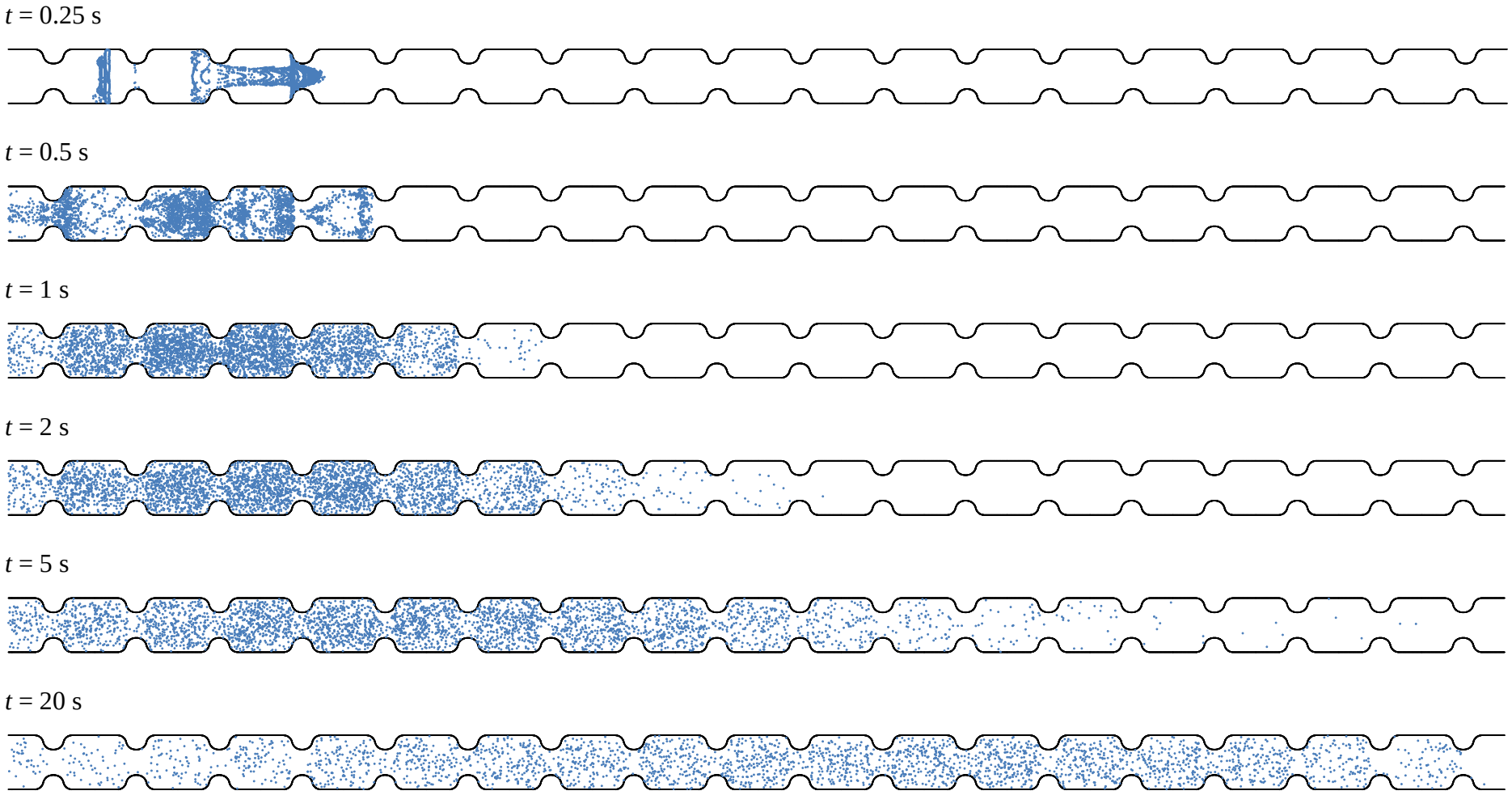

Figure 7.13. *Position of massless particles (tracer) at different times (Q = 100 ml min^{-1}, f = 2Hz, x_o = 7mm)*

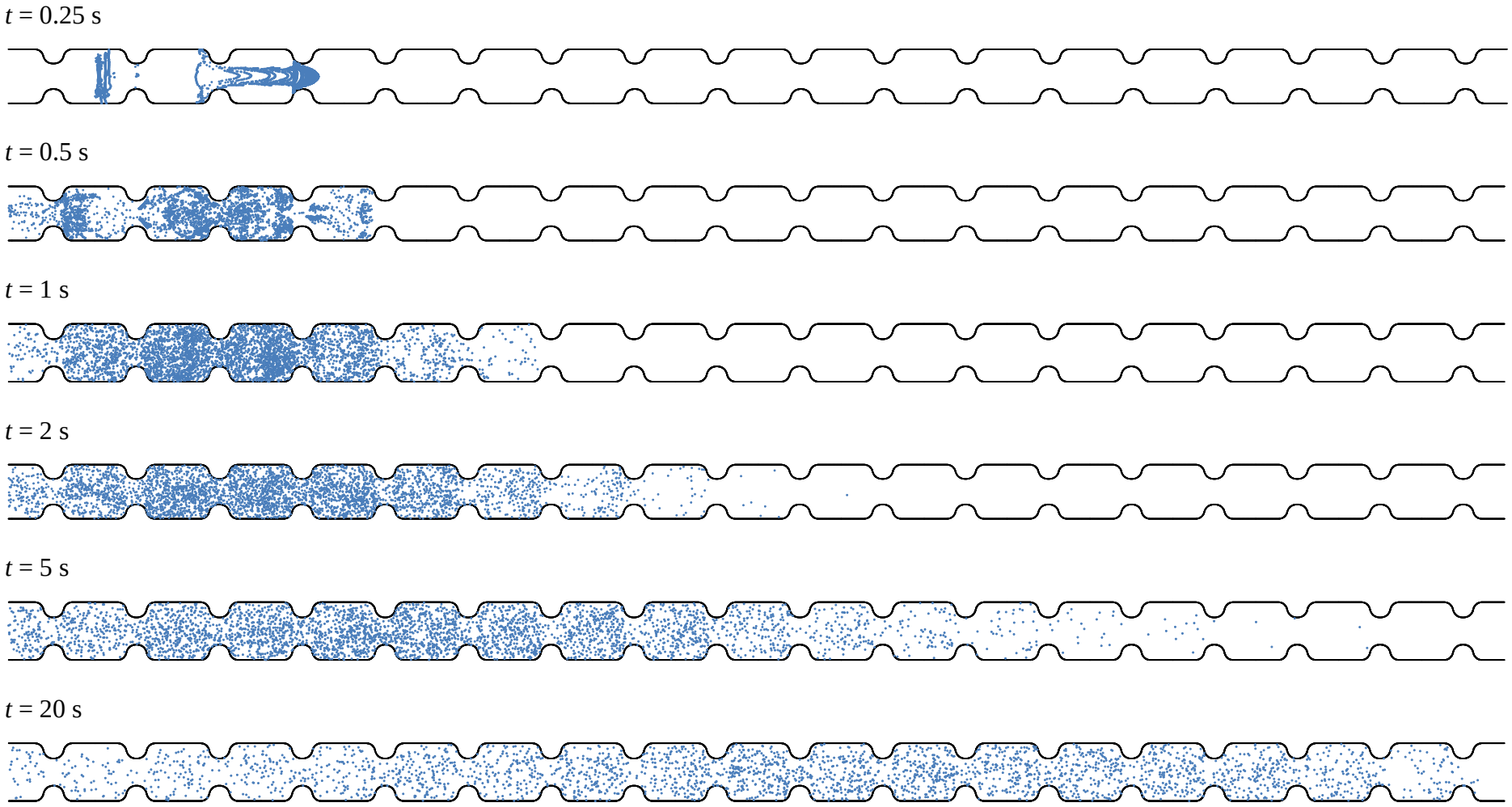

Figure 7.14. *Position of paracetamol particles (D_p = 50 μm) at different times (Q = 100 ml min^{-1}, f = 2Hz, x_o = 7mm)*

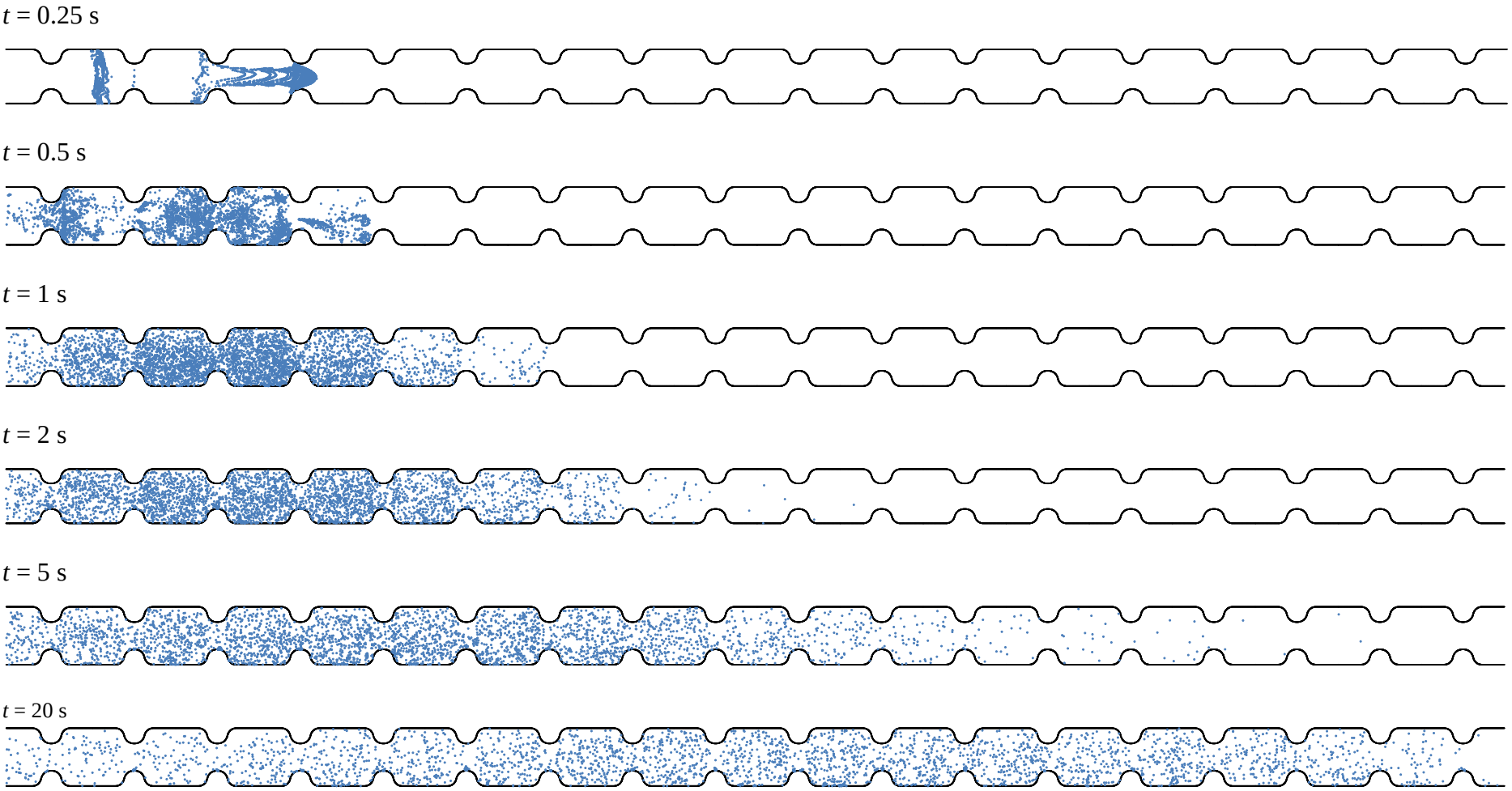

Figure 7.15. *Position of paracetamol particles (D_p = 100 μm) at different times (Q = 100 ml min^{-1}, f = 2Hz, x_o = 7mm)*

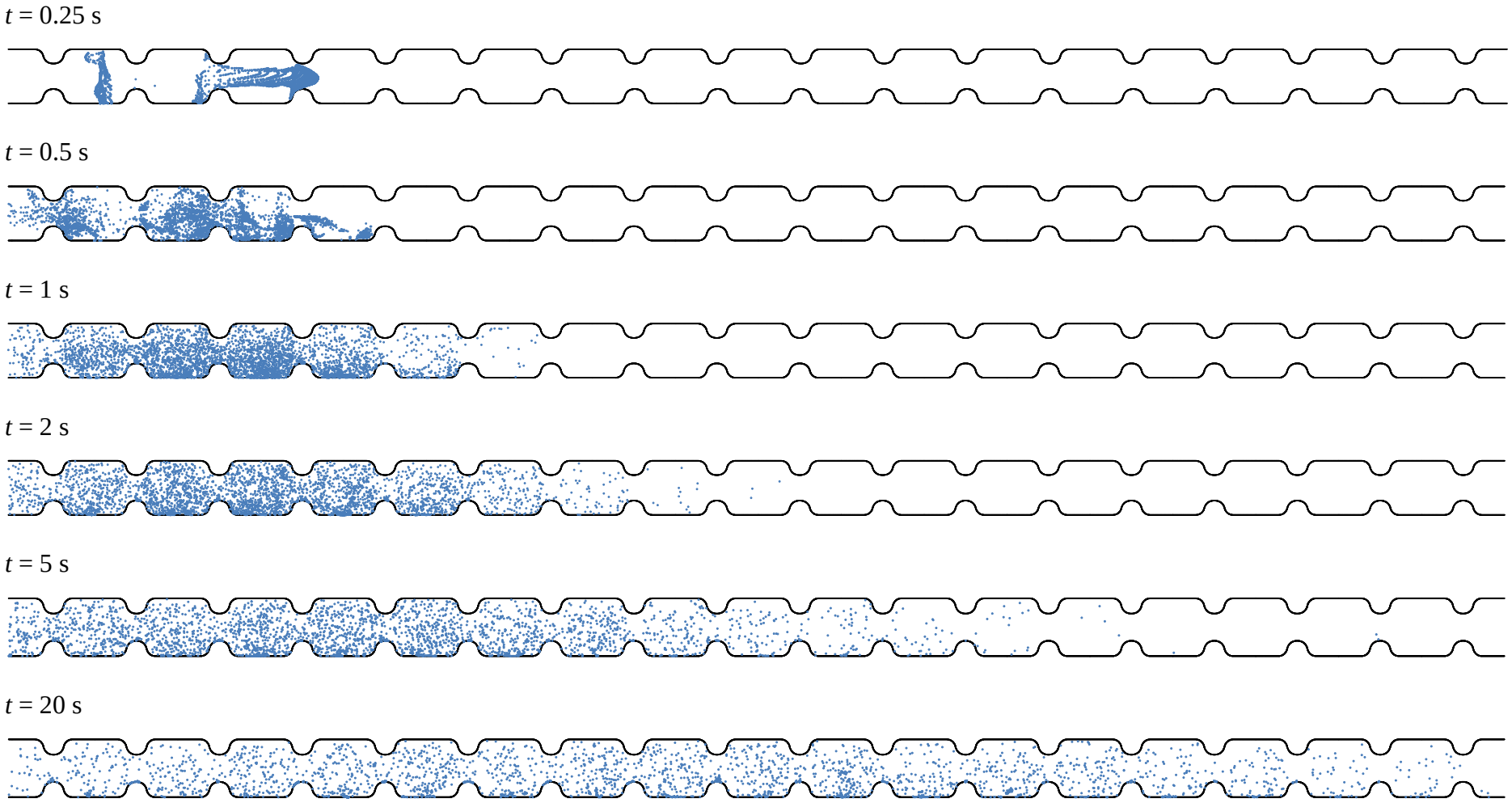

Figure 7.16. *Position of paracetamol particles (D_p = 150 μm) at different times (Q = 100 ml min^{-1}, f = 2Hz, x_o = 7mm)*

Quantitatively, the suspension of particles was analysed by monitoring their positions in the vertical axis, *y*, throughout all simulated time-steps and averaging it over the total number of particles present in the entirety of the system, *N*, for each condition as:

$$\bar{y}(t) = \frac{\sum_{i=1}^{N(t)} y_i(t)}{N(t)} \tag{7.21}$$

As expected, Figure 7.17 shows that the average vertical position, $\bar{y}$, decreases as particle size increases. While the average position of liquid phase particles and small solid particles (50 µm) stays at the centre of the device (y = 0), particles of 100 and 150 µm lose their height and tended to stay closer to the bottom wall of the reactor (y = -7.5 mm) as they move axially downstream. However, complete settlement of particles was not observed even for the largest particles considered in this study. The reduction in the degree of suspension experienced by solid particles is due to the effect of the gravitational force; particles of bigger size contain more mass, m_p, which increases their downwards acceleration as a result of their weight, thus decreasing their suspension altitude with respect to the horizontal plane.

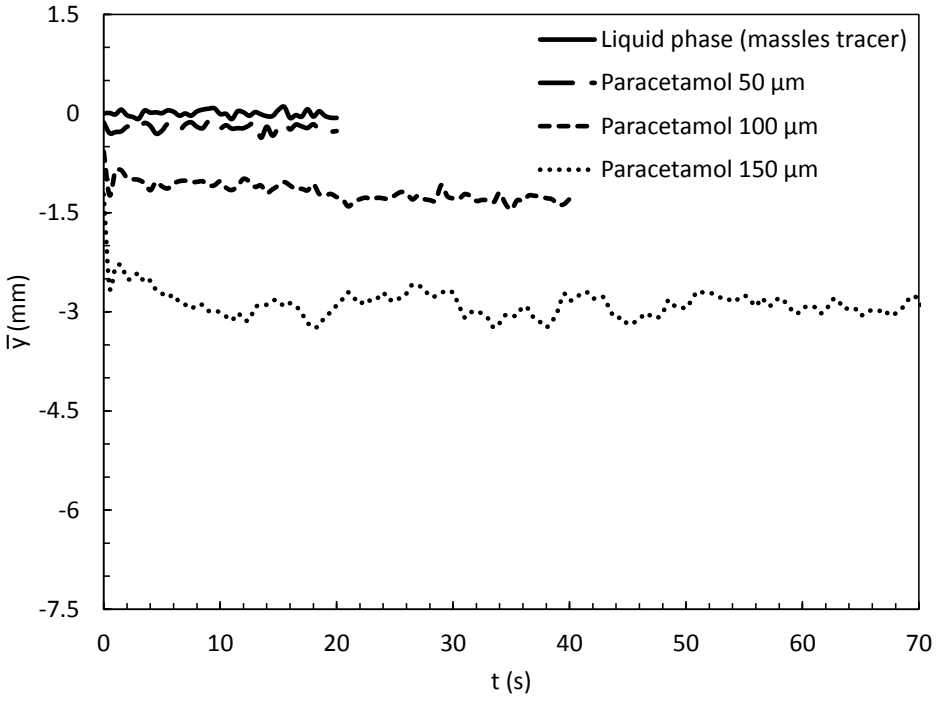

Figure 7.17. *Position in the y-axis evolution with time for particles of different sizes (Q = 100 ml min^{-1}, f = 2Hz, x_o = 7mm)*

In view of the current findings, the fraction of the number of particles present at the top, middle and bottom regions of the devices, x_1, x_2 and x_3, respectively, was monitored. Figure 7.18 displays a sketch describing the dimensions of these regions in the DN15. The fraction of particles is then monitored and plotted with time in Figure 7.19. For the liquid phase (massless tracer), around 45% of the particles stay consistently in the middle region, while the rest stay in the top (27.5%) and bottom (27.5%) of the device. While all particles, massless and solid, start off with the same distribution along a cross-sectional plane, they re-arrange themselves as they move downstream according to the drag and gravitational forces they experience, which are heavily influenced by the sizes of particles. Small particles (50 μm diameter) show a minute reduction in the number of particles present in the middle and top regions, 43% and 26% respectively, and a slight increment in those gathered at the bottom (31%). As particles increase in size, these patterns become more noticeable, e.g. approximately, 35% of 100 μm diameter particles stay in the middle region, only 19% in the top and up to 46% in the bottom region. This behaviour is highly exacerbated for particles of 150 μm, whose fractions of particles present in the middle and top regions are reduced down to 24% and 11%, respectively, and up to 65% of the particles gather down the bottom of the device. While complete settlement of particles was not observed, there is a clear potential for this phenomenon to fulfil when a certain particle size has been reached. This should be accounted for in experimental and industrial processes by adjusting the intensity of the oscillatory velocity according to the target particle size, in order to maintain solids suspended and avoid settling.

For convenience, the asymptotic values of the fraction of particles presented in each region are gathered in Table 7.5.

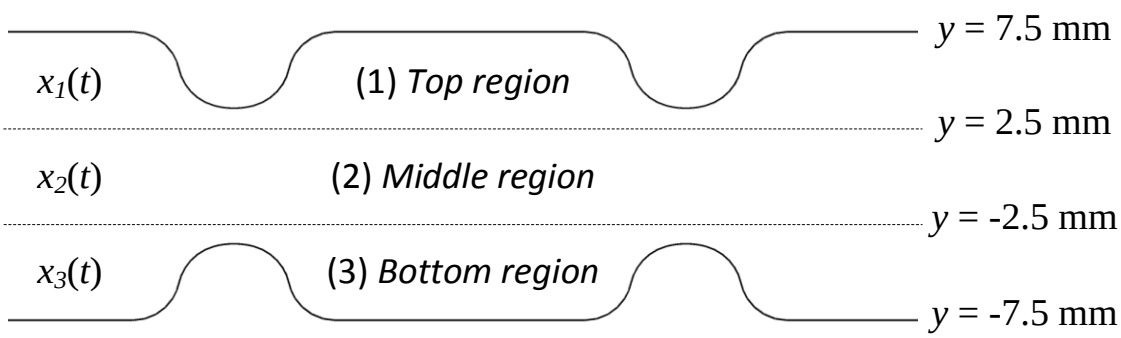

Figure 7.18. *Definition of the top, middle and bottom region for the monitoring of fraction of particles present in the system*

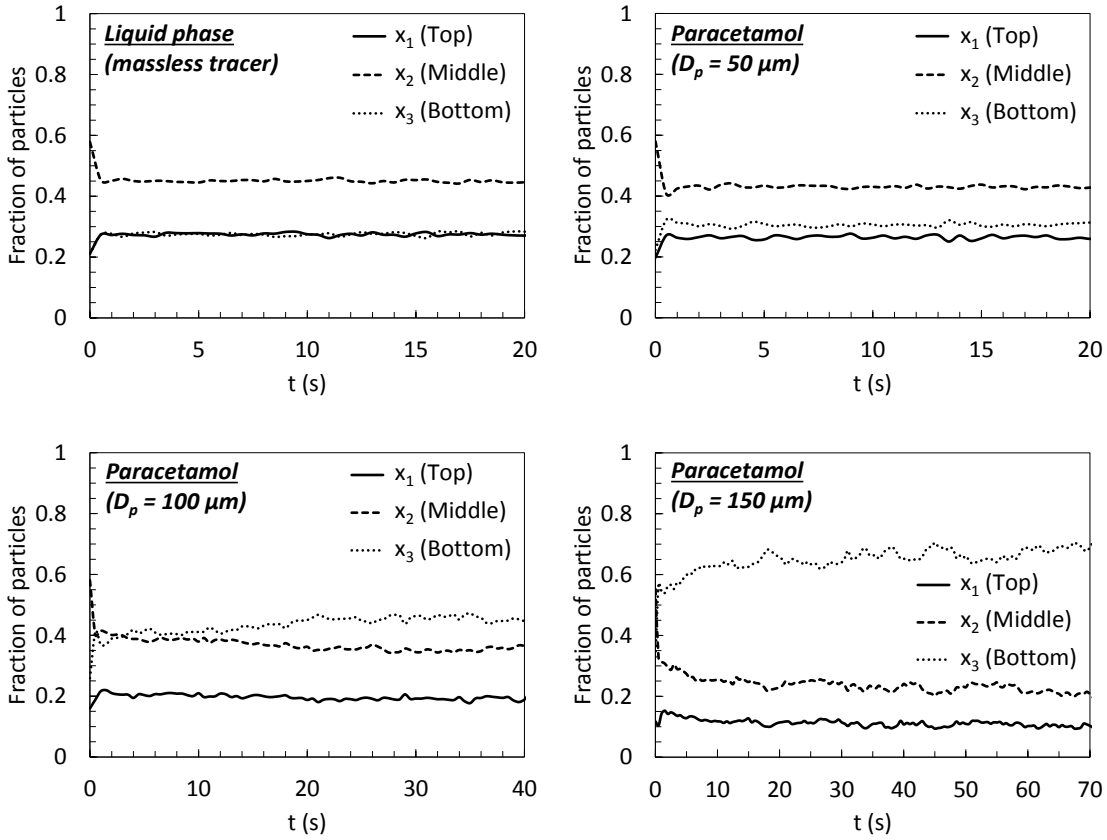

Figure 7.19. *Fraction of particles present at different regions of the DN15 as a function of time (Q = 100 ml min^{-1}, f = 2Hz, x_o = 7mm)*

Table 7.5. *Asymptotic values for the fraction of particles present at different regions of the DN15 (Q = 100ml min^{-1}, f = 2Hz, x_o = 7mm)*

	x_1 (%)	x_2 (%)	x_3 (%)
Tracer (massless)	27.5	45	27.5
Paracetamol 50 µm	26	43	31
Paracetamol 100 µm	19	35	46
Paracetamol 150 µm	11	24	65

7.7 Conclusions

For the first time, a primary Eulerian liquid phase was coupled with a secondary discrete Lagrangian phase in the modelling of solid-liquid fluid flow in a continuous oscillatory baffled reactor; ANSYS® Fluent's Discrete Phase Model is proved as a viable methodology for this purpose. This work, for the first time, reports a detailed analysis on the effect of particle size on axial dispersion, evaluates residence times and velocities experienced by solid particles in a COBR, as well as their impact on solid

suspension. Results show a decreasing trend in oscillatory axial velocity as particle size increases, leading to smaller axial dispersion and longer residence times. These findings agree with the work by Ejim et al. and Kacker et al. [46, 47]. This work has also provided qualitative and quantitative analysis between particle size and the oscillation dampening effect experienced by solids.

On the determination of axial dispersion of secondary phase, two methodologies were utilised in this study: the perfect pulse method (PPM) and the imperfect pulse method (IMP). The latter provided constant results at different lengths of the device for all the simulated cases, while the former did not. This is most certainly due to the formulation of the IPM that avoids the assumption of a perfect pulse injection of the secondary phase; IPM calculates axial dispersion through a convolution integral equation to minimize a target function, utilising data from two RTD profiles measured at two points along the length of the reactor. By doing so, it also allows the IMP to give a better estimation of the mean net velocity of the secondary phase travelling from one measuring point to another, unlike the PPM, which assumes a constant velocity of QL/V.

While this work involves mono-size spherical particles simulated at smaller oscillatory amplitudes than those commonly used in crystallisation processes, the understanding of dispersion of a solid phase in liquid is much needed in order to fill the knowledge gap in the area of COBR research and development, where there has been exclusive reliance on correlations obtained from single phase studies.

Chapter 8 Smoothed Particle Hydrodynamics - A New Approach for Modelling Flow in OBRs

8.1 Introduction

As aforementioned, uniform mixing and linear scale up offered by Oscillatory Baffled Reactors (OBR) are the key drivers for research and industrial applications in reactions [18, 165-168] and crystallisation [2, 6, 10, 11, 148, 169-173]. From a modelling viewpoint, Computational Fluid Dynamic (CFD) solvers have been employed to simulate hydrodynamic flow profiles in OBR from initially 2-dimensional in the 1990s [28, 48-53] to 3-D in the following decades [36, 40, 54-64], however the majority of the numerical modelling work was Eulerian based [43, 44] mostly for single phase. The validation of these numerical models with experimental data has mostly been limited to qualitative comparison of eddy formation patterns. There were few modelling work involving two phases, e.g. massless tracer and liquid [65], which is largely limited by the expensive computational costs of coupling continuous Eulerian-Lagrangian phases for dynamic fluid-solids modelling and their complex interactions. Coupling CFD with the Population Balance Equation (PBE) to model crystallisation processes in stirred tank crystallisers is a well-documented example [137]. The question remains if the complexity of these coupled methodologies can be avoided and if all phases can be modelled using a Lagrangian scheme; the Smoothed-Particle Hydrodynamics (SPH) is thus the one considered in the current study. The SPH methodology provides historical information of individual fluid packets or particles in the domain of interest by tracking these particles; this implicit SPH capability opens up opportunities for better understanding of flow rheology behaviour. This is of special interest in complex processes where L-L and S-L interactions play a key role, such as the chemical processes commonly undertaken in OBRs, e.g. crystallisation. This can greatly improve the accuracy in the prediction of mixing, since historical information of particles allows for alternative ways to quantify mixing, as opposed to residence time distributions and axial dispersion assessments traditionally used in OBRs. The quantification of mixing efficiency in OBRs is of great interest and has been a hot topic of research since the 1990s in both experimental [29-31, 33, 37-39, 42, 123] and numerical studies [28, 36, 40, 43-45, 109], since both uniform mixing and heat transfer control in OBRs are the essential elements for achieving consistent product properties in these undertaken processes, e.g. narrow crystal size distribution, constant polymorph. In addition, SPH

allows for the implementation of new physics based on particle-particle interaction, which has great potential for modelling solids formation and growth in crystallisation processes.

SPH was first developed in 1977 by Gingold and Monaghan [174] for astrophysical applications where no restrictions or boundaries are imposed by a numerical mesh, such as galaxy formation. The application of SPH into fluid flow problems was proposed by Monaghan in the early 1990s [175]. In SPH methodology, a continuous fluid domain is defined as a set of discrete Lagrangian particles and its continuum properties are approximated by local quantities that are smoothed with a mathematical kernel. This methodology, despite being less popular than traditional standard CFD approaches, is well documented [176, 177], and has augmented vast research attention in recent years in solving complex fluid flow problems [178-183] in micro and macro-scales. To the authors' knowledge there has been no reported work on the application of SPH for modelling fluid flows in tubular baffled reactors. The aims of this work are to explore and investigate the feasibility of SPH in OBR by developing a bespoke solver; to compare flow characteristics of single phase flow predicted by SPH with those obtained with an Eulerian based model, e.g. Finite Volume (FV), via a commercial software package (ANSYS® Fluent 15) and to provide quantitative assessment of mixing efficiency using the proposed methodology. This chapter has been published in the Journal of Computers & Chemical Engineering, Vol. 124, 2019, pages 14-27 [68].

8.2 Geometry & Operating Conditions

The target device of this study is a simplified two-dimensional version of the NiTech DN15 COBR reactor described in Section 3.1. The schematic and geometry of the oscillatory baffled reactor modelled in this study are presented in Figure 8.1 and Table 8.1.

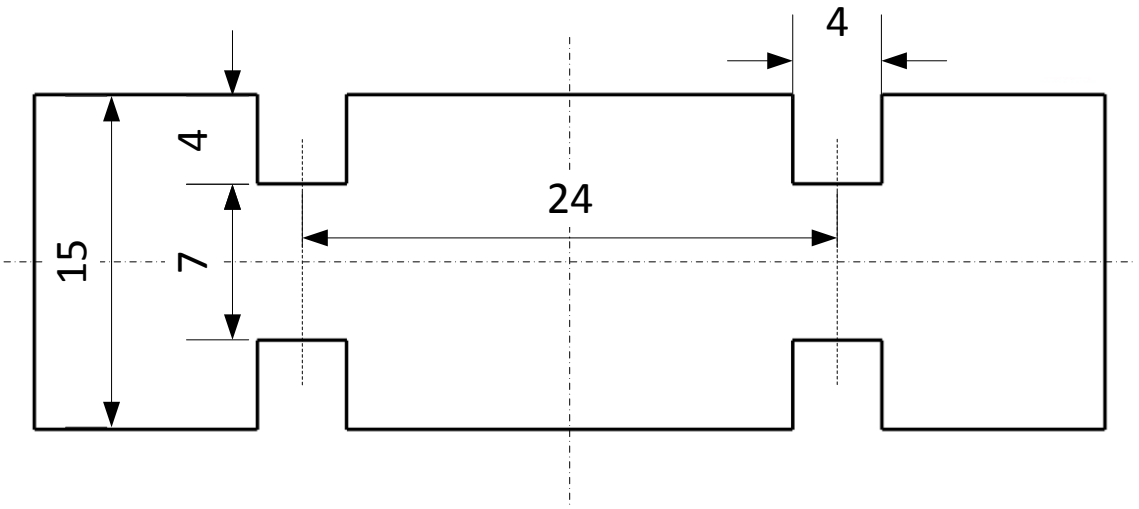

Figure 8.1. *Schematic of the modelled OBR; all dimensions are in mm* [68]

Table 8.1. *Geometry dimensions of the OBR*

D (mm)	15
D_b (mm)	7
L_b (mm)	24
L (mm)	48
Baffled cells in reactor (#)	2

Water (ρ = 998.2 kg m^{-3}, μ = 1.003·10^{-3} kg m^{-1} s^{-1}) is used as the working fluid with oscillatory conditions of x_o = 5 mm and f = 1 Hz (Re_o = 471 and St = 0.239); these conditions are chosen to avoid interactions among eddies generated during the forward and backward strokes so that symmetrical flow patterns are expected.

8.3 Numerical Formulation

The simulated system comprises a 2-dimensional domain and it is assumed iso-thermal. Navier-Stokes equations for mass and momentum conservation are solved as per Equations (3.1) and (3.2), which are discretised and solved separated using SPH and FV in their respective solvers. Note that the governing equations have been solved in a 2-dimensional form, neither for FV nor SPH were these solved axi-symmetrically.

8.3.1 Smoothed-Particle Hydrodynamic

SPH discretises the fluid domain using a fixed number of infinitesimal particles that are tracked individually. Assuming that the system is fully flooded with a single-phase

fluid, no external forces are considered; hence Equations (3.1) and (3.2) can be written in their Lagrangian form as:

$$\frac{D\rho}{Dt} = -\rho \nabla \cdot \vec{u} \tag{8.1}$$

$$\frac{D\vec{u}}{Dt} = -\frac{1}{\rho}\nabla p + \frac{1}{\rho}\nabla \cdot \underline{\underline{\tau}} \tag{8.2}$$

and the position of each infinitesimal particle $\vec{r}$ is governed by:

$$\frac{d\vec{r}}{dt} = \vec{u} \tag{8.3}$$

This system of equations is closed using the relationship between density and pressure. Here, the fluid domain is treated as weakly compressible, for which this relationship is given by the Equation-Of-State (EOS) [175]. The most common EOS was proposed by Batchelor [184], the so-called *Tait's* equation:

$$p = B\left[\left(\frac{\rho}{\rho_0}\right)^{\gamma} - 1\right] \tag{8.4}$$

where γ usually takes a value of 7 for water, ρ_0 is the reference density of the fluid at atmospheric pressure and the constant B is defined as $B = \frac{\rho_0 c_0^{\,2}}{\gamma}$; c_0 is the reference speed of sound. The use of *Tait's* equation as EOS highly reduces computational time, as oppose to solving the Poisson's equation for incompressible flows [185]. The compressibility of the fluid in the SPH's weakly compressible approach is controlled by c_o, which also determines the size of the time-step based on the Courant–Friedrichs–Lewy condition [141], refer to Equation (8.30). High values of speed of sound result in both incompressible behaviour and very small time-steps. However, Monaghan [186] demonstrated that c_0 values of ten to a hundred times the maximum velocity in the system, corresponding to a Mach number of less than 0.1, replicate incompressible flow with density fluctuations within 1%. A value of c_0 = 10 m s^{-1} was then chosen for the simulations performed in this study.

8.3.1.1 Discretisation

SPH treats a continuous medium as a discrete set of particles. At time zero, particles are uniformly distributed and are equidistantly spaced from each other, i.e. a distance Δx in all directions. Hence, all particles have an initial volume of Δx^n where n is the dimensions of the domain. The discretisation of Equations (3.1) and (3.2) is derived from the Dirac distribution δ. Thus, the value of a function at a certain time and space of the domain can be written as:

$$f(\vec{r},t) = \int_{\Omega} f(\vec{r}',t)\,\delta(\vec{r}-\vec{r}')\,d^n\vec{r}' \tag{8.5}$$

where Ω denotes the domain, f is a function of position vectors $\vec{r}$ and $\vec{r}'$ – the former refers to the particle of interestes and the latter to each of its neighouring particles – and the Dirac distribution takes a value of 1 and 0 when $\vec{r} = \vec{r}'$ and $\vec{r} \neq \vec{r}'$, respectively. The use of a kernel, W, to approximate the Dirac delta function results in:

$$f(\vec{r},t) \approx \int_{\Omega_r} f(\vec{r}',t)\,W(\vec{r}-\vec{r}',h)\,d^n\vec{r}' \tag{8.6}$$

where h is the smoothing length of the chosen kernel function and is defined as $h = \eta\,\Delta x$; η typically takes a value of 1.2 – 1.3, the latter is chosen for this work, and $\Omega_{\mathbf{r}}$ denotes the $\vec{r}$ point-centred continuous domain. For the $W(\vec{r}-\vec{r}',h)$ function to be considered a kernel function, it must satisfy the following set of conditions [176, 177]:

- The *Delta function property* that the kernel function must exhibit when smoothing length approaches zero:

$$\lim_{h\to 0} W(\vec{r}'-\vec{r},h) = \delta(\vec{r}-\vec{r}') \tag{8.7}$$

- The *compact condition*, which defines the area under which the kernel function operates:

$$W(\vec{r}-\vec{r}',h) = 0 \qquad \text{when } |\vec{r}-\vec{r}'| > \kappa h \tag{8.8}$$

  where κ is a smoothing length related constant, and κh defines the effective area of the kernel function, this area is commonly referred to as support domain (see Figure 8.2).

- The *normalisation condition*, also known as *unity condition*, since the integration of the kernel function should be equal to one:

$$\int_{\Omega} W\left(\vec{r}-\vec{r}',h\right)d^{n}\vec{r}'=1 \tag{8.9}$$

- The *symmetry condition*, as $W\left(\vec{r}-\vec{r}',h\right)$ must be an even function:

$$W\left(\vec{r}-\vec{r}',h\right)=W\left(\vec{r}'-\vec{r},h\right) \tag{8.10}$$

- Hence, the kernel gradient must be an odd function:

$$\nabla W\left(\vec{r}-\vec{r}',h\right)=-\nabla W\left(\vec{r}'-\vec{r},h\right) \tag{8.11}$$

- This yields to:

$$\int_{\Omega} \nabla W\left(\vec{r}-\vec{r}',h\right)d^{n}\vec{r}'=0 \tag{8.12}$$

Equation (8.6), which denotes the function of an arbitrary point or particle, *i*, can then be re-written using the integral or summation of contributions from its neighbouring particles, *j*. The contribution of each neighbouring particle is weighted by the use of the kernel function, based on the distance between particles *i* and *j*:

$$f\left(\vec{r}_i,t\right)\approx\sum_{j=1}^{N} f\left(\vec{r}_j,t\right)W\left(\vec{r}_i-\vec{r}_j,h\right)\Delta\vec{r}_j^{\,n} \tag{8.13}$$

where *N* is the number of neighbouring particles within the kernel domain and $d^{n}\vec{r}_j$ is the infinitesimal volume of *j*, which can be notated as $\Delta\vec{r}_j$ and is described by the relationship:

$$m_j=\Delta\vec{r}_j\rho_j \tag{8.14}$$

Equation (8.13) hence overtakes the form of:

$$f\left(\vec{r}_i,t\right)\approx\sum_{j=1}^{N}\frac{m_j}{\rho_j} f\left(\vec{r}_j,t\right)W\left(\vec{r}_i-\vec{r}_j,h\right) \tag{8.15}$$

From this point onwards, for simplicity purposes $W\left(\vec{r}_i-\vec{r}_j,h\right)$ will be denoted as W_{ij} and $\left(\vec{r}_i-\vec{r}_j\right)$ as $\vec{r}_{ij}$. Following the same argument that led to Equation (8.15), mathematical expressions for a function's spatial derivative, i.e. gradient, and divergence are given by Equations (8.16) and (8.17), respectively:

$$\nabla f\left(\vec{r}_i,t\right)\approx\sum_{j=1}^{N}\frac{m_j}{\rho_j}f\left(\vec{r}_j,t\right)\nabla_i W_{ij} \tag{8.16}$$

$$\nabla\cdot f\left(\vec{r}_i,t\right)\approx\sum_{j=1}^{N}\frac{m_j}{\rho_j}f\left(\vec{r}_j,t\right)\cdot\nabla_i W_{ij} \tag{8.17}$$

The derivation of Equations (8.16) and (8.17) is further explained in Appendix 4. As in finite-difference methods, the gradients in Equation (8.16) and (8.17) can be written in several ways in SPH formalism. Among them are symmetric and anti-symmetric ones, more details of which can be found in the work by Liu and Liu [177] and Violeau [176]. In the same way, several SPH forms for the divergence field can be established. The two most commonly used forms for the gradient and divergence of a function were proposed by Monaghan (1992) [175], who suggested to include the scalar density, ρ, within the gradient operator as:

$$\nabla f=\frac{1}{\rho}\left[\nabla\left(\rho f\right)-f\nabla\rho\right] \tag{8.18}$$

or

$$\nabla f=\rho\left[\nabla\left(\frac{f}{\rho}\right)+\frac{f}{\rho^2}\nabla\rho\right] \tag{8.19}$$

Equation (8.18) can be re-written as:

$$\begin{aligned}\nabla f_i&=\frac{1}{\rho_i}\left[\nabla\left(\rho_i f_i\right)-f_i\nabla\rho_i\right]\\&\doteq\frac{1}{\rho_i}\int_\Omega\nabla\left(\rho_j f_j\right)W\left(\vec{r}_i-\vec{r}_j,h\right)d^n\vec{r}_j-\frac{f_i}{\rho_i}\int_\Omega\left(\nabla\rho_j\right)W\left(\vec{r}_i-\vec{r}_j,h\right)d^n\vec{r}_j\\&\doteq\frac{1}{\rho_i}\sum_{j=1}^{N}\frac{m_j}{\rho_j}\left(\rho_j f_j\right)\nabla W\left(\vec{r}_i-\vec{r}_j,h\right)-\frac{f_i}{\rho_i}\sum_{j=1}^{N}\frac{m_j}{\rho_j}\rho_j\nabla W\left(\vec{r}_i-\vec{r}_j,h\right)\\&\doteq\frac{1}{\rho_i}\sum_{j=1}^{N}m_j f_j\nabla_i W_{ij}-\frac{1}{\rho_i}\sum_{j=1}^{N}m_j f_i\nabla_i W_{ij}\end{aligned}$$

where $f_i = f\left(\vec{r}_i, t\right)$. This expansion of Equation (8.18) results in Equation (8.20a); in a similar way, the particle approximation for the divergence of a function is given by Equation (8.20b):

$$\nabla f\left(\vec{r}_i, t\right) \approx -\frac{1}{\rho_i} \sum_{j=1}^{N} m_j f\left(\vec{r}_{ij}, t\right) \nabla_i W_{ij} \tag{8.20a}$$

$$\nabla \cdot f\left(\vec{r}_i, t\right) \approx -\frac{1}{\rho_i} \sum_{j=1}^{N} m_j f\left(\vec{r}_{ij}, t\right) \cdot \nabla_i W_{ij} \tag{8.20b}$$

Following the same logic, Equation (8.19) can be re-written as:

$$\begin{aligned}
\nabla f_i &= \rho \left[\nabla\left(\frac{f_i}{\rho_i}\right) + \frac{f_i}{\rho_i^{\,2}} \nabla \rho_i \right] \\
&\doteq \rho_i \int_\Omega \nabla\left(\frac{f_j}{\rho_j}\right) W\left(\vec{r}_i - \vec{r}_j, h\right) d^n \vec{r}_j + \rho_i \frac{f_i}{\rho_i^{\,2}} \int_\Omega \left(\nabla \rho_j\right) W\left(\vec{r}_i - \vec{r}_j, h\right) d^n \vec{r}_j \\
&\doteq \rho_i \sum_{j=1}^{N} \frac{m_j}{\rho_j} \left(\frac{f_j}{\rho_j}\right) \nabla W\left(\vec{r}_i - \vec{r}_j, h\right) + \rho_i \frac{f_i}{\rho_i^{\,2}} \sum_{j=1}^{N} \frac{m_j}{\rho_j} \rho_j \nabla W\left(\vec{r}_i - \vec{r}_j, h\right) \\
&\doteq \rho_i \left(\sum_{j=1}^{N} \frac{m_j}{\rho_j^{\,2}} f_j \nabla_i W_{ij} + \frac{f_i}{\rho_i^{\,2}} \sum_{j=1}^{N} m_j \nabla_i W_{ij} \right)
\end{aligned}$$

Hence, Equation (8.19) yields Equation (8.21a). Analogously, Equation (8.21b) gives the particle approximation for the divergence of a function:

$$\nabla f\left(\vec{r}_i, t\right) \approx \rho_i \sum_{j=1}^{N} m_j \left(\frac{f\left(\vec{r}_i, t\right)}{\rho_i^{\,2}} + \frac{f\left(\vec{r}_j, t\right)}{\rho_j^{\,2}} \right) \nabla_i W_{ij} \tag{8.21a}$$

$$\nabla \cdot f\left(\vec{r}_i, t\right) \approx \rho_i \sum_{j=1}^{N} m_j \left(\frac{f\left(\vec{r}_i, t\right)}{\rho_i^{\,2}} + \frac{f\left(\vec{r}_j, t\right)}{\rho_j^{\,2}} \right) \cdot \nabla_i W_{ij} \tag{8.21b}$$

Figure 8.2 displays a schematic the particle approximation using neighbouring particles within the support domain of the kernel function, which is defined as κh, in a two-dimensional problem domain Ω with a surface S.

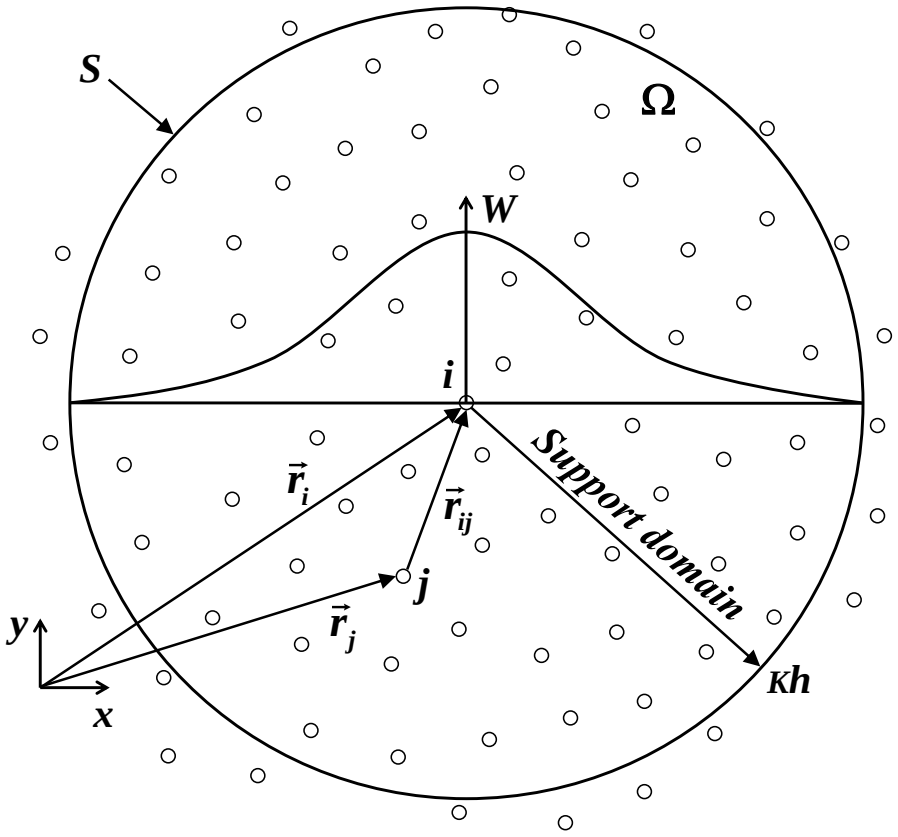

Figure 8.2. *Particle approximation using neighbouring particles within the supporting domain of the kernel function W for particle i*

8.3.1.2 Kernel Approximation

The kernel function W_{ij} and its gradient $\nabla_i W_{ij}$, for smoothing length h, depend on the magnitude of the position vector $\vec{r}_{ij}$ as:

$$W_{ij} = \frac{\alpha_{w,n}}{h^n} f_w(q) \tag{8.22}$$

$$\nabla_i W_{ij} = \frac{\partial W_{ij}}{\partial \vec{r}_{ij}} = \frac{\partial W_{ij}}{\partial \left|\vec{r}_{ij}\right|} \frac{\partial \left|\vec{r}_{ij}\right|}{\partial \vec{r}_{ij}} = \frac{\partial W_{ij}}{\partial \left|\vec{r}_{ij}\right|} \frac{\vec{r}_{ij}}{\left|\vec{r}_{ij}\right|} = W_{ij}' \frac{\vec{r}_{ij}}{\left|\vec{r}_{ij}\right|} = \frac{\alpha_{w,n}}{h^n} f_w'(q) \frac{\vec{r}_{ij}}{\left|\vec{r}_{ij}\right|} \tag{8.23}$$

where $\alpha_{w,n}$ is the kernel renormalisation term that depends on the kernel and dimensionality of the problem, W'_{ij} is the kernel derivative and $f_w(q)$ represents the kernel function that is a positive, symmetric and at least once continuously derivable function with $q = \frac{\left|\vec{r}_{ij}\right|}{h}$. In this study, the Wendland is employed, as it provides high order of interpolation with reasonable computational cost [181]; a high order of interpolation is required to capture complex fluid flow phenomena, leading to high

degrees of accuracy and stability of the SPH scheme [187]. The Wendland kernel [188] is defined as:

$$f(q)=\begin{cases}\left(1-\frac{q}{2}\right)^4(1+2q) & 0\le q\le 2\\ 0 & 2<q\end{cases} \tag{8.24a}$$

$$f'(q)=\begin{cases}-5q\left(1-\frac{q}{2}\right)^3 & 0\le q\le 2\\ 0 & 2<q\end{cases} \tag{8.24b}$$

where $\alpha_{w,1}=\frac{3}{4}$, $\alpha_{w,2}=\frac{7}{4\pi}$, $\alpha_{w,3}=\frac{21}{16\pi}$ for 1, 2 and 3 dimensions respectively.

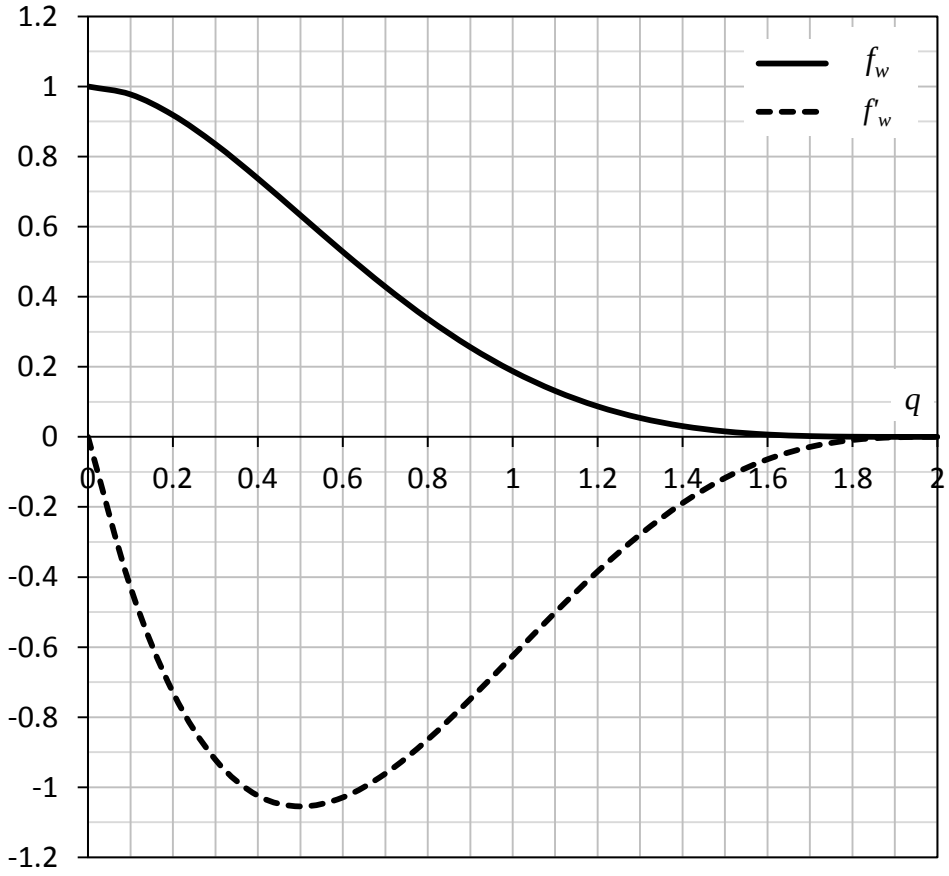

Figure 8.3. *Wendland kernel function, f(q), and its first derivative, f'(q)Position of lines at which results are extracted and evaluated*

8.3.1.3 Continuity Equation

The continuity equation, in its SPH formulation, is discretised in this work as proposed by Monaghan (1992). The divergence of the velocity function is implemented as per Equation (8.20b); substituting this into Equation (8.1) yields [175]:

$$\frac{D\rho_i}{Dt} = \sum_{j=1}^{N} m_j \vec{u}_{ij} \cdot \nabla_i W_{ij} \tag{8.25}$$

where i is the interested particle, j any neighbouring particle within the kernel domain, i.e. $\left|\vec{r}_{ij}\right| < 2h$ for the Wendland kernel, ∇_i the gradient of the kernel function with respect to the position vector $\vec{r}_{ij}$ and $\vec{u}_{ij} = \vec{u}_i - \vec{u}_j$ is the relative velocity between the particles.

8.3.1.4 Momentum Equation

The momentum equation, in its SPH formulation, was proposed by Monaghan (1992), where the gradient of pressure is implemented as per Equation (8.21a) [175]. Similarly, if the divergence of the viscus stress tensor is taken as per Equation (8.21b); substituting these into Equation (8.2) yields:

$$\frac{D\vec{u}_i}{Dt} = -\sum_{j=1}^{N} m_j \left(\frac{p_j}{{\rho_j}^2} + \frac{p_i}{{\rho_i}^2} \right) \nabla_i W_{ij} + \sum_{j=1}^{N} m_j \left(\frac{\underline{\underline{\tau}}_j}{{\rho_j}^2} + \frac{\underline{\underline{\tau}}_i}{{\rho_i}^2} \right) \cdot \nabla_i W_{ij} \tag{8.26}$$

The particle approximation of the viscus stress tensor is given in SPH literature as [189]:

$$\underline{\underline{\tau}}_i = -\sum_{j=1}^{N} \frac{m_j}{\rho_j} \mu_i \vec{u}_{ij} \nabla_i W_{ij} - \sum_{j=1}^{N} \frac{m_j}{\rho_j} \mu_i \nabla_i W_{ij} \left(\vec{u}_{ij} \right) + \left(\frac{2}{3} \sum_{j=1}^{N} \frac{m_j}{\rho_j} \mu_i \vec{u}_{ij} \cdot \nabla_i W_{ij} \right) \underline{\underline{I}} \tag{8.27}$$

The viscus forces in Equations (8.26) and (8.27) were estimated by Morris et al. (1997) [190] based on an expression proposed by Monaghan (1995) [191] to model heat conduction. This work made use of Morris et al.'s formulation of viscosity, thus the momentum equation was discretised as [190]:

$$\frac{D\vec{u}_i}{Dt} = -\sum_{j=1}^{N} m_j \left(\frac{p_j}{{\rho_j}^2} + \frac{p_i}{{\rho_i}^2} \right) \nabla_i W_{ij} + \sum_{j=1}^{N} m_j \left(\frac{\mu_i + \mu_j}{\rho_i \rho_j} \right) \vec{u}_{ij} \left(\frac{1}{\left|\vec{r}_{ij}\right|} \frac{\partial W_{ij}}{\partial \left|\vec{r}_{ij}\right|} \right) \tag{8.28}$$

8.3.1.5 Density-Smoothing Method

Equations (8.25) and (8.28) are solved and regarded as the standard weakly compressible SPH method. However, while kinematics in SPH is well understood, the weakly compressible approach can result in pressure fluctuations between particles, translating into numerical noise in the velocity field, which may exacerbate disorder and erratic motions of the fluid particles. One of the most straightforward and computationally least expensive approaches to tackle this issue is to perform a smoothing filter over the density of the particles [181]. In the past, this has commonly been done by re-assigning a reference density value to each particle at set time intervals [192-194]. A more elegant approach, utilised in this work, is to implement a simple density-smoothing model, analogous to the α–XSPH model as proposed by Violeau [176]:

$$\hat{\rho}_i = \rho_i - \varepsilon \sum_{j=1}^{N} m_j \frac{\rho_{ij}}{\bar{\rho}_{ij}} W_{ij} \tag{8.29}$$

where ε is a dimensionless coefficient, $\rho_{ij} = \rho_i - \rho_j$ and $\bar{\rho}_{ij}$ is the harmonic average. Values of the order of 10^{-2} are often recommended for the constant ε of the density-smoothing function [176]; ε = 0.01 is chosen in the present study. When this density-smoothing method is implemented, Equation (8.29) is solved immediately after solving Equation (8.25).

8.3.1.6 Time Integration

An adaptive time-stepping algorithm is used for calculating time-steps Δt. Here, three criteria are used which include the Courant–Friedrichs–Lewy condition [141]:

$$\Delta t_{CFL} \leq C_{CFL} \frac{h}{c_0} \tag{8.30}$$

a constraint based on the force per unit mass of each particle [175], which is essentially the magnitude of particle acceleration $\left|\vec{f}_i\right|$:

$$\Delta t_{force} \leq C_{force} \min_i \left(\sqrt{\frac{h}{\left|\vec{f}_i\right|}} \right) \tag{8.31}$$

and an additional constraint due to viscous diffusion [190]:

$$\Delta t_{visc} \leq C_{visc} \min_i \left(\frac{h^2}{\upsilon_i} \right) \tag{8.32}$$

where the kinematic viscosity $\upsilon_i = \mu_0 / \rho_i$ and μ_0 is the reference viscosity of the fluid. Values for C_{CFL}, C_{force} and C_{visc} of 0.01, 0.0125 and 0.0125, respectively, are conservatively chosen to ensure stability of the solution. The final time-step was chosen as the minimum of these three conditions:

$$\Delta t \leq \min\left(\Delta t_{CFL}, \Delta t_{force}, \Delta t_{visc} \right) \tag{8.33}$$

Time was integrated explicitly using the second order accurate Verlet algorithm [195]:

$$\rho_{i,n+1} = \rho_{i,n-1} + \left(\Delta t_{n-1} + \Delta t_n \right) \left(\frac{D\rho_i}{Dt} \right)_n \tag{8.34}$$

$$\vec{u}_{i,n+1} = \vec{u}_{i,n-1} + \left(\Delta t_{n-1} + \Delta t_n \right) \left(\frac{D\vec{u}_i}{Dt} \right)_n \tag{8.35}$$

$$\vec{r}_{i,n+1} = \vec{r}_{i,n} + \vec{u}_{i,n} \Delta t_n + \frac{\Delta t_n^{\,2}}{2} \left(\frac{D\vec{u}_i}{Dt} \right)_n \tag{8.36}$$

where the past, current and future temporal steps are represented by n-1, n and n+1, respectively. Note that the use of Equations (8.34) and (8.35) will eventually lead to a decoupled system. In order to prevent the solution at odd and even time-steps from diverging, an Euler upwind integration:

$$\rho_{i,n+1} = \rho_{i,n} + \Delta t_n \left(\frac{D\rho_i}{Dt} \right)_n \tag{8.37}$$

$$\vec{u}_{i,n+1} = \vec{u}_{i,n} + \Delta t_n \left(\frac{D\vec{u}_i}{Dt} \right)_n \tag{8.38}$$

is performed at every M time steps; a value of M of 50 is presently used.

8.3.1.7 Boundary Conditions

The walls that define the limits of the fluid domain were simulated using dynamic boundary conditions [179], chosen for its computational simplicity. Particles comprising dynamic boundaries are solved like any other fluid particles following the solution of

Equations (8.4), (8.25) and (8.28). However, the particle positions remain fixed and are not updated in subsequent iterations in time. In order to ensure all fluid particles have consistently the same number of neighbouring particles at all times, solid wall boundaries were modelled with three consecutive rows of dynamic particles.

In order to model the oscillatory behaviour of the fluid, two pistons, one on the left and another one on the right, are defined on both ends of the OBR, as shown in Figure 8.4, using dynamic particles whose positions and velocities are controlled by Equations (2.1) and (2.2).

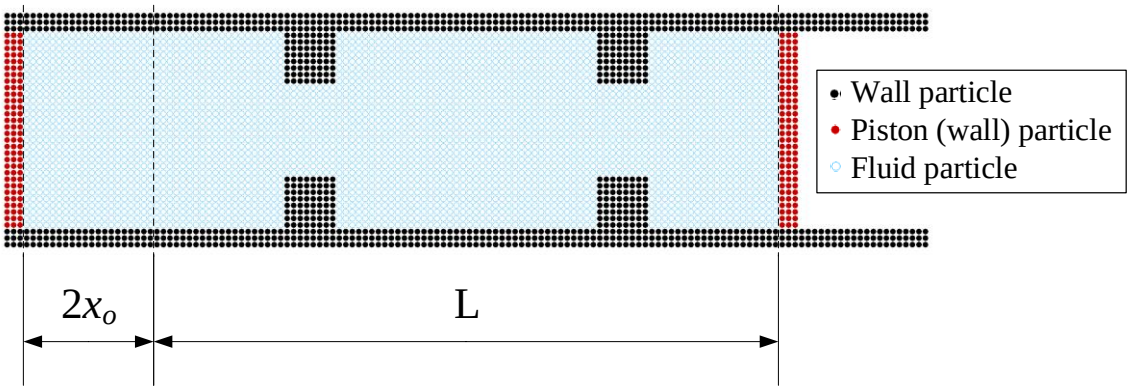

Figure 8.4. *SPH OBR model for Δx = 0.0005m*

8.3.1.8 Post-Processing Monitors

The velocity profiles of the flow in the OBR are evaluated along three different lines as depicted in Figure 8.5: a vertical line at the middle of the left baffle (Line 1) – the section experiencing the highest velocity; a centred vertical line (Line 2) – the area where the strongest eddy dissipation occurs; and a centre horizontal line (Line 3) – the area with the weakest eddy interaction as aforementioned. The velocity magnitude u_m at each point of a line, defined at equidistance intervals of Δx along the monitor lines, is calculated analogously to Equation (8.15), given by:

$$u_{m,i} = \sum_{j=1}^{N} \frac{m_j}{\rho_j} u_{m,i} W_{ij} \tag{8.39}$$

where i is the interpolated monitor point that utilises information from surrounding particles within the kernel smoothing length.

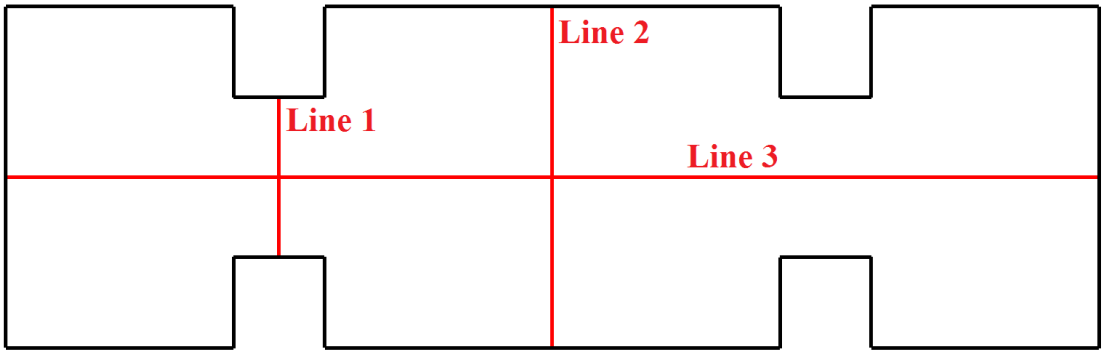

Figure 8.5. *Position of lines at which results are extracted and evaluated* [68]

8.3.2 Finite Volume Method

For the purpose of comparison, the Eulerian based Finite Volume (FV) method is also applied to the same geometry and operational conditions as given in Table 8.1 and Figure 8.1. The following Navier Stokes for continuity and momentum conservation equations, given by Equations (3.1) and (3.2), are simplified and solved for incompressible flow as per Equations (3.6) and (3.7)

8.3.2.1 Numerical Setup

All the numerical FV modelling is performed using the ANSYS® Fluent 15.0 CFD package. Simulations are done by the pressure-based segregated solver, using the SIMPLE pressure-velocity coupling algorithm. A *second order upwind* scheme was utilised for the spatial discretisation of the momentum equation; a *second order* scheme for the interpolation of pressure at the faces of the grid and a *second order implicit* scheme for time discretisation. The time-step employed is 0.001 seconds throughout all simulations and the convergence criteria is set to residuals of 10^{-5} for solving both Equations (3.6) and (3.7) to ensure accuracy. The average value of the Courant–Friedrichs–Lewy (CFL) coefficient was kept below 0.6 and the maximum CLF value below 4.1.

To replicate the OBR with the double piston in the SPH approach, flat velocity profiles are defined on both ends of the OBR using a customized User Defined Function (UDF) in ANSYS® Fluent given by Equation (2.2); walls were model as *no-slip* boundaries. Equations (3.6) and (3.7) were solved as laminar, i.e. no turbulence model was implemented. This is in agreement with literature, where laminar solver has been the norm for simulating flows in oscillatory baffled reactors in the past [54, 57, 59] and

present decade [44, 45, 64, 65, 109] under a FV framework, including flows with Re_o values up to 8043 [43, 58].

8.3.2.2 Mesh

A mesh sensitivity analysis is performed using a selection of computational nodes per baffled cell. Meshes of the two baffled-cell domain of five different resolutions are analysed for ten oscillatory cycles. Profiles of velocity magnitude extracted at Lines 1, 2 and 3, as shown in Figure 8.5, are then cycle-averaged over all ten oscillatory cycles and compared for strokes 1 to 4 (refer to Figure 2.1) for various mesh densities. The coefficient of determination, R^2, was selected for comparison between meshes, as described in Section 3.3. A summary of the mesh independency analysis is shown in Table 8.2, clearly indicating that the resolution of mesh #2 is the desired choice on the balance between accuracy and computation time, which is selected for this work.

Figure 8.6 illustrates the resolution and distribution of mesh #2, which is generated using ANSYS® ICEM containing only hexahedral elements.

Table 8.2. *Mesh sensitivity analysis results (R^2) where results from mesh #1 are used as the based for comparison*

Line 1					
Mesh #	# Nodes*	Stroke 1	Stroke 2	Stroke 3	Stroke 4
1	38 k	–	–	–	–
2	**17 k**	**0.999**	**0.997**	**0.999**	**0.945**
3	10 k	0.999	0.997	0.997	0.896
4	6 k	0.994	0.989	0.999	0.948
5	3 k	0.982	0.952	0.993	0.953

Line 2					
Mesh #	# Nodes*	Stroke 1	Stroke 2	Stroke 3	Stroke 4
1	38 k	–	–	–	–
2	**17 k**	**0.988**	**0.988**	**0.966**	**0.972**
3	10 k	0.986	0.994	0.948	0.933
4	6 k	0.968	0.925	0.893	0.867
5	3 k	0.971	0.760	0.918	0.621

Line 3					
Mesh #	# Nodes*	Stroke 1	Stroke 2	Stroke 3	Stroke 4
1	38 k	–	–	–	–
2	**17 k**	**0.997**	**0.983**	**0.994**	**0.983**

3	10 k	0.996	0.989	0.989	0.962
4	6 k	0.984	0.978	0.975	0.965
5	3 k	0.924	0.952	0.911	0.922

[*] *The values of number of nodes are per baffled cell.*

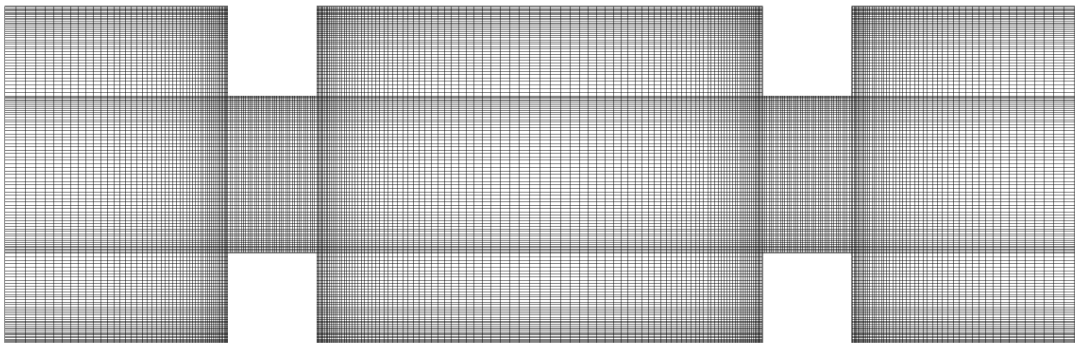

Figure 8.6. *Finite volume chosen mesh (#2): 17k nodes per baffled cell* [68]

8.4 Results & Discussions

8.4.1 Profile Development

Previous CFD work on oscillatory baffled reactors by Jian [144] showed that flow patterns in an OBR become repeatable and achieved a quasi-steady-state after 5-7 oscillation cycles. Following the same methodology, the volume-weighted averaged strain rate as a function of time is shown in Figure 8.7, displaying a similar quasi-steady state after cycle 4. In this work, cycle-averaged parameters generated between cycles 6 to 10 are used for comparison.

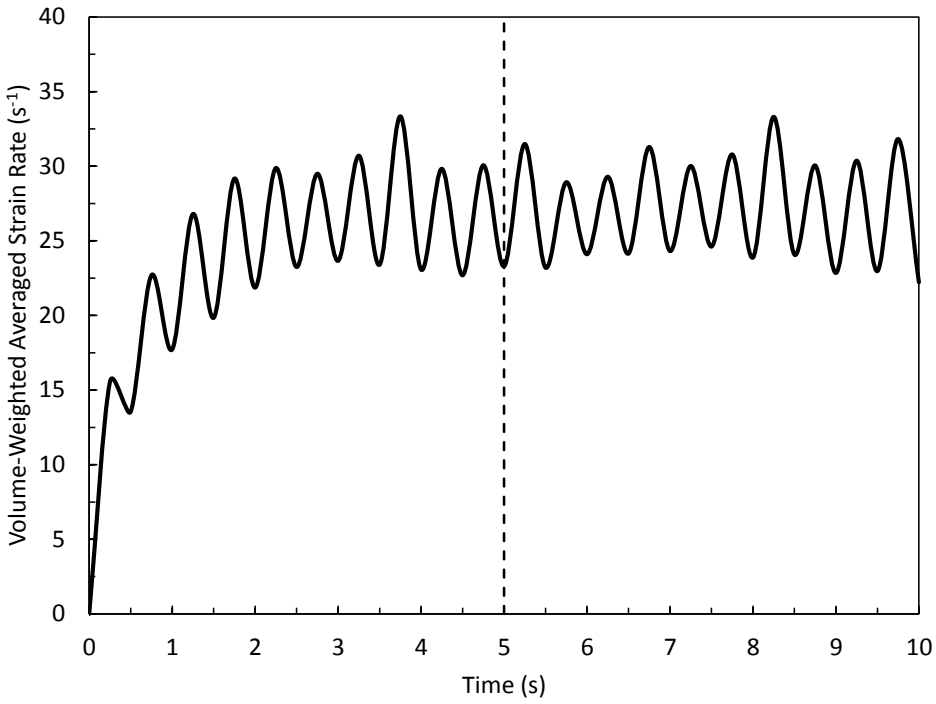

Figure 8.7. *Convergence of strain rate with time in Fluent* [68]

8.4.2 Sensitivity Test of SPH Particles

Figure 8.8 shows the cycle-averaged velocity magnitude profiles of Line 3 (see Figure 8.5), generated by SPH, at strokes 1 and 3 (see Figure 8.2.1) for three different resolutions in terms of the initial particle distribution spacing, Δx. Strokes 1 and 3 were chosen because the flow at these instances experiences the maximum local velocities, leading to potential lower rates of convergence. A clear convergence in the cycle-averaged velocities is observed with decreasing Δx, and the results become resolution independent at $\Delta x = 0.00025$ m, which is therefore chosen for the investigation.

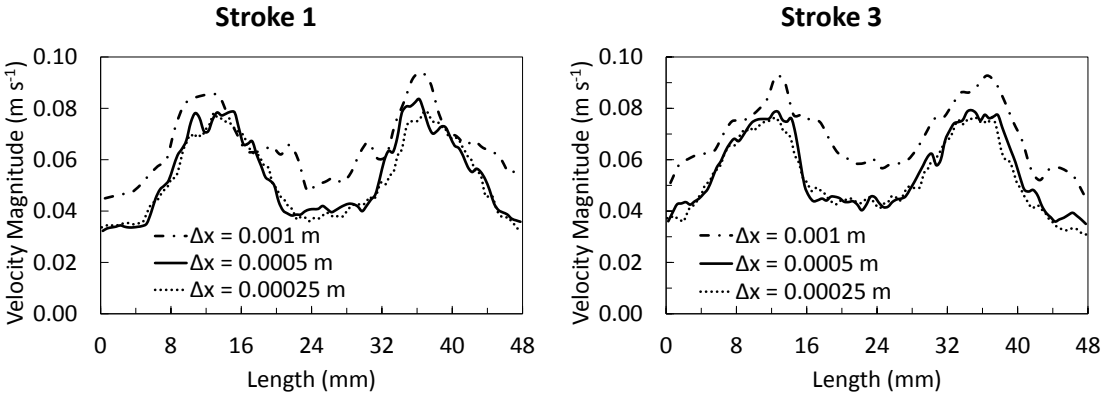

Figure 8.8. *SPH cycle-averaged velocity magnitude profiles of Line 3 for different Δx values* [68]

8.4.3 Flow Patterns & Velocity Profiles

8.4.3.1 Flow Patterns

Figure 8.9 shows the cycle-averaged flow patterns modelled by both the FV and the SPH with an additional density-smoothing function (SPH D-S for short) at strokes 1 to 4 of an oscillation cycle (see Figure 8.2.1). Both methods predict similar eddy formation throughout the oscillation, leading to good comparison. The subtle differences between the two models are the relative size and the intensity (by colour) of eddies. The intensity of flow restriction in strokes 1 and 3 is higher for SPH D-S than that for FV, resulting in larger recirculating velocities at the top and bottom of the baffled cell, causing the eddy structures generated during strokes 2 and 4 to remain closer to the baffle's walls. On the contrary, results generated by the FV have slightly larger velocities along the centre of the baffled domain, enhancing a small displacement of eddies towards the centre of the baffled cell. This slight difference in eddy displacement is reflected in the velocity profiles presented in the next sub-section and the maximum velocities listed in Table 8.3. Flow patterns observed during strokes 1 and 2 and eddy structures formed in strokes 2 and 4 are of high resemblance for the two methodologies nonetheless. Overall, the results show that the SPH D-S is a viable method in modelling flows in OBR.

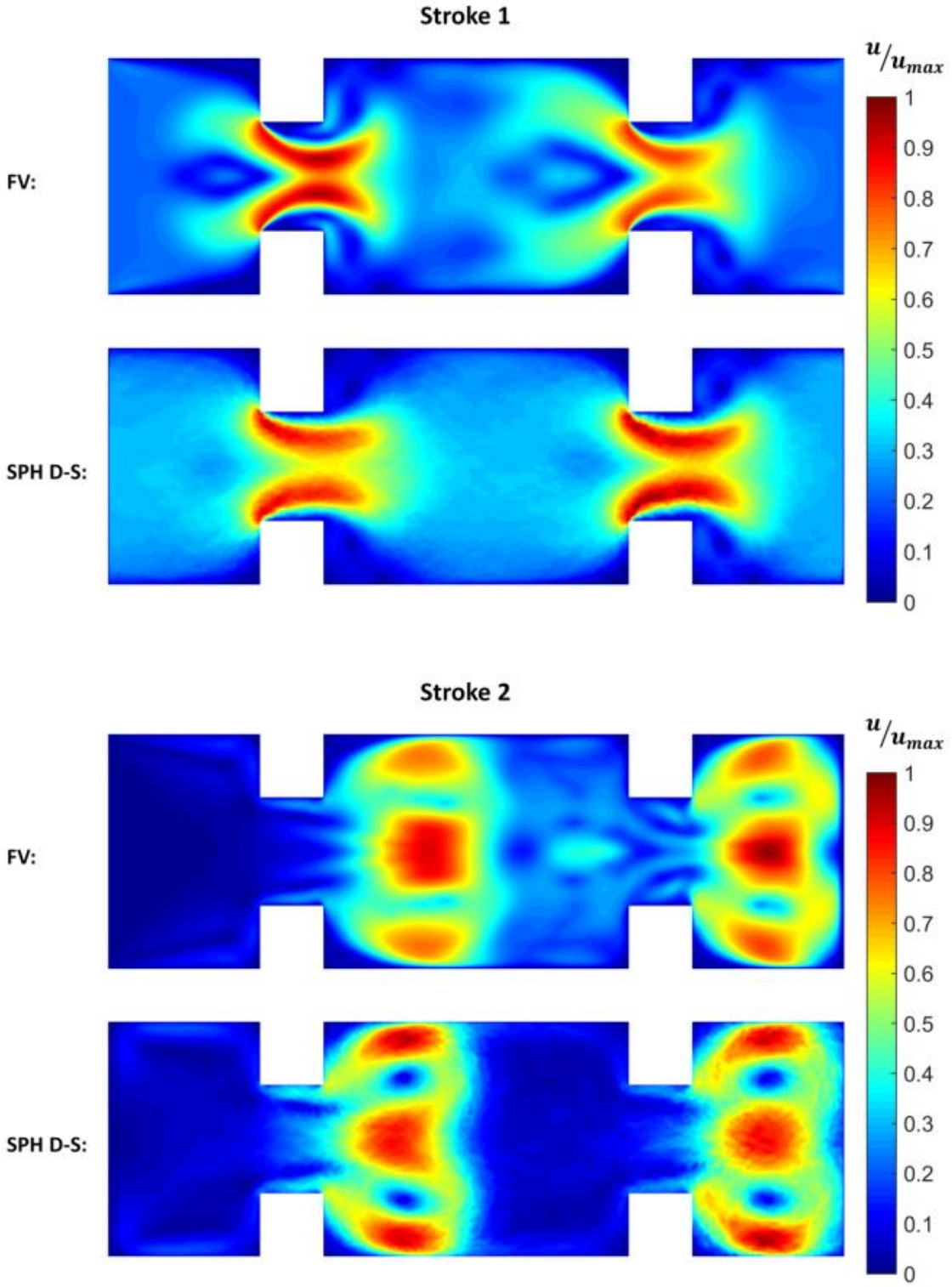

Figure 8.9. *Cycle-averaged velocity magnitude contours at strokes 1 to 4 for FV and SPH D-S* [68]

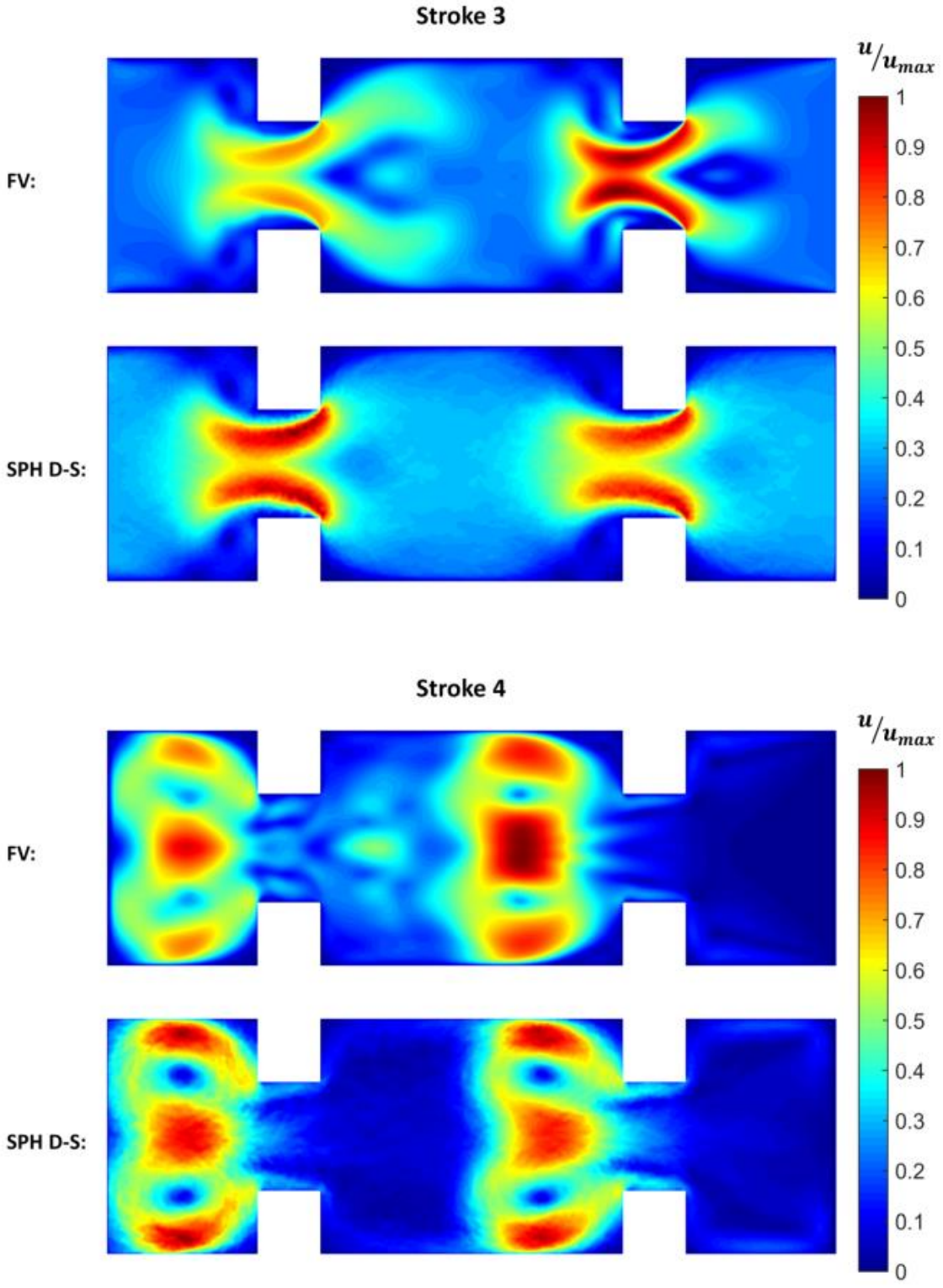

Figure 8.9. (continuation) *Cycle-averaged velocity magnitude contours at strokes 1 to 4 for FV and SPH D-S* [68]

Table 8.3. *u_{max} for different strokes and methodologies*

	Strokes 1 & 3	Strokes 2 & 4
Finite Volume Method	0.1476 m s^{-1}	0.0897 m s^{-1}
SPH with Density-Smoothing model	0.1127 m s^{-1}	0.0531 m s^{-1}

8.4.3.2 Velocity Profiles

The cycle-averaged velocity magnitude profiles at Lines 1, 2 and 3 computed by the FV, the standard SPH and SPH D-S methodologies are shown in Figures 8.10 – 8.12, respectively; the density-smoothing function was added in a separate simulation to assess its effect individually.

Figure 8.9 neatly displays how two noticeable high velocity regions (red colour) occur through the baffle constriction during strokes 1 and 3, which is shown in Figure 8.10 as a double-peak velocity profile across Line 1. The velocities obtained with the SPH methodology alone do not display the expected double-peak pattern as the FV did in the forward (1) and reverse (3) strokes, but exhibit parabolic-like characteristics which indicate excessive localized density fluctuations due to the weakly compressible limitation across the constriction of the baffle. This effect is then minimized when the density-smoothing (D-S) function is introduced to limit the "noise" in density distribution. In doing so, the double-peak velocity profiles are reproduced during strokes 1 and 3, highly resembling those modelled by the FV method. Figure 8.9 also provides qualitative evidence of how, during strokes 2 and 4, the changes in direction of the flow lead to local stalling across the baffle constriction, which translates into lower and more uniform velocity components in the baffle constriction area as shown in Figure 8.10. The results from the SPH simulation echo the above nonetheless; again the results from the SPH D-S improve the accuracy of the velocity field and are similar to those provided by the FV method.

For the given geometry and operating conditions, symmetrical-mirrored flow patterns and similar velocity magnitudes between the peak and trough are expected (see Figure 8.9). The velocity profiles predicted by SPH D-S (in Figure 8.10) at strokes 1 and 3 are indeed very similar in both shape and magnitude with a maximum difference of 4.7%, while the results computed by the FV approach at the same strokes have a larger discrepancy, of 18.5%. A similar outcome is likewise seen for strokes 2 and 4.

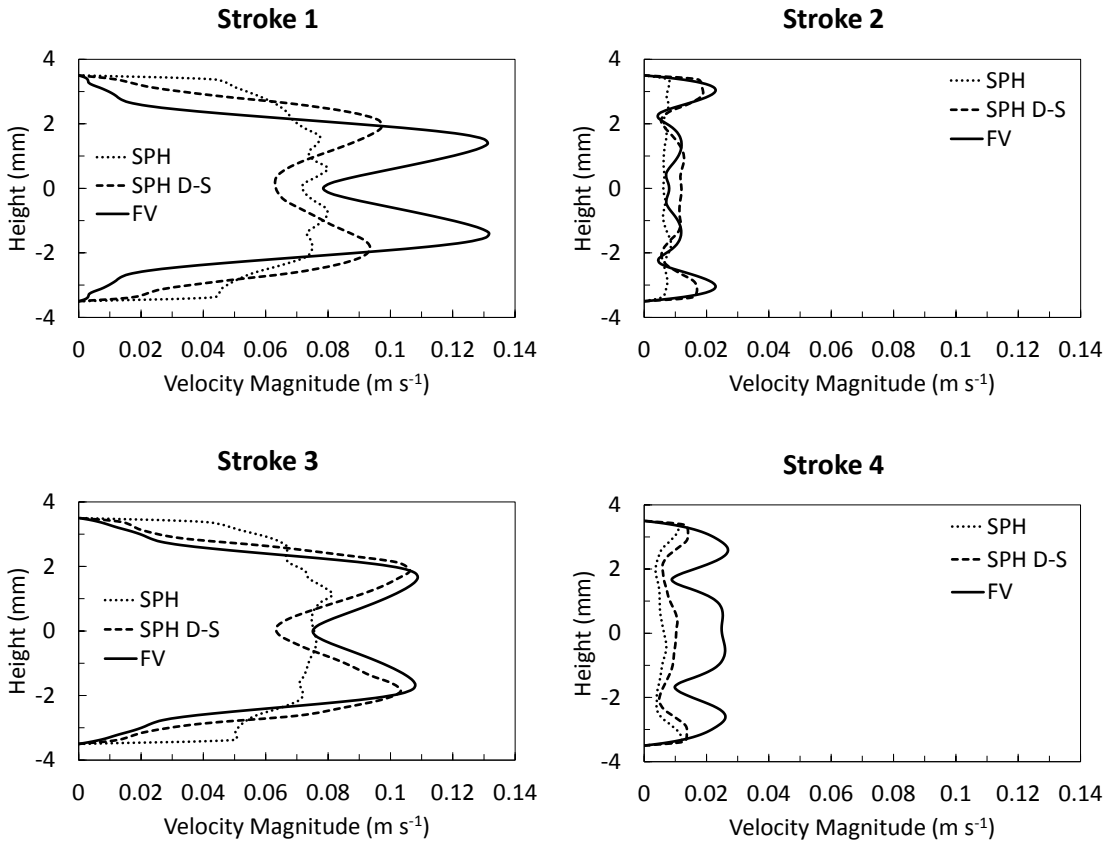

Figure 8.10. *Cycle-averaged velocity magnitude profiles of Line 1 for SPH, SPH D-S and FV methods* [68]

The cycle-averaged velocity magnitude profiles across Line 2 (in the middle of the baffled cell, see Figure 8.5) are shown in Figure 8.11 for the FV, SPH and SPH D-S approaches. It is seen that the velocity profiles at the strokes 1 and 3 by the FV not only differ in velocity amplitude with a maximum error of 8.7%, but also differ in shape. Conversely, the velocity profiles by the SPH D-S method display repeatable cyclic flow with a maximum error of 0.5% at the same strokes. It demonstrates again that a density-smoothing method is essential to provide regular and predictable flow patterns with SPH, showing good reproducibility and consistency for modelling oscillatory transient problems.

For strokes 2 and 4 representing the end of both the forward and backward strokes respectively, the comparisons of velocity profiles are better for both the FV and SPH D-S methods; however the magnitudes for the former are larger than for the latter.

These differences in the magnitude and shape of velocity profiles among FV strokes, and between FV and SPH D-S, at Line 2, are due to the earlier mentioned phenomenon: Figure 8.9 showed that while eddy structures generated by SPH D-S remain close to the

walls of the baffles, eddies observed in FV solutions are slightly displaced towards the centre of the baffled cell. This leads to an increment in velocity magnitude at Line 2, in comparison with those obtained with SPH D-S. This eddy displacement shown in FV results occurs at every cycle; the distance travelled by the eddies remains significantly constant throughout cycles, leading to a quasi-steady-state, hence a stable cycle-averaged velocity field is obtained (Figure 8.9). However, subtle alterations in the distances travelled by eddies from cycle to cycle manifest into significant differences in the magnitude of velocity and the shape of velocity profiles at Line 2 among FV strokes. This is clearly observed in Figure 8.13, where velocity magnitude profiles, obtained with FV and extracted at Line 2, are presented at strokes 1 to 4 for different oscillatory cycles. Likewise, Figure 8.14 shows the analogous for SPH D-S. Undoubtedly, SPH D-S does a better job at producing cycle-repeatable results than FV, especially for velocity profiles at a vertical centred line (at the middle of the baffled cell). Nonetheless, despite this phenomenon and its impact on velocity profiles at Line 2, both methodologies present very similar cycle-repeatable velocity fields across the entire domain, capturing almost identical eddy generation patterns, as stated in section 4.3.1.

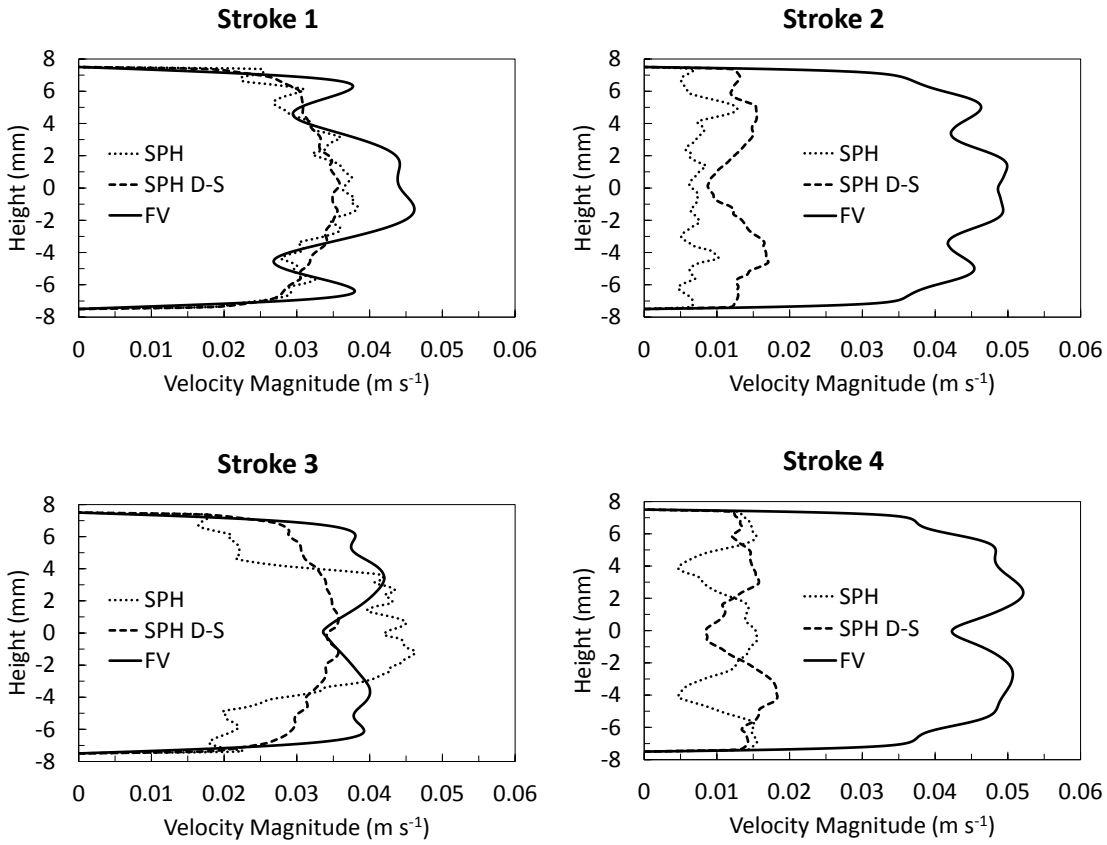

Figure 8.11. *Cycle-averaged velocity magnitude profiles of Line 2 for SPH, SPH D-S and FV methods* [68]

The cycle-averaged velocity magnitude profiles shown in Figure 8.12 are measured across a horizontal centre line (Line 3 in Figure 8.5). Again, the standard SPH approach suffers from noise arising from its density distribution, consequently, the velocity magnitudes for all strokes display small fluctuations that have a dampening effect on the overall flow profile, in particular in strokes 2 and 4 where the velocity components are small. These density fluctuations and the associated velocity dampening effect are eliminated by the use of SPH D-S. As earlier mentioned, the numerical solution for strokes 1 and 3, and strokes 2 and 4, should ideally yield a profile that mirrors one another; this is especially expected at Line 3, as it is positioned across the axial direction. Both FV and SPH D-S methodologies successfully predict mirror-shaped velocity profiles among strokes, and show good agreement and resemblance among one another. Local differences in velocity magnitude are the results of the aforementioned eddy displacement produced by FV.

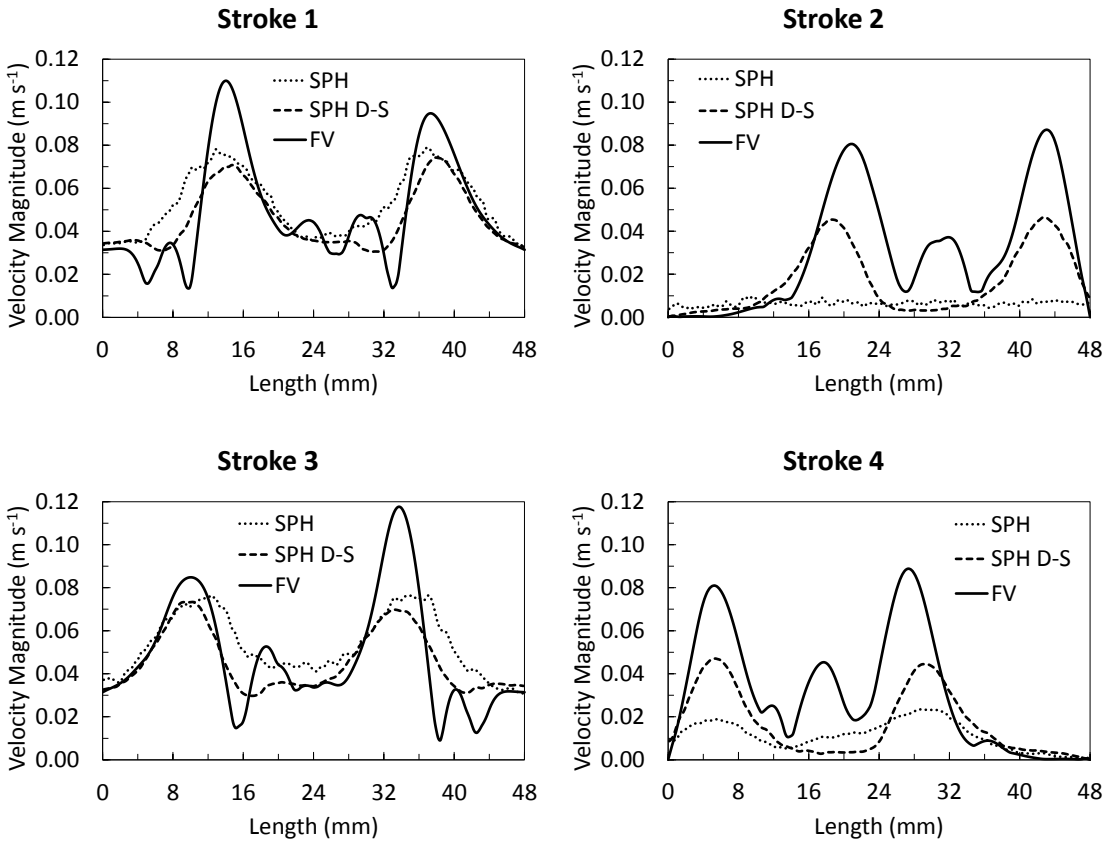

Figure 8.12. *Cycle-averaged velocity magnitude profiles of Line 3 for SPH, SPH D-S and FV methods* [68]

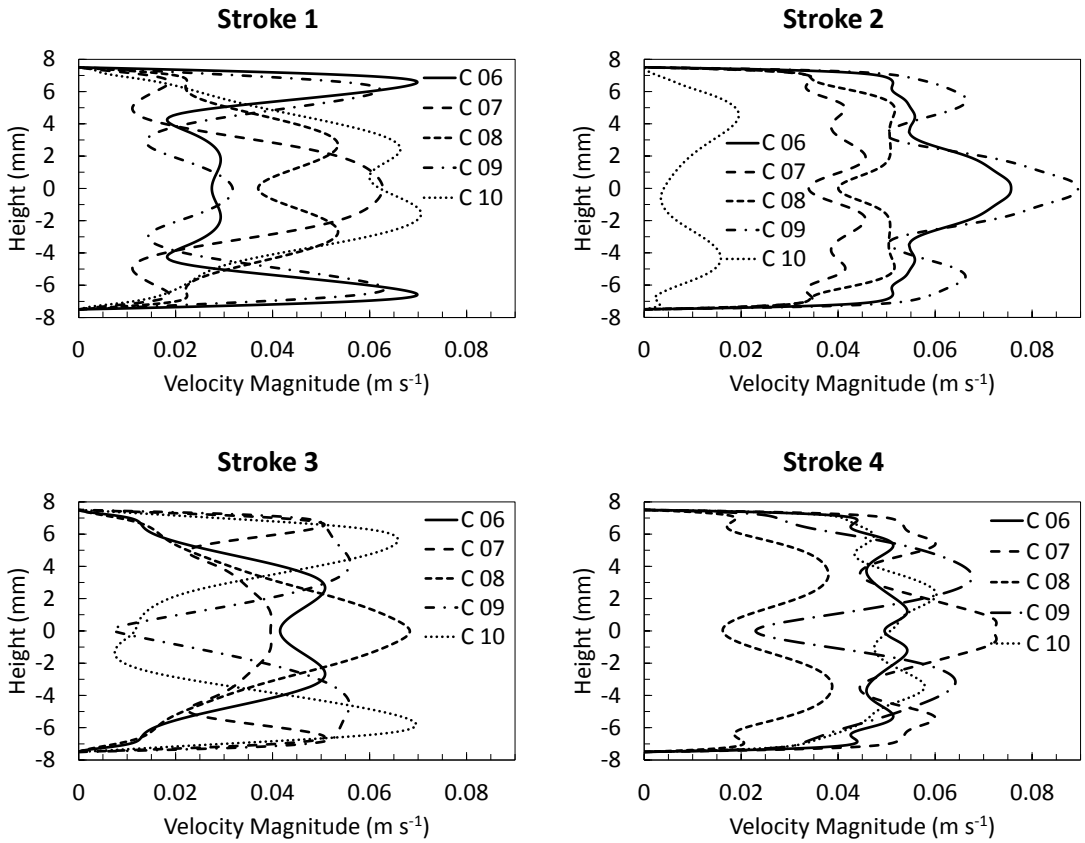

Figure 8.13. *Velocity magnitude profiles of Line 2 obtained with Finite Volume (FV) method for different oscillatory cycles* [68]

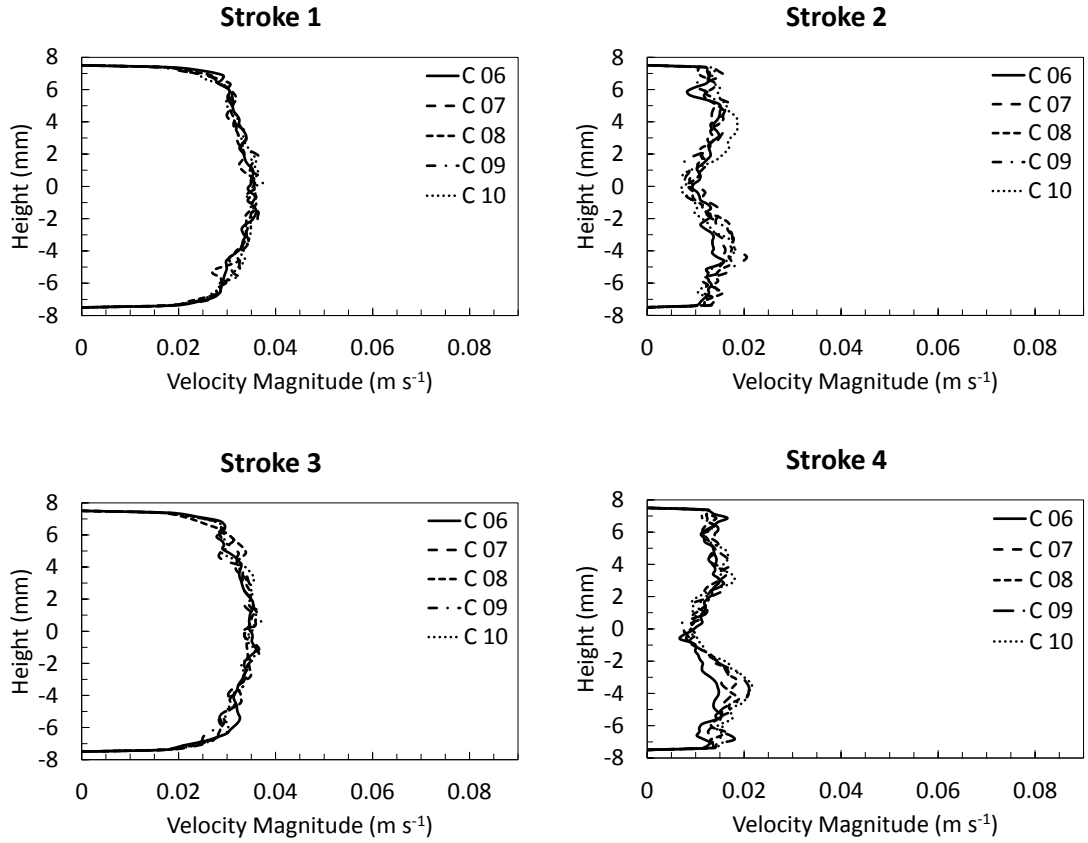

Figure 8.14. *Velocity magnitude profiles of Line 2 obtained with SPH Density-Smoothing (SPH D-S) method for different oscillatory cycles* [68]

8.4.4 Mixing Assessment

Diverse methods and indexes have been used in the past in order to quantitatively assess mixing efficiency in OBR, for example, the velocity ratio [43, 57, 58] and stretch rates [50, 53]. Simulated data obtained with the SPH can directly be utilised to do the same analysis.

8.4.4.1 Velocity Ratio

The axial to radial velocity ratio (R_V) was proposed by Ni et al. (2003) [55] in order to correlate results between those obtained from a three-dimensional numerical simulation and the two-dimensional experimental measurements from digital particle image velocimetry (DPIV) in a OBR. The axial to radial velocity ratio was defined as:

$$R_V(t) = \frac{\sum_{i=1}^{N_T}\left(\left|u_{x,i}\right|\frac{m_i}{\rho_i}\right)}{\sum_{i=1}^{N_T}\left(\left|u_{y,i}\right|\frac{m_i}{\rho_i}\right)} \tag{8.40}$$

where $u_{x,i}$ and $u_{y,i}$ are, respectively, the axial and radial velocity components of a particle i, and N_T is the total number of fluid particles in the domain. By directly utilising the velocity data generated by the SPH D-S method, the cycle-averaged velocity ratio is obtained and plotted against the period of an oscillatory cycle in Figure 8.15; the shape of which is the same as that reported by Jian and Ni [58]. Past work [43, 57, 58] correlated R_V as a function of oscillatory Reynolds number (Re_o) for fluids of different viscosities in OBRs and an inversely proportional relationship was established for $Re_o < 1000$. The average R_V value of 3.18 in this work is slightly higher than in the aforementioned work [58], due to the lower oscillatory Reynolds number (Re_o = 471) under which the current study was performed.

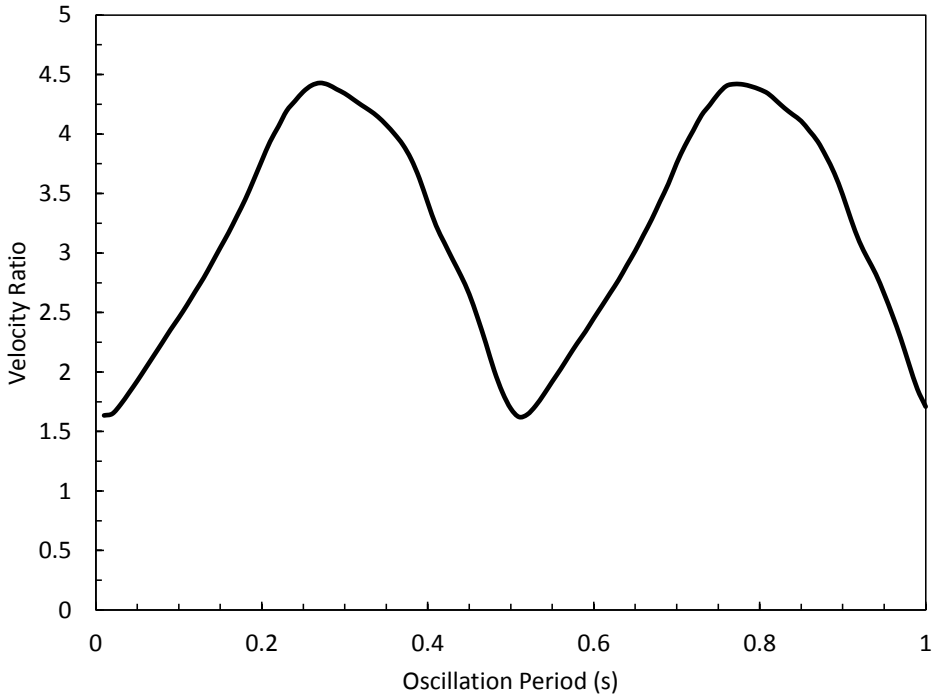

Figure 8.15. *Cycle-averaged velocity ratio for the period of an oscillatory cycle* [68]

8.4.4.2 Stretch Rates

Another way of quantifying the rates of mixing in a system, due to its fluid dynamics, is by analysing the rates at which infinitesimal lines of the fluid domain are stretched [196]. Fluid motion may imply stretching and folding actions, which are characteristic of chaotic advection; thus its analysis is key to the understanding of the mixing mechanism in chaotic flows. The examination of stretch rates requires Lagrangian tracking of these infintesimal lines that compose the domain under evaluation and was for the first time utilised for the assessment of mixing efficiency in oscillatory baffled flows by Roberts and Mackley (1995) [50]. Advantageously, by modelling the flow

field with SPH, the necessity of superimpossing a Largrangian tracer whose movement is integrated based on an Eulerian velocity field [50, 53] is avoided. It is an easy task to assign an infinitesimal line to each fluid particle that comprises the domain in SPH; these lines are then ascribed an initial orientation (at time = 0 s) relative to the axis in the *x*-direction, defined by the anticlokwise angle θ. (see Figure 8.16).

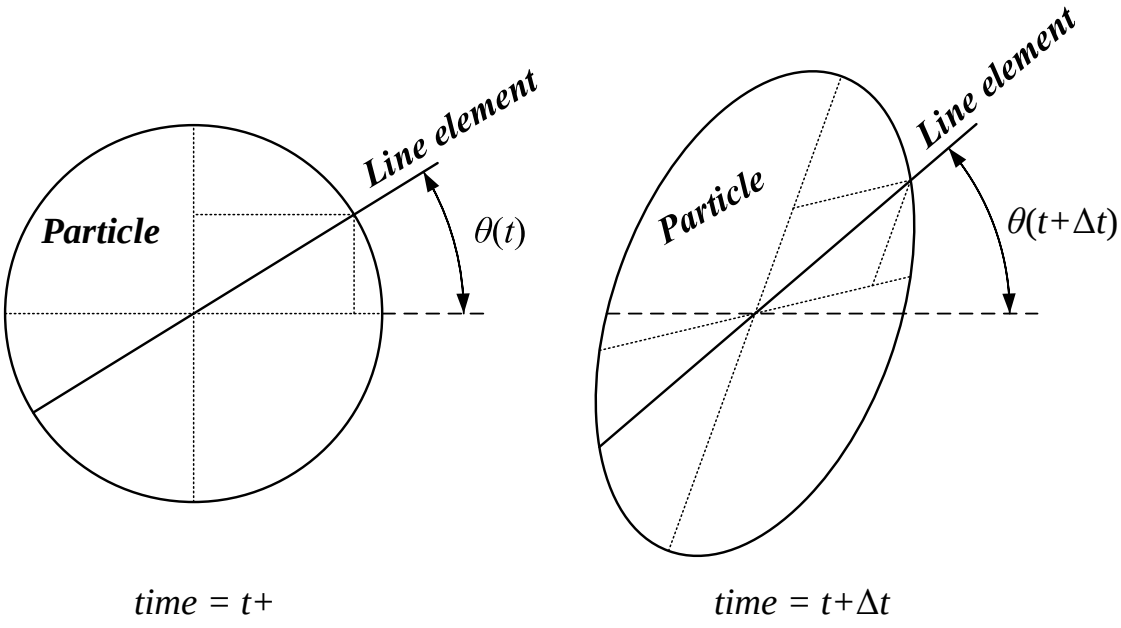

Figure 8.16. *Schematic showing the change in orientation of a lime element assigned to a fluid particle*

The rate of rotation is thus given by:

$$\frac{d\theta}{dt} = \cos^2\theta\frac{\partial u_y}{\partial x} + \sin\theta\cos\theta\left(\frac{\partial u_y}{\partial y} - \frac{\partial u_x}{\partial x}\right) - \sin^2\theta\frac{\partial u_x}{\partial y} \tag{8.41}$$

and the instantaneous exponential stretch rate of an infitesimal line is defined as:

$$\frac{d\left(\ln l\right)}{dt} = \sin^2\theta\frac{\partial u_y}{\partial y} + \sin\theta\cos\theta\left(\frac{\partial u_y}{\partial x} + \frac{\partial u_x}{\partial y}\right) + \cos^2\theta\frac{\partial u_x}{\partial x} \tag{8.42}$$

The derivation of the rate of rotation and the exponential stretch rate of a line element, Equations (8.41) and (8.42) respectively, is explained in Appendix 5. The time-averaged exponentatial stretch rate *S(t)* of a line can be integrated as:

$$S\left(t\right) = \frac{1}{t}\int_0^t \frac{d\left(\ln l\right)}{dt}dt \tag{8.43}$$

The above is then volume-averaged for all the lines comprising the system – $\overline{S}(t)$ – and plotted with time, giving an asymptotic value $\overline{S}_{as}$. Exponential stretch rates have units of s^{-1}, and are scaled with the frequency of the oscillation (f) in order to obtain dimensionless values. Roberts and Mackley (1995) [50] obtained $\overline{S}(t) - Re$ and $\overline{S}(t) - St$ relations, while the effect of Re_o on $\overline{S}(t)$ was later established by Mackley and Neves Saraiva (1999) [53]. Based on their findings, $\overline{S}_{as}$ values between 0.5 and 1 are expected for the operational conditions of the current system under evaluation; the asymptotic values in Table 8.4 fall within the range. Figure 8.17 shows the evolution of $\overline{S}(t)$ for different initial values of θ; the profiles and trends are identical to those of the aforementioned research works.

Table 8.4. *Effect of the initial orientation of the infinitesimal lines on the asymptotic value of the systems exponential stretch rate*

$\theta_{initial}$	$\overline{S}_{as}$
0°	0.83
45°	0.98
90°	0.97
135°	0.94

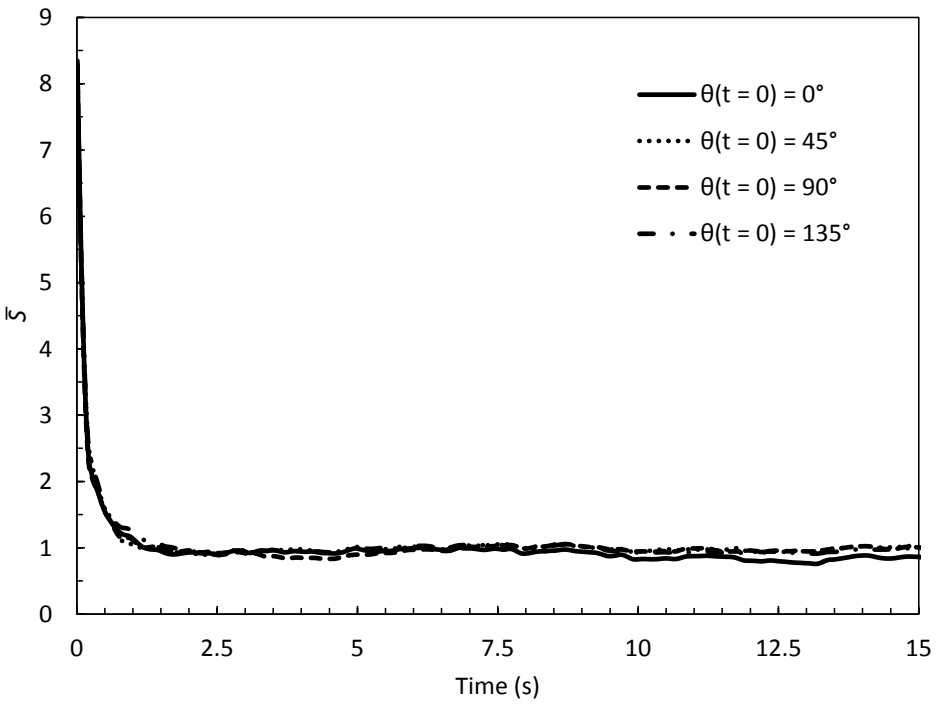

Figure 8.17. *Effect of the initial orientation of the infinitesimal lines on the time evolution of the time-averaged exponentatial stretch rate* [68]

8.4.4.3 Distribution of Neighbouring Fluid Particles

Using the SPH approach, an alternative mixing assessment can be proposed by defining the domain as two identical immiscible fluids; these fluids can initially be displayed in serial or in parallel, as shown in Figures 8.18 and 8.16 (time = 0 s). As the simulation advances with time, visual and qualitative assessment of axial and radial mixing efficiency are observed in Figures 8.18 and 8.19, respectively.

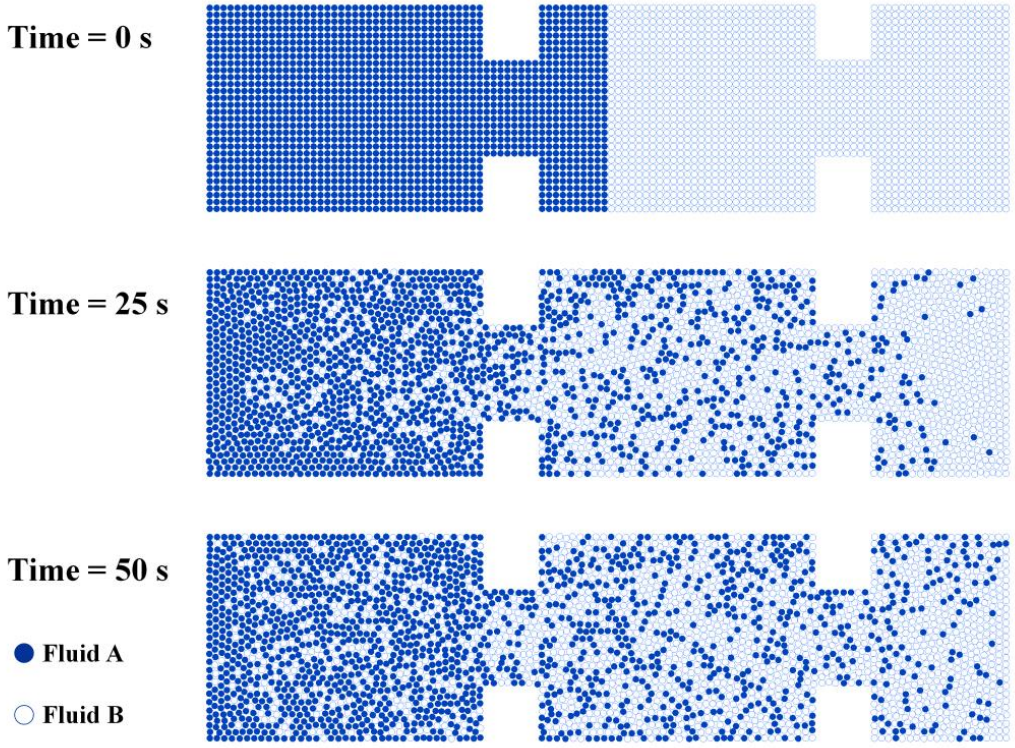

Figure 8.18. *Qualitative axial mixing assessment for SPH D-S and Δx = 0.0005m* [68]

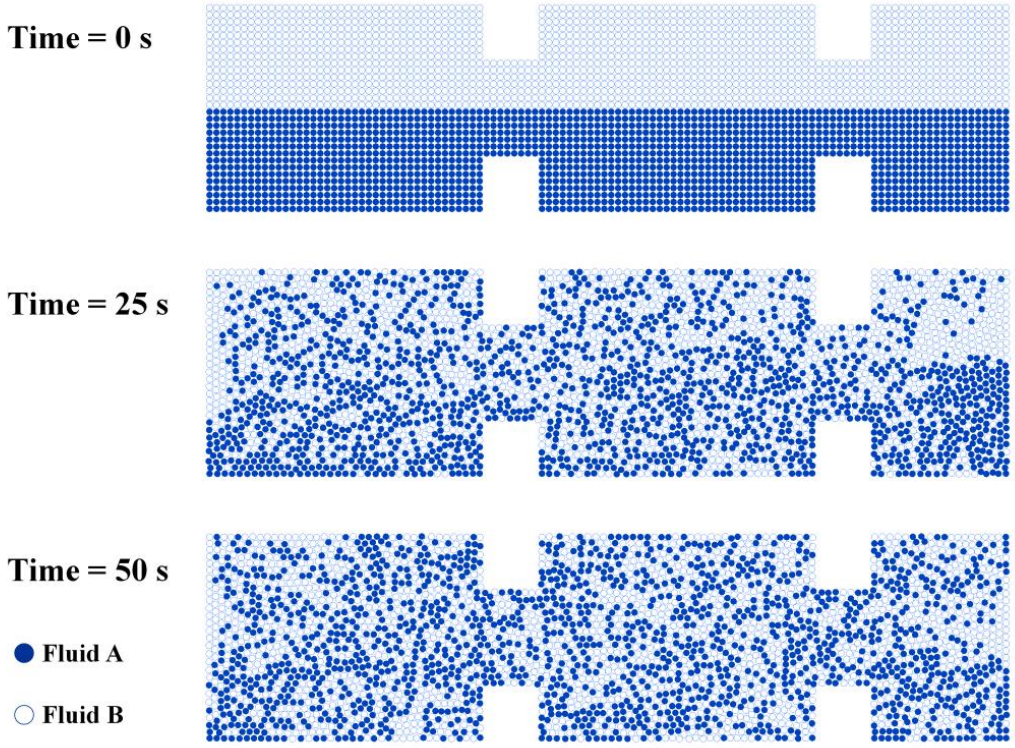

Figure 8.19. *Qualitative radial mixing assessment for SPH D-S and Δx = 0.0005m* [68]

The evolution of mixing efficiency with time can be obtained by quantifying, for each particle, how many of its neighbouring particles are of Fluid A, and how many of its neighbours are of fluid B. Numerically, this is done as follows. Let each particle *i* carry a dimensionless binary variable J_i, whose value can be 0 (if it is a Fluid A particle) or 1 (Fluid B). By doing so, a time-dependent dimensionless "neighbouring mixing index", *NM(t)*, is defined for each particle as:

$$NM_i(t) = \sum_{j=1}^{N} 2\frac{m_j}{\rho_j}\left|J_i - J_j\right|\tilde{W}_{ij} \tag{8.44}$$

where the kernel W_{ij} has been corrected using the Shepard filter [197], in order to avoid irregularities with particles close to the boundaries, as those will have a lower number of neighbouring fluid particles than particles in the bulk. $\tilde{W}_{ij}$ is defined as:

$$\tilde{W}_{ij} = \frac{W_{ij}}{\sum_{j=1}^{N}\frac{m_j}{\rho_j}W_{ij}} \tag{8.45}$$

The neighbouring mixing index is averaged over all the particles comprissing the fluid domain. At time zero, every Fluid A particle has a certain number of neighbouring particles, all of which are of Fluid A; likewise, every Fluid B particle only has Fluid B neighbours. This will be true for all particles, except those at the interface that separates the two types of fluids, hence yielding a $NM(t=0s) \approx 0$. On the contrary, a fully mixed system is achieved when each particle has an equal number of neighbours of Fluid A and Fluid B, resulting in $NM = 1$.

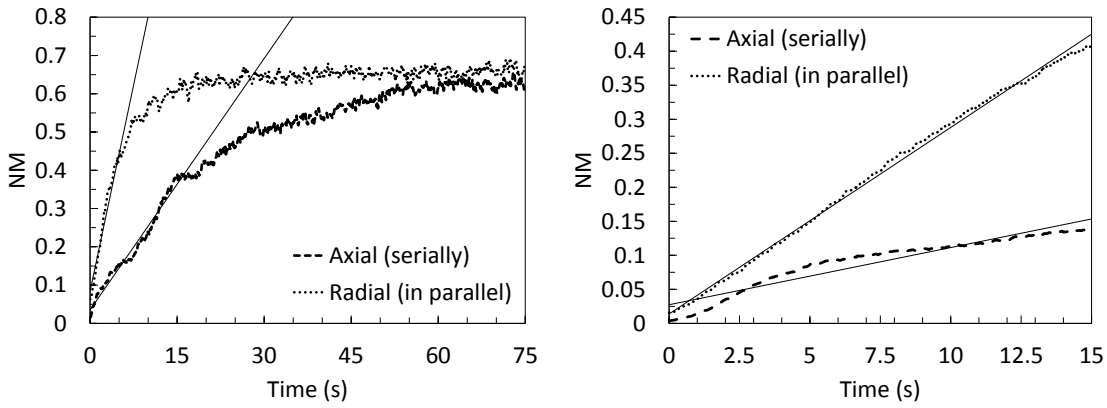

Figure 8.20. *Effect of the initial display of fluids A and B on the time evolution of NM for $\Delta x = 0.001m$ (left) and $\Delta x = 0.00025m$ (right)* [68]

Figure 8.20 plots the *NM* as a function of time for both fluid placements as shown in Figures 8.18 and 8.19, for two initial particle distribution spacing (Δx). It is seen that both the axial and radial neighbouring mixing indices increase with time and level off at about 0.6 (Figure 8.20 left). This is expected, as there is no interaction between eddies at the selected operational conditions. Using a smaller Δx (higher resolution), increments of both axial and radial neighbouring mixing indices with time are slower, as the domain is composed by a larger number of particles, taking longer times for them to intermix. Figure 8.20 also shows a better mixing performance in the radial than in the axial direction as the asymptotic value is reached faster when fluids A and B are initially displayed in parallel. Using the rate at which *NM* changes with time (i.e. *dMN/dt*) during the first oscillatory cycles for both initial fluid placements, a new index for plug flow (*PF*) can be defined as:

$$PF = \frac{\left(dNM/dt\right)_{axial}}{\left(dNM/dt\right)_{radial}} \tag{8.46}$$

The lower the value of *PF*, the better the plug flow behavior the system can achieve. The slopes in Figure 8.20 together with *PF* values are listed in Table 8.5 where a small *PF* value (0.31) is consistently obtained regardless of Δx, indicating near plug flow performance. Note that computational time constrictions prevented simulaitions with small Δx values from running long enough for an asymptotic *NM(t)* value to be achieved. However, for the sake of demonstration, the results for Δx = 0.001 m are presented here, which accurately predict the ratio of axial to radial *NM* change with time.

Table 8.5. *Change rates of NM and PF values for different flow field resolutions (Δx)*

Δx (m)	$(dNM/dt)_{axial}$	$(dNM/dt)_{radial}$	*PF*
0.001	0.0084	0.0274	0.31
0.00025	0.0219	0.0718	0.31

It should be noted that a more complex and computationally expensive Eulerian-Lagrangian coupled solver (Discrete Phase Model) is required by the FV methodology to provide similar information of individual particles as the one obtained with the SPH.

8.5 Conclusions

In this study, SPH, a relatively new Lagrangian approach, has successfully been implemented and utilised for the first time to model and predict symmetrical flow patterns and to assess mixing efficiency in a 2-dimensional OBR system.

The SPH has effectively captured the expected flow characteristics in an oscillatory baffled reactor and produced clear higher velocity regions at the baffle constriction during strokes 1 and 3, and eddy formation during the change in direction at strokes 2 and 4. The density-smoothing function in SPH is important to offset density fluctuations stemmed from the weakly compressible model. The results from SPH D-S provide a more consistent quasi-steady-state flow and show a higher degree of cycle-repeatability than that from its Eulerian counterpart.

An added advantage of SPH is that it allows quantitative assessments of mixing without the need for additional models like Eulerian based methods, due to its readily available information of individual fluid particles. This work has not only demonstrated its potential to easily implement the existing methods to quantify mixing, such as

velocity ratio and stretch rates, but also proposed new indexes for assessing mixing and plug flow efficiency by making full use of SPH's capabilities. The proposed SPH methodology has great potential for modelling flows when two phases are involved, e.g. solids in liquid in crystallisation processes, as the flow in SPH is driven by particle-particle interaction, allowing for the implementation of new physics based on these interactions; successfully modelling single phase flow is an essential first step forward for multiphase cases.

Chapter 9 Conclusions & Recommendation of Future Work

This chapter presents a summary of the conclusions reached by analysing the findings of this PhD research and lists out some potential future work.

In the area of power density estimation in oscillatory baffled reactors, this work for the first time conducts a detailed analysis and examination of the applicability, capability and deficiencies of two existing models using CFD methodology. The "quasi-steady" model (QSM) [115] over-estimates power dissipation rates due to the inaccurate formulation of two of its geometric parameters for modern COBRs. By using a revised power law dependency on the number-of-baffles term (n^x) and an appropriate orifice discharge coefficient (C_D), it was demonstrated that the updated QSM can not only be used for a much wider application range than previously outlined, but also for both batch and continuous operations. The "eddy enhancement" model (EEM) [116, 117]; generally provides better predictions of power density for the conditions tested; however, its accuracy can substantially be enhanced by applying the aforementioned power law dependency on n and by using an empirical correlation proposed in this work to estimate EEM's "mixing length". After full validation, both models give very similar power density estimations and can be used interchangeably with high confidence.

The causes of energy losses reported by a liquid phase in a COBR, as reported in previous studies [14, 121] and confidential industrial trials, have been analysed by examining power dissipation rates for a wide range of operational and geometrical conditions. This study provides detailed insights into the relationship between power dissipation and pressure drop profiles and reveals that geometries that are perfectly symmetric in the axial direction, i.e. periodically repeatable, do not present signs of energy losses. This was the case even under fully compressible conditions, therefore disregarding the potential energy losses caused by the presence of air bubbles in the system. These findings led to the analysis of the effect of different geometric events that disrupt the axial symmetry of the system, i.e. joints without baffle constriction, sections with a reduced cross-sectional area of the baffle constriction and bend joints. The results revealed that the presence of sections missing one or multiple baffle constrictions led to a decrement in power dissipation rates, which is caused by the eddy shedding phenomenon within the missing baffle sections. Inevitably, this translates in lower velocities experienced by the fluid within certain sections of the device. On the other hand, sections with a reduced cross-sectional area of the baffle constriction and bend

joints do not yield energy losses in the device; as a matter in fact, they require a higher power density for the flow to overcome these constraints. This is in agreement with the early work of Brunold et al. (1989) [78] on energy losses for oscillatory flow in ducts containing sharp edges.

In the area of multiphase (S-L) flow in COBR, this work, for the first time, investigates the effects of particle size on axial dispersion, evaluates particles' residence times and velocities and quantifies the oscillation dampening experienced by solid particles in a COBR. A primary Eulerian liquid phase is coupled with a secondary discrete Lagrangian phase consisting of solid particles of given density and size, providing insights on how particles behave in a COBR. It was observed that as particles increases in size, dampening of their oscillatory velocity occurred, translating into smaller axial dispersion and longer residence times; this agrees with experimental observation reported by Ejim et al. and Kacker et al. [46, 47]. This phenomenon inevitably translates into reduction of particles' suspension, which was quantified in this work. Additionally, both perfect and imperfect pulse methods are used to determine axial dispersion, the latter providing more reliable results.

Finally, in the front of numerical modelling, this PhD research presents an alternative Lagrangian based methodology, Smoothed-Particle Hydrodynamics (SPH), for the numerical prediction of flow patterns in OBRs and for the assessment of their mixing performance. An SPH solver is hence developed and employed, for the first time, in the modelling of single phase flow in a two-dimensional OBR. The results obtained were compared with those from Eulerian modelling, i.e. Finite Volume (FV) method. SPH has successfully captured the expected flow characteristics in OBR as clearly and equally as its Eulerian counterpart, thereby validating the SPH method. Since SPH provides historical information of individually tracked fluid packets/particles in the domain of interest, it allows for readily quantitative assessments of mixing without additional models. Two new indexes to assess mixing and plug flow efficiency have been proposed by making full use of SPH's capabilities.

Here is by no means an exhaustive list for some potential future work:

- In the area of energy loss assessment for single liquid phase, the current work presented the impact that some geometric events may have. However, the effect of common foreign geometries in experimental setups, such as PAT probes, on energy lose is worth investigating. Moreover, the current research was

conducted exclusively in DN15 COBRs; future research could broaden this area of knowledge by examining different operating and geometric conditions in reactors of different scales.

- This research set the basis for understanding the behaviour of solid particles of different sizes for multiphase flows in COBRs. However, other features that should be considered in future research are: collision between particles of the same size, collision between particles of different size, breakage and agglomeration of particles.

- The current research presented Smoothed-Particle Hydrodynamics (SPH) as a viable methodology for the simulation of fluid flow in OBRs. While this work was exclusively carried out for a single liquid phase, it was a necessary step towards multiphase modelling. SPH, due to its Lagrangian implicit nature, offers a wide range of possibilities for the inclusion of new physics, e.g. nucleation and growth kinetics of solids, rules for agglomeration and breakage, and the inclusion of population balance equations; all this is based on particle-particle interaction, since it is the driving force behind SPH methodology. Therefore, a new door has been opened into the future for multiphase flow modelling in OBRs. Additionally, future work may consider more complex geometries in three dimensions, which will demand higher computational power. Thus, the self-written SPH solver should be parallelised; this will permit running simulations in multiple cores, enhancing its computational efficiency.

References

1. Chew, C.M., et al., *Crystallization of Paracetamol under Oscillatory Flow Mixing Conditions.* Crystal Growth & Design, 2004. **4**(5): p. 1045-1052.

2. Ni, X., et al., *On the Crystal Polymorphic Forms of l-Glutamic Acid Following Temperature Programmed Crystallization in a Batch Oscillatory Baffled Crystallizer.* Crystal Growth & Design, 2004. **4**(6): p. 1129-1135.

3. Chew, C.M. and R.I. Ristic, *Crystallization by oscillatory and conventional mixing at constant power density.* AIChE Journal, 2005. **51**(5): p. 1576-1579.

4. Ristic, R.I., *Oscillatory Mixing for Crystallization of High Crystal Perfection Pharmaceuticals.* Chemical Engineering Research and Design, 2007. **85**(7): p. 937-944.

5. Ni, X. and A. Liao, *Effects of Cooling Rate and Solution Concentration on Solution Crystallization of l-Glutamic Acid in an Oscillatory Baffled Crystallizer.* Crystal Growth & Design, 2008. **8**(8): p. 2875-2881.

6. Lawton, S., et al., *Continuous Crystallization of Pharmaceuticals Using a Continuous Oscillatory Baffled Crystallizer.* Organic Process Research & Development, 2009. **13**(6): p. 1357-1363.

7. Caldeira, R. and X. Ni, *Evaluation and Establishment of a Cleaning Protocol for the Production of Vanisal Sodium and Aspirin Using a Continuous Oscillatory Baffled Reactor.* Organic Process Research & Development, 2009. **13**(6): p. 1080-1087.

8. Ni, X. and A. Liao, *Effects of mixing, seeding, material of baffles and final temperature on solution crystallization of l-glutamic acid in an oscillatory baffled crystallizer.* Chemical Engineering Journal, 2010. **156**(1): p. 226-233.

9. Brown, C.J. and X.-W. Ni, *Evaluation of Growth Kinetics of Antisolvent Crystallization of Paracetamol in an Oscillatory Baffled Crystallizer Utilizing Video Imaging.* Crystal Growth & Design, 2011. **11**(9): p. 3994-4000.

10. Brown, C.J. and X.-W. Ni, *Determination of metastable zone width, mean particle size and detectable number density using video imaging in an oscillatory baffled crystallizer.* CrystEngComm, 2012. **14**(8): p. 2944-2949.

11. Callahan, C.J. and X.-W. Ni, *Probing into Nucleation Mechanisms of Cooling Crystallization of Sodium Chlorate in a Stirred Tank Crystallizer and an Oscillatory Baffled Crystallizer.* Crystal Growth & Design, 2012. **12**(5): p. 2525-2532.

12. Callahan, C.J., *PhD thesis: The influence of hydrodynamic environment on the nucleation mechanism of a chiral crystallization*, in *Department of Chemical Engineering*. 2014, Heriot-Watt University: Edinburgh, Scotland.

13. Callahan, C.J. and X.-W. Ni, *An investigation into the effect of mixing on the secondary nucleation of sodium chlorate in a stirred tank and an oscillatory baffled crystallizer.* CrystEngComm, 2014. **16**(4): p. 690-697.

14. Briggs, N.E.B., *PhD thesis: Polymorph control of pharmaceuticals within a continuous oscillatory baffled crystalliser*, in *Institute of Pharmacy and Biomedical Sciences*. 2015, University of Strathclyde: Glasgow, Scotland.

15. Briggs, N.E.B., et al., *Seeded Crystallization of β-l-Glutamic Acid in a Continuous Oscillatory Baffled Crystallizer.* Organic Process Research & Development, 2015. **19**(12): p. 1903-1911.

16. Brown, C.J., J.A. Adelakun, and X.-w. Ni, *Characterization and modelling of antisolvent crystallization of salicylic acid in a continuous oscillatory baffled crystallizer.* Chemical Engineering and Processing: Process Intensification, 2015. **97**: p. 180-186.

17. Su, Q., et al., *Mathematical Modeling, Design, and Optimization of a Multisegment Multiaddition Plug-Flow Crystallizer for Antisolvent Crystallizations.* Organic Process Research & Development, 2015. **19**(12): p. 1859-1870.

18. Ni, X., Y. Zhang, and I. Mustafa, *Correction of Polymer Particle Size with Droplet Size in Suspension Polymerisation of Methylmethacrylate in a Batch*

Oscillatory Baffled Reactor. Chemical Engineering Science, 1999. **54**: p. 841-850.

19. Phan, A.N., A.P. Harvey, and M. Rawcliffe, *Continuous screening of base-catalysed biodiesel production using New designs of mesoscale oscillatory baffled reactors.* Fuel Processing Technology, 2011. **92**(8): p. 1560-1567.

20. Phan, A.N., A.P. Harvey, and V. Eze, *Rapid Production of Biodiesel in Mesoscale Oscillatory Baffled Reactors.* Chemical Engineering & Technology, 2012. **35**(7): p. 1214-1220.

21. Wilson, B., X. Ni, and D.C. Sherrington, *On the Investigation of a Phase-Transfer Catalysis Reaction in an Oscillatory Baffled Reactor.* Industrial & Engineering Chemistry Research, 2001. **40**(23): p. 5300-5304.

22. Eze, V.C., et al., *Heterogeneous catalysis in an oscillatory baffled flow reactor.* Catalysis Science & Technology, 2013. **3**(9): p. 2373-2379.

23. Navarro Fuentes, F., M.A. Keane, and X. Ni, *A comparative evaluation of a multiphase catalytic hydrogenation in an oscillatory baffled reactor and a stirred tank reactor.* Organic Process Research & Development, 2018. **Submitted**.

24. Gaidhani, H.K., B. McNeil, and X.-W. Ni, *Production of pullulan using an oscillatory baffled bioreactor.* Journal of Chemical Technology & Biotechnology, 2003. **78**(2-3): p. 260-264.

25. Jambi, E., et al., *Comparative study of the power consumption on the production of xanthan using the traditional industrial stirred tank reactor and a novel oscillatory baffled reactor.* Life Science Journal, 2013. **10**(4): p. 2241-2249.

26. McDonough, J.R., A.N. Phan, and A.P. Harvey, *Rapid process development using oscillatory baffled mesoreactors – A state-of-the-art review.* Chemical Engineering Journal, 2015. **265**(0): p. 110-121.

27. Dickens, A.W., M.R. Mackley, and H.R. Williams, *Experimental residence time distribution measurements for unsteady flow in baffled tubes.* Chemical Engineering Science, 1989. **44**(7): p. 1471-1479.

28. Howes, T., M.R. Mackley, and E.P.L. Roberts, *The simulation of chaotic mixing and dispersion for periodic flows in baffled channels.* Chemical Engineering Science, 1991. **46**(7): p. 1669-1677.

29. Mackley, M.R. and X. Ni, *Experimental fluid dispersion measurements in periodic baffled tube arrays.* Chemical Engineering Science, 1993. **48**(18): p. 3293-3305.

30. Ni, X., *Residence time distribution measurements in a pulsed baffled tube bundle.* Journal of Chemical Technology & Biotechnology, 1994. **59**(3): p. 213-221.

31. Ni, X., *A study of fluid dispersion in oscillatory flow through a baffled tube.* Journal of Chemical Technology & Biotechnology, 1995. **64**(2): p. 165-174.

32. Ni, X., et al., *A Systematic Study of the Effect of Geometrical Parameters on Mixing Time in Oscillatory Baffled Columns.* Chemical Engineering Research and Design, 1998. **76**(5): p. 635-642.

33. Ni, X. and C.C. Stevenson, *On the effect of gap size between baffle outer diameter and tube inner diameter on the mixing characteristics in an oscillatory-baffled column.* Journal of Chemical Technology & Biotechnology, 1999. **74**(6): p. 587-593.

34. Ni, X. and N.E. Pereira, *Parameters affecting fluid dispersion in a continuous oscillatory baffled tube.* AIChE Journal, 2000. **46**(1): p. 37-45.

35. Ni, X., et al., *On the effect of tracer density on axial dispersion in a batch oscillatory baffled column.* Chemical Engineering Journal, 2002. **85**(1): p. 17-25.

36. Jian, H. and X.-W. Ni, *On modelling turbulent flow in an oscillatory baffled column – RANS model or large-eddy simulation?* Journal of Chemical Technology & Biotechnology, 2003. **78**(2-3): p. 321-325.

37. Reis, N., et al., *Residence times and mixing of a novel continuous oscillatory flow screening reactor.* Chemical Engineering Science, 2004. **59**(22–23): p. 4967-4974.

38. Zheng, M. and M. Mackley, *The axial dispersion performance of an oscillatory flow meso-reactor with relevance to continuous flow operation.* Chemical Engineering Science, 2008. **63**(7): p. 1788-1799.

39. Phan, A.N. and A. Harvey, *Development and evaluation of novel designs of continuous mesoscale oscillatory baffled reactors.* Chemical Engineering Journal, 2010. **159**(1–3): p. 212-219.

40. Reis, N., A.A. Vicente, and J.A. Teixeira, *Liquid backmixing in oscillatory flow through a periodically constricted meso-tube.* Chemical Engineering and Processing: Process Intensification, 2010. **49**(7): p. 793-803.

41. Phan, A.N., A. Harvey, and J. Lavender, *Characterisation of fluid mixing in novel designs of mesoscale oscillatory baffled reactors operating at low flow rates (0.3–0.6 ml/min).* Chemical Engineering and Processing: Process Intensification, 2011. **50**(3): p. 254-263.

42. Phan, A.N. and A.P. Harvey, *Effect of geometrical parameters on fluid mixing in novel mesoscale oscillatory helical baffled designs.* Chemical Engineering Journal, 2011. **169**(1–3): p. 339-347.

43. Manninen, M., et al., *Evaluation of axial dispersion and mixing performance in oscillatory baffled reactors using CFD.* Journal of Chemical Technology & Biotechnology, 2013. **88**(4): p. 553-562.

44. González-Juárez, D., et al., *Residence time distribution in multiorifice baffled tubes: A numerical study.* Chemical Engineering Research and Design, 2017. **118**: p. 259-269.

45. Kimuli, E.N., et al., *Characterisation of axial dispersion in a Meso-scale Oscillatory Baffled Crystalliser using a Numerical Approach,* in *Computer Aided Chemical Engineering*, A. Espuña, M. Graells, and L. Puigjaner, Editors. 2017, Elsevier. p. 223-228.

46. Ejim, L.N., et al., *A factorial approach to understanding the effect of inner geometry of baffled meso-scale tubes on solids suspension and axial dispersion in continuous, oscillatory liquid–solid plug flows.* Chemical Engineering Journal, 2017. **308**: p. 669-682.

47. Kacker, R., S.I. Regensburg, and H.J.M. Kramer, *Residence time distribution of dispersed liquid and solid phase in a continuous oscillatory flow baffled crystallizer.* Chemical Engineering Journal, 2017. **317**(Supplement C): p. 413-423.

48. Mackley, M.R. and E.P.L. Roberts, *Mixing and flow patterns for unsteady flow in baffled channels.* Generals Papers in Fluid Engineering AIChE. , 1991. **127**: p. 57-64.

49. Roberts, E.P.L., *A numerical and experimental study of transition processes in an obstructed channel flow.* Journal of Fluid Mechanics, 1994. **260**: p. 185-209.

50. Roberts, E.P.L. and M.R. Mackley, *The simulation of stretch rates for the quantitative prediction and mapping of mixing within a channel flow.* Chemical Engineering Science, 1995. **50**(23): p. 3727-3746.

51. Roberts, E.P.L. and M.R. Mackley, *The development of asymmetry and period doubling for oscillatory flow in baffled channels.* Journal of Fluid Mechanics, 1996. **328**: p. 19-48.

52. Howes, T. and P.J. Shardlow, *Simulation of mixing in unsteady flow through a periodically obstructed channel.* Chemical Engineering Science, 1997. **52**(7): p. 1215-1225.

53. Mackley, M.R. and R.M.C. Neves Saraiva, *The quantitative description of fluid mixing using Lagrangian- and concentration-based numerical approaches.* Chemical Engineering Science, 1999. **54**(2): p. 159-170.

54. Ni, X., H. Jian, and A.W. Fitch, *Computational fluid dynamic modelling of flow patterns in an oscillatory baffled column.* Chemical Engineering Science, 2002. **57**(14): p. 2849-2862.

55. Ni, X., H. Jian, and A. Fitch, *Evaluation of Turbulent Integral Length Scale in an Oscillatory Baffled Column Using Large Eddy Simulation and Digital Particle Image Velocimetry.* Chemical Engineering Research and Design, 2003. **81**(8): p. 842-853.

56. Chew, C.M., et al., *Characterisation of impeller driven and oscillatory mixing by spatial and temporal shear rate distributions.* Chemical Engineering Science, 2004. **59**(7): p. 1557-1568.

57. Fitch, A.W., H. Jian, and X. Ni, *An investigation of the effect of viscosity on mixing in an oscillatory baffled column using digital particle image velocimetry and computational fluid dynamics simulation.* Chemical Engineering Journal, 2005. **112**(1–3): p. 197-210.

58. Jian, H. and X. Ni, *A numerical study on the scale-up behaviour in oscillatory baffled columns.* Chemical Engineering Research and Design, 2005. **83**(10): p. 1163-1170.

59. Reis, N., et al., *Fluid mechanics and design aspects of a novel oscillatory flow screening mesoreactor.* Chemical Engineering Research and Design, 2005. **83**(4): p. 357-371.

60. Zheng, M., et al., *The development of asymmetry for oscillatory flow within a tube containing sharp edge periodic baffles.* Physics of Fluids, 2007. **19**(11): p. 114101.

61. Deng, R., et al., *Taylor vortex flow in presence of internal baffles.* Chemical Engineering Science, 2010. **65**(16): p. 4598-4605.

62. Hamzah, A.A., et al., *Effect of oscillation amplitude on velocity distributions in an oscillatory baffled column (OBC).* Chemical Engineering Research and Design, 2012. **90**(8): p. 1038-1044.

63. Nogueira, X., et al., *Experimental and computational modeling of oscillatory flow within a baffled tube containing periodic-tri-orifice baffle geometries.* Computers & Chemical Engineering, 2013. **49**(0): p. 1-17.

64. Mazubert, A., et al., *Hydrodynamics and mixing in continuous oscillatory flow reactors—Part I: Effect of baffle geometry.* Chemical Engineering and Processing: Process Intensification, 2016. **108**: p. 78-92.

65. Mazubert, A., et al., *Hydrodynamics and mixing in continuous oscillatory flow reactors—Part II: Characterisation methods.* Chemical Engineering and Processing: Process Intensification, 2016. **102**: p. 102-116.

66. Jimeno, G., Y.C. Lee, and X.-W. Ni, *On the evaluation of power density models for oscillatory baffled reactors using CFD.* Chemical Engineering and Processing - Process Intensification, 2018. **134**: p. 153-162.

67. Jimeno, G., Y.C. Lee, and X.-W. Ni, *The effect of particle size on flow in a continuous oscillatory baffled reactor using CFD.* **Submitted to Computers & Chemical Engineering**.

68. Jimeno, G., Y.C. Lee, and X.-W. Ni, *Smoothed particle hydrodynamics – A new approach for modeling flow in oscillatory baffled reactors.* Computers & Chemical Engineering, 2019. **124**: p. 14-27.

69. Mackley, M.R. and X. Ni, *Mixing and dispersion in a baffled tube for steady laminar and pulsatile flow.* Chemical Engineering Science, 1991. **46**(12): p. 3139-3151.

70. Ni, X., et al., *Scale-up of single phase axial dispersion coefficients in batch and continuous oscillatory baffled tubes.* The Canadian Journal of Chemical Engineering, 2001. **79**(3): p. 444-448.

71. Van Dijck, W.J.D., *Tower with internal perforated plate suitable for extracting liquids by treatment with other liquids and for similar concurrent processes.* US Patent, 1935. **2011186**.

72. Karr, A.E., *Performance of a reciprocating-plate extraction column.* AIChE Journal, 1959. **5**(4): p. 446-452.

73. Bellhouse, B.J., et al., *A high efficiency membrane oxygenator and pulsatile pumping system, and its application to animal trials.* ASAIO Journal, 1973. **19**(1): p. 72-79.

74. Sobey, I.J., *On flow through furrowed channels. Part 1. Calculated flow patterns.* Journal of Fluid Mechanics, 1980. **96**(1): p. 1-26.

75. Stephanoff, K.D., I.J. Sobey, and B.J. Bellhouse, *On flow through furrowed channels. Part 2. Observed flow patterns.* Journal of Fluid Mechanics, 1980. **96**(1): p. 27-32.

76. Knott, G.F. and M.R. Mackley, *On Eddy Motions Near Plates and Ducts, Induced by Water Waves and Periodic Flows.* Philosophical Transactions of the Royal Society of London. Series A, Mathematical and Physical Sciences, 1980. **294**(1412): p. 599-623.

77. Mackley, M.R., *Using oscillatory flow to improve performance.* Chemical Engineer, 1987. **443**: p. 18-20.

78. Brunold, C.R., et al., *Experimental observations on flow patterns and energy losses for oscillatory flow in ducts containing sharp edges.* Chemical Engineering Science, 1989. **44**(5): p. 1227-1244.

79. Howes, T. and M.R. Mackley, *Experimental axial dispersion for oscillatory flow through a baffled tube.* Chemical Engineering Science, 1990. **45**(5): p. 1349-1358.

80. Howes, T., *PhD Thesis: On the dispersion of unsteady flow in bafled tubes*. 1988, University of Cambridge: Cambridge, England.

81. Hewgill, M.R., et al., *Enhancement of gas-liquid mass transfer using oscillatory flow in a baffled tube.* Chemical Engineering Science, 1993. **48**(4): p. 799-809.

82. Ni, X. and S. Gao, *Mass transfer characteristics of a pilot pulsed baffled reactor.* Journal of Chemical Technology & Biotechnology, 1996. **65**(1): p. 65-71.

83. Mackley, M.R., G.M. Tweddle, and I.D. Wyatt, *Experimental heat transfer measurements for pulsatile flow in baffled tubes.* Chemical Engineering Science, 1990. **45**(5): p. 1237-1242.

84. Ni, X. and S. Gao, *Scale-up correlation for mass transfer coefficients in pulsed baffled reactors.* The Chemical Engineering Journal, 1996. **63**(3): p. 157-166.

85. Ni, X., et al., *A comparative study of mass transfer in yeast for a batch pulsed baffled bioreactor and a stirred tank fermenter.* Chemical Engineering Science, 1995. **50**(13): p. 2127-2136.

86. Mackley, M.R., et al., *Residence time distribution enhancement in reactors using oscillatory flow.* Chemical Engineering Research & Design, 1996. **74**(5): p. 541-545.

87. Callahan, C.J. and X.-W. Ni, *On the investigation of the effect of apparatus configurations on the nucleation mechanisms in a cooling crystallization of sodium chlorate.* The Canadian Journal of Chemical Engineering, 2014. **92**(11): p. 1920-1925.

88. Brown, C.J., et al., *Evaluation of crystallization kinetics of adipic acid in an oscillatory baffled crystallizer.* CrystEngComm, 2014. **16**(34): p. 8008-8014.

89. McLachlan, H. and X.-W. Ni, *An Investigation into Parameters Affecting Crystal Purity of Urea in a Stirred Tank and an Oscillatory Baffled Crystallizer.* Chemical Engineering Communications, 2016. **203**(9): p. 1189-1197.

90. McLachlan, H. and X.-W. Ni, *On the effect of added impurity on crystal purity of urea in an oscillatory baffled crystallizer and a stirred tank crystallizer.* Journal of Crystal Growth, 2016. **442**: p. 81-88.

91. Zhao, L., et al., *From discovery to scale-up: α-lipoic acid : nicotinamide co-crystals in a continuous oscillatory baffled crystalliser.* CrystEngComm, 2014. **16**(26): p. 5769-5780.

92. Adelakun, J.A. and X.-W. Ni, *On the Kinetics of Palm Oil Crystallisation.* International Journal of Engineering Research & Science (IJOER) 2016. **2**(10): p. 1-12.

93. Brown, C.J. and X. Ni, *Evaluation of rate of cyclopentane hydrate formation in an oscillatory baffled column using laser induced fluorescence and energy balance.* Chemical Engineering Journal, 2010. **157**(1): p. 131-139.

94. Agnew, L.R., et al., *Continuous Crystallization of Paracetamol (Acetaminophen) Form II: Selective Access to a Metastable Solid Form.* Crystal Growth & Design, 2017. **17**(5): p. 2418-2427.

95. Brown, C.J. and X. Ni, *Online Evaluation of Paracetamol Antisolvent Crystallization Growth Rate with Video Imaging in an Oscillatory Baffled Crystallizer.* Crystal Growth & Design, 2011. **11**(3): p. 719-725.

96. Bird, R.B., W.E. Stewart, and E.N. Lightfoot, *Transport Phenomena*. 2007: Wiley.

97. Binnie, A.M., *A double-refraction method of detecting turbulence in liquids.* Proceedings of the Physical Society, 1945. **57**(5): p. 390.

98. Sarpkaya, T., *Experimental Determination of the Critical Reynolds Number for Pulsating Poiseuille Flow.* Journal of Basic Engineering, 1966. **88**(3): p. 589-598.

99. Wang, Y., et al., *Oscillatory flow within porous tubes containing wall or central baffles.* Chemical Engineering Research & Design, 1994. **72**: p. 686-694.

100. Sobey, I.J., *Observation of waves during oscillatory channel flow.* Journal of Fluid Mechanics, 1985. **151**: p. 395-426.

101. Ni, X. and P. Gough, *On the discussion of the dimensionless groups governing oscillatory flow in a baffled tube.* Chemical Engineering Science, 1997. **52**(18): p. 3209-3212.

102. Stonestreet, P. and P.M.J. Van Der Veeken, *The Effects of Oscillatory Flow and Bulk Flow Components on Residence Time Distribution in Baffled Tube Reactors.* Chemical Engineering Research and Design, 1999. **77**(8): p. 671-684.

103. Harvey, A.P., M.R. Mackley, and P. Stonestreet, *Operation and Optimization of an Oscillatory Flow Continuous Reactor.* Industrial & Engineering Chemistry Research, 2001. **40**(23): p. 5371-5377.

104. McGlone, T., et al., *Oscillatory Flow Reactors (OFRs) for Continuous Manufacturing and Crystallization.* Organic Process Research & Development, 2015. **19**(9): p. 1186-1202.

105. Zhang, Y., X. Ni, and I. Mustafa, *A study of oil–water dispersion in a pulsed baffled reactor.* Journal of Chemical Technology & Biotechnology, 1996. **66**(3): p. 305-311.

106. Gough, P., X. Ni, and K.C. Symes, *Experimental Flow Visualisation in a Modified Pulsed Baffled Reactor.* Journal of Chemical Technology & Biotechnology, 1997. **69**(3): p. 321-328.

107. Ni, X., et al., *On the measurement of strain rate in an oscillatory baffled column using particle image velocimetry.* Chemical Engineering Science, 2000. **55**(16): p. 3195-3208.

108. Fitch, A.W., X. Ni, and J. Stewart, *Characterisation of flexible baffles in an oscillatory baffled column.* Journal of Chemical Technology & Biotechnology, 2001. **76**(10): p. 1074-1079.

109. González-Juárez, D., R. Herrero-Martín, and J.P. Solano, *Enhanced heat transfer and power dissipation in oscillatory-flow tubes with circular-orifice baffles: a numerical study.* Applied Thermal Engineering, 2018. **141**: p. 494-502.

110. Ni, X., Y. Zhang, and I. Mustafa, *An investigation of droplet size and size distribution in methylmethacrylate suspensions in a batch oscillatory-baffled reactor.* Chemical Engineering Science, 1998. **53**(16): p. 2903-2919.

111. Ni, X., G. Nelson, and I. Mustafa, *Flow patterns and oil – water dispersion in a 0.38 m diameter oscillatory baffled column.* The Canadian Journal of Chemical Engineering, 2000. **78**(1): p. 211-220.

112. Aoun Nabli, M., P. Guiraud, and C. Gourdon, *Numerical experimentation: a tool to calculate the axial dispersion coefficient in discs and doughnuts pulsed solvent extraction columns.* Chemical Engineering Science, 1997. **52**(14): p. 2353-2368.

113. Nagata, S., *Mixing: Principles and applications*. 1975, Tokyo: Kodansha Ltd.

114. Ni, X. and M.R. Mackley, *Chemical reaction in batch pulsatile flow and stirred tank reactors.* The Chemical Engineering Journal, 1993. **52**(3): p. 107-114.

115. Jealous, A.C. and H.F. Johnson, *Power requirements for pulse generation in pulse columns.* Industrial & Engineering Chemistry, 1955. **47**(6): p. 1159-1166.

116. Baird, M.H.I. and P. Stonestreet, *Energy dissipation in oscillatory flow within a baffled tube.* Trans. IChem.E., 1995. **73**(A): p. 503-511.

117. Mackley, M.R. and P. Stonestreet, *Heat transfer and associated energy dissipation for oscillatory flow in baffled tubes.* Chemical Engineering Science, 1995. **50**(14): p. 2211-2224.

118. Stonestreet, P. and A.P. Harvey, *A Mixing-Based Design Methodology for Continuous Oscillatory Flow Reactors.* Chemical Engineering Research and Design, 2002. **80**(1): p. 31-44.

119. Lobry, E., et al., *Liquid–liquid dispersion in a continuous oscillatory baffled reactor – Application to suspension polymerization.* Chemical Engineering Journal, 2015. **259**: p. 505-518.

120. Mackay, M., M.R. Mackley, and Y. Wang, *Oscillatory flow within tubes containing wall or central baffles.* Trans I.Chem.E., 1991. **69**: p. 506-513.

121. Taylor, B.J., *PhD thesis: Oscillatory Flow Mixing in a Novel Photobioreactor for Enhanced Algal Growth*, in *Department of Chemical Engineering and Biotechnology*. 2011, University of Cambridge: Cambridge, England.

122. Levenspiel, O. and W.K. Smith, *Notes on the diffusion-type model for the longitudinal mixing of fluids in flow.* Chemical Engineering Science, 1957. **6**: p. 227-233.

123. Palma, M. and R. Giudici, *Analysis of axial dispersion in an oscillatory-flow continuous reactor.* Chemical Engineering Journal, 2003. **94**(3): p. 189-198.

124. Smith, K.B. and M.R. Mackley, *An Experimental Investigation into the Scale-up of Oscillatory Flow Mixing in Baffled Tubes.* Chemical Engineering Research and Design, 2006. **84**(11): p. 1001-1011.

125. Oliva, J.A., et al., *Experimental investigation of the effect of scale-up on mixing efficiency in oscillatory flow baffled reactors (OFBR) using principal component based image analysis as a novel noninvasive residence time distribution measurement approach.* Chemical Engineering Journal, 2018. **351**: p. 498-505.

126. Fitch, A.W. and X. Ni, *On the determination of axial dispersion coefficient in a batch oscillatory baffled column using laser induced fluorescence.* Chemical Engineering Journal, 2003. **92**(1–3): p. 243-253.

127. Fitch, A.W. and X. Ni, *Using non-intrusive laser-induced fluorescence in the characterisation of mixing in an oscillatory baffled column.* Journal of Chemical Technology & Biotechnology, 2003. **78**(2-3): p. 326-331.

128. Baptista, P.N., et al., *The effect of mixing particles with different characteristics on the residence time distribution of particles in two-phase flow in a tubular system.* Journal of Food Engineering, 1996. **29**(3): p. 361-373.

129. Levenspiel, O., *Chemical Reaction Engineeing*. Third ed. 2006: John Wiley & Sons.

130. Mecklenburg, J.C. and S. Hartland, *The theory of backmixing*. 1975, London: John Wiley & Sons.

131. Anderson, C.J., M.C. Harris, and D.A. Deglon, *Flotation in a novel oscillatory baffled column.* Minerals Engineering, 2009. **22**(12): p. 1079-1087.

132. Sobey, I.J., *The occurrence of separation in oscillatory flow.* Journal of Fluid Mechanics, 1983. **134**: p. 247-257.

133. Ralph, M.E., *Oscillatory flows in wavy-walled tubes.* Journal of Fluid Mechanics, 1986. **168**: p. 515-540.

134. Ghaddar, N., A. Patera, and B. Mikic, *Heat transfer enhancement in oscillatory flow in a grooved channel*, in *22nd Aerospace Sciences Meeting*. 1984, American Institute of Aeronautics and Astronautics.

135. Ghaddar, N.K., et al., *Numerical investigation of incompressible flow in grooved channels. Part 2. Resonance and oscillatory heat-transfer enhancement.* Journal of Fluid Mechanics, 1986. **168**: p. 541-567.

136. Roberts, E.P.L., *PhD Thesis: Unsteady flow and mixing in baffled channels*. 1992, University of Cambridge: Cambridge, England.

137. Yang, C. and Z.-S. Mao, *Chapter 6 - Crystallizers: CFD–PBE modeling*, in *Numerical Simulation of Multiphase Reactors with Continuous Liquid Phase*. 2014, Academic Press: Oxford. p. 263-294.

138. Pozrikidis, C., *Introduction to Theoretical and Computational Fluid Dynamics*. 2011: OUP USA.

139. ANSYS, I., *ANSYS® Fluent Theory Guide, Release 15.0*. 2013.

140. Chorin, A.J., *Numerical Solution of the Navier-Stokes Equations.* Mathematics of Computation, 1968. **22**(104): p. 745-762.

141. Courant, R., K. Friedrichs, and H. Lewy, *Über die partiellen Differenzengleichungen der mathematischen Physik.* Mathematische Annalen, 1928. **100**(1): p. 32-74.

142. Ekambara, K. and M.T. Dhotre, *Simulation of oscillatory baffled column: CFD and population balance.* Chemical Engineering Science, 2007. **62**(24): p. 7205-7213.

143. Panton, R.L. and A.L. Goldman, *Correlation of nonlinear orifice impedance.* The Journal of the Acoustical Society of America, 1976. **60**(6): p. 1390-1396.

144. Jian, H., *PhD thesis: Understanding unsteadiness and turbulence in two chemical engineering systems*, in *Department of Chemical Engineering*. 2002, Heriot-Watt University: Edinburgh, Scotland.

145. W. Miller, R., *Flow Measurement Engineering Handbook*. Third ed. 1996: McGraw-Hill Education.

146. Taylor, G.I., *The dispersion of matter in turbulent flow through a pipe.* Proceedings of the Royal Society of London. Series A. Mathematical and Physical Sciences, 1954. **223**(1155): p. 446-468.

147. Eze, V.C., et al., *Intensification of carboxylic acid esterification using a solid catalyst in a mesoscale oscillatory baffled reactor platform.* Chemical Engineering Journal, 2017. **322**: p. 205-214.

148. Brown, C.J., et al., *Enabling precision manufacturing of active pharmaceutical ingredients: workflow for seeded cooling continuous crystallisations.* Molecular Systems Design & Engineering, 2018. **3**(3): p. 518-549.

149. Vilar, G., et al., *On line analysis of structure of dispersions in an oscillatory baffled reactor using electrical impedance tomography.* Chemical Engineering Journal, 2008. **141**(1–3): p. 58-66.

150. Ristic, R.I., et al., *Macro- and Micromorphology of Monoclinic Paracetamol Grown from Pure Aqueous Solution.* The Journal of Physical Chemistry B, 2001. **105**(38): p. 9057-9066.

151. Nagy, Z.K., et al., *Determination of the Kinetic Parameters for the Crystallization of Paracetamol from Water Using Metastable Zone Width Experiments.* Industrial & Engineering Chemistry Research, 2008. **47**(4): p. 1245-1252.

152. Li, J. and M.F. Doherty, *Steady State Morphologies of Paracetamol Crystal from Different Solvents.* Crystal Growth & Design, 2017. **17**(2): p. 659-670.

153. Jolliffe, H.G. and D.I. Gerogiorgis, *Process modelling, design and technoeconomic evaluation for continuous paracetamol crystallisation.* Computers & Chemical Engineering, 2018. **118**: p. 224-235.

154. Barthe, S.C., M.A. Grover, and R.W. Rousseau, *Observation of Polymorphic Change through Analysis of FBRM Data: Transformation of Paracetamol from Form II to Form I.* Crystal Growth & Design, 2008. **8**(9): p. 3316-3322.

155. Morsi, S.A. and A.J. Alexander, *An investigation of particle trajectories in two-phase flow systems.* Journal of Fluid Mechanics, 1972. **55**(2): p. 193-208.

156. ANSYS, I., *ANSYS® Fluent User's Guide, Release 15.0*. 2013.

157. Aubin, J., et al., *Effect of microchannel aspect ratio on residence time distributions and the axial dispersion coefficient.* Chemical Engineering and Processing: Process Intensification, 2009. **48**(1): p. 554-559.

158. Aris, R., *Notes on the diffusion-type model for longitudinal mixing in flow.* Chemical Engineering Science, 1959. **9**(4): p. 266-267.

159. Göebel, J.C., K. Booij, and J.M.H. Fortuin, *Axial dispersion in single-phase flow in pulsed packed columns.* Chemical Engineering Science, 1986. **41**(12): p. 3197-3203.

160. Fogler, H.S., *Elements of Chemical Reaction Engineering*. 2006: Prentice Hall PTR.

161. Westerterp, K.R., W.P.M. Van Swaaij, and A.A.C.M. Beenackers, *Chemical Reactor Design and Operation*. 1984: John Wiley & Sons.

162. Smith, K.B., *PhD thesis: Scale-up of oscillatory flow mixing*, in *Department of Chemical Engineering*. 2000, University of Cambridge: Cambridge, England.

163. Heywood, N.I., *Stop your slurries from stirring up trouble.* Chem. Eng. Prog., 1999. **95**(9): p. 21-41.

164. Yang, X., et al., *Risk Considerations on Developing a Continuous Crystallization System for Carbamazepine.* Organic Process Research & Development, 2017. **21**(7): p. 1021-1033.

165. Wilson, B., X. Ni, and D.C. Sherrington, *On the investigation of phase-transfer catalysis reaction in an oscillatory baffled reactor.* Journal of Industrial and Engineering Chemistry Research, 2001. **40**(23): p. 5300-5304.

166. Phan, A.N., A.P. Harvey, and V. Eze, *Rapid production of biodiesel in mesoscale oscillatory baffled reactors.* Chemical Engineering and Technology, 2012. **35**(7): p. 1214-1220.

167. Eze, V.C., et al., *Intensification of carboxylic acid esterification using a solid catalyst in a mesoscale oscillatory baffled reactor platform.* The Chemical Engineering Journal, 2017. **322**: p. 205-214.

168. Navarro Fuentes, F., M.A. Keane, and X. Ni, *A comparative evaluation of a multiphase catalytic hydrogenation in an oscillatory baffled reactor and a stirred tank reactor.* Organic Research Process and Development, 2018. **Submitted**.

169. Agnew, L.R., et al., *Continuous crystallisation of paracetamol (acetaminophen) form II: selective access to a metastable solid form.* Journal of Crystal Growth and Design, 2017. **17**: p. 2418-2427.

170. Brown, C.J. and X. Ni, *Evaluation of growth kinetcis of antisolvent crystallisation of paracetamol in an oscillatory baffled crystalliser utilizing video imaging.* Crystal Growth and Design, 2011. **11**: p. 3994-4000.

171. Brown, C.J., J.A. Adelakun, and X. Ni, *Characterisation and modelling of antisolvent crystallisation of salicylic acid in a continuous oscillatory baffled crystallizer.* Chemical Engineering and Processing, 2015. **97**: p. 180-186.

172. Su, Q., et al., *Mathematical modeling, design, and optimization of a multi-segment multi-addition plug-flow crystallizer for anti-solvent crystallizations.* Organic Process Research & Development, 2015. **19**(12): p. 1859-1870.

173. Feilden, H., *CMAC Bulletin*. 2017: Glasgow, Scotland.

174. Gingold, R.A. and J.J. Monaghan, *Smoothed particle hydrodynamics: theory and application to non-spherical stars.* Monthly Notices of the Royal Astronomical Society, 1977. **181**(3): p. 375-389.

175. Monaghan, J.J., *Smoothed Particle Hydrodynamics.* Annual Review of Astronomy and Astrophysics, 1992. **30**(1): p. 543-574.

176. Violeau, D., *Fluid mechanics and the SPH method : theory and applications*. 2012, Oxford: Oxford University Press.

177. Liu, G.R. and M.B. Liu, *Smoothed Particle Hydrodynamics: A Meshfree Particle Method*. 2003: World Scientific.

178. Dalrymple, R.A. and B.D. Rogers, *Numerical modeling of water waves with the SPH method.* Coastal Engineering, 2006. **53**(2): p. 141-147.

179. Crespo, A.J.C., M. Gomez-Gesteira, and R. Dalrymple, *Boundary conditions generated by dynamic particles in SPH methods.* Computers, Materials, & Continua - Tech Science Press, 2007. **5**(3): p. 173-184.

180. Ferrari, A., et al., *A new 3D parallel SPH scheme for free surface flows.* Computers & Fluids, 2009. **38**(6): p. 1203-1217.

181. Gomez-Gesteira, M., et al., *State-of-the-art of classical SPH for free-surface flows.* Journal of Hydraulic Research, 2010. **48**(sup1): p. 6-27.

182. Adami, S., X.Y. Hu, and N.A. Adams, *A transport-velocity formulation for smoothed particle hydrodynamics.* Journal of Computational Physics, 2013. **241**: p. 292-307.

183. Zhang, C., X.Y. Hu, and N.A. Adams, *A weakly compressible SPH method based on a low-dissipation Riemann solver.* Journal of Computational Physics, 2017. **335**: p. 605-620.

184. Batchelor, G.K., *An Introduction to Fluid Dynamics*. 1974: Cambridge University Press.

185. Lee, E.S., A. University of Manchester. School of Mechanical, and C. Engineering, *Truly Incompressible Approach for Computing Incompressible Flow in SPH and Comparisons with the Traditional Weakly Compressible Approach*. 2007: University of Manchester.

186. Monaghan, J.J., *Simulating Free Surface Flows with SPH.* Journal of Computational Physics, 1994. **110**(2): p. 399-406.

187. Morris, J.P., *A Study of the Stability Properties of Smooth Particle Hydrodynamics.* Publications of the Astronomical Society of Australia, 1996. **13**(1): p. 97-102.

188. Wendland, H., *Piecewise polynomial, positive definite and compactly supported radial functions of minimal degree.* Adv. Comput. Math., 1995. **4**: p. 389-396.

189. Zhang, M., *PhD thesis: Smoothed Particle Hydrodynamics in Materials Processing: Code Development and Applications*. 2007, State University of New York at Stony Brook.

190. Morris, J.P., P.J. Fox, and Y. Zhu, *Modeling Low Reynolds Number Incompressible Flows Using SPH.* Journal of Computational Physics, 1997. **136**(1): p. 214-226.

191. Monaghan, J.J., *Heat conduction with discontinuous conductivity.* Applied Mathematics Reports and Preprints, 1995. **95**(18): p. 7-1.

192. Belytschko, T., et al., *On the completeness of meshfree particle methods.* International Journal for Numerical Methods in Engineering, 1998. **43**(5): p. 785-819.

193. Dilts, G.A., *Moving-least-squares-particle hydrodynamics—I. Consistency and stability.* International Journal for Numerical Methods in Engineering, 1999. **44**(8): p. 1115-1155.

194. Colagrossi, A. and M. Landrini, *Numerical simulation of interfacial flows by smoothed particle hydrodynamics.* Journal of Computational Physics, 2003. **191**(2): p. 448-475.

195. Verlet, L., *Computer "Experiments" on Classical Fluids. I. Thermodynamical Properties of Lennard-Jones Molecules.* Physical Review, 1967. **159**(1): p. 98-103.

196. Ottino, J.M., *The Kinematics of Mixing: Stretching, Chaos, and Transport*. 1989: Cambridge University Press.

197. Panizzo, A., *PhD thesis: Physical and numerical modelling of subaerial landslide generated waves*. 2004, Universita degli Studi di L'Aquila.

198. Daily, J.W. and D.R.F. Harleman, *Fluid dynamics*. 1966, Reading, MA: Addison-Wesley.

199. Schlichting, H., *Boundary-layer theory*. 1979, New York: McGraw-Hill.

200. White, F.M., *Viscous fluid flow, 3rd Ed.* 2000, New York: McGraw-Hill.

201. Seymour, L., S. Murray, and L. John, *Schaum's Outline of Mathematical Handbook of Formulas and Tables, 4th Edition*. Schaum's Outline. 2012: McGraw-Hill.